

**GEOCHEMISTRY OF URANIUM AT MINERAL-WATER
INTERFACES: RATES OF SORPTION-DESORPTION AND
DISSOLUTION-PRECIPIATION REACTIONS**

Thesis by

Daniel Giammar

In Partial Fulfillment of the Requirements

for the Degree of

Doctor of Philosophy

California Institute of Technology

Pasadena, California

2001

(Defended May 8, 2001)

© 2001

Daniel Giammar

All Rights Reserved

Acknowledgments

My advisor Janet Hering has supported and encouraged me throughout my graduate student career. From her I have learned a great deal about aquatic chemistry and, by her example, much about scientific curiosity and discipline. She is consistently my best and most thorough critic. Michael Hoffmann's encouragement and suggestions have contributed in many ways to my work. George Rossman's mineralogical insight led to some of the most interesting experiments in this work. Jim Morgan has been a mentor and role model throughout my study at Caltech, and I would particularly like to thank him for his emphasis on the fundamentals, both scientifically and on the basketball court.

I would like to acknowledge the profound influence that Susan Leach, my middle school life and earth sciences teacher, had on my decision to pursue a career in environmental science and engineering. David Dzombak at Carnegie Mellon encouraged me to go to graduate school and remains a great role model for me. At Caltech, Gerald Wasserburg's enthusiasm for geochemistry got me interested in uranium and his encouragement contributed to the initiation of this work.

The summer undergraduate research projects of Helen Claudio and Yi-Ping Liu constitute portions of this work. When I would run into a problem with the X-ray diffractometer or scanning electron microscope, Chi Ma was always there to bail me out. Yulia Goreva gave generously of her time to get me started with SEM. Liz Arredondo helped me collect Raman spectra with remarkable efficiency. Andrea Belz sparked my interest in transmission electron microscopy, and Carol Garland's expertise with the TEM made it possible to acquire meaningful images in the final weeks of this project. Peter

Green and Yaniv Dubowski kept the ICP-MS running. Tatiana Piatina and Penny Kneebone lit my path at Caltech by getting me started in the lab. The smiles of Fran, Linda, Irene, Elena, and Belinda have all made Keck a great place to work.

Outside of the lab, bicycling up Mount Wilson or over the Glendora Mountain Road with David Anderson and Piet Moeleker were real highlights. I will certainly miss Sunday soccer and all of my teammates. Wednesday noon basketball was the carrot-on-a-stick that got me through some long weeks, and I'd like to thank Rob, Jeff, Jason, Mike, Pat, Denis, Gordon, Jim, and all the others who made it so much fun. Delores Bing and Allen Gross offered great musical outlets in chamber music and the Caltech-Occidental Orchestra. I would particularly like to acknowledge Isaac See, David Fang, and Nick Knouf who have made string quartets such a joy over the last two years.

My fellow 1996 first-years David Cocker, Tina Salmassi, Yael Dubowski, and Catherine Cornu have been great friends and colleagues. Life at Caltech would not have been the same without Rob Griffin, Ann McAdam, Peter Adams, Amy Rigsby, Matt Fraser and Brian King. I would particularly like to thank Jennie Stephens, Hugo Destailats, and Tim Lesko for helping me through some difficult times.

Far and away the biggest thanks go to my parents, Robert and Betty Giammar. By showing me the beauty in the natural world, valuing education so highly, acting as my financial safety net, and most importantly serving as my emotional support and inspiration, they have made everything possible for me.

Lastly, I thank my wife and best friend Michelle Vollmar for her unwavering support through five long years. Her love has made it all worthwhile. Whenever my walls are collapsing, she is the truth standing in the center.

Abstract

The extraction and processing of uranium for use in the nuclear weapons program and in commercial nuclear energy has led to extensive contamination of the environment. Migration of uranium is also a concern for the proposed long-term nuclear waste disposal in geologic repositories. Reactions occurring at mineral surfaces significantly affect the mobility of uranium in the environment. Both the equilibrium and kinetics of reactions at mineral surfaces must be understood in order to predict the extent of reactions on time scales pertinent to human exposure. Such information is needed to establish input parameters for reactive transport models and to design remediation technologies.

Rates of uranium sorption on mineral surfaces and the dissolution of uranium-containing minerals have been investigated. Rates of sorption onto and desorption from goethite, an important environmental sorbent, were determined by measuring the responses of goethite suspensions (pre-equilibrated with or without uranium) to perturbations of the solution chemistry. Dissolution rates were measured for a set of laboratory-synthesized minerals: the uranyl oxide hydrate schoepite, the uranyl silicate soddyite, and a uranyl phosphate phase. These minerals have been observed in contaminated environments and are produced during the corrosion of spent nuclear fuel. Mineral dissolution and transformation were monitored in batch reactors, while dissolution rates were quantified in flow-through reactors. In both sorption and dissolution-precipitation studies, measurements of bulk solution chemistry were integrated with solid phase characterization.

While sorption processes were rapid, dissolution and surface-precipitation reactions occurred more slowly. Adsorption and desorption reactions of uranium onto or from goethite reached greater than 50% completion within minutes and completion on a time-scale of hours. In some uranium-goethite suspensions, a meta-stable sorption state persisted for as long as three weeks before a schoepite-like phase precipitated. Dissolution reactions proceeded at time-scales of hours for schoepite and days to weeks for soddyite and the uranyl phosphate. Common groundwater cations affected dissolution rates and, in several cases, resulted in the precipitation of uranium in secondary phases. In several schoepite and soddyite batch dissolution experiments, uranium ultimately reprecipitated in sodium or cesium uranyl oxide hydrate phases which subsequently controlled the dissolved uranium concentration.

Contents

Acknowledgments	iii
Abstract	v
1	Introduction	1-1
	1.1	Motivation	1-1
	1.2	Research Scope and Objectives	1-7
	1.3	Research Approach	1-10
2	Environmental Geochemistry of Uranium in Soil, Sediment, and Groundwater Systems	2-1
	2.1	Aqueous Uranium Geochemistry	2-1
	2.2	Uranium in Sediments and Soils	2-5
		2.2.1	Overview	2-5
		2.2.2	Contamination at Department of Energy of Facilities	2-5
		2.2.3	San Joaquin Valley	2-8
		2.2.4	Uncontaminated Soils	2-9
		2.2.5	Ore Bodies	2-10
		2.2.6	Transport Modeling in Natural Systems	2-11
	2.3	Uranium Sorption on Mineral Surfaces	2-12
		2.3.1	Overview of Sorption Equilibrium and Kinetics	2-12
		2.3.2	Uranyl Sorption on Iron Oxyhydroxide Minerals	2-13

2.3.3	Uranyl Sorption on Aluminosilicate Minerals	..	2-16
2.3.4	Uranyl Association with Natural Organic Materials	..	2-18
2.4	Mineralogy of Uranium-Containing Minerals	2-19
2.4.1	Uranyl Mineral Structures	2-19
2.4.2	Environmental Uranyl Mineral Transformations	..	2-19
2.4.3	Uranyl Oxide Hydrates	2-21
2.4.4	Uranyl Silicates	2-24
2.4.5	Uranyl Phosphates	2-25
3	Kinetics of Uranyl Sorption on Goethite	3-1
3.1	Introduction	3-1
3.2	Materials and Methods	3-4
3.2.1	Materials	3-4
3.2.2	Experimental Methods	3-4
3.3	Results and Discussion	3-7
3.3.1	Adsorption and Surface Precipitation	3-7
3.3.2	Sorption Kinetics	3-10
3.3.3	Environmental Implications	3-17
	Acknowledgments	3-18
4	Investigation of Uranium-Loaded Goethite By Electron Microscopy		4-1
4.1	Introduction and Background	4-1
4.2	Experimental Materials and Methods	4-4

4.3	Results	4-7
	4.3.1	Scanning Electron Microscopy	4-7
	4.3.2	Transmission Electron Microscopy	4-9
4.4	Discussion	4-15
	4.4.1	Nature of Solid-associated Uranium	4-15
	4.4.2	Utility of Electron Microscopy	4-17
	4.4.3	Need for Additional Characterization..	4-18
	4.4.4	Conclusions	4-19
5	Dissolution and Transformation of Uranyl Oxide Hydrates	5-1
5.1	Introduction and Background	5-1
5.2	Experimental Materials and Methods	5-4
	5.2.1	Materials	5-4
	5.2.2	Batch Dissolution and Transformation Experiments	5-6
	5.2.3	Flow-through Dissolution	5-7
	5.2.4	Analytical Methods	5-7
	5.2.5	Equilibrium Calculations	5-9
5.3	Results	5-9
	5.3.1	Characterization of Synthesized Solids	5-9
	5.3.2	Batch Dissolution Experiments	5-12
		5.3.2.1 Determining the Influence of Sodium	5-12
		5.3.2.2 Experiments with Cesium, Ripened Schoepite, Dilute Solution, and Fluoride	5-19

	5.3.2.3	Post-equilibration Electrolyte Addition Experiments	5-26
	5.3.2.4	Raman Spectroscopy	5-29
	5.3.3	Flow-through Dissolution Experiments	5-30
5.4	Discussion	5-34
	5.4.1	Identification and Equilibrium Solubility of Endmember	
		Phases	5-34
	5.4.2	Role of Monovalent Cations	5-39
	5.4.3	Schoepite Dissolution Rate	5-43
	5.4.4	Schoepite Transformation Rate	5-45
5.5	Conclusions	5-47
	5.5.1	Summary of Observations	5-47
	5.5.2	Environmental Implications	5-48
6	Soddyite Dissolution and Transformation Rates	6-1
	6.1	Introduction	6-1
	6.2	Experimental Materials and Methods	6-3
	6.2.1	Soddyite Synthesis	6-3
	6.2.2	Dissolution Experiments	6-4
	6.2.3	Analytical Methods	6-5
	6.2.4	Equilibrium Calculations	6-6
	6.3	Results	6-8
	6.3.1	Soddyite Characterization	6-8
	6.3.2	Batch Dissolution Experiments	6-9

	6.3.2.1	Solution Chemistry	6-9
	6.3.2.2	Characterization of Partly-reacted Solids	..				6-11
	6.3.3	Flow-through Dissolution Experiments			6-13
6.4	Discussion	6-17
	6.4.1	Equilibrium Soddyite Solubility		6-17
	6.4.2	Predicted Equilibrium of Mixed Solid System	..				6-20
	6.4.3	Evolution of Solid Phases and Dissolved Concentrations					6-21
	6.4.4	Soddyite Dissolution Rate Quantification			6-23
6.5	Conclusions	6-24
	Acknowledgments	6-26
7	Uranyl Phosphate Dissolution and Transformation				7-1
	7.1	Introduction and Background	7-1
	7.2	Experimental	7-5
	7.2.1	Synthesis of Solid Phases	7-5
	7.2.2	Dissolution Experiments	7-6
	7.2.3	Analytical Methods	7-8
	7.3	Results	7-9
	7.3.1	Characterization of Synthesized Solids			7-9
	7.3.2	Batch Dissolution	7-15
	7.3.2	Flow-through Dissolution	7-17
	7.4	Discussion	7-20
	7.4.1	Evolution of Calcium-Uranyl-Phosphate Toward					

	Equilibrium	7-20
7.4.2	Dissolution Rate Quantification	7-23
7.4.3	Environmental Implications	7-25
8	Conclusions	8-1
8.1	Summary of Experimental Work	8-1
8.1.1	Uranium Uptake on Mineral Surfaces	8-1
8.1.2	Dissolution and Transformation of Uranyl Minerals	8-2
8.2	Environmental Implications	8-4
8.2.1	Mobility of Uranium at Contaminated Sites	8-4
8.2.2	Long-term Behavior of Geologic Repositories	8-6
8.3	Suggestions for Future Research	8-7
8.3.1	Extension to Different Materials and Solution Compositions	8-7
8.3.2	Phenomena in Aquatic Chemistry	8-8
8.3.3	Extension to the Field Environment	8-10
References	R-1
A	Thermodynamic Database Review	A-1
A.1	Introduction	A-1
A.2	Dissolved Species	A-2
A.2.1	Selected Databases	A-2

	A.2.2	Calculation of Activity Coefficients	A-2
	A.2.3	Hydrolysis Species	A-3
	A.2.4	Uranyl Carbonate Complexes	A-8
	A.2.5	Uranyl Phosphate Complexes	A-9
	A.3	Schoepite Solubility	A-10
B		Rates of Uranium(VI) Sorption on Montmorillonite	B-1
	B.1	Introduction	B-1
	B.2	Experimental	B-4
	B.2.1	Materials	B-4
	B.2.2	Sorption Equilibrium	B-6
	B.2.3	Sorption Kinetics	B-7
	B.3	Results and Discussion	B-8
	B.3.1	Equilibrium Sorption	B-8
	B.3.2	Adsorption Kinetics	B-10
	B.3.3	Responses of Pre-equilibrated Suspensions to Dilution						B-12
	B.3.4	Rates of Response to pH Adjustment				B-14
	B.3.5	Rates of Ion-exchange		B-16
	B.3.6	Environmental Implications		B-16

C	Uranium Release from Mixed Goethite-Schoepite Systems	..						C-1
C.1	Introduction	C-1
C.2	Materials and Methods		C-3
C.3	Results and Discussion		C-5
	C.3.1 Characterization of Stock Goethite-Schoepite Suspensions							C-5
	C.3.2 Release of Uranium Following Dilution					C-8
D	Becquerelite Dissolution and Transformation				D-1
D.1	Introduction	D-1
D.2	Materials and Methods		D-2
D.3	Results	D-3
	D.3.1 Characterization of Synthetic Becquerelite					D-3
	D.3.2 Batch Dissolution Experiments				D-6
D.4	Discussion	D-8

List of Figures

1.1	Locations of U.S. Sites with Uranium Contamination of Soils and/or Groundwater	1-3
1.2	Conceptualization of the Distribution of Uranium in Saturated or Unsaturated Porous Media	1-7
2.1	pe-pH Diagram for the System U-O ₂ -CO ₂ -H ₂ O	2-3
2.2	Speciation of Dissolved Uranium as a Function of pH	2-4
3.1	Metastable Sorption of Uranyl on Goethite	3-8
3.2	Time-dependence of Uranium Partitioning	3-9
3.3	X-ray Diffraction Patterns of Solids from Uranium-goethite Suspensions	3-11
3.4	Complementary Adsorption and Desorption of Uranium on Goethite	3-12
3.5	Fluoride-induced Desorption of Uranium from Goethite	3-13
3.6	Isotope Exchange between Dissolved and Sorbed Uranium	3-14
3.7	Effects of Aging Time on Desorption of Uranium from Goethite .. .	3-16
4.1	Scanning Electron Micrographs and X-ray Element Mapping of Uranium- Loaded Goethite Samples Aged in Suspension for 96 Days	4-8
4.2	Time-series of Scanning Electron Micrographs and X-Ray Elemental Mapping of Uranium-loaded Goethite Samples ([U] _{tot} = 40 μM) .. .	4-9
4.3	Time-series of Scanning Electron Micrographs and X-Ray Elemental Mapping of Uranium-loaded Goethite Samples ([U] _{tot} = 80 μM) .. .	4-10
4.4.	Transmission Electron Microscope Images and Selected Area Diffraction Patterns of Clusters Containing Only Goethite or Uranyl Oxide Hydrate	

	Particles	4-11
4.5	Transmission Electron Microscope Images of a Mixed Aggregate of Goethite Particles and Particles of a Uranium-containing Phase from 3-month 500 μ M Uranium Sample	4-12
4.6	Transmission Electron Microscope Images of Solids From Suspension Isolated After 3 Days of Equilibration with 80 μ M Uranium ..	4-13
4.7	Transmission Electron Microscope Images of Solids From Goethite Suspension Isolated After 1 Day of Contact with 80 μ M Uranium	4-14
4.8	Schematic Representation of the Growth of Uranium-Containing Precipitates Following Adsorption on Goethite	4-16
5.1	X-ray Diffraction Patterns of Synthetic Schoepite	5-11
5.2	Raman Spectra of Synthetic Schoepite	5-11
5.3	Batch Schoepite Dissolution at pH 6 in NaNO_3	5-14
5.4	Scanning Electron Micrographs of Schoepite Before and After Dissolution	5-15
5.5	Time-series of X-ray Diffraction Patterns Following the Dissolution of Schoepite in 0.01 M NaNO_3 Solution at pH 6	5-16
5.6	Scanning Electron Micrographs of Schoepite Before and After Dissolution in NaNO_3 , CsNO_3 , and Dilute Solution.	5-17
5.7	Time-series of X-ray Diffraction Patterns of the Transformation of Residual Solids from a Batch Dissolution Experiment Upon Resuspension ..	5-18
5.8	Batch Schoepite Dissolution at pH 6 in CsNO_3 Solution	5-20
5.9	Time-series of X-ray Diffraction Patterns Following the Dissolution of Schoepite at pH 6 in 0.1 M CsNO_3	5-20

5.10	X-ray Diffraction Patterns of Parr Bomb-Ripened Schoepite Before and After Batch Dissolution	5-21
5.11	Batch Schoepite Dissolution at pH 6 in Dilute Solution	5-23
5.12	Batch Dissolution of Schoepite at pH 6 in Dilute Solution Following the Addition of 0, 1, and 5 mM Sodium Fluoride	5-24
5.13	X-ray Diffraction Patterns of Stock Schoepite and Material Subjected To Batch Dissolution in Dilute or Sodium Fluoride Solution ..	5-26
5.14	Evolution of Dissolved Uranium and pH Following the Addition of NaNO_3 or CsNO_3 to Pre-equilibrated Suspensions in Dilute Solution	5-27
5.15	X-ray Diffraction Patterns of Solids from Suspensions Originally Pre-equilibrated with Schoepite in Dilute Solution and then Adjusted with NaNO_3 or CsNO_3	5-28
5.16	Raman Spectra of Uranyl Oxide Hydrates	5-29
5.17	Influent and Effluent Uranium Concentrations in Flow-through Dissolution Experiments	5-32
5.18	Schoepite Dissolution Rate Versus the Dissolved Uranium Concentration from Flow-through Reactor Data	5-33
6.1	Synthetic Soddyite X-ray Diffraction Patterns	6-7
6.2	DRIFTS Spectrum of Synthetic Soddyite	6-8
6.3	Batch Soddyite Dissolution	6-9
6.4	Dissolved Uranium Versus Silicon Concentrations During Batch Soddyite Dissolution	6-11

6.5	Time Series of X-ray Diffraction Patterns for Solids Collected from Batch Soddyite Dissolution Experiments	6-12
6.6	Scanning Electron Micrographs of Solids Collected During Batch Soddyite Dissolution	6-14
6.7	Raman Spectra of Stock and Reacted Soddyite	6-15
6.8	Flow-through Soddyite Dissolution	6-17
7.1	Uranium Speciation in Uranyl-Phosphate-Carbonate Solution ..	7-3
7.2	X-ray Diffraction Patterns of the Synthesized Uranyl Phosphate Solids	7-10
7.3	Scanning Electron Micrographs of Uranyl Phosphate Solids ..	7-12
7.4	Raman Spectra of Uranyl Phosphate Solids	7-13
7.5	Evolution of Dissolved Concentrations of Uranium, Phosphorus, and Calcium in Batch Dissolution Experiments	7-14
7.6	Time-series of X-ray Diffraction Patterns of Solids During Batch Dissolution	7-16
7.7	Effluent Uranium and Phosphorus Concentrations From Flow-through Reactors	7-18
A.1	Schoepite Solubility Calculated Using the Thermodynamic Constants of Four Previous Studies	A-12
A.2	Schoepite Solubility and Dissolved Speciation as a Function of pH ..	A-13
B.1	Effects of pH and Ionic Strength on Uranium Sorption on Montmorillonite	B-3
B.2	X-ray Diffraction Patterns of Untreated and Treated Montmorillonite	B-5
B.3	Equilibrium Sorption of Uranium on Montmorillonite	B-9
B.4	Dissolved and Sorbed Uranium Concentrations During Adsorption on	

	Montmorillonite	B-11
B.5	Dissolved and Sorbed Uranium Concentrations Following the 1:10 Dilution of Pre-equilibrated Uranium-Montmorillonite Suspensions	B-13
B.6	Dissolved and Sorbed Uranium Concentrations Following the pH Adjustment of Pre-equilibrated Uranium-Montmorillonite Suspensions	B-15
B.7	Dissolved and Sorbed Uranium Concentrations Following the Ionic Strength Adjustment of a Pre-equilibrated Uranium-Montmorillonite Suspension	B-17
C.1	X-ray Diffraction Patterns of Solids Collected from Mixed Suspensions of Goethite and Schoepite	C-7
C.2	Scanning Electron Micrographs of Solids Collected from a Suspension with Sorbed Uranium and a Mixed Goethite-Schoepite Suspension ..	C-8
C.3	Evolution of the Uranium Distribution Following the Dilution of Equilibrated Goethite-Schoepite Suspensions	C-9
D.1	X-ray Diffraction Patterns of Becquerelite and Schoepite	D-4
D.2	Scanning Electron Micrograph of Solids from Becquerelite Synthesis	D-5
D.3	Raman Spectra of Schoepite and Becquerelite	D-5
D.4	Batch Dissolution of Becquerelite at pH 6 in 0.1 M NaNO ₃ Solution	D-7

List of Tables

2.1	Reduction Potentials of Uranium Half Reactions	2-3
2.2	Uranyl Minerals That May Form in Porous Media	2-20
4.1	Uranium Concentrations in Solid-Phase Samples as a Function of Total Uranium Concentration and Time	4-5
5.1	Representative Uranyl Oxide Hydrate Minerals	5-2
5.2	X-ray Diffraction Reflections of Uranyl Oxide Hydrate Solids	5-10
5.3	Batch Schoepite Dissolution Experiments Performed	5-13
5.4	Flow-through Schoepite Dissolution Experiments Performed	5-31
5.5	Equilibrium Solubility Constants for Schoepite	5-36
5.6	Evolution of Solution Chemistry and the Net Change in Alkalinity During Post-equilibration Electrolyte Spike Experiments	5-41
6.1	Aqueous Phase Reactions and Thermodynamic Stability Constants for Soddyite System	6-7
6.2	Soddyite Solubility Products	6-18
7.1	Compositions of Environmentally Significant Uranyl Phosphate Minerals	7-2
7.2	Dissolution Reactions and Associated Solubility Products	7-4
7.3	Experimental and Reference X-ray Diffraction Lattice Spacings	7-11
7.4	Conditions and Calculated Dissolution Rates of Flow-through Dissolution Experiments	7-19

A.1	Aqueous Phase Uranium Complexation Reactions and Thermodynamic Stability Constants	A-4
A.2	Thermodynamic Stability Constants for Auxiliary Reactions ..	A-5
A.3	Published Formation Constants for UO_2OH^+	A-6
A.4	Published Formation Constants for $\text{UO}_2(\text{OH})_{2(\text{aq})}$	A-6
A.5	Published Formation Constants for $\text{UO}_2(\text{OH})_3^-$	A-7
A.6	Published Formation Constants for $(\text{UO}_2)_2(\text{OH})_2^{2+}$	A-7
A.7	Published Formation Constants for $(\text{UO}_2)_3(\text{OH})_5^+$	A-8
A.8	Published Formation Constants for $(\text{UO}_2)_3(\text{OH})_7^-$	A-8
A.9	Published Formation Constants for Uranyl Carbonate Complexes ..	A-9
A.10	Published Formation Constants for Uranyl Phosphate Complexes ..	A-9
A.11	Previous Investigations of Schoepite Solubility	A-11
B.1	Batch Sorption Kinetics Performed for Uranium-Montmorillonite System	B-7
C.1	Goethite-Schoepite Mixed Suspensions	C-4
D.1	X-ray Diffraction Reflections of Synthetic Uranyl Oxide Hydrate Solids	D-4

List of Abbreviations

DRIFTS – diffuse reflectance infrared fourier transform spectroscopy

EDX – energy dispersive X-ray analysis

EXAFS – extended X-ray absorption fine structure spectroscopy

FEMP – Fernald Environmental Management Project

NEA – Nuclear Energy Agency

OECD – Organisation for Economic Co-operation and Development

ORNL – Oak Ridge National Laboratory

SEM – scanning electron microscopy

SIT – specific ion interaction theory

SKB – Swedish Nuclear Fuel and Waste Management Company

SRS – Savannah River Site

SXRF – synchrotron X-ray fluorescence

TEM – transmission electron microscopy

XANES - X-ray absorption near-edge structure spectroscopy

XRD – X-ray diffraction

Chapter 1

INTRODUCTION

1.1 Motivation

The contamination of groundwater by heavy metals and radionuclides poses a direct threat to water supplies, while the contamination of surface soils poses an unrealized but equally important threat to groundwater resources. The fate and transport of metals and radionuclides in porous media is strongly influenced by interactions occurring at mineral-water interfaces. A comprehensive understanding of the equilibrium and kinetics of the chemical reactions occurring at mineral-water interfaces is essential to the management of contaminated soil and groundwater systems. As a result of the processing and disposal of materials during nuclear energy and weapons production, uranium is a ubiquitous contaminant in many environmental systems.

A Federal standard for uranium in drinking water was recently promulgated; the maximum contaminant level (MCL) of $30 \mu\text{g L}^{-1}$ will become effective in December 2003 (U.S.EPA, 2000). California has already adopted an MCL of 20 pCi/L ($\sim 25 \mu\text{g L}^{-1}$) based on renal toxicity (Wong et al., 1999). The adverse effects of uranium on kidney function are the dominant toxic effects of this element, a function of its chemical properties rather than its radioactivity. The radioactivity of uranium does pose additional

carcinogenic risks; however, the very long half-lives of the dominant uranium isotopes generally make radiotoxicity a secondary consideration (U.S.EPA, 2000).

The United States' nuclear weapons program has left a legacy of environmental contamination. The contamination is extensive and widespread, associated with the manufacturing of nuclear weapons in a network of 113 installations around the country. Cleaning up the contamination caused by the manufacturing of nuclear weapons in the United States has been called "the most monumental environmental restoration task in history" (MacDonald, 1999). Uranium mining, milling, and refining generated the largest volume of weapons-related waste. The U.S. Department of Energy (DOE) manages about 79 million cubic meters of contaminated solid media (mostly soils) and about 1,800 million cubic meters of contaminated water (mostly groundwater). Contaminated environmental media from nuclear weapons activities are located at 64 DOE environmental management sites in 25 states. Remediation decisions have not been made for many contaminated sites, and, in some cases, remediation is considered either unnecessary or impractical (U.S.DOE, 1997). The map in Figure 1.1 shows the locations of the sites discussed below in more detail.

At the Hanford site in Washington, perhaps the best known contaminated site in the United States, uranium contamination of soil and groundwater has resulted from storage and waste disposal practices. An estimated 4000 kg of uranium was disposed of to cribs receiving processing plant drainage. Uranium is present in groundwater plumes intersecting the Columbia River and was detected in the river in 1997 (U.S.DOE, 1998). Similar plutonium production processes to those at Hanford were performed at the Savannah River Site (SRS), Aiken, South Carolina. Soils and sediments at the SRS have

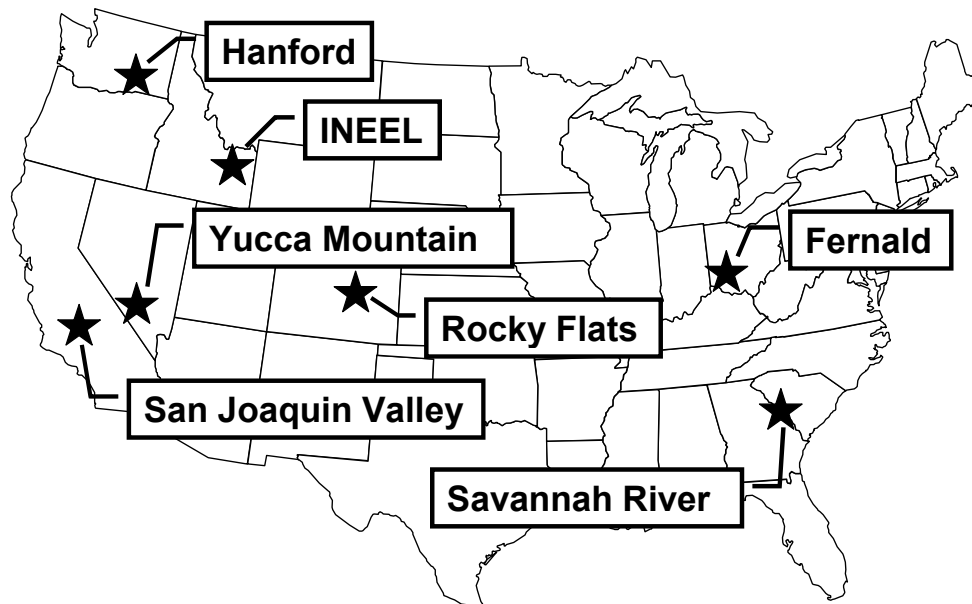


Figure 1.1: Locations of U.S. sites discussed in the text with uranium contamination of soils and/or groundwater. While the proposed geologic repository for nuclear waste at Yucca Mountain currently does not have uranium contamination, it would become the most concentrated anthropogenic uranium deposit should it become operational.

been contaminated by past waste disposal practices, which included disposal of acidic aqueous wastes to infiltration ditches and the disposal of 45,000 kg of uranium to a settling basin (Batson et al., 1996; Kaplan et al., 1994a).

As a consequence of uranium ore processing at the Fernald Environmental Project (FEMP) in southwestern Ohio, the aqueous and airborne release of uranium contaminated approximately two million m³ of soils above the regulatory level of 52 mg kg⁻¹ (Elless and Lee, 1998). At the FEMP, significant mobilization has occurred in the vadose zone and has extended into the saturated zone of the Great Miami Aquifer (Elless and Lee, 1998; Sidle and Lee, 1996). Soils at the Rocky Flats Plant (RFP) near Golden, Colorado, are contaminated with uranium as a result of past waste storage practices. Approximately 31 kg of uranium was released at RFP, most of it as airborne particles. The deposition of

the particles contaminated the surface soil and may have leached down into deeper soil horizons (Litaor, 1995). Groundwater plumes of uranium contamination have been studied at the Idaho National Engineering and Environmental Laboratory (Beasley et al., 1998; Luo et al., 2000) and at the Nevada test site (Copenhaver et al., 1992).

The mining of uranium for use in subsequent processing can lead to extensive contamination, particularly when tailings storage barriers are breached (Landa and Gray, 1995). In situ pressure-leach mining with acidic oxidizing solutions can lead to extensive soil contamination (Duff et al., 1998). Significant amounts of uranium can be leached from exposed mine tailings by rainwater in only a few years (Schimmack et al., 2000). Vegetation and small animals in the habitat surrounding two open pit uranium mines in northern Saskatchewan have been impacted by off-site migration, and surface soils have elevated uranium concentrations when compared with a control site (Thomas, 2000a; Thomas, 2000b; Thomas, 2000c). Groundwater transport of uranium from mining locations has been studied in Brazil (Cross et al., 1991) and Germany (Biehler and Falck, 1999; Nitzsche and Merkel, 1999).

Not all sites with elevated uranium are the result of past waste management practices at DOE facilities; some dangerously high levels of uranium are also present in natural systems. Groundwater in California has been found to contain uranium at concentrations as high as $135.6 \mu\text{g L}^{-1}$ and 30% of wells tested in a recent study had concentrations greater than $35 \mu\text{g L}^{-1}$ (Wong et al., 1999). Agricultural drainage waters in California's San Joaquin Valley have particularly high uranium concentrations with values as high as $22,300 \mu\text{g L}^{-1}$. The uranium in the drainage waters is derived from

marine cretaceous shale materials and is leached from the soils by intensive irrigation (Duff and Amrhein, 1996).

Concentrated deposits of uranium in the environment occur in uraninite, $U(IV)O_2(s)$, ore bodies, and may be generated in the future at geologic repositories for nuclear waste, which consists primarily of uranium-rich spent nuclear fuel. During the weathering of uraninite, a series of secondary minerals including uranium (VI) oxyhydroxides, phosphates, silicates, sulfates, and carbonates is precipitated (Finch and Murakami, 1999). The secondary minerals then constitute source phases for uranium mobilization. An alteration sequence similar to that observed in the environment for uraninite is observed in the alteration of spent nuclear in contact with synthetic groundwater solutions (Wronkiewicz and Buck, 1999). The mobilization of uranium and associated radionuclides from the corrosion of spent nuclear fuel is retarded by precipitation in secondary uranyl phases (Chen et al., 2000; Finn et al., 1996). Shoesmith (2000) has reviewed the mechanisms of spent nuclear fuel corrosion under conditions expected in the Yucca Mountain geologic repository.

The intersection of human and environmental time-scales necessitates an understanding of reaction kinetics as well as equilibrium. The time-scales of sorption and precipitation-dissolution reactions are similar to the residence times of natural water systems including groundwaters, and consequently many natural water systems are not at chemical equilibrium (Langmuir, 1997). Kinetic and equilibrium information together can explain the behavior of metals in non-equilibrium systems.

The determination of reaction rates has important applications in the management and remediation of contaminated sites. Reaction mechanisms and reaction rate constants

can be incorporated into hydrogeochemical reactive transport models for contaminant mobility. Many coupled hydrogeochemical reactive transport models have recently been developed (Lichtner, 1996; Steefel and MacQuarrie, 1996), but they frequently suffer from a lack of information regarding chemical equilibrium and kinetics. Reaction rates are also key parameters for the design of water treatment and site remediation strategies. For example, removal of uranium from contaminated media has been performed in bench- and pilot-scale soil washing systems with a variety of extractants (Buck et al., 1996; Dhoum and Evans, 1998; Duff et al., 1998; Francis and Dodge, 1998; Francis et al., 1999; Mason et al., 1997). The design of a soil washing system can be optimized if the distribution of uranium in the soil matrix is known, and if the relevant chemical equilibrium and kinetics constants are available. Reaction rates can also be important parameters in the design of conventional water treatment processes like ion-exchange and enhanced coagulation by which uranium can be removed from potable water.

The study of uranium can also yield information about the behavior of other heavy metal and radionuclide contaminants. Uranium is convenient for investigation because it is easily analyzed by mass spectrometric techniques because of its high mass to charge ratio. Uranium can also be used as a proxy for transuranic actinides like plutonium and neptunium, which are often found at the same contaminated sites as uranium. The direct study of plutonium and neptunium is often difficult because of the low concentrations and high toxicities of these radionuclides. The behavior of the transuranic actinides can be related to that of uranium because of the similar chemical properties of these elements.

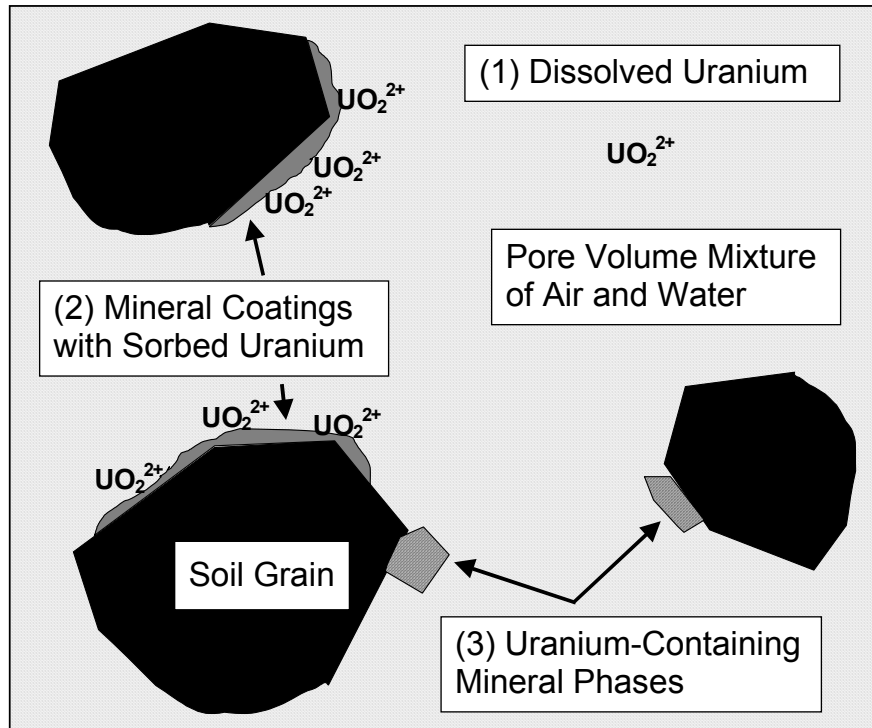


Figure 1.2: Conceptualization of the distribution of uranium in saturated or unsaturated porous media. Uranium can be present either (1) as dissolved species in the pore water, (2) adsorbed onto reactive mineral surfaces, or (3) precipitated in discrete uranium-containing mineral phases.

1.2 Research Scope and Objectives

The central hypothesis of this work is that the rate of uranium release in oxidized environments is governed by the speciation of uranium in the solid phase. In oxidized environments, uranium is thermodynamically stable in the +VI oxidation state and reduction to uranium(IV) is not considered in this study. In contaminated porous media, uranium is distributed among (1) dissolved species in the pore water, (2) sorbed species on mineral surfaces, and (3) discrete uranium-containing mineral phases (Fig. 1.2). A preliminary question addressed in this study is whether the release of uranium into solution by desorption and dissolution can be distinguished based on characteristic time-scales for these processes.

In the examination of sorption processes, the primary goals are the determination of characteristic time-scales and the identification of the mechanisms for adsorption and desorption reactions and the consequent limits on reaction rates. It is anticipated that sorption will be rapid if limited only by the rate of chemical attachment to the surface, but slower if limited by diffusion in the solid phase(s). Rates of desorption from different minerals can be compared to probe the effects of the surface site type and sorption mechanism (i.e., inner- versus outer-sphere coordination) on the desorption reaction. Ultimately, an understanding of the structure of the uranium surface complex can provide a mechanistic basis for interpreting sorption rates.

As the uranium loading increases, surface-precipitation of uranium will succeed the initial sorption of uranium on mineral surfaces. It is hypothesized that the rate of uranium release from surface precipitates will be intermediate between the rates for desorption and dissolution. The formation of surface precipitates will likely be slower than simple adsorption, and initially a metastable state may exist in which the dissolved uranium concentration is controlled by sorption despite being supersaturated with respect to a uranium-containing solid. Since surface precipitation is not easily distinguishable from sorption solely on the basis of bulk solution measurements, spectroscopic techniques must be applied to identify surface precipitates.

The dissolution of uranium-containing minerals is expected to be slower than either desorption or the dissolution of surface-precipitates. When present, uranium-containing minerals should control the dissolved concentration and mobility of uranium. In the study of dissolution processes, the primary goal is the quantification of the dissolution rates of different uranium-containing minerals. Differences in dissolution

rates are expected for different classes of minerals (i.e., oxyhydroxides, silicates, and phosphates). Since dissolution rates can only be properly interpreted if equilibrium solubility constraints are understood, an ancillary objective is the determination of solubility products for uranium-containing minerals. A related question is the relationship between the dissolution rate and the thermodynamic driving force of the dissolution reaction.

In addition to the quantification of dissolution rates, the issue of transformation is examined. The exposure of a mineral to solutions undersaturated with respect to that phase may lead not only to dissolution, but also to the formation of secondary phases. It may be possible to relate the effect of solution chemistry on the long-term behavior of uranium minerals to the chronological sequence of mineral formation in heterogeneous systems. Ultimately, a combination of equilibrium and kinetic information can assist in developing a quantitative model for the paragenetic sequence of minerals formed during the weathering of uraninite or spent nuclear fuel.

Throughout the project, an auxiliary objective is the identification of analytical tools applicable to the characterization of solid-associated uranium. It is hoped that a comprehensive understanding of the uranium distribution in a heterogeneous system can be achieved by applying an appropriate suite of techniques. An optimal suite of techniques will span a range of spatial scales, allow high sample throughput, and minimize sample disturbance.

1.3 Research Approach

To meet the objectives discussed above, a series of controlled laboratory experiments was designed and conducted. Controlled laboratory experiments were selected over field investigations for several reasons. Because this work focused on the mechanistic understanding of chemical processes, it was desirable to isolate particular processes for extensive study. Once individual processes are understood in isolation, their operation in the highly complex field setting can be identified and further characterized. Additionally, practical considerations of resource limitations and the difficulty of gaining access to nuclear waste contaminated sites contributed to the selection of laboratory-based research. The control of the master variables of pH and p_e is fundamental to these experiments. All experiments were performed under oxidizing conditions and, with very few exceptions, at pH 6.

The kinetics of uranium sorption on mineral surfaces was studied for the iron oxyhydroxide mineral goethite and the clay mineral montmorillonite. In the sorption studies, the equilibrium sorption behavior of a uranium-mineral system for given solution conditions was first established, and then reaction kinetics were investigated by measuring the responses of pre-equilibrated systems to perturbations. Adsorption and desorption rates were observed following major perturbations of the equilibrium, and solution-surface exchange under near equilibrium conditions was measured by isotope exchange. Sorption and surface-precipitation of uranium on goethite results are presented in Chapter 3, and the sorption of uranium on montmorillonite is discussed in Appendix B.

In all experiments, an approach was followed that integrates macroscopic solution chemistry measurements with microscopic and molecular-scale characterization of the

reacting solids. Multiple techniques were used to probe specific aspects of the system at different spatial scales. In the characterization of uranium-containing minerals, X-ray diffraction was the most widely used technique, providing information on the crystal structure of the minerals. Scanning electron microscopy (SEM) with energy dispersive X-ray analysis (EDX) was used to image individual grains and map the distribution of uranium. The molecular bonding environment of uranium atoms was investigated with infrared and Raman spectroscopies. Chapter 4 discusses the characterization of surface-precipitated uranium on goethite with SEM-EDX and transmission electron microscopy (TEM).

The dissolution behavior of uranium (VI) oxide hydrate, silicate, and phosphate minerals was investigated in batch and flow-through dissolution experiments. Batch experiments allowed the observation of the long-term behavior of the system, including the formation of secondary phases. Batch experiments were continued until dissolved concentrations reached constant values, allowing the evaluation of the equilibrium solubility. Mineral dissolution rates were quantified in flow-through dissolution experiments conducted under steady-state conditions. In flow-through reactors, the effect of changes in the driving force for the dissolution reaction were evaluated by altering the composition of the influent to the reactors. The dissolution and transformation of the uranyl oxide hydrate mineral schoepite is examined in Chapter 5, the uranyl silicate mineral soddyite in Chapter 6, and uranyl phosphate minerals in Chapter 7.

Finally, in Chapter 8 the major results of this research are summarized. Important accomplishments are highlighted, and areas for future research are identified.

Chapter 2

ENVIRONMENTAL GEOCHEMISTRY OF URANIUM IN SOIL, SEDIMENT AND GROUNDWATER SYSTEMS

2.1 Aqueous Uranium Geochemistry

Uranium in the +VI oxidation state is relatively soluble and can be detected in almost any natural water. Seawater is the largest reservoir of dissolved uranium and contains uranium at a highly uniform value of $3.3 \mu\text{g L}^{-1}$. The concentration of uranium in groundwater is usually in the range $0.1\text{-}50 \mu\text{g L}^{-1}$. In groundwaters, the weathering of uranium-bearing rocks and minerals is the source of dissolved uranium. Uranium is most concentrated in sedimentary rocks, particularly organic shales, and is also found in significant amounts in metamorphic and igneous rocks, with higher concentrations in granites than in basalts (Gascoyne, 1992).

Uranium is in the actinide series, which corresponds to the filling of the $5f$ electron orbital subshell. The six valence electrons of uranium are $5f^3 6d^1 7s^2$. The actinides have large atomic radii and, as a result, often have high coordination numbers (Shriver et al., 1994). Primordial uranium is present primarily as the isotope ^{238}U with a minor amount as ^{235}U . The isotope ^{234}U occurs naturally as a daughter in the ^{238}U

radioactive decay series. Following the advent of man-made nuclear fission, ^{233}U and ^{236}U are now present in appreciable amounts.

Uranium solubility in aqueous systems is predominantly controlled by three factors: oxidation-reduction potential, pH, and dissolved carbonate (Murphy and Shock, 1999). In aqueous solution uranium can exist in oxidation states of +III, +IV, +V, and +VI; however, under environmental conditions only the tetravalent and hexavalent states are stable. The reduction half reactions and associated potentials for all of the uranium oxidation states are given in Table 2.1. A pe-pH plot showing the domains of stability of dissolved and solid uranium species is given in Figure 2.1. Uranium(VI) is considerably more soluble than uranium(IV). Under reducing conditions, uranium(IV) complexes with hydroxide or fluoride are the only dissolved species (Gascoyne, 1992). The precipitation of uranium(IV) under reducing conditions is the dominant process leading to naturally enriched zones of uranium in the subsurface (Osmond and Cowart, 1992).

The reduction of uranium from the hexavalent to the tetravalent state can be microbially mediated. The geomicrobiology of uranium was recently reviewed by Suzuki and Banfield (1999). The organisms capable of reducing uranium(VI) are iron-reducing (Fredrickson et al., 2000; Lovley et al., 1991) and sulfate-reducing organisms (Lovley and Phillips, 1992; Spear et al., 1999; Spear et al., 2000). This microbially mediated reduction has been proposed as an in-situ remediation strategy for contaminated sites (Abdelouas et al., 2000; Abdelouas et al., 1999; Bender et al., 2000).

In oxidizing aqueous environments, uranium (VI) is present as the linear uranyl dioxo ion (UO_2^{2+}) and an array of mononuclear and polynuclear hydrolysis species. With increasing carbonate concentrations, mononuclear uranyl carbonate species become

Table 2.1: Reduction potentials of uranium half reactions.

Reaction	E_H° (V)	pe°	$\log K$
$U^{4+} + e^- = U^{3+}$	-0.553	-9.35	-9.35
$4H^+ + UO_2^{2+} + 2e^- = 2H_2O(l) + U^{4+}$	+0.267	4.51	4.51
$UO_2^{2+} + e^- = UO_2^+$	+0.088	1.49	1.49
$UO_2^{2+} + 2e^- = UO_2(s)$	+0.411	6.95	13.89
$U_4O_9(s) + 2H^+ + 2e^- = 4UO_2(s) + H_2O(l)$	+0.456	7.71	15.41
$4\beta-U_3O_7(s) + 2H^+ + 2e^- = 3U_4O_9(s) + H_2O(l)$	+0.517	8.74	17.48
$U_3O_8(s) + 2H^+ + 2e^- = \beta-U_3O_7(s) + H_2O(l)$	+0.565	9.55	19.10

(Grenthe et al., 1992)

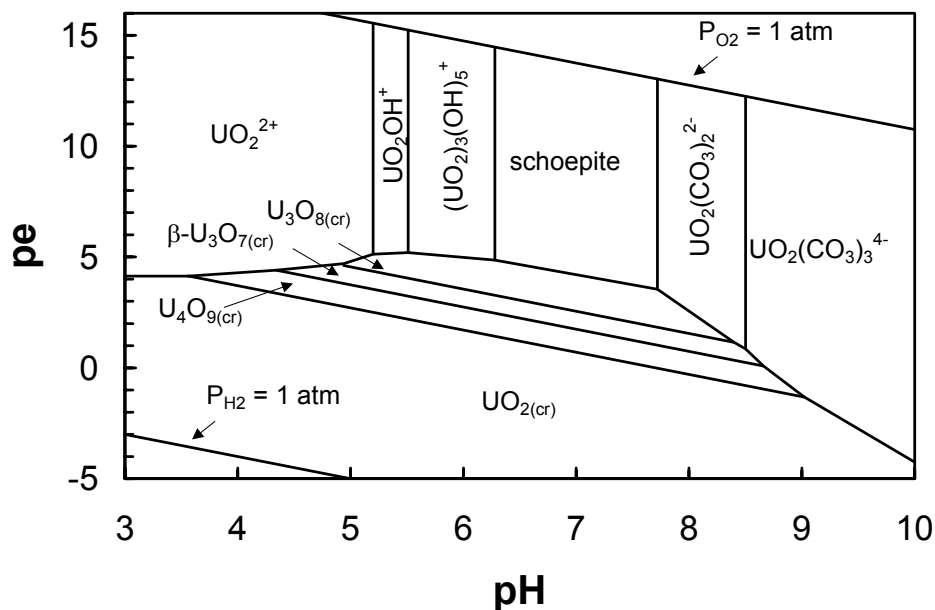


Figure 2.1: pe - pH diagram for aqueous species and solids in the system U - O_2 - CO_2 - H_2O at $25^\circ C$ and 1 bar total pressure for $[U]_{tot} = 5 \mu M$ and $P_{CO_2} = 10^{-3.5}$ atm. The diagram was constructed using the database of Grenthe et al. (1992) with the exception of the formation constants for $UO_2(OH)_2(aq)$ and schoepite, which were taken from Silva (1992). No ionic strength corrections have been made. A complete presentation and discussion of the selection of thermodynamic equilibrium constants is given in Appendix A.

increasingly important. Relevant aqueous complexes and their stability constants for the uranium (VI) system are given in Table A.1 of Appendix A. Dissolved uranium speciation as a function of pH in an open system is plotted in Figure 2.2 for a total uranium concentration of $5 \mu M$.

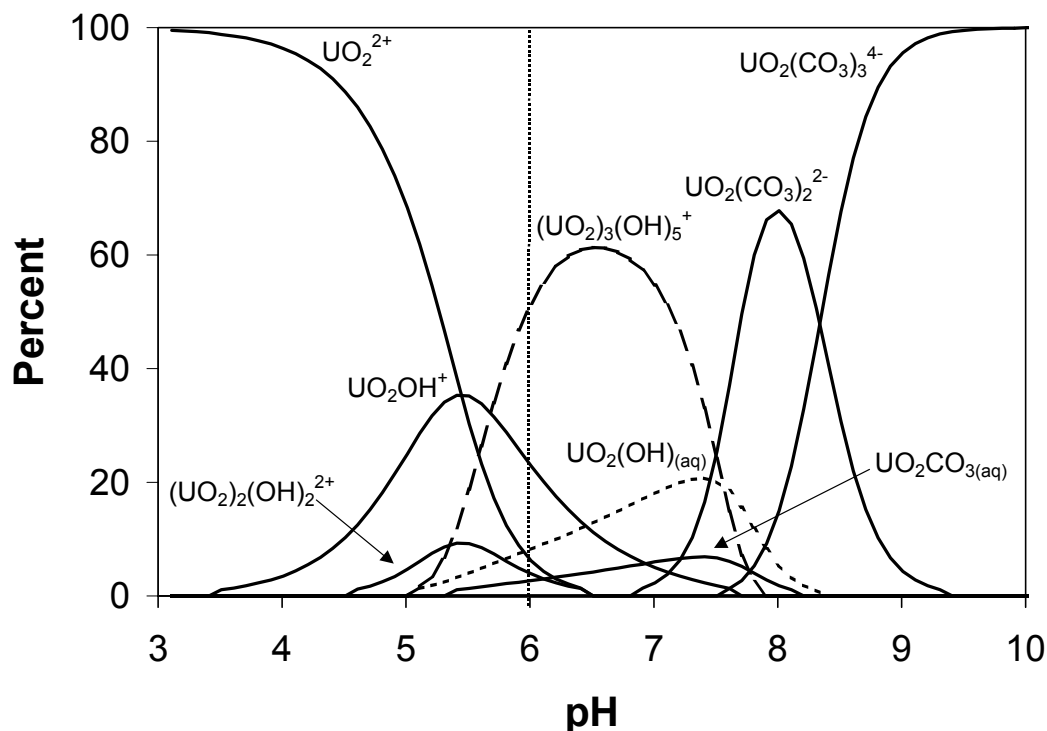


Figure 2.2: Speciation of dissolved uranium as a function of pH for $[\text{U}]_{\text{tot}} = 5 \mu\text{M}$, $I = 0.1 \text{ M}$, and $P_{\text{CO}_2} = 10^{-3.5} \text{ atm}$. Calculations were made without considering the precipitation of any solid phases.

Although the speciation of dissolved U(VI) is likely to be dominated by hydrolysis and carbonato complexes, complexes with sulfate, fluoride, and organic ligands may also occur in environmental systems. Carboxyl groups on naturally occurring humic and fulvic acids can strongly bind uranium (Gascoyne, 1992). Uranyl speciation with humic and fulvic acids has been studied by ion exchange (Lenhart et al., 2000; Montavon et al., 2000), potentiometry, and spectroscopy (Lubal et al., 2000). Results suggest that natural organic matter can significantly influence uranium speciation in environmental settings.

2.2 Uranium in Sediments and Soils

2.2.1 Overview

The behavior and speciation of the uranium in sediments and soils will be illustrated by examining a few sites with uranium from natural and contamination sources. Uranium is immobile when present in a precipitated form or adsorbed to immobilized solid media and mobile when present in the dissolved phase or associated with mobile colloids. Figure 1.2 is a schematic representation of the distribution of uranium in porous media.

Clearly the association of uranium with solid phases and the mobility of uranium is dependent on site-specific conditions. A few general trends describe the behavior of uranium in porous media. When dissolved carbonate concentrations are high, uranium is highly mobile due to the formation of uranyl-carbonate species. The sorption of uranium to aquifer materials is frequently dominated by association with iron oxyhydroxide minerals. The sorption of a variety of heavy metals to natural porous media can be modeled with only a $\text{Fe}(\text{OH})_3$ component (Davis et al., 1998). High phosphate in a system can lead to the precipitation of uranium in very insoluble uranyl phosphate minerals.

2.2.2 Contamination at Department of Energy Facilities

At the Fernald Environmental Management Project (FEMP) in Southwestern Ohio, high natural carbonate concentrations have led to uranium migration through the vadose zone and contamination of the underlying aquifer (Sidle and Lee, 1996).

Uranium migration through the surface soils has been modeled by considering two separate pools of solid-associated uranium, which the authors distinguish as soluble and insoluble (Killough et al., 1999). The distribution between soluble and insoluble pools may be correlated with the distribution between sorbed and precipitated uranium.

Discrete U(IV) particles in contaminated soils are surrounded by U(VI) particles and surface associated uranium (Hunter and Bertsch, 1998). The U(VI) particles have been identified as uranyl phosphate and oxide minerals (Buck et al., 1996; Morris et al., 1996).

The solubility of uranyl phosphate minerals was identified as the critical factor controlling uranium concentrations in porewater and groundwater wells (Elless and Lee, 1998). Airborne uranium-laden dust at the site contained a uranium (VI) oxide (UO_3) and a mixed oxidation state uranium oxide (U_3O_8) (Heffernan et al., 2001). Solid-associated uranium has been removed with 85% efficiency by washing with citric acid solution (Francis and Dodge, 1998), and with 75-90% efficiency with bicarbonate solution. The kinetics of release during bicarbonate washing were biphasic. A rapid initial release as uranium desorbed from the surface was followed by a slower continuing release controlled by the diffusion of uranium toward particle surfaces (Mason et al., 1997).

At the Hanford site, the sorption of uranium to sediments is correlated with the iron content (Barnett et al., 2000). The solution-solid partitioning of uranium on Hanford sediments increases with time and is affected by the moisture content of the sediment (Kaplan et al., 1996). In column experiments with contaminated Hanford sediments, the reduction of natural iron(III) minerals by injection of a sodium dithionite solution created an effective barrier to uranium transport by forming a zone where uranium(VI) was

reduced to uranium(IV) and precipitated on the surfaces of iron minerals (Szecsody et al., 1998).

At Oak Ridge National Laboratory (ORNL), uranium sorption on weathered limestone with extensive clay lenses is controlled by iron oxide coatings (Barnett et al., 2000). A sequential extraction of soils from two ORNL sites leached 45% of the total uranium with an extractant that targets carbonates and 40% with an extractant that targets iron oxides. The uranyl minerals schoepite, uranophane, coffinite, a uranyl-calcium oxide, and a uranyl-calcium phosphate were also identified in soils (Roh et al., 2000). Citric acid washing removed more than 85% of the uranium from a sludge sample (Francis and Dodge, 1998).

The uranium contamination at the Savannah River Site (SRS) is almost entirely in the +VI oxidation state and is observed both in highly enriched zones, which are likely to contain discrete uranium-containing particles, and also diffusely distributed as sorbed or coprecipitated phases (Bertsch et al., 1994). The uranium in soil from the contaminated zone is more labile than in soil from control samples (Clark et al., 1996). A sequential extraction demonstrated that the majority of uranium is associated with the organic bound fraction for organic rich (8-12% OC) sediment and with the amorphous iron oxide fraction for organic-poor (<2% OC) sediment (Hunter and Bertsch, 1998). Uranium sorption to a sandy soil is dominated by sorption to iron oxide coatings (Barnett et al., 2000). Uranium transport is enhanced by association with kaolinite and iron oxide colloids (Kaplan et al., 1994a; Kaplan et al., 1994b). Uranium in a drained sedimentation basin is primarily associated with MnO₂ and organic extractable fractions (Arey et al., 1999). In pond sediments contaminated with plutonium but not uranium, naturally

occurring uranium was predominantly in the residual solids following a sequential extraction procedure (Loyland et al., 2000). During episodic storm events, uranium is transported from the basin through association with suspended solids containing quartz, kaolinite, gibbsite, and goethite (Batson et al., 1996).

2.2.3 San Joaquin Valley

The sediments of two agricultural drainage ponds which have become enriched in uranium have been extensively characterized. One pond (pond 14) is generally more oxidized than the other (pond 16). The dominant minerals in pond 14 surface sediments are quartz, calcite/aragonite, montmorillonite and pyrite. The uranium content of the sediments is 5-280 mg/kg and is 72-75% U(VI) as determined by X-ray absorption near-edge structure spectroscopy (XANES). Considerable uranium was released during a leach with sulfuric acid, ammonium carbonate, and sodium bicarbonate. Luminescence spectroscopy characterized the uranium present in the surface sediments of Pond 14 as a uranyl tricarbonate phase and a uranyl hydroxide or hydroxycarbonate phase (Duff et al., 2000). The water in pond 14 has measured alkalinities between 50 and 98 meq/L and ionic strengths above 1 M. The reduction and reoxidation of uranium have also been studied for the sediments (Duff et al., 1997; Duff et al., 1999). The reduction of uranium(VI) is only partially dependent on E_h , and is also influenced by nutrient concentrations.

2.2.4 Uncontaminated Soils

A high degree of uranyl sorption on laterite soils was attributed to the amount of goethite present in the soils (Syed, 1999). A study of five U.S. soils found that the solid-water partitioning of radionuclides is related to the distribution of particles among three size classes: colloidal particles, humic acid polymers, and larger soil particles (Sheppard et al., 1980). A study of 13 French soils found a strong correlation between uranyl sorption and soil pH with sorption decreasing with increasing pH, an effect related to the inhibition of uranium sorption by carbonate in the higher pH soils (Echevarria et al., 2001). In arid zone soils with low carbonate, uranyl sorption increased up to pH 7 (Payne and Harries, 2000). Sorption of uranium to quartz-dominated sandy sediments was well correlated with the concentration of extractable iron and aluminum in the sediment (Rosentreter et al., 1998). As much as 91% of uranium in an upland organic soil was extracted in the iron oxide fraction (Dowdall and O'Dea, 1999). Approximately half of the uranium in a weathered granite soil was associated with goethite on soil particle surfaces (Megumi, 1979).

Uranium release from two soils was found to be kinetically and not thermodynamically controlled; the rate of uranium release decreased with time, but even after 400 days uranium release from the soils was still observed. The release of uranium could not be described by a single reaction, and at least three reactions were necessary to model the release to solution (Braithwaite et al., 1997). Uranium uptake on a glacial sediment was more rapid, and 2- and 3-box models were required for fitting the multiphasic sorption kinetics (Braithwaite et al., 2000).

2.2.5 Ore Bodies

The distribution of uranium around ore bodies is determined by sorption to mineral surfaces and the formation of secondary uranium minerals. The Koongarra Uranium ore body in Australia has been studied extensively. Selective extractions of uranium downgradient of the primary ore body showed that the majority of uranium is contained in iron and aluminum oxyhydroxides of the assemblage, with a highly mobile fraction associated with aluminol sites (Fenton and Waite, 1996; Payne et al., 1994; Yanase et al., 1991). In other studies, uranium sorption could be modeled by considering only the iron content (Jung et al., 1999; Payne and Waite, 1991; Waite et al., 2000), an assumption supported by transmission electron microscopy with goethite identified as the dominant sorbent by electron diffraction (Lumpkin et al., 1999). Uranyl phosphate micro-precipitates identified downgradient of a uranium ore deposit are thought to have nucleated on the surfaces of iron oxyhydroxides at sites of uranium adsorption (Murakami, 1997; Sato et al., 1997).

Uranium associated with soil in the vicinity of the Australian Ranger ore body was reversibly sorbed to amorphous iron oxides, and sequestered on a longer time-scale in crystalline iron oxides (Lowson et al., 1986). Only 3% of the uranium from an iron and manganese rich clayey sample from the Bangombe natural reactor zone in Gabon was exchangeable. During selective extraction, however, 40% of the uranium was extracted with crystalline iron oxide phases which are rich in phosphorous and may contain microcrystalline uranyl phosphates (Del Nero et al., 1999). Uraninite from the Athabasca basin has undergone alteration to calcium-rich uranyl oxide hydrates and coffinite (Fayek et al., 2000). At the Nopal I deposit in Mexico, which has been studied

as an analogue for the unsaturated zone at Yucca Mountain, the majority of uranium has been oxidized and is now present in uranyl silicate minerals and adsorbed to kaolinite (Ildefonse et al., 1990).

At a mined granitic pluton in Spain, uranium is primarily precipitated as distinct mineral phases or with carbonate, and iron oxyhydroxides play only a minor role in uranium retention (Crespo et al., 1996). Microcrystalline uranium clusters in a granitic uranium mine are present in silicon/aluminum-rich and iron-rich gels (Allard et al., 1999). In mine drainage waters, uranium is sorbed to 50-400 nm iron- and aluminum-rich colloids from pH 4-7, but above pH 7 uranium is entirely in the dissolved phase because of the formation of dissolved uranium carbonate complexes (Zänker et al., 2000). Sorption on rock materials from a mine tailing pile in Germany is highest on phyllite and less for other minerals (Geipel et al., 1996).

2.2.6 Transport Modeling in Natural Systems

The transport of uranium in natural waters has been investigated for a variety of systems. The transport of uranium associated with colloidal phases in surface waters (Andersson et al., 2001; Andersson et al., 1998; Porcelli et al., 1997) has been studied and shown to be a significant transport pathway. A large effort has been dedicated to measuring and modeling uranium transport in groundwaters for the purpose of hydrogeologic dating of groundwater by uranium isotopic disequilibria. The isotope ^{238}U is a parent of ^{234}U and is less mobile than its daughter isotope. The principle mode of enhanced ^{234}U mobility is alpha recoil in the decay of ^{238}U to ^{234}Th (which subsequently decays through an intermediate step to ^{234}U) (Osmond and Cowart, 1992). The most

sophisticated models attempt to model the transport of the uranium series radionuclides by including sorption and precipitation processes in the transport equations (Fröhlich and Gellermann, 1987; Fröhlich et al., 1991; Ivanovich et al., 1991; Ivanovich et al., 1992a; Ivanovich et al., 1992b; Tricca et al., 2000).

2.3 Uranium Sorption on Mineral Surfaces

2.3.1 Overview of Sorption Equilibrium and Kinetics

Sorption is often reversible and definable by a constant for equilibrium partitioning between the solid and dissolved phases. Langmuir isotherms are frequently used to interpret the sorption of metals on mineral surfaces. This model assumes that there is a finite number of sites on a surface where sorption may occur and that sorption occurs by binding a sorbate molecule at a specific site. Langmuir sorption behavior follows a linear relationship between dissolved and sorbed concentrations at low concentrations, but as the dissolved concentration increases, the surface becomes saturated and the sorbed concentration asymptotically approaches an upper limit. A more complex and rigorous interpretation of metal sorption behavior can be accomplished by surface complexation modeling. This modeling approach is based on the formation of surface complexes of metals coordinated by reactive surface groups in a manner analogous to the formation of solution complexes (Stumm, 1992).

The kinetics of metal sorption on mineral surfaces are affected by both physical and chemical processes. The chemical sorption of heavy metals to soil minerals is generally rapid, occurring on millisecond time scales; however, this rapid initial sorption

is often followed by a slower period of sorption occurring on time scales of days and longer (Sparks, 1999). This slow sorption phase has generally been attributed to interparticle or intraparticle diffusion in pores (Barrow et al., 1989; Brümmer et al., 1988; Scheinost, 2001; Trivedi and Axe, 2000), sites of low reactivity, and surface precipitation (Sparks, 1999). Slow chemical sorption has been explained as the coordination of a metal to the mineral surface to form an inner-sphere complex, which occurred on a time-scale of hours to tens of hours for vanadium(IV) and chromium(III) sorption on aluminum oxide (Wehrli et al., 1990).

2.3.2 Uranyl Sorption on Iron Oxyhydroxide Minerals

As discussed earlier, uranium sorption on iron minerals is significant in contaminated and natural systems. Controlled laboratory experiments with a variety of iron oxyhydroxide minerals have provided mechanistic insight into the sorption process. Before discussing specific mineral systems, some general trends should be mentioned. Uranium(VI) sorption on iron oxyhydroxides occurs through the formation of inner-sphere surface complexes, which frequently have bidentate coordination to the mineral surface. Sorption increases from essentially none to a maximum value across a sharp sorption edge in the region pH 4-6. In the presence of carbonate, sorption decreases at higher pH because of the formation of uranyl-carbonato complexes. Adsorption of uranium can be a precursor step to surface catalyzed uranium reduction if ferrous iron is also present in the system.

Maximum sorption of uranium on goethite in open systems occurs between pH 5-6 with the decrease at higher pH values attributed to the stabilization of uranium in

solution as non-sorbing uranyl-carbonate complexes (Duff and Amrhein, 1996; Hsi and Langmuir, 1985; Jung et al., 1999; Liger et al., 1999; Tripathi, 1984). Sorption on goethite can be enhanced by the addition of citrate, probably through the formation of a ligand-bridging ternary surface complex (Redden et al., 1998). In these studies, the sorption of uranium on goethite was considered a reversible phenomenon; however, uranium sorption in the presence of a crystallizing goethite was not entirely reversible (Ohnuki et al., 1997). Sorption on goethite and lepidocrocite was consistent with a Langmuir isotherm interpretation (Moyes et al., 2000). Early work modeled the uranyl-goethite surface complexes as monodentate, but more recent work has modeled the sorption behavior with bidentate surface complexes (Gabriel et al., 1998), which are suggested by extended X-ray absorption fine structure spectroscopy (EXAFS) (Moyes et al., 2000).

Surface complexation modeling of the uranium-hematite system has been performed in numerous studies (Ho and Doern, 1985; Ho and Miller, 1986; Hsi and Langmuir, 1985; Jung et al., 1999; Liger et al., 1999) and in ternary humic acid-uranium-hematite systems (Lenhart and Honeyman, 1999; Murphy et al., 1999). Although sorption on hematite does decrease with increasing carbonate concentration, spectroscopic and electrophoretic mobility data indicate that uranyl-carbonate surface complexes are formed with bidentate coordination to the hematite surface (Bargar et al., 1999; Bargar et al., 2000; Ho and Miller, 1986). Uranium retardation through columns of crushed granite was much greater when small amounts of hematite were added (Casas et al., 1994b).

Ferrihydrite, an iron oxyhydroxide that can transform to form goethite and hematite, also has a high sorption affinity for uranium. Uranium sorption on ferrihydrite (Hsi and Langmuir, 1985; Morrison et al., 1995; Waite et al., 1994) and amorphous ferric oxyhydroxide (U.S.DOE, 1999) has been measured and modeled with monodentate or bidentate surface complexes with the uranyl-hydroxo species. EXAFS measurements offer evidence for bidentate surface complexes (Waite et al., 1994). Uranium sorption on ferrihydrite-coated kaolinite was essentially identical to sorption on pure ferrihydrite, and enhanced sorption at low pH in the presence of phosphate was interpreted by invoking a ternary surface complex (Payne et al., 1998). The sorption behavior of uranium on crystallizing ferrihydrite has been considered as both sorption (Ohnuki et al., 1997) and coprecipitation (Bruno et al., 1995) phenomena. Biphase adsorption kinetics of uranium on ferrihydrite consisted of a rapid initial phase lasting a few hours followed by a longer phase extending for at least 200 hours (Waite et al., 1994).

Uranium can also be immobilized at the surfaces of iron minerals by reduction from the hexavalent state to the insoluble tetravalent state. Reduction of uranium(VI) in contact with zerovalent iron has led to significant uranium immobilization in permeable reactive barriers (PRBs) (Fiedor et al., 1998; Gu et al., 1998; Morrison et al., 2001; U.S.DOE, 1999). The dominant removal mechanism of uranium by zerovalent iron is the reduction of uranium(VI) and not the sorption of uranium(VI) on iron corrosion products (Morrison et al., 2001). Although dissolved ferrous iron can not reduce uranium(VI), uranium(VI) can be reduced by ferrous iron in a surface mediated process involving ferric iron minerals. Uranium(VI) adsorbed to hematite was reduced by Fe(II) with

biphasic kinetics (Liger et al., 1999). Abiotic surface mediated uranium(VI) reduction was also observed for the goethite system with ferrous iron (Fredrickson et al., 2000).

2.3.3 Uranyl Sorption on Aluminosilicate Minerals

Clay minerals present in soils can contribute significantly to U(VI) sorption. Studies of uranyl adsorption onto montmorillonite have demonstrated U(VI) uptake consistent with both ion exchange and specific coordination. Ion exchange occurs through the formation of outer-sphere complexes with the fixed charge sites of the clay interlayers, and inner-sphere coordination occurs through specific coordination at silanol and aluminol sites (McKinley et al., 1995; Turner et al., 1996; Zachara and McKinley, 1993)). A sorption study with montmorillonite in the presence of carbonate and over a wide pH range (2-9) was conducted at high ionic strength to favor specific coordination at edge sites. In this study, monodentate surface complexes of UO_2^{2+} and $(\text{UO}_2)_3(\text{OH})_5^+$ with aluminum and silicon surface hydroxyl groups were used in surface complexation modeling (Pabalan and Turner, 1997). EXAFS studies of uranyl sorbed on Ca-montmorillonite indicated that the coordination geometry of sorbed U(VI) varies with surface coverage; this behavior was attributed to sorption at different surface binding sites (Chisholm-Brause et al., 1994). An outer-sphere complex at low pH and ionic strength (consistent with an exchange complex) and an inner-sphere complex at higher pH and ionic strength were observed with EXAFS (Sylwester et al., 2000). EXAFS has also indicated that uranium sorbed to Na-montmorillonite occurs in a hydrolyzed form which is most consistent with outer-sphere coordination (Dent et al., 1992). More recent

spectroscopic information suggested four separate surface complexes, two outer-sphere complexes and two inner-sphere complexes (Chisholm-Brause et al., 2001).

Sorption of uranium on a variety of other phyllosilicate minerals has been investigated. Uranyl sorption on the clay mineral kaolinite was attributed to the formation of inner-sphere complexes and, in some conditions, multinuclear sorption complexes are evident (Thompson et al., 1998). Using analytical electron microscopy, uranium sorption on kaolinite was found to be concentrated at anatase (TiO_2) impurities (Payne et al., 1998). Sorption on kaolinite and gibbsite followed typical cation sorption behavior but was inhibited by the addition of citric acid (Redden et al., 1998). Uranium sorption on bentonite has been studied (Olguin et al., 1997) and slow diffusion through a bentonite barrier was observed (Ramebäck et al., 2000). Sorption on phyllite, a metamorphic rock composed of silicate minerals, was highest from pH 6-7, though the sorption may actually have been due to trace amounts of iron (Arnold et al., 1998) and was successfully modeled with a trace ferrihydrite component dominating sorption (Arnold et al., 2001). Measurable sorption was also found for muscovite and chlorite (Arnold et al., 1998). Uranyl sorption complexes on hydrobiotite and vermiculite include outer-sphere complexes at interlayer positions and inner-sphere complexes at surface hydroxyl groups as observed by EXAFS and XANES (Hudson et al., 1999).

Although, compared with other minerals, quartz does not significantly adsorb uranium (Arnold et al., 1998; Jung et al., 1999), sorption onto quartz has been modeled with two-site nonelectrostatic (Kohler et al., 1996) and diffuse layer (Prikryl et al., 2001) models. The higher surface area of amorphous silica and hydrous silica gels allows for more sorption. Early work identified the sorption complexes as inner-sphere (Maya,

1982). Mixed silica-titania gels have a sorption maximum from pH 4-7 and high sorption capacity (Yinjie et al., 1995). The structure of adsorbed surface complexes were determined to be inner-sphere polynuclear complexes at high loading and pH (Dent et al., 1992; Sylwester et al., 2000) but, at lower loading and pH, a mononuclear bidentate structure is suggested (Sylwester et al., 2000). Adsorption on zeolites is interpreted as specific coordination to silanol edge groups through bidentate coordination (Vochten et al., 1990).

2.3.4 Uranyl Association with Natural Organic Materials

Uranium association with colloidal material can occur through complexation with coagulated humic acids or with humic substances sorbed on inorganic materials (Choppin, 1988). Two freshwater algae species have very high sorption capacities for uranium (Mann and Fyfe, 1985). Uranium sorption on *Sargassum fluitans* and seaweed biomass was interpreted with a single-site nonelectrostatic model for the binding of the uranyl ion and two hydrolysis species (Yang and Volesky, 1999). Uranium binding to the bacterium *Bacillus subtilis* is very strong even at low pH (<2) and is interpreted with a surface complexation model including both phosphate and carboxyl groups (Fowle et al., 2000), which has been confirmed by recent EXAFS measurements (Kelly et al., 2001). *Bacillus* isolates from a uranium mining waste pile sorb uranium by the formation of inner-sphere complexes with surface phosphate groups (Panak et al., 2000).

2.4 Mineralogy of Uranium-containing Minerals

2.4.1 Uranyl Mineral Structures

The uranyl cation is a basic structural constituent of nearly 200 minerals. While the axial oxygen atoms forming the uranyl group remain essentially linear, the equatorial positions can be occupied by four, five, or six oxygen atoms. In this way structures of square, pentagonal, and hexagonal bipyramidal polyhedra are built up by edge and corner sharing and the incorporation of corresponding anions. The most common uranyl mineral structures are sheet structures, with sheets built along the equatorial planes of the uranyl polyhedra. An anion topology was developed for the classification of sheet structures. In addition to sheets, uranyl mineral structures are built on chains, finite clusters, and frameworks (Burns, 1999).

2.4.2 Environmental Uranyl Mineral Transformations

The specific minerals formed in a given environment are determined by the composition of the fluids from which they precipitate. Uranium (VI) minerals of environmental interest are primarily oxides, carbonates, silicates, and phosphates. Uranyl minerals that may be relevant in environmental situations are listed in Table 2.2 (Burns, 1999). The uranyl minerals found naturally are weathering products of U(IV) minerals, primarily uraninite (UO_2). Spent nuclear fuel is greater than 96% uranium(IV) oxide (UO_2), similar to uraninite, and the alteration of spent nuclear fuel in a geologic repository for nuclear waste will also lead to the formation of uranyl minerals (Wronkiewicz and Buck, 1999). During the dissolution of uranium(IV) oxide in granitic groundwater under oxidizing conditions, the solubility of uranium may be controlled by several uranyl

Table 2.2: Uranyl minerals that may form in porous media.

Mineral	Composition
Oxides and Hydroxides:	
schoepite	$(\text{UO}_2)_8\text{O}_8(\text{OH})_{12} \cdot 12\text{H}_2\text{O}$
meta-schoepite	$(\text{UO}_2)_8\text{O}_8(\text{OH})_{12} \cdot 10\text{H}_2\text{O}$
dehydrated schoepite	$\text{UO}_3 \cdot (2-x)\text{H}_2\text{O}$
becquerelite	$\text{Ca}(\text{UO}_2)_6\text{O}_4(\text{OH})_6 \cdot 8\text{H}_2\text{O}$
clarkeite	$\text{Na}[(\text{UO}_2)\text{O}(\text{OH})] \cdot \text{H}_2\text{O}$
compreignacite	$\text{K}_2\text{U}_6\text{O}_{19} \cdot 11\text{H}_2\text{O}$
Carbonates:	
rutherfordine	UO_2CO_3
liebigite	$\text{Ca}_2\text{UO}_2(\text{CO}_3)_3 \cdot 11\text{H}_2\text{O}$
Silicates:	
soddyite	$(\text{UO}_2)_2\text{SiO}_4 \cdot 2\text{H}_2\text{O}$
uranophane	$\text{Ca}(\text{H}_3\text{O})_2(\text{UO}_2\text{SiO}_4)_2 \cdot 3\text{H}_2\text{O}$
β -uranophane	$\text{Ca}(\text{UO}_2)\text{SiO}_3(\text{OH})_2 \cdot 5\text{H}_2\text{O}$
weeksite	$\text{K}_2(\text{UO}_2)_2\text{Si}_6\text{O}_{15} \cdot 4\text{H}_2\text{O}$
Phosphates:	
autunite	$\text{Ca}(\text{UO}_2)_2(\text{PO}_4)_2 \cdot 10\text{H}_2\text{O}$
meta-autunite	$\text{Ca}(\text{UO}_2)_2(\text{PO}_4)_2 \cdot (2-6)\text{H}_2\text{O}$
uranyl orthophosphate	$(\text{UO}_2)_3(\text{PO}_4)_2 \cdot 4\text{H}_2\text{O}$
sodium meta-autunite	$\text{Na}_2(\text{UO}_2)_2(\text{PO}_4)_2 \cdot 8\text{H}_2\text{O}$
meta-ankoleite	$\text{K}_2(\text{UO}_2)_2(\text{PO}_4)_2 \cdot 6\text{H}_2\text{O}$
phosphuranylite	$\text{Ca}(\text{UO}_2)_3(\text{PO}_4)_2(\text{OH})_2 \cdot 6\text{H}_2\text{O}$
saleeite	$\text{Mg}(\text{UO}_2)_2(\text{PO}_4)_2 \cdot 10\text{H}_2\text{O}$

phases (Finn et al., 1996; Trocellier et al., 1998).

The dissolution of uranium(IV) oxides has been studied under a variety of conditions, generally oxidizing, leading to the formation of oxidized secondary phases (Casas et al., 1994a; Casas et al., 1998; De Pablo et al., 1999; Finn et al., 1996; Guilbert et al., 2000; Steward and Mones, 1997; Torrero et al., 1994; Trocellier et al., 1998; Wronkiewicz et al., 1992; Wronkiewicz et al., 1996). The mechanisms of uraninite dissolution have been reviewed by Shoesmith (2000). Typically a paragenetic sequence, a chronological formation of secondary phases, is observed, in which more stable uranyl phases replace less stable phases over time (Finch and Murakami, 1999). Remarkably

similar sequences of alteration phases are observed for synthetic and natural UO_2 in silica weathering environments. Schoepite or dehydrated schoepite forms first, followed by uranyl oxide hydrates with interlayer cations (e.g., becquerelite and compreignacite), then soddyite, and ultimately uranyl alkaline silica hydrates such as uranophane and boltwoodite (Wronkiewicz and Buck, 1999).

The exact paragenetic sequence of secondary uranyl minerals will be governed by both equilibrium and kinetic factors (Casas et al., 1994a). Rates of release of the constituent ions into solution can be governed by surface-controlled or transport-controlled processes; comparison of laboratory and field-weathering rates suggests that both types of controls can be operative in soils (Schnoor, 1990) (Stumm, 1992). The dissolved uranium concentration at equilibrium is determined by the distribution of uranium among the dissolved species listed in Table A.1 of Appendix A and by the equilibrium solubility products of the solid phases. Experimentally determined equilibrium solubility products for schoepite are reviewed in Appendix A and, for soddyite and uranyl phosphates, in Chapters 6 and 7 respectively. In addition to experimental measurements, efforts have been made to determine phase solubilities by calculating Gibbs free energies of formation based on the contribution of component oxides (Finch, 1997) or structural components (Chen et al., 1999).

2.4.3 Uranyl Oxide Hydrates

Despite their simple compositions, the uranyl oxide hydrates are an amazingly complex family of minerals. The simplest minerals compositionally are schoepite, meta-schoepite, and dehydrated schoepite. The structure of schoepite was determined by Finch

et al. (1996) using a single crystal X-ray diffractometer; the distinction among related phases by X-ray diffraction (XRD) has been an area of recent research (Finch et al., 1997; Finch et al., 1992). The schoepite structure is composed of sheets of uranyl pentagonal bipyramidal polyhedra, connected through edge and corner sharing of equatorial oxygen atoms. The sheets are bound together by hydrogen bonding involving water molecules that occupy the interlayer spaces between the sheets. Meta-schoepite and dehydrated schoepite have similar structures, but with some sheet rearrangement and contraction of the interlayer spacing due to the loss of interlayer water molecules (Finch et al., 1998). EXAFS measurements of a synthetic schoepite are consistent with the structure determined by XRD (Allen et al., 1996).

Schoepite is a common early weathering product of uraninite, but it is not a long-term solubility-controlling phase in natural waters (Finch et al., 1992). Schoepite has a strong tendency to incorporate cations into the interlayer spacings, and it is very difficult to prepare phases with uranium as the sole cation (Hoekstra and Siegel, 1973). In natural environments, the cation most commonly incorporated is calcium, leading to the formation of becquerelite (Finch and Murakami, 1999). In laboratory experiments schoepite transformed to becquerelite within a month when contacted with calcium solutions of 10 mM or greater (Sandino and Grambow, 1994; Sowder et al., 1996; Sowder et al., 1999; Vochten and Van Haverbeke, 1990). Exposure of schoepite to potassium led to compregnacite formation (Sandino and Grambow, 1994), and exposure to barium and lead yielded billietite and wölsendorffite respectively (Vochten and Van Haverbeke, 1990). Other layered cation uranyl oxide hydrates have been formed only in the laboratory, incorporating strontium (Burns and Hill, 2000a; Cahill and Burns, 2000),

cesium (Hill and Burns, 1999), potassium in a phase distinct from compreignacite (Burns and Hill, 2000b), magnesium, manganese, and nickel (Vochten et al., 1991). Uranyl oxide hydrates can also incorporate ammonium (Debets and Loopstra, 1963; Hoekstra and Siegel, 1973).

The formation of sodium uranyl oxide hydrates has been so widely discussed and plays so crucial a role in this work that it merits additional discussion. Clarkeite is the only sodium uranyl oxide hydrate mineral observed in the environment (Finch and Murakami, 1999). Clarkeite has a sheet structure composed of either pentagonal or hexagonal uranyl bipyramidal polyhedra with sodium occupying interlayer positions (Finch and Ewing, 1997). Clarkeite has structural similarities with the sodium uranate $\text{Na}_2\text{U}_2\text{O}_7$, but is a distinct phase. As the pH of a schoepite suspension was raised by addition of sodium hydroxide, the formation of an orange sodium uranyl oxide hydrate phase was accompanied by spectral changes of the solid (Allen et al., 1996; Baran, 1988). A solid dried at 100°C was characterized by XRD and had the composition $\text{Na}_2\text{U}_2\text{O}_7$ (Malý and Veselý, 1958), a phase identified as the most stable of the sodium uranates for a wide temperature range (Cordfunke and Loopstra, 1971). The formation of sodium polyuranates has been interpreted as a solid solution between NaOH and $\text{UO}_3\cdot\text{H}_2\text{O}$ with $\text{Na}_2\text{U}_2\text{O}_7$ as an intermediate phase (Ricci and Loprest, 1955; Wamser et al., 1952).

Schoepite can also be transformed without the incorporation of interlayer cations. When exposed to phosphate, schoepite was transformed to autunite through several uranyl phosphate intermediates (Sowder et al., 1996). In the presence of an elevated carbon dioxide partial pressure (greater than 2.8%), schoepite was transformed to rutherfordine (Meinrath and Kimura, 1993).

A tremendous number of investigations have reported thermodynamic constants for the equilibrium solubility of schoepite. Unfortunately, the reported constants and methods of determination vary significantly. The equilibrium solubility of schoepite is reviewed in detail in Appendix A. The values of Silva (1992) and Diaz Arocas and Grambow (1998) were determined using conditions similar to those of the current work and provide estimates of the schoepite solubility that are consistent with observations in this work.

2.4.4 Uranyl Silicates

Because of the high dissolved silicon concentrations in many groundwaters, uranyl silicates are often observed as alteration phases of uraninite weathering. The crystal chemistry of common silicate minerals are reviewed by Burns (1999) and Stohl and Smith (1981). The majority of uranyl silicate minerals have structures based on sheets of uranyl and silicate polyhedra; however, soddyite and weeksite possess framework structures (Burns, 1999). A variety of silicate minerals have been synthesized under hydrothermal conditions (Nguyen et al., 1992; Vochten et al., 1997a; Vochten et al., 1997b).

Soddyite is favored in environments with high dissolved silicon and low to neutral pH (Finch and Murakami, 1999). High dissolved silica in the seepage waters from a German mining site prompted an investigation of the solubility of uranyl silicate minerals in which uranyl orthosilicate was synthesized and characterized (Moll et al., 1995). Soddyite solubility has been investigated at low pH (Moll et al., 1996; Nguyen et al., 1992) and at high pH and carbonate concentration (Pérez et al., 1997).

The release of uranium during the dissolution of synthetic (Pérez et al., 2000) (Casas et al., 1994a) and natural uranophane in the presence of high bicarbonate concentrations was essentially linear with respect to time. Natural uranophane dissolution in dilute aqueous solution followed a unique pattern of initial dissolution, followed by precipitation of uranium in a new phase. This dissolution-precipitation pattern suggests that in dilute solution, uranium released from uranophane was precipitated in freshly nucleated soddyite.

2.4.5 Uranyl Phosphates

Many uranyl phosphate minerals have been observed in nature, frequently as large crystals. All of the uranyl phosphate minerals possess sheet structures, often with very complex anion topologies (Burns, 1999). The autunite and meta-autunite groups contain the most minerals of all of the uranyl phosphate groups. In addition to autunite, sodium autunite, sodium meta-autunite, and chernikovite have been observed. The transitions among these closely related phases are considered to be reversible (Finch and Murakami, 1999).

Phosphates are among the most insoluble uranium (VI) solids, and when phosphate is present at appreciable concentrations, uranyl phosphates can control dissolved uranium concentrations. This low solubility was exploited in a study in which hydroxyapatite ($\text{Ca}_5(\text{PO}_4)_3\text{OH}$) was added to uranium contaminated sediments to immobilize uranium as phosphate phases (Arey et al., 1999). Sowder (1998) found that uranyl phosphate phases were markedly more resistant than schoepite or becquerelite to dissolution by deionized water, acetic acid, EDTA, and bicarbonate.

Chapter 3

KINETICS OF URANYL SORPTION ON GOETHITE

* draft of submission to *Environmental Science and Technology*, December 2000

3.1 Introduction

The United States' nuclear weapons program has left a legacy of environmental contamination. Uranium mining, milling, and refining generated the largest volume of weapons waste (U.S.DOE, 1997), and uranium is a principal contaminant in soils at Department of Energy weapons processing plants (Riley and Zachara, 1992). The federal standard for uranium in drinking water, promulgated in December 2000 by the U.S. Environmental Protection Agency (USEPA), is 30 ppb; the rule will become effective in December 2003 (U.S.EPA, 2000).

At the Fernald Environmental Management Project (FEMP) in Ohio, high carbonate concentrations have resulted in mobilization of uranium from contaminated soils in the form of uranyl-carbonate complexes and contamination of the underlying aquifer (Elless and Lee, 1998; Sidle and Lee, 1996). At the carbonate-poor Savannah River Site (SRS), colloidal transport of uranium in groundwater has been observed (Kaplan et al., 1994a) and the association of uranium with colloids of kaolinite and iron oxides has been demonstrated by synchrotron X-ray fluorescence (SXRF) measurements

(Kaplan et al., 1994b). In SRS surface waters, the transport of uranium during storm events is enhanced by its association with suspended quartz, kaolinite, gibbsite, and goethite solids (Batson et al., 1996).

Because of their high reactive surface areas, iron minerals can strongly influence the fate and transport of uranium. Despite differences in bulk mineralogy, similarities in iron content among Hanford, SRS, and Oak Ridge soils led to similar pH-dependent uranium adsorption (Barnett et al., 2000). Sequential extraction of contaminated SRS aquifer solids showed uranium to be associated with amorphous (Hunter and Bertsch, 1998) and crystalline (Clark et al., 1996) iron oxides, and the association of uranium with zones enriched in iron and manganese was verified by SXRF (Bertsch et al., 1994). The association of uranium with iron and aluminum oxyhydroxide minerals downgradient of a uranium ore body was suggested by selective extraction (Fenton and Waite, 1996; Yanase et al., 1991), and has been incorporated into surface complexation models with iron oxides as the dominant sorbent (Jung et al., 1999; Payne et al., 1994).

Uranium sorption in single-mineral systems has been investigated for goethite (Duff and Amrhein, 1996; Gabriel et al., 1998; Hsi and Langmuir, 1985; Tripathi, 1984) hematite (Bargar et al., 2000; Ho and Miller, 1986; Hsi and Langmuir, 1985; Liger et al., 1999), and ferrihydrite (Hsi and Langmuir, 1985; Morrison et al., 1995; Ohnuki et al., 1997; Waite et al., 1994). Uranium sorption occurs through the formation of inner-sphere surface complexes, which are most likely in bidentate coordination with surface iron centers (Bargar et al., 1999; Bargar et al., 2000; Gabriel et al., 1998). Sorption increases from none at low pH to a maximum at near-neutral pH; in the case of goethite this sorption edge occurs between pH 5 and 6 (Duff and Amrhein, 1996; Hsi and Langmuir,

1985; Tripathi, 1984). Uranyl complexation by carbonate leads to a significant decrease in sorption, although Bargar et al. (1999; 2000) have presented spectroscopic evidence for ternary uranyl-carbanato surface complexes.

Uranium uptake (Braithwaite et al., 2000) and release (Braithwaite et al., 1997; Mason et al., 1997) from heterogeneous soils is often kinetically controlled. Uranium uptake on hematite (Bargar et al., 1999) and ferrihydrite (Waite et al., 1994) exhibited a rapid phase of 30 minutes to several hours and a longer phase extending for tens and hundreds of hours. Slow sorption has been attributed to interparticle or intraparticle diffusion in pores (Barrow et al., 1989; Brümmer et al., 1988; Trivedi and Axe, 2000), sites of low reactivity, and surface precipitation (Sparks, 1999).

Surface precipitation is a consideration under conditions near or exceeding the solubility of uranyl minerals. Uranium uptake by ferrihydrite has been interpreted as co-precipitation (Bruno et al., 1995). Uranyl phosphate micro-precipitates identified downgradient of a uranium ore deposit are thought to have nucleated on the surfaces of iron oxyhydroxides at sites of uranium adsorption (Murakami, 1997; Sato et al., 1997). As dissolved uranium concentrations increase, monomeric surface complexes may convert to polymeric surface complexes, and ultimately to oligomeric clusters and surface precipitates (Chisholm-Brause et al., 2001).

The objectives of this work were to determine the partitioning of uranium between the solution and the goethite surface and to measure the rates of adsorption and desorption at constant pH and ionic strength. Partitioning experiments were conducted to define a sorption isotherm and determine conditions necessary for heterogeneous

nucleation of a uranium-containing precipitate. Sorption rates were investigated following perturbation of equilibrium states and by isotope exchange.

3.2 Materials and Methods

3.2.1 Materials

Goethite was synthesized by heating freshly precipitated ferrihydrite (Schwertmann and Cornell, 1991). The resulting solid was washed by dialysis and then freeze-dried. X-ray diffraction (XRD) and diffuse reflectance Fourier transform infrared spectroscopy confirmed the identity of the solid as goethite. The surface area of the goethite was measured as 42.2 m²/g by the BET method with nitrogen adsorption using a Micromeritics Gemini surface area analyzer.

Stock solutions of uranium for all experiments were prepared by dissolution of UO₂(NO₃)₂•6H₂O (Alfa Aesar) in Milli-Q water. A ²³⁵U spike of 99% purity in 5% HNO₃ was obtained from L. Silver (Caltech). The pH was buffered with 5 mM 2-(n-morpholino)ethanesulfonic acid (MES) and adjusted to pH 6.00 with NaOH. The ionic strength was fixed at 0.1 M with NaNO₃. Calibration standards for inductively coupled plasma - mass spectrometry (ICP-MS) analysis were prepared from a 1000 ppm standard solution (Alfa Aesar).

3.2.2 Experimental Methods

All experiments were conducted at pH 6, 0.1 M ionic strength, and the ambient temperature of the laboratory (22 ± 2°C). Although experiments were conducted under

ambient atmosphere, uranyl-carbonato complexes are calculated to be minor species based on critically evaluated stability constants (Grenthe et al., 1992).

In partitioning experiments, uranyl nitrate solution was added to goethite suspensions in both batch and titration modes and mixed. A 48 hour contact time was used in initial batch experiments. In titration mode, increments of uranyl nitrate solution were added at intervals greater than 4 hours. After the specified contact time, 10 mL samples of suspension were filtered through 0.22 μm cellulose nitrate (Millipore) or 0.2 μm polycarbonate membranes (Millipore) and the last 5 mL was collected and acidified. Data were fit to a Langmuir isotherm by a non-linear fitting procedure with least squares optimization using the software application Scientist[®] (MicroMath).

In kinetics experiments, pre-equilibrated suspensions were perturbed and the time required to re-establish equilibrium was measured. Kinetics experiments were initiated for adsorption by addition of uranium to a goethite suspension, and for desorption either by dilution of a uranium-loaded goethite suspension into uranium-free solution or by addition of fluoride as a complexing ligand to a pre-equilibrated uranium-goethite suspension. Collected samples were filtered and acidified prior to analysis for dissolved uranium. Sorbed uranium concentrations were calculated as the difference between known total and measured dissolved concentrations. Samples of whole suspension were periodically acidified and filtered to determine if the total uranium concentration was affected by sorption to reactor walls.

The effect of pre-equilibration time on the rate of desorption was investigated in a set of dilution-induced desorption experiments initiated from the same uranium-goethite suspension after 1 day, 1 month, and 6 months of mixing. Following the 6 month

experiment, a 50 mL portion of the remaining suspension was put through a sequential extraction procedure. In each extraction cycle, the solid was vigorously mixed with 50 mL of extractant for 30 minutes at a solid to solution ratio of 0.03 g/L, goethite-extractant suspensions were centrifuged, a filtered supernatant sample was collected, the supernatant was decanted, and fresh extractant was added. The complete extraction process was composed of three cycles with deionized water, three with 1 M acetic acid at pH 5, and three with 1% HNO₃.

An isotope exchange experiment was used to examine the rate of solution-surface exchange in a system with minimal equilibrium perturbation. After four days of equilibration with uranium depleted in ²³⁵U, goethite suspensions were spiked with a small aliquot of ²³⁵U-enriched solution at the same pH and ionic strength. The addition of the ²³⁵U significantly affected the isotope ratio in the dissolved phase but not the dissolved uranium concentration. As the dissolved uranium exchanged with the surface, the isotope ratio in solution evolved to match the isotope ratio in the suspension (i.e., solution plus solid). Samples for dissolved and total uranium were taken following the same procedure used in batch equilibrium and equilibrium-perturbation experiments.

A series of experiments was performed to determine the conditions necessary for the heterogeneous nucleation of uranium surface precipitates on goethite. Uranyl nitrate was added incrementally to goethite suspensions to achieve final total uranium concentrations ranging from 20 to 1000 μM. The incremental addition process lasted from a few hours for low total uranium concentrations to 8 days for the maximum addition. At each point of addition, the pH was measured and adjusted as necessary with NaOH. Throughout the experiment the suspensions were mixed on an orbital shaker.

Samples were taken at specific intervals for determination of dissolved and total uranium; suspended solids were collected on the membrane filter used to process each dissolved sample. The membrane filters were mounted on glass slides, air-dried at room temperature, and then analyzed by XRD.

Dissolved uranium and iron concentrations were determined by ICP-MS on either a Perkin Elmer ELAN 5000 or a Hewlett Packard 4500 instrument. Uranium isotope ratio measurement was performed with a Finnigan Element ICP-MS. XRD was performed with a Scintag Pad V instrument with a Cu K-alpha X-ray source and germanium detector.

3.3 Results and Discussion

3.3.1 Adsorption and Surface Precipitation

The metastable partitioning of uranium to the goethite surface displays a pattern corresponding to a Langmuir isotherm (Figure 3.1), where sorbed uranium is plotted as a function of the total dissolved uranium concentration without distinguishing among dissolved species. The data were fit to a Langmuir isotherm to obtain parameter values

$$\Gamma = \frac{\Gamma_{\max} K_L C}{1 + K_L C} \quad (1)$$

for the sorption constant K_L of $0.653 \mu\text{M}^{-1}$ and the maximum sorbed density Γ_{\max} of $114.4 \mu\text{mol g}^{-1}$ or $2.71 \mu\text{mol m}^{-2}$ normalized to surface area, where C and Γ are the dissolved and sorbed uranium concentrations respectively. It should be noted that almost all of the data with dissolved concentrations greater than $5 \mu\text{M}$ are from the titration-

mode sorption experiments. Under the admittedly simple assumption of monodentate sorption, the value of $2.71 \mu\text{mol}/\text{m}^2$ corresponds to $1.63 \text{ sorption sites}/\text{nm}^2$. This value is comparable to the estimate of $2.3 \text{ sites}/\text{nm}^2$ suggested by Davis and Kent (1990) as a uniform standard for oxide minerals.

This isotherm provides a description of metastable partitioning of uranium between the surface and aqueous phase before the onset of uranyl oxide hydrate precipitation. After uranyl oxide hydrate precipitation, the solubility of the precipitate controls the dissolved uranium concentration. In a set of experiments specifically designed to be supersaturated, the formation of surface precipitates was monitored. For systems with

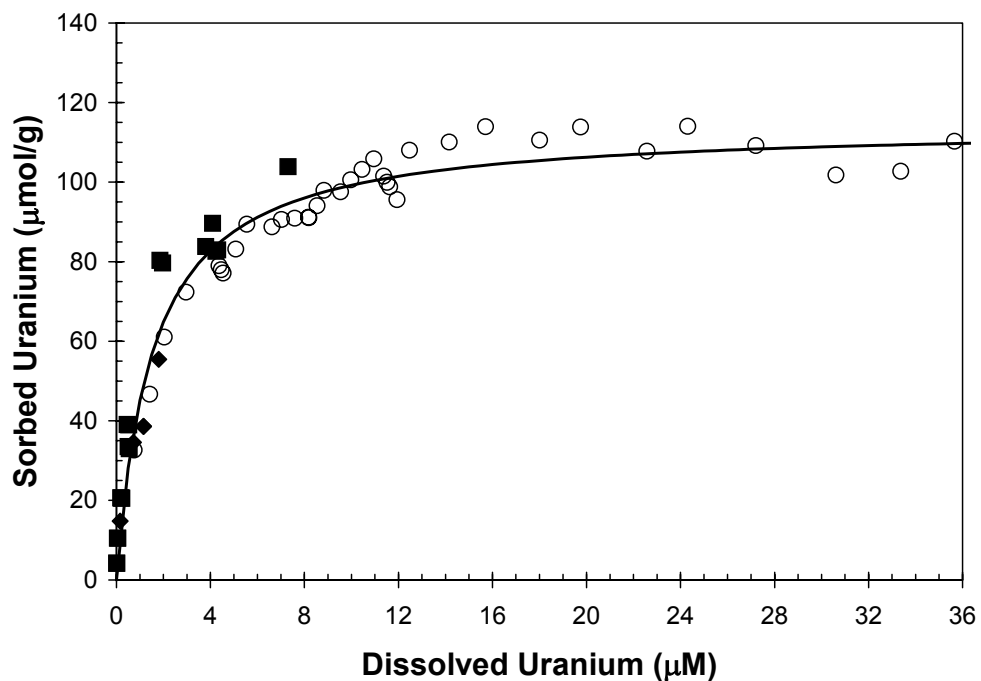


Figure 3.1: Metastable sorption of uranyl on goethite at pH 6 and $I = 0.1 \text{ M}$. Symbols: data from (■) batch equilibration (0.1-2.5 g/L goethite), (◆) endpoints of kinetics experiments (0.010-0.035 g/L goethite), and (○) incremental loading experiments (0.10 g/L goethite); (—) Langmuir isotherm.

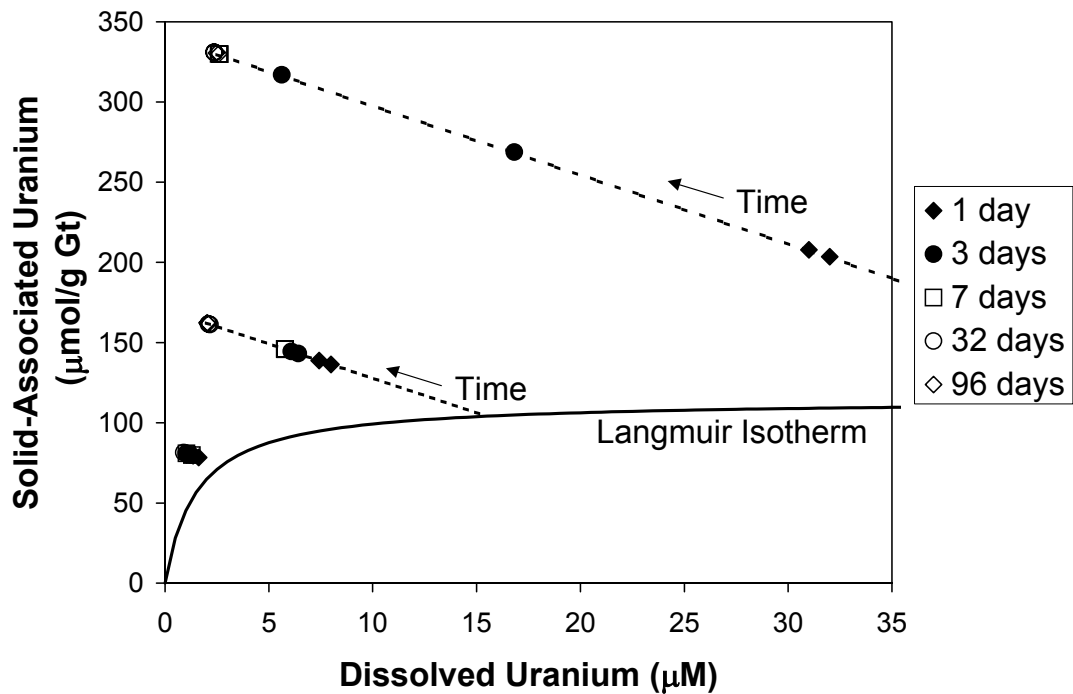


Figure 3.2: Time-dependence of uranium partitioning between dissolved and solid-associated phases at pH 6 and $I = 0.1$ M. Symbols: (■) 1 day, (□) 3 days, (●) 7 days, (○) 32 days, and (◇) 96 days.

20-80 μM total uranium, the change in solid-solution partitioning over time is plotted together with the Langmuir isotherm in Figure 3.2. The dissolved concentration was observed to decrease over as long as 32 days; this corresponds to an increase in the solid-associated (i.e., sorbed and precipitated) concentration. After 96 days, the dissolved uranium concentration was 1.9-2.8 μM for experiments with total uranium greater than 40 μM , a strong indication that a solubility-controlling solid had formed. The experiment with 20 μM total uranium had a lower final dissolved concentration. Sorption partitioning experiments with dissolved concentrations above 2.8 μM are supersaturated with respect to the surface precipitate. Supersaturated conditions may persist for

considerable periods of time at low degrees of supersaturation; the supersaturated data in Figure 3.1 correspond to contact times as long as 30 days.

Uranium-loaded goethite samples from the surface-precipitation experiments were analyzed by XRD to probe for crystalline uranyl-containing precipitates. The XRD pattern of the system with 20 μM total uranium (Fig. 3.3a) contains only the peaks for goethite (21.5°) and the polycarbonate filter membrane ($16-19^\circ$) even after 96 days. For the experiments with 40 and 80 μM total uranium, the XRD patterns of the solids have only goethite and filter peaks for the 1 day sample, but then peaks at 12° and 24° grow in for the 1 month and 3 month samples (40 μM in Fig. 3.3b). These peaks are characteristic of the uranyl oxide hydrate mineral schoepite $((\text{UO}_2)_8\text{O}_8(\text{OH})_{12}\cdot 12\text{H}_2\text{O})$ or a closely related phase. For the systems with 140 μM and 500 μM total uranium, the schoepite peaks are the dominant peaks after only 1 day and, over time, increase relative to the goethite peak (500 μM in Fig. 3.3c). Calculations of the solubility of uranium in equilibrium with schoepite are complicated by the significant variability in the published values of the solubility product and stability constants for uranyl hydrolysis. At pH 6 and 0.1 M ionic strength, a reasonable range for the concentration of dissolved uranium in equilibrium with schoepite is 0.9 μM (Díaz Arocas and Grambow, 1998) to 7.5 μM (Silva, 1992) which is consistent with our measurements.

3.3.2 Sorption Kinetics

Complementary adsorption and desorption experiments with the same total uranium and goethite concentrations display rapid kinetics in both directions (Fig. 3.4). The reactions proceed to 75% completion within only 2-5 minutes. Following

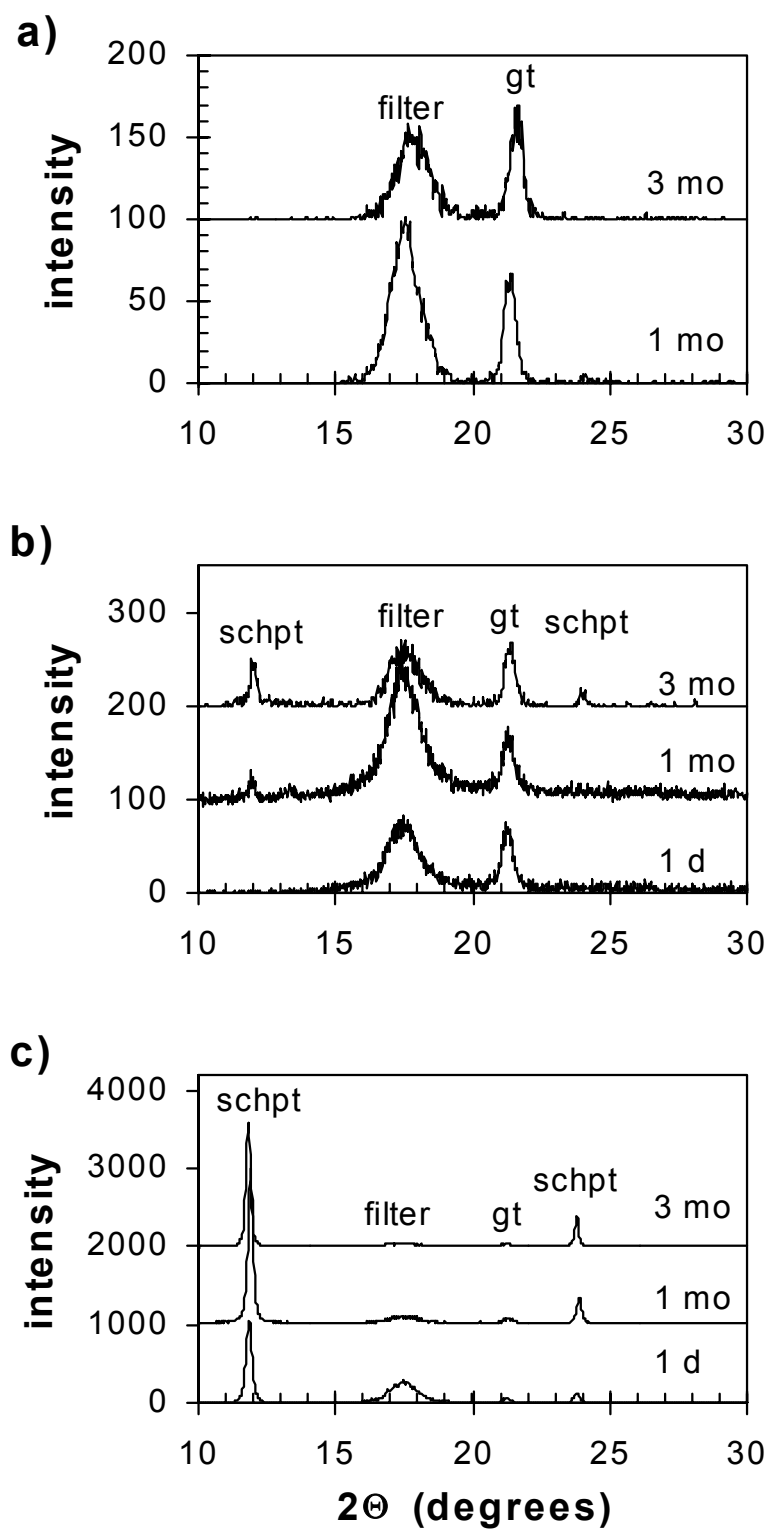


Figure 3.3: X-ray diffraction pattern of solids from a suspension of 0.22-0.23 g/L goethite with $[U]_{\text{tot}} = 20 \mu\text{M}$ (a), $40 \mu\text{M}$ (b), and $500 \mu\text{M}$ (c). $I = 0.1 \text{ M}$, $\text{pH } 6$.

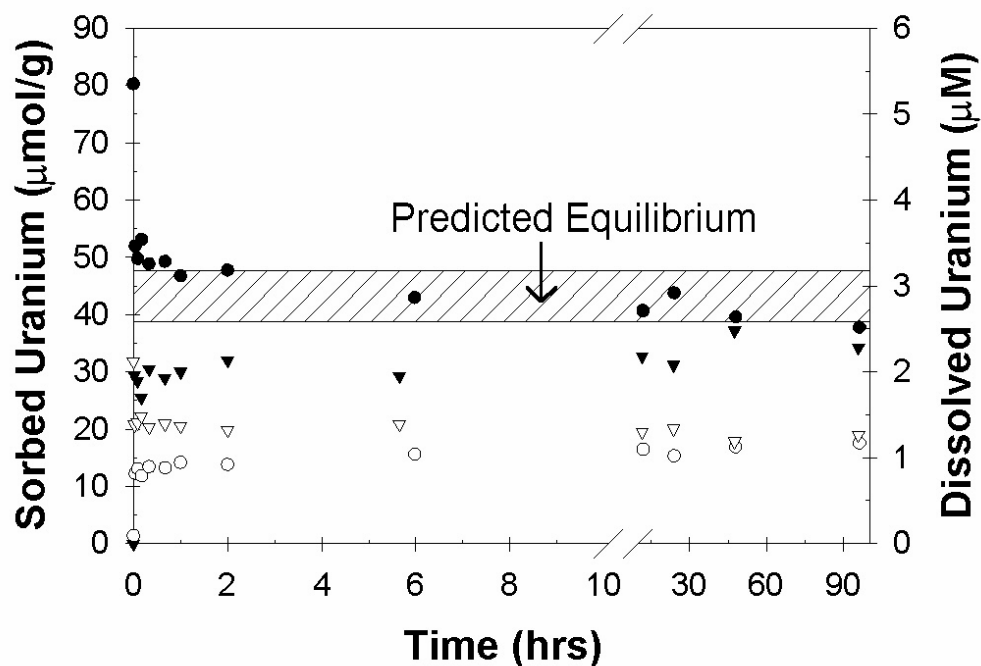


Figure 3.4: Dissolved (open) and sorbed (closed) uranium concentrations in complementary adsorption (triangles) and desorption (circles) experiments of uranyl on goethite for $[\text{U}]_{\text{tot}} = 2 \mu\text{M}$, 0.025 g/L goethite, pH 6, and $I = 0.1 \text{ M}$. Predicted equilibrium range of the sorbed concentration calculated using the Langmuir isotherm with isotherm parameters at 95% confidence values.

dilution-induced perturbations, equilibrium is re-established within one hour, and fluoride-induced desorption occurs on a similar time scale (Fig. 3.5). The predicted equilibrium lines in Figure 3.5 were calculated by assuming that only the uranyl hydrolysis species adsorb to the goethite (Tripathi, 1984). Dissolved uranium speciation in the presence of fluoride was calculated using critically evaluated stability constants (Grenthe et al., 1992).

Results of a duplicate set of solution-surface isotope exchange experiments are displayed in Figure 3.6. The $^{238}\text{U}/^{235}\text{U}$ isotope ratio of the depleted uranium used for

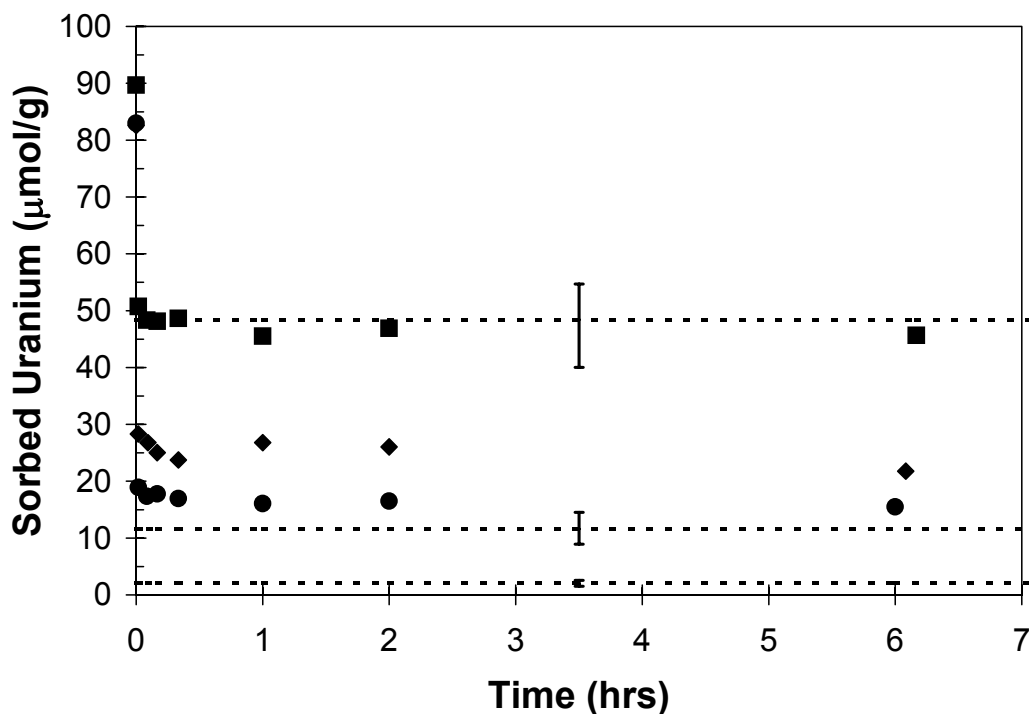


Figure 3.5: Kinetics of desorption following the addition of sodium fluoride to pre-equilibrated uranium-goethite suspensions at pH 6 and $I = 0.1$ M. The pre-equilibrated suspension contained $[U]_{\text{tot}} = 12.5\text{-}13.1$ μM , 0.10 g/L goethite, $[U]_{\text{sorbed}} = 82.6\text{-}89.7$ $\mu\text{mol/g}$. Data are shown for 0.62 mM (■), 1.85 mM (◆), and 4.05 mM (●) fluoride additions together with predicted sorbed concentrations (lines). Predicted concentrations calculated using the Langmuir isotherm and the assumption that only the uranyl ion and uranyl hydrolysis species can sorb; range based on the 95% confidence values of the isotherm parameters.

suspension pre-equilibration was 433.9 and that of the ^{235}U spike was 0.0117. The pH was unaffected by the spike addition, and the total and dissolved uranium concentrations also varied by less than 10%. The addition of 1 mL of 0.252 μM ^{235}U spike yielded an instantaneous $^{238}\text{U}/^{235}\text{U}$ ratio of 239-242 for dissolved uranium and 417 for total uranium. The dissolved phase isotope ratio increased from its initial value to match that of the total uranium within the 45 seconds between spike addition and collection of the first sample. As validated by analysis of goethite-free solutions, isotope ratios of 200-300 can be

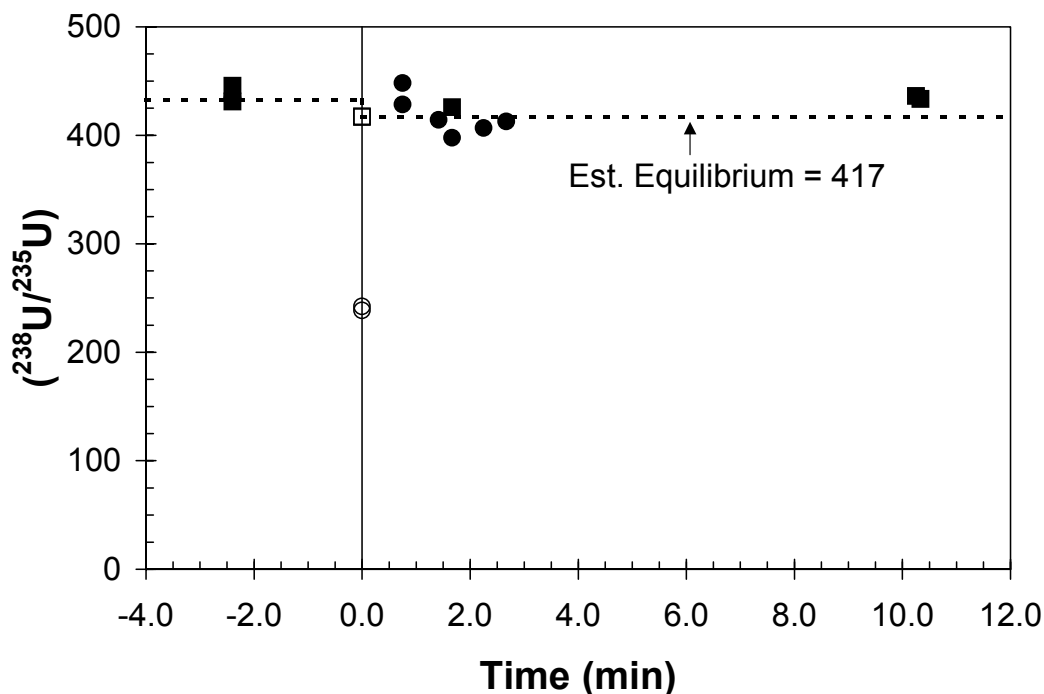


Figure 3.6: The isotope ratio of the total system uranium (■, □) and dissolved uranium (●, ○) during isotope exchange between the dissolved and sorbed phases. Closed symbols indicate measured values and open symbols indicate calculated values. ^{235}U spike introduced at $t = 0$ to goethite pre-equilibrated with depleted uranium.

measured by the technique used, but were not observed in this work because exchange occurred so rapidly.

In the present work, adsorption of uranium on goethite occurs in a single rapid step reaching completion within a few minutes. In a previous study, Hsi and Langmuir (1985) noted biphasic adsorption kinetics with a rapid first step completed within minutes and a second step continuing for several days. Gabriel et al. (1998) determined a first-order rate constant of 1.7 h^{-1} for the adsorption of uranium on goethite in column experiments with goethite-coated cristobalite sand. The rapid nature of the uranium release during desorption experiments suggests that desorption is being controlled by the rate of chemical detachment from the surface and not by diffusion-limited mass-transfer

processes. It is not surprising that the desorption is free of the effects of diffusion, because a synthetic goethite prepared under controlled laboratory conditions should have minimal microporosity.

The convergence of the sorbed uranium concentration in complementary adsorption and desorption experiments (Fig. 3.4) indicates reversibility, and the final sorbed concentration falls within the predicted range. The range was determined using the Langmuir isotherm with isotherm parameters at their 95% confidence values. Another set of dilution-induced desorption experiments terminated with sorbed concentrations in agreement with values calculated from the Langmuir isotherm (Fig. 3.1). During fluoride-induced desorption with 0.62 mM sodium fluoride, the experimental data match the predicted equilibrium remarkably well; however, for the higher fluoride additions, the measured extent of desorption is less than predicted. This discrepancy could be explained by a distribution in the binding-strengths of sites on the goethite surface. In this case, the fraction of the sorbed uranium that was expected but not observed to desorb may be coordinated at strong sites that are energetically more favorable than fluoride for binding uranyl. The distinction between strong and weak sites on the goethite surface has been employed previously in surface complexation models of uranium on iron oxyhydroxides (Gabriel et al., 1998; Lenhart and Honeyman, 1999; Waite et al., 1994).

In experiments conducted to evaluate the effect of aging, constant sorbed uranium concentrations were established within one hour for all aging times (Fig. 3.7). The aged suspension was prepared with sorbent and uranium concentrations that correspond to sorption and not to surface-precipitation. Experiments initiated after 1 day and 1 month

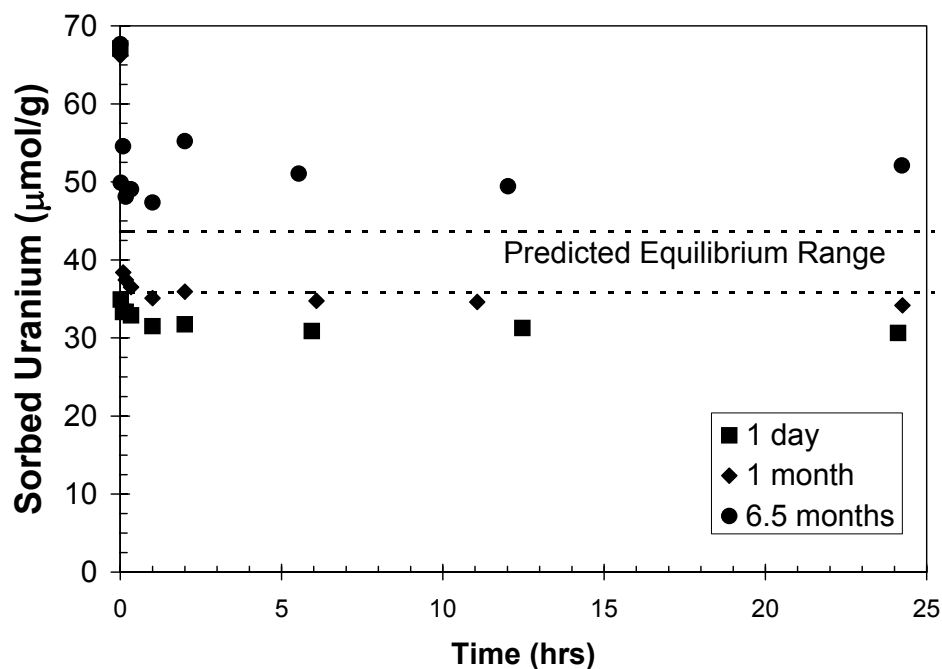


Figure 3.7: Effects of aging time on desorption following a 1:100 dilution of a pre-equilibrated suspension. The pre-equilibrated suspension contained $[U]_{\text{tot}} = 200 \mu\text{M}$, 2.94 g/L goethite, $[U]_{\text{sorbed}} = 66.2\text{-}67.7 \mu\text{mol/g}$ at pH 6 and $I = 0.1 \text{ M}$. Suspension aged for (■) 1 day, (◆) 1 month, and (●) 6.5 months of contact.

both have final sorbed concentrations that agree with the predicted equilibrium value of $38.3 \mu\text{mol/g}$. The desorption initiated after 6.5 months is as rapid as for the earlier times, but the final sorbed uranium concentration is substantially higher than in the other cases and persists to the end of the experiment at nearly 1500 hours (data not shown). During sequential extraction of the solids remaining at the end of the 6.5 month experiment, nearly all (90%) of the uranium was extracted with acetic acid and coincided with a substantial release of iron (~25% of the total). The complete digestion of the remaining material contained the majority of the iron but almost no uranium. The results suggest that, during the aging process, a portion of the readily exchangeable uranium may have diffused into the solid or been occluded within an amorphous iron oxide phase that coats the goethite particles. Ohnuki et al. (1997) found that, during the crystallization process,

a portion of the uranium sorbed to amorphous ferric hydroxide was fixed to the crystalline minerals and was not easily removed.

3.3.3 Environmental Implications

The desorption reactions measured in this work occur on time-scales much shorter than those of environmental processes such as the flow of groundwater. Rapid partitioning of uranium between solution and surfaces and rapid release of sorbed uranium in response to changing solution conditions are expected. Diffusion-controlled mass transfer processes may still kinetically limit rates of uptake and release in environmental settings. In an environmental setting, the long residence of uranium in contact with iron oxyhydroxide minerals may lead to partial sequestration of uranium in the structure of surface coatings and micropores.

As long as dissolved uranium concentrations are low, sorption will dominate uranium mobility, but elevated dissolved concentrations will initiate surface precipitation and actually decrease the dissolved concentration. Elevated concentrations may be found in highly contaminated systems and also during the evaporative concentration of uranium in the pore water of unsaturated soils. The heterogeneous nucleation of a uranyl precipitate may be kinetically limited, and metastable sorption may control the dissolved concentration even when the dissolved concentration exceeds the solubility limit. The mobility of uranium in response to changes in solution conditions may be affected by the distribution of solid-associated uranium between adsorbed and precipitated phases.

Acknowledgments

Lee Silver generously provided the ^{235}U spike. Ken Farley provided time and assistance in the operation of his laboratory's Finnigan Element ICP-MS. Funding was provided to Daniel Giammar through a National Science Foundation Graduate Fellowship.

Chapter 4

INVESTIGATION OF URANIUM-LOADED GOETHITE BY ELECTRON MICROSCOPY

4.1 Introduction and Background

The spatial distribution and speciation of uranium in contaminated porous media are a key parameters governing the environmental fate and transport of uranium in the environment. A first order distinction can be made between sorbed and precipitated phases, and a second order distinction between different sorbent phases or different precipitates. The mobility of uranium in soils and groundwaters will be influenced by the nature of the association of uranium with solid phases. Although control of dissolved uranium concentrations is often attributed to sorption processes, precipitation may also play a controlling role in some systems. In the aquifer underlying the Fernald Environmental Management Project (FEMP) in Ohio, dissolved uranium concentrations are controlled by the solubility of uranyl phosphate solids (Elless and Lee, 1998). In a treatment system based on soil washing, the optimal extractant solutions were those capable of solubilizing uranium-containing precipitates and not just inducing desorption (Francis et al., 1999).

Iron oxide phases are ubiquitous constituents of soils and aquifer sediments. Because of their high specific surface areas and surface reactivity, these phases can significantly influence the mobility of metals (Coston et al., 1995; Davis et al., 1998).

The sorption of uranium on natural materials (e.g., material from the weathered zone of the Koongarra ore deposit) appears to be dominated by either amorphous iron oxyhydroxides (Payne and Waite, 1991) or goethite (Jung et al., 1999). Sorption to crushed phyllite, a metamorphic rock composed of quartz, chlorite, muscovite, and albite, can be accurately modeled as sorption onto ferrihydrite, which is formed from the leaching of ferrous iron from chlorite and its subsequent oxidation (Arnold et al., 1998; Arnold et al., 2001). Sorption on kaolinite with a surface coating of ferrihydrite was observed to be nearly identical to sorption on pure ferrihydrite (Payne et al., 1998). Sorption on lateritic soils was found to be dominated by goethite (Syed, 1999), and the behavior of uranium in contaminated soils from three Department of Energy Facilities could be rationalized on the basis of the iron content of the soil (Barnett et al., 2000). Sequential extractions of uranium-containing materials have also demonstrated the association of uranium with iron-rich phases. Solutions which dissolve amorphous and crystalline iron oxides extracted significant uranium from organic-rich peat (Dowdall and O'Dea, 1999), granitic soils (Megumi, 1979), contaminated soil from the Oak Ridge National Laboratory (ORNL) (Roh et al., 2000), the weathered zone of the Koongarra deposit (Payne et al., 1994; Yanase et al., 1991), and colloidal material in a mine drainage gallery (Zänker et al., 2000).

At high uranium concentrations, sorption sites become saturated and surface precipitates can form. Precipitation or occlusion of uranium may also occur during the aging and crystallization of amorphous iron oxyhydroxides (Bruno et al., 1995; Ohnuki et al., 1997; Payne et al., 1994). Uranyl phosphate micro-precipitates at the Koongarra deposit are thought to have formed subsequent to the immobilization of uranium by

sorption on iron oxides (Murakami, 1997; Sato et al., 1997). The relative contributions of adsorption and surface precipitation to the association of uranium with solid phases can not be determined solely from bulk solution chemistry data.

Electron microscopy can be used to determine the spatial distribution of uranium in solids and to characterize uranium-containing phases. Extensive study of materials from the FEMP with scanning electron microscopy (SEM) and transmission electron microscopy (TEM) identified both enriched zones of diffuse uranium as well as micron-scale particulate uranium in autunite, uranyl phosphate, and uranyl oxide phases (Bertsch et al., 1994; Buck et al., 1996; Elless and Lee, 1998; Morris et al., 1996). Precipitated schoepite, uranophane, coffinite and other uranium-containing phases were observed in soils at ORNL with SEM (Roh et al., 2000). In laboratory studies of uranium sorption on material from the Koongarra weathered zone, the association of uranium with iron oxides was determined by TEM and uranyl oxide hydrate precipitates were identified with electron diffraction at the highest uranium loading (Lumpkin et al., 1999). Also with material from the Koongarra weathered zone, the association of uranium-containing minerals with iron oxides was observed with SEM, and phase identification of uranyl phosphates was accomplished by measuring the lattice fringes with high resolution TEM (Murakami, 1997). Uranyl clusters and microcrystals were observed with SEM and TEM in goethite suspensions in the presence of microbes (Fredrickson et al., 2000) and preferential adsorption of uranium to an anatase impurity in a kaolinite standard was demonstrated with TEM (Lumpkin et al., 1999; Payne et al., 1998). TEM of samples with uranium sorbed to ferrihydrite-coated kaolinite clearly showed the correlation

between uranium and iron, but no discrete particles of either ferrihydrite or a uranium-containing solid were observed (Payne et al., 1998).

In the current work, SEM and TEM were used to examine solids isolated from suspensions of goethite contacted with uranium. From the observed concentrations of dissolved uranium, the nature of the association appeared to shift from sorption to surface precipitation with either (or both) increasing uranium concentration and equilibration time. The spatial relationship between the goethite sorbent and the schoepite-like precipitate which formed in the systems over time was examined by SEM and TEM to gain insight into the mechanisms through which the system shifts from sorption- to precipitation-control of the dissolved uranium concentration.

4.2 Experimental Materials and Methods

Uranium-loaded goethite samples were isolated by filtration from uranium-goethite suspensions that had been mixed for varying lengths of time. A complete description of the preparation and solution chemistry of the uranium-goethite suspensions was presented in Chapter 3. In brief review, uranium was incrementally added to 0.23 g L⁻¹ goethite suspensions in 0.1 M NaNO₃ solution at pH 6.0 (buffered by 5 mM MES buffer). Throughout the experiments the pH was measured and adjusted with sodium hydroxide or nitric acid if necessary. After prescribed periods of equilibration, suspensions were filtered through 0.2 µm polycarbonate membrane filters (Millipore). After wasting the first 3-5 mL, the filtrate was collected and acidified for the determination of dissolved uranium concentrations. For each sample, the membrane

Table 4.1: Uranium concentrations normalized to the goethite mass ($\mu\text{mol g}^{-1}$) in solid-phase samples as a function of initial dissolved concentration and time. All samples were isolated from suspensions with 0.1 M NaNO_3 , pH 6.0 (buffered by 5 mM MES), and 0.21-0.23 g L^{-1} goethite. The background pattern indicates the intensity of schoepite X-ray diffraction peaks for each sample: no schoepite peaks (white), schoepite peak intensity lower than goethite peak intensity (hatched), schoepite peak intensity higher than goethite peak intensity (gray).

		Total Uranium Concentration (μM)					
		20	40	80	140	500	1000
Contact Time (days)	1	78	136	203	561	2290	4817
	3	80	143	269	585	2290	4829
	7	81	146	330	590	2291	4861
	30	82	162	331	590	2292	4808
	90	80	162	331	589	2291	4861
	400	79	157	325	584	2283	4848

filter and collected solids were removed from the filter assembly and air-dried at room temperature. Aliquots of whole suspension were also acidified and subsequently filtered to measure total uranium concentrations, verifying that uranium was conserved in suspension and not lost to the vessel walls.

The distribution of uranium between the solution and solid phase was determined by measuring dissolved uranium concentrations. With increasing time and total uranium concentration, the partitioning behavior shifted from a sorption-mode to a surface precipitation-mode (Fig. 3.2). X-ray diffraction results (Fig. 3.3) suggest the formation of a schoepite-like uranyl oxide hydrate solid at the highest uranium concentrations and the longest equilibration times. A summary of the solid-associated (sorbed plus precipitated) uranium concentrations and X-ray diffraction results of all samples is organized in Table 4.1.

Scanning electron microscopy was performed on solids collected on the membrane filters; air-dried samples were stored for between 10 and 13 months before SEM analysis. Sections of filter membranes were cut out and mounted for analysis with double-sided tape. The samples were carbon coated with an Edwards E306A coating system. Microscopy was conducted using a Camscan Series II instrument at an accelerating voltage of 20 kV. A Robinson-type backscattered electron detector was used. Elemental composition was determined with a Link Analytical pentafet SiLi energy-dispersive X-ray spectrometer, interfaced to an Oxford 2040 pulse processor, a 4Pi Systems scanning interface unit and a Spectral Engine II multichannel analyzer board. Digital images were collected with NIH Image software and EDX element maps were collected with the DeskTop Spectrum Analyzer software running on a PowerMac 8100/100.

Samples for transmission electron microscopy were prepared by scraping about a milligram of solid off of the membrane filters; air-dried samples were stored between 13 and 16 months before TEM analysis. The powders were dispersed in epoxy and cured overnight at 65° C. Immediately prior to analysis, each sample was ultramicrotomed to a thickness of 50-80 nm. The sections were placed on holey carbon substrates on copper grids. A Philip's EM430 transmission electron microscope was used at 300 kV for analysis. EDX data were obtained with an Oxford INCA system.

4.3 Results

4.3.1 Scanning Electron Microscopy

For each sample studied, imaging and EDX element mapping of iron and uranium were performed on the same sample region. All images were collected at 5000X magnification. In element maps, the brightness corresponds to the detection of either iron or uranium. Images and element maps of uranium-loaded goethite as a function of the total uranium concentration are displayed for the solids collected after a 3-month equilibration time (Fig. 4.1 and bottom row of Figs. 4.2 and 4.3). Images and element maps are also presented as a function of time for 40 μM (Fig. 4.2) and 80 μM (Fig. 4.3) total uranium concentrations.

In all of the images, goethite is visible as the fibrous background of small (length $< 1 \mu\text{m}$) needle-like crystals. Iron element maps indicate the presence and homogeneous spatial distribution of goethite. The spatial distribution of uranium can be characterized as either homogeneous or heterogeneous, with heterogeneous distribution indicated by clusters in uranium element maps. Clusters in the uranium element maps correspond to bright regions in the images, a correlation expected because of the higher backscattering efficiency of uranium as compared to iron. A bright region in an SEM image and a heterogeneous uranium distribution in an element map indicate the presence of discrete particles or aggregates of a uranium-containing precipitate. For the 96-day equilibration, uranium is homogeneously distributed only for the lowest total uranium concentration of 20 μM (Fig. 4.1, top row) and heterogeneous distributions are observed in samples with higher uranium contents. For the time-series with 40 μM total uranium, uranium is homogeneously distributed for as long as 32 days, but after 96 days of equilibration,

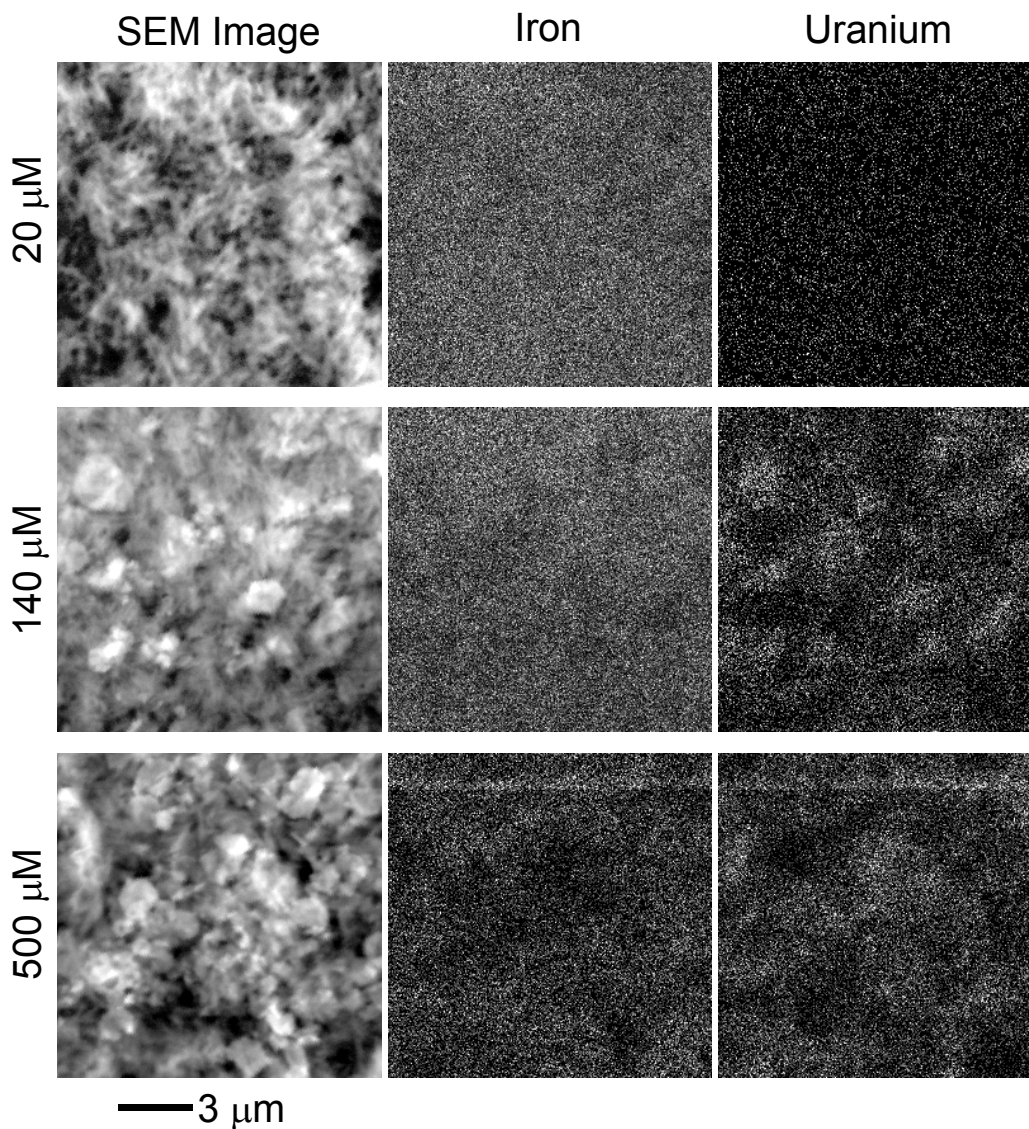


Figure 4.1: Scanning electron micrographs and X-ray elemental mapping of uranium-loaded goethite samples aged in suspension for 96 days. Suspensions contained 0.21-0.23 g L⁻¹ goethite, 20-500 μM total uranium, and 0.1 M NaNO₃ at pH 6.0 (buffered by 5 mM MES).

uranium clustering is apparent (Fig. 4.2). With 80 μM total uranium, uranium is homogeneously distributed after 1 day but is heterogeneously distributed after 32 and 96 days (Fig. 4.3). As a general trend, uranium clustering was only observed in samples that had X-ray diffraction patterns with greater peak intensities for schoepite than for goethite (Table 4.1).

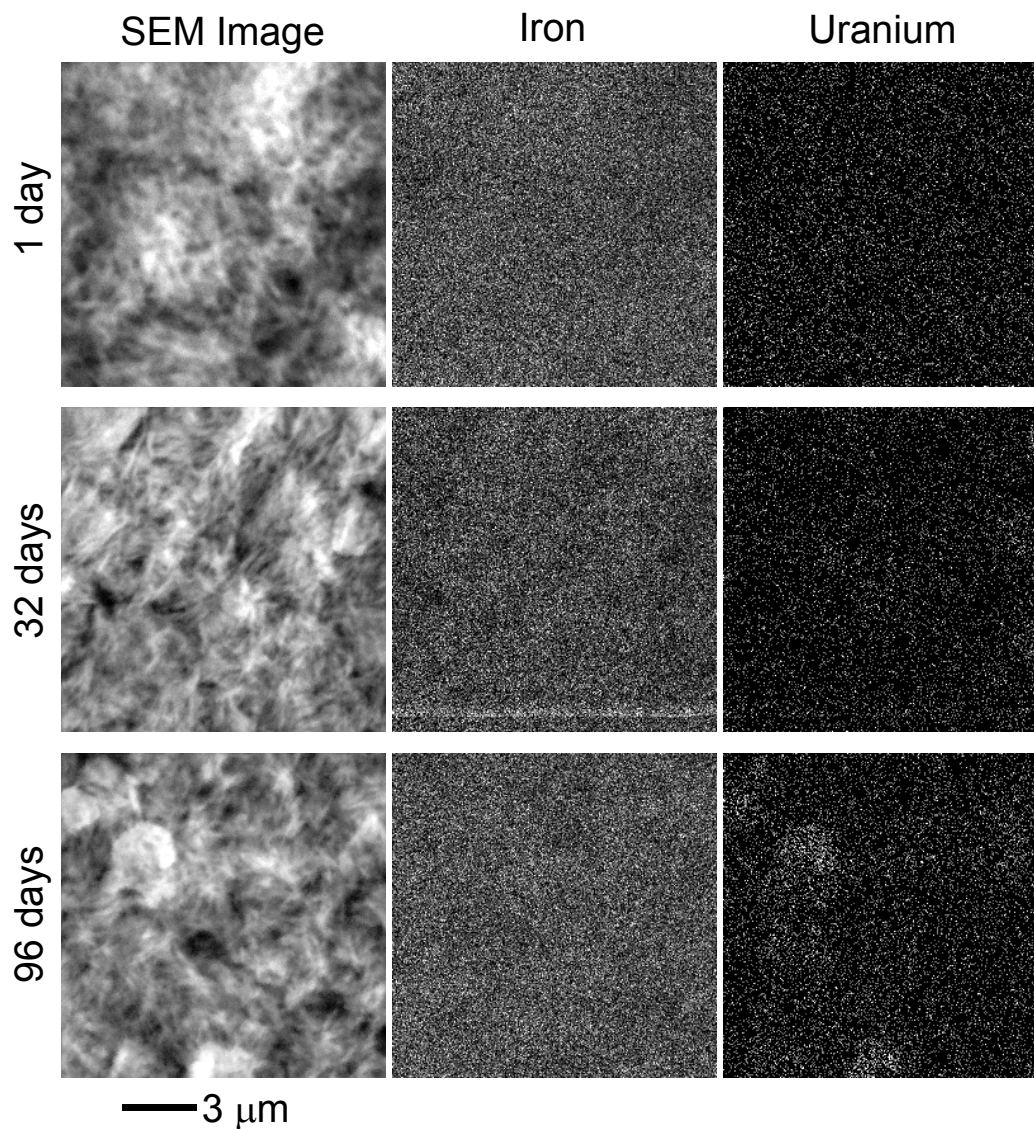


Figure 4.2: Time series of scanning electron micrographs and X-ray elemental mapping of uranium-loaded goethite samples. Suspensions contained 0.23 g L^{-1} goethite, 40 μM total uranium, and 0.1 M NaNO_3 at pH 6.0 (buffered by 5 mM MES).

4.3.2 Transmission Electron Microscopy

The effects of both the uranium content and equilibration time on the uranium distribution were investigated by TEM. Samples equilibrated for 3 months with total uranium contents of 20 , 40 , 80 , and 500 μM were analyzed. A time series of the samples with 80 μM total uranium was collected for equilibration times of 1 , 3 , and 96 days.

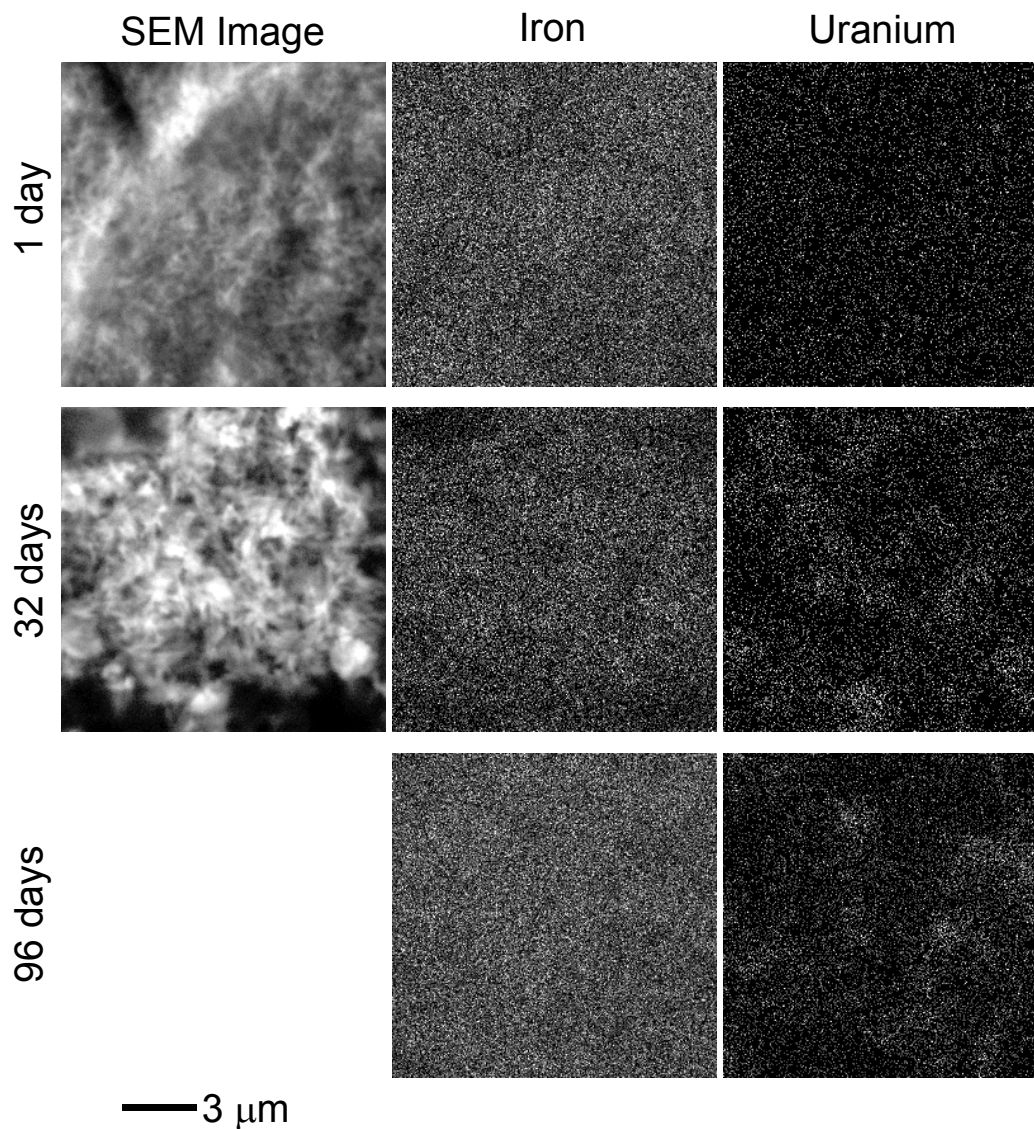
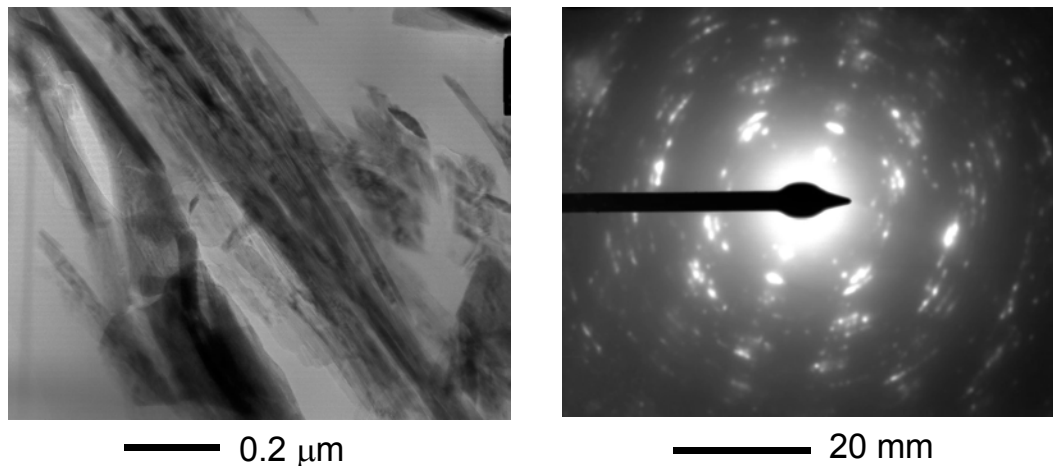


Figure 4.3: Time series of scanning electron micrographs and X-ray elemental mapping of uranium-loaded goethite samples. Suspensions contained 0.23 g L^{-1} goethite, $80 \text{ } \mu\text{M}$ total uranium, and 0.1 M NaNO_3 at pH 6.0 (buffered by 5 mM MES). The SEM image of the 96 d sample was accidentally lost.

With the TEM system used, element mapping by EDX was not possible, but the elemental composition of individual particles was determined by spot EDX analysis. Electron diffraction was particularly useful for distinguishing among different phases. Characteristic selected area diffraction patterns for goethite and uranyl oxide hydrate particles (Fig. 4.4) were determined, and electron diffraction was then used to identify

Goethite Particles



Uranyl Oxide Hydrate Particles

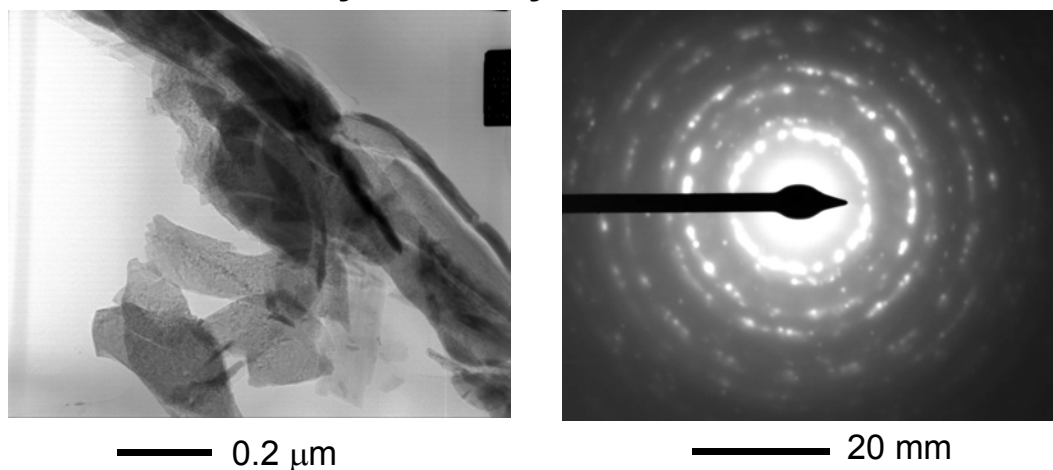


Figure 4.4: Transmission electron microscope images of clusters containing only goethite or uranyl oxide hydrate particles and their characteristic selected area electron diffraction patterns. Electron diffraction patterns were collected at a 1979 mm camera length with a 300 kV accelerating potential ($\lambda = 0.0197 \text{ \AA}$). The single-phase clusters of particles are from the sample isolated from the suspension containing 500 μM uranium after 3 months.

specific particles in mixtures of the two phases. Lattice spacings determined from the electron diffraction patterns agree with those measured previously with X-ray diffraction.

At high uranium loading and contact time (500 μM after 3 months), goethite particles are intermixed in relatively equal proportion to larger uranyl oxide

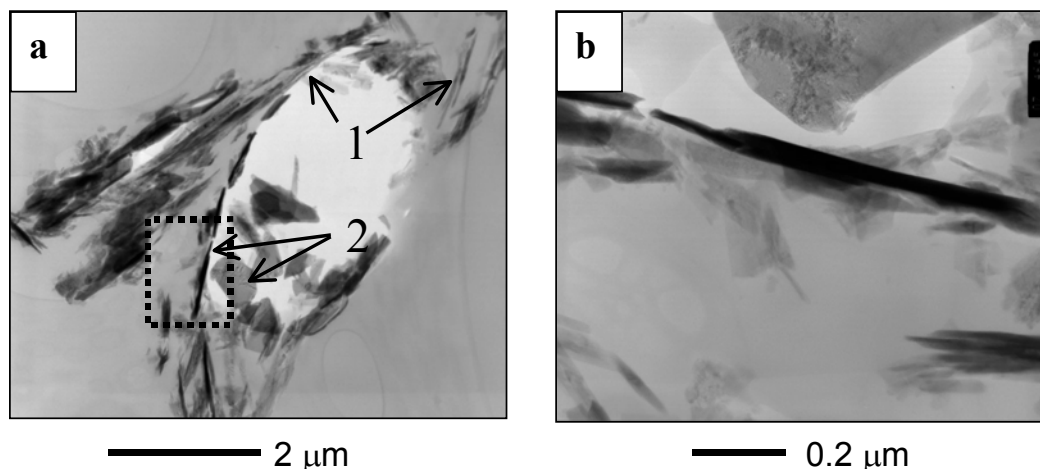


Figure 4.5: Low (a) and high (b) magnification transmission electron microscope images of a mixed aggregate of goethite particles and particles of uranium-containing phase from 3-month 500 μM uranium sample. Goethite particles (1) have a translucent appearance and generally occur as aggregates of 0.5 μm long needles. The uranium containing-phase (2) is darker in TEM and occurs as blocky plates (or as needles when only the plate edges are visible).

hydrate particles (Fig. 4.5). In transmission electron microscopy, the denser uranium-containing phase generally appears darker than the goethite particles. The goethite particles in Figure 4.5 are translucent gray, 0.5 μm long needles, and are generally observed as aggregates. The uranium-containing phase consists of blocky plates, but appears as dark needles when plates were cut on edge (Fig. 4.5).

At intermediate uranium loading (80 μM), discrete uranium-containing particles were observed in samples from suspensions aged for 3 days and 3 months. After 3 days of aging, discrete uranium-containing particles were only found at the edges of goethite-rich regions as a minor component in the samples (Fig. 4.6); a similar distribution was observed in samples aged for 3 months (data not shown). Goethite particles were closely associated with uranium-containing particles, and the two phases

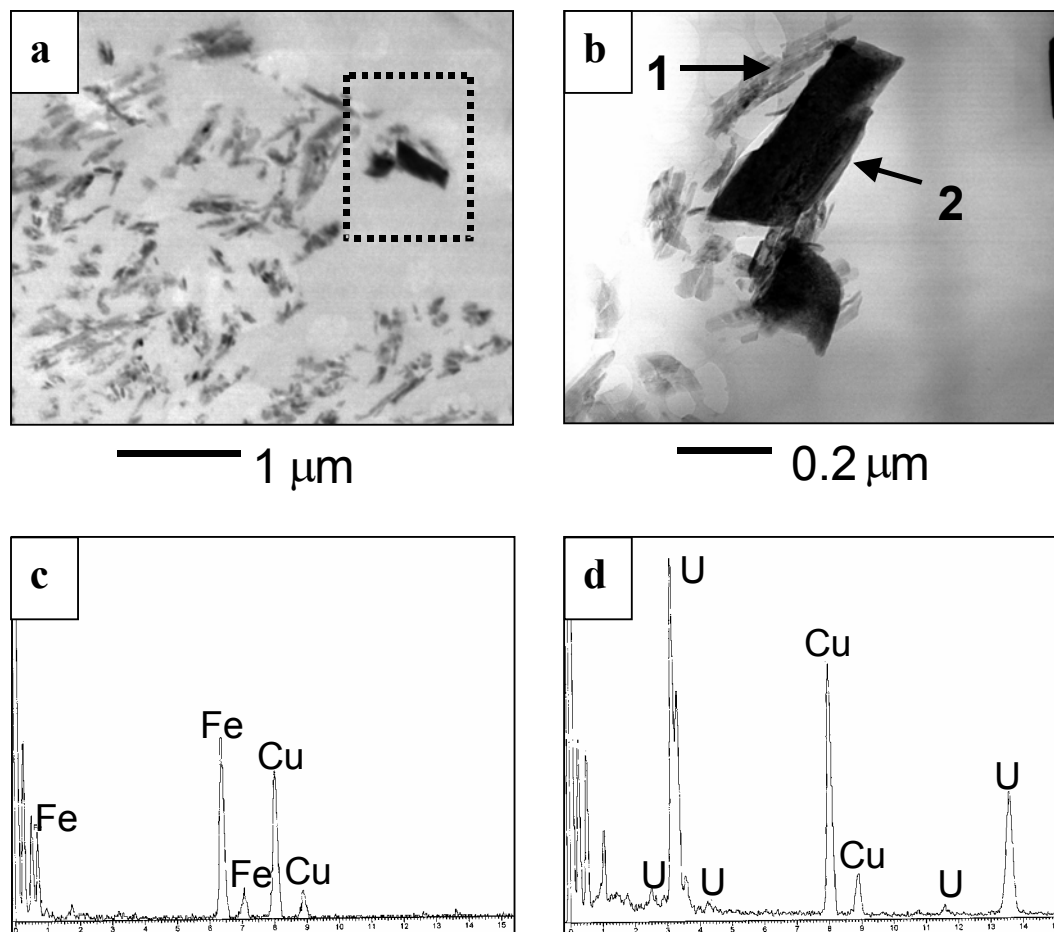


Figure 4.6: Transmission electron microscope images (at low (a) and high (b) magnification) of solids from suspension isolated after 3 days of equilibration with $80 \mu\text{M}$ uranium. The only uranium found in the high magnification image (b) is in the dark particles on the left side of the image. Goethite particles (1) are seen in close association with the uranium-containing particles (2). The EDX spectra, shown in panel (c) for particle (1) and in panel (d) for particle (2), were used to identify the phases.

were distinguished by EDX and electron diffraction (Fig. 4.6). Electron diffraction patterns of the uranium-rich particles included the patterns of both phases.

The sample of the goethite suspension loaded with $80 \mu\text{M}$ uranium and equilibrated for only 1 day displays entirely different behavior from the samples from suspensions aged for 3 days and 3 months. For the 1-day equilibration, no discrete uranium-containing particles were present. Instead, uranium was present at lower

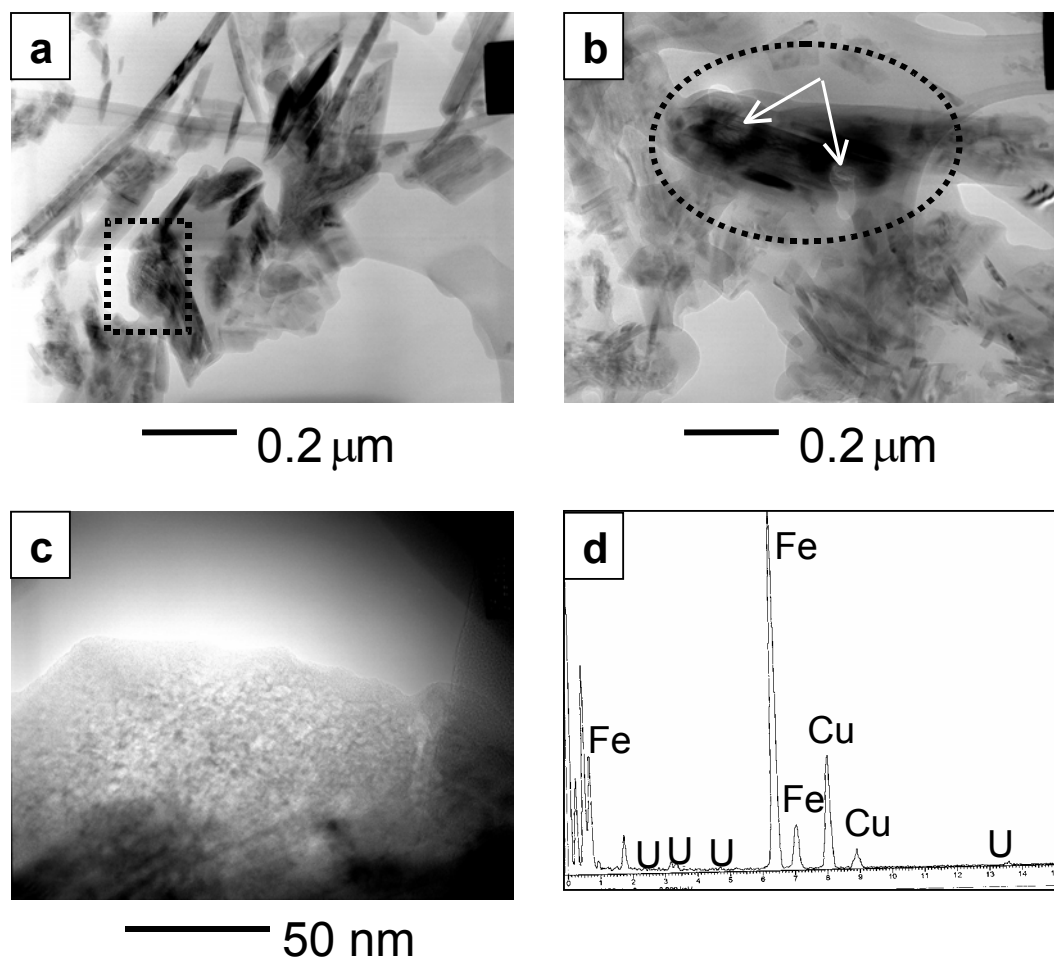


Figure 4.7: Transmission electron microscopy images of solids from goethite suspensions isolated after 1 day of contact with 80 μM uranium. Uranium-rich zones (inside dotted regions) are present as either a fuzzy agglomerate near the tip of a goethite particle (a) or as a dark speckled phase on top of a goethite particle (b). Higher magnification of the fuzzy agglomerate in panel (a) and the EDX of the agglomerate are presented in panels (c) and (d) respectively. The light spots (indicated by arrows) in panel (b) resulted from the beam burning the sample during EDX analysis (EDX spectra not shown for (b)).

concentrations and distributed throughout the sample. Uranium was closely associated with goethite particles (Fig. 4.7a and b), and could be identified only with EDX because the goethite electron diffraction pattern overshadowed any pattern of the uranium-containing phase. At high magnification, one of the uranium-rich clusters has a speckled

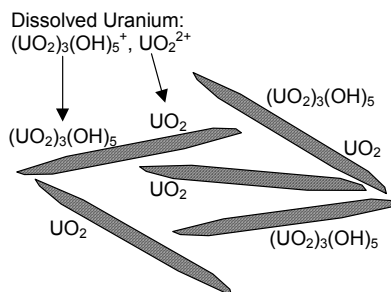
texture, which indicates that the uranium-rich cluster is not entirely amorphous, but rather has some crystallinity (Fig. 4.7c).

4.4 Discussion

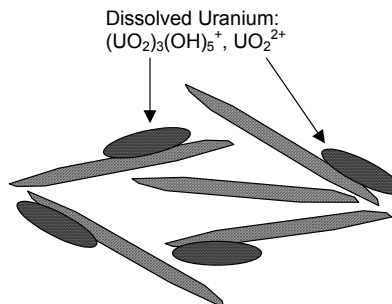
4.4.1 Nature of Solid-associated Uranium

Electron microscopy has confirmed the hypothesis that uranium can be adsorbed on mineral surfaces, present as a surface-precipitated phase, or precipitated in discrete uranium-containing particles. The distribution of uranium among these three types of solid-associated phases is a function of the equilibration time of goethite with uranium and the degree to which the dissolved phase is supersaturated with respect to a uranium-containing solid phase. Observations of discrete uranium-containing particles in electron micrographs and uranium clustering in element maps are consistent with observations of X-ray diffraction peaks for schoepite (reported in Chapter 3). Furthermore, the low crystallinity uranium surface precipitate observed with TEM (Fig. 4.7) is consistent with the absence of a signal for schoepite in the X-ray diffraction pattern (Table 4.1) and the homogenous distribution of uranium in the SEM-EDX element map (Fig. 4.3). Although air-dried samples were stored for as long as 16 months before SEM and TEM analyses, the consistency of SEM, TEM (3 months longer storage for TEM than for SEM), and XRD measurements (generally performed within a week of sample collection) suggests that no significant redistribution of uranium occurred in the dried samples during the storage period.

- 1. Adsorption:**
Rapid uptake of uranium from solution as monomeric or polymeric surface complexes.



- 2. Surface Precipitation:**
Continuing uptake of uranium from solution as oligomeric surface clusters form.



- 3. Precipitation:**
Discrete uranium-containing phases form by ripening and detach into solution.

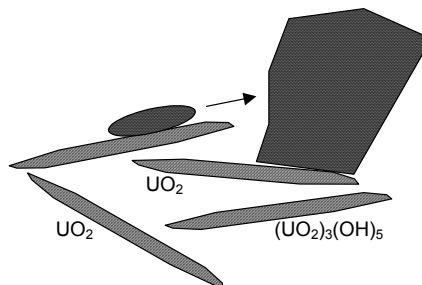


Figure 4.8: Schematic representation of the growth of uranium-containing precipitates following adsorption on goethite.

A three-step mechanism is suggested for the growth of discrete uranium-containing particles at low degrees of supersaturation (Fig. 4.8). In the first step, uranium adsorbs to the goethite surface as monomeric or polymeric surface complexes on the short time-scales discussed in Chapter 3. In the second step, oligomeric surface clusters form on the goethite surface, possibly nucleating at sites of initial uranium sorption. In the third step, the oligomeric surface clusters ripen with uranium migrating from smaller to larger particles, until the particles are sufficiently large to be stable in solution. The close association of goethite particles with the larger uranium-containing particles in

TEM images suggests that the initial coordination of uranium to the goethite surface may persist even once discrete uranium-containing particles have formed.

The transformation from monomeric surface complexes to schoepite-like polymeric surface complexes was recently observed spectroscopically as the loading of uranium on montmorillonite increased (Chisholm-Brause et al., 2001). According to the mechanism illustrated in Figure 4.8, the uranium concentration at the goethite surface should actually decrease as oligomeric surface clusters ripen into larger discrete uranium-containing particles that detach from the surface. This phenomenon was observed with quantitative EDX analysis of uranium sorbed on goethite particles in material from the Koongarra ore deposit. The solid-associated uranium concentration on goethite increased with the total uranium content until the precipitation of a uranyl oxyhydroxide solid, and then the solid-associated concentration decreased dramatically (Lumpkin et al., 1999).

4.4.2 Utility of Electron Microscopy

Both scanning and transmission electron microscopy were useful in determining the distribution of uranium in goethite suspensions as a function of uranium concentration and equilibration time. Although SEM did not provide the high resolution of TEM, its advantages were the ease of sample preparation, high sample throughput (about two samples per hour), and collection of element maps (though this can also be done on many TEM systems). Further, SEM analysis served as a screening tool for selecting samples for TEM analysis. TEM analysis was more time consuming, but ultimately offered higher resolution images and the opportunity for phase identification with electron diffraction.

4.4.3 Need for Additional Characterization

It would be naïve to suggest that complete characterization of uranium-contaminated solids can be accomplished through the use of any single technique. In the current study, information about the crystalline structure of the solid phases was gained through X-ray diffraction measurements, which complemented imaging and element composition information achieved with SEM and TEM. In addition to electron microscopy, other techniques are available for determining the spatial distribution of a contaminant. Spatially resolved elemental composition data for plutonium on Yucca Mountain zeolitic tuff were acquired by electron microprobe analysis (EMPA) and micro-synchrotron X-ray fluorescence (SXRF) (Duff et al., 2001). SXRF has also been used to examine FEMP soils (Bertsch et al., 1994) and evaporation basin sediments (Duff et al., 1997; Duff et al., 2000).

Various spectroscopic techniques can probe the bonding environment of uranium, providing additional information for characterization of the uranium-goethite system. Infrared spectroscopy was used to identify ternary uranyl-carbonate sorption complexes on hematite (Bargar et al., 1999). Raman spectroscopy was used in conjunction with SEM and TEM to identify uranium-containing phases at the FEMP (Morris et al., 1996), and was also used to characterize different types of surface complexes on montmorillonite (Morris et al., 1994). Different montmorillonite surface complexes were also characterized with luminescence spectroscopy (Chisholm-Brause et al., 2001), a technique also used in identifying sorption complexes and uranium-containing precipitates in evaporation basin sediments (Duff et al., 2000). Recently, extended X-ray

absorption fine structure spectroscopy (EXAFS) has been used to determine the structure of surface complexes and precipitates by identifying the nearest neighbors to sorbed uranium atoms. The structures of uranium surface complexes on goethite (Moyes et al., 2000), hematite (Bargar et al., 1999; Bargar et al., 2000), montmorillonite (Chisholm-Brause et al., 1994; Dent et al., 1992; Sylwester et al., 2000), vermiculite and hydrobiotite (Hudson et al., 1999), kaolinite (Thompson et al., 1998), and silica (Dent et al., 1992; Sylwester et al., 2000) have been determined using EXAFS.

4.4.4 Conclusions

Electron microscopy was useful in distinguishing among sorbed uranium, surface-precipitated uranium, and discrete uranium-containing precipitates. Imaging and element mapping with SEM-EDX showed the clustering of uranium with both increasing uranium content and equilibration time. Higher magnification imaging with TEM was used to observe both surface precipitates and discrete uranium-containing particles. The SEM-EDX and TEM measurements are consistent with each other and also with solution chemistry and XRD measurements. Electron microscopy can be an important component of a suite of techniques used in the characterization of uranium in contaminated environmental media. Determination of the solid phase speciation of uranium can yield useful information for predicting uranium mobility in the environment.

Chapter 5

DISSOLUTION AND TRANSFORMATION OF URANYL OXIDE HYDRATES

5.1 Introduction and Background

The mobility of uranium in the environment is frequently controlled by uranium (VI) minerals. Schoepite is of particular environmental importance because of its occurrence at contaminated sites and crucial role in the corrosion of spent nuclear fuel. Schoepite or schoepite-like phases have been identified in soils at the Fernald Environmental Management Site (Buck et al., 1996; Morris et al., 1996) and Oak Ridge National Laboratory (Roh et al., 2000). During the corrosion of spent nuclear fuel, schoepite is the first phase formed in a sequence of uranium(VI) phases (Wronkiewicz and Buck, 1999). The formation of schoepite may control the solubility of uranium in a corrosive environment and is the starting material for the formation of more stable secondary phases. Schoepite plays a similar role in the weathering of natural ore deposits (Finch and Murakami, 1999), and is ubiquitous at uraninite deposits of the Colorado Plateau (Zhao and Ewing, 2000).

Despite their simple compositions, the uranyl oxide hydrates are an amazingly diverse family of minerals (Table 5.1). The simplest minerals compositionally are schoepite, meta-schoepite, and dehydrated schoepite. The structure of schoepite was determined by Finch et al. (1996) using a single crystal X-ray diffractometer; the distinction among related phases by X-ray diffraction (XRD) has been an area of recent

Table 5.1: Representative uranyl oxide hydrate minerals.

Mineral	Composition ^a	Space Group ^b	Uranyl Equatorial Coordination ^c
billietite	Ba(UO ₂) ₆ O ₄ (OH) ₆ ·8H ₂ O	<i>Pbn2</i> ₁	pentagonal
becquerelite	Ca(UO ₂) ₆ O ₄ (OH) ₆ ·8H ₂ O	<i>Pn2</i> ₁ <i>a</i>	pentagonal
clarkeite	Na[(UO ₂)O(OH)]·H ₂ O	<i>R</i> $\bar{3}$ <i>m</i>	pentagonal or hexagonal
compreignacite	K ₂ (UO ₂) ₆ O ₄ (OH) ₆ ·7H ₂ O	<i>Pnmm</i>	pentagonal
dehydrated schoepite	(UO ₂)O _{0.15-x} (OH) _{1.5+2x} (0<x<0.25)	<i>Abcm</i> ?	pentagonal
metaschoepite	(UO ₂) ₈ O ₂ (OH) ₁₂ ·10H ₂ O	<i>Pbna</i>	pentagonal
schoepite	(UO ₂) ₈ O ₂ (OH) ₁₂ ·12H ₂ O	<i>P2</i> ₁ <i>ca</i>	pentagonal
vandenbrandeite	Cu(UO ₂)(OH) ₄	<i>P</i> $\bar{1}$	pentagonal
vandendriesscheite	Pb _{1.5} (UO ₂) ₁₀ O ₆ (OH) ₁₁ ·11H ₂ O	<i>Pbca</i>	pentagonal

^a All compositions are from Finch and Murakami (1999).

^b Space groups are those given in Burns (1999) with the exception of clarkeite (Finch and Ewing, 1997), dehydrated schoepite, and meta-schoepite (Finch et al., 1998).

^c From Burns (1999) with the exception of clarkeite (Finch and Ewing, 1997).

research (Finch et al., 1997; Finch et al., 1992). The schoepite structure is composed of sheets of uranyl pentagonal bipyramidal polyhedra, connected through edge and corner sharing of equatorial oxygen atoms. The sheets are bound together by hydrogen bonding through water molecules, which occupy the interlayer spaces between the sheets. Meta-schoepite and dehydrated schoepite are structurally similar to schoepite, but with sheet rearrangement and contraction of the interlayer spacing due to the loss of interlayer water molecules (Finch et al., 1998). Extended X-ray absorption fine structure spectroscopy (EXAFS) measurements of a synthetic schoepite are consistent with the structure determined by XRD (Allen et al., 1996).

Schoepite has a strong tendency to incorporate cations into interlayer spaces (Hoekstra and Siegel, 1973). At natural uraninite deposits, trace elements preferentially enter the structures of secondary uranium phases (Zhao and Ewing, 2000). In the environment, the most commonly incorporated cation is calcium, leading to the formation of becquerelite (Finch and Murakami, 1999). This transformation has also been observed

in numerous laboratory experiments (Sandino and Grambow, 1994; Sowder et al., 1996; Sowder et al., 1999; Vochten and Van Haverbeke, 1990). Exposure of schoepite to potassium leads to compregnacite formation (Sandino and Grambow, 1994), and exposure to barium and lead yields billietite and wölsendorfite respectively (Vochten and Van Haverbeke, 1990). Other layered cation uranyl oxide hydrates have been formed only in the laboratory, incorporating strontium (Burns and Hill, 2000a; Cahill and Burns, 2000), cesium (Hill and Burns, 1999), potassium in a phase distinct from compregnacite (Burns and Hill, 2000b), magnesium, manganese, and nickel (Vochten et al., 1991). Clarkeite is the only sodium uranyl oxide hydrate mineral found in nature (Finch and Murakami, 1999), but many hydrated and anhydrous sodium uranates have been formed synthetically with $\text{Na}_2\text{U}_2\text{O}_7$ the most commonly observed form (Allen et al., 1996; Baran, 1988; Cordfunke and Loopstra, 1971; Malý and Veselý, 1958; Ricci and Loprest, 1955; Wamser et al., 1952). Schoepite can also undergo transformation without the incorporation of interlayer cations. When exposed to phosphate, schoepite was transformed to autunite through several uranyl phosphate intermediates (Sowder et al., 1996). In the presence of elevated carbon dioxide partial pressures (greater than 2.8%), schoepite was transformed to rutherfordine (Meinrath and Kimura, 1993).

Numerous investigations have reported thermodynamic constants for the equilibrium solubility of schoepite. Unfortunately the reported constants and methods of determination vary significantly with solubility products ranging from $10^{4.70}$ (Díaz Arocas and Grambow, 1998) to $10^{6.33}$ (Sandino and Bruno, 1992). The dissolution rates of natural (Casas et al., 1994) and synthetic (Steward and Mones, 1997) schoepite have recently been studied with widely divergent results. Issues of schoepite solubility and

dissolution kinetics will be discussed in later sections of this chapter, and a review of schoepite solubility products is presented in Appendix A.

In the current work, batch and flow-through experiments were performed to probe the equilibrium and kinetics of schoepite dissolution in solutions of varying composition and using solids from several syntheses. All experiments were conducted at or near pH 6 in order to isolate the effects of monovalent cation and fluoride concentrations, and to avoid the influence of uranyl-carbonate complexation in systems open to the ambient atmosphere. The evaluation of the solution chemistry was integrated with the characterization of solids collected over the course of the experiments. The large number of experiments performed allows for an evaluation of the equilibrium solubilities of schoepite and of the secondary phases formed through the incorporation of interlayer cations. Dissolution rates are quantified from flow-through reactor data, while batch experiments provide additional information on the time-scales of dissolution and transformation reactions.

5.2 Experimental Materials and Methods

5.2.1 Materials

Three separate batches of schoepite were synthesized following an adaptation of published methods (Sowder et al., 1996; Torrero et al., 1994), in which 0.01 M uranyl nitrate solutions, prepared from uranyl nitrate hexahydrate (Johnson Matthey), were titrated with freshly prepared 0.1 M strong base to pH 5.5-6.0. Two batches were synthesized using sodium hydroxide (Mallinckrodt) and one using tetrabutylammonium

hydroxide (TBAOH) (Aldrich), hereafter referred to as Na-syntheses #1 and #2 and TBA-synthesis. The titration was performed in the laboratory atmosphere, but uranyl carbonate species are insignificant below pH 7. Almost immediately following the addition of base, a bright yellow precipitate formed, which was aged for 7-14 days and then rinsed to remove excess reactants. Rinsing consisted of repeated centrifugation or sedimentation, decantation, and resuspension in deionized water. Na-synthesis #1 was rinsed by performing six rinsing steps with centrifugation, and Na-synthesis #2 was rinsed with eight steps. The solid synthesized with TBAOH was rinsed over the course of nine days with eight steps using sedimentation in place of centrifugation. Following the final washing steps, the solids were resuspended in deionized water to make up the stock suspensions used in subsequent experiments. Portions of Na-synthesis #2 and TBA-synthesis were freeze-dried in preparation for surface area measurements. A portion of Na-synthesis #2 was subjected to high temperature (150°C) and pressure in a Teflon-lined Parr bomb for three days in an effort to ripen the solid to a more crystalline phase.

Water used in all experiments was Milli-Q grade with resistivity greater than 18.2 M Ω cm supplied by a laboratory treatment system (Millipore Corp.). Sodium nitrate (Mallinckrodt) and cesium nitrate (Alfa Aesar) were used in their solid forms. Sodium fluoride was used from a 100 mg L⁻¹ standard solution (Orion). Many experiments included 2-(n-morpholino)ethanesulfonic acid (MES) as a pH buffer (Avocado Research Chemicals), adjusted to pH 6 with sodium hydroxide.

5.2.2 Batch Dissolution and Transformation Experiments

Although a large number of batch experiments were performed, the experimental methodology remained simple and consistent throughout. Batch dissolution experiments were initiated by adding an aliquot of stock schoepite suspension to 250-500 mL of magnetically-stirred solution of varied composition. Original solutions contained sodium nitrate, cesium nitrate, sodium fluoride, or no dissolved solids. In pH-buffered experiments, the solution contained 5 mM MES buffer and was adjusted to pH 6 (providing an additional 2.3 mM sodium) prior to the addition of schoepite. All experiments were conducted at the ambient temperature of the laboratory ($22 \pm 2^\circ\text{C}$).

Several simple variations of this basic method were also employed. In several cases, referred to as residuals experiments, the solids remaining at the conclusion of one batch experiment were collected on a 0.2 μm polycarbonate filter membrane (Millipore), rinsed off the filter with a small volume of water, and then used to initiate a subsequent batch experiment. In one experiment, the pH was not buffered with 5 mM MES, but instead was periodically adjusted with first nitric acid (prepared from concentrated trace metal grade (EM Science)) and then sodium hydroxide. A final set of experiments involved the equilibration of schoepite suspensions for 43 days in dilute solution followed by the addition of sodium nitrate or cesium nitrate; these experiments will be referred to as post-equilibration electrolyte addition experiments.

The sampling procedure for all experiments was identical. Dissolved uranium samples were filtered using syringe-mounted 0.2 μm polycarbonate filter membranes; the first 3 mL or more of filtrate were sent to waste, and the remainder of the filtrate was collected and acidified (1% nitric acid). Samples for total uranium were collected by

diluting an aliquot of whole suspension in 10% nitric acid to dissolve all particles. The filter membranes used in dissolved uranium sampling were removed from their filter holders and air-dried to isolate solids from the batch reactors for subsequent analyses. The sampling procedure was used throughout batch experiments and also to sample the stock schoepite suspension and uranium-free batch reactor solution before the initiation of experiments.

5.2.3 Flow-through Dissolution

Flow-through dissolution experiments were conducted to complement the batch dissolution experiments. In flow-through experiments, stock schoepite (Na-synthesis #1) suspension was added to approximately 50 mL stirred, flow-through polymethylmethacrylate reactors with outlets sealed by 0.2 μm polycarbonate filter membranes. The influent solutions for all flow-through reactors were 0.1 M sodium nitrate, 5 mM MES at pH 6.0, and 0-20 μM dissolved uranium. Flow to the reactors was controlled by a peristaltic pump and stirring was provided by a magnetic stir bar and stir plate. One set of experiments was conducted at a nearly constant residence time of 3.5 hours with 5, 10, or 20 μM uranium in the influent. A second set of experiments was conducted with no uranium in the influent, but with the residence time incrementally increased from 0.25 to 4.43 hours.

5.2.4 Analytical Methods

Dissolved concentrations of uranium and, in some cases, sodium and cesium were determined by inductively coupled plasma mass spectrometry (ICP-MS) with a Hewlett

Packard HP4500 instrument. Samples were diluted so that the actual samples analyzed would have uranium concentrations in the optimal range 0.5 – 25 ppb (detection limit 0.01 ppb). Sample dilutions for uranium were prepared with 1% nitric acid and 10 ppb thallium (SPEX Chemical) as an internal standard. Calibration standards for uranium were prepared from a standard solution (Alfa Aesar). Solution pH was measured with a Ross glass electrode and Orion 720A pH meter, calibrated with commercially available standards.

The synthesized and partly-reacted solids were characterized and identified by X-ray powder diffraction (XRD), diffuse reflectance infrared spectroscopy (DRIFTS), scanning electron microscopy (SEM), Raman spectroscopy, and BET surface area analysis. XRD analyses were performed on a Scintag Pad V X-ray powder diffractometer with a Cu k-alpha X-ray source and germanium detector. Powdered schoepite diluted in potassium bromide was analyzed with a Bio-Rad FTS-45 Fourier transform infrared spectrometer with a DRIFTS sample stage. SEM images were collected on gold- and carbon-coated samples with a Camscan Series II scanning electron microscope. Raman spectra were measured with a 514.5 nm argon ion laser or 782 nm diode laser on a Renishaw MicroRaman Spectrometer with a spectral resolution of 1 cm^{-1} . Samples for Raman analysis were prepared by evaporating aliquots of concentrated suspensions on glass slides. The surface area was determined on freeze-dried samples by BET N_2 adsorption using a Micromeritics Gemini surface area analyzer.

5.2.5 Equilibrium Calculations

Equilibrium calculations were performed using the aquatic chemical equilibrium software program MINEQL⁺ (Schecher and McAvoy, 1998). Ionic strength corrections in MINEQL⁺ are made using the Davies equation. The database of thermodynamic constants of dissolved uranyl species used in calculations are taken from the critical review of Grenthe et al. (1992) amended to use the $\text{UO}_2(\text{OH})_{2(\text{aq})}$ formation constant of Silva (1992) (Table A.1). Input parameters for calculations were total concentrations of components, ionic strength, pH, and a carbon dioxide partial pressure of $10^{-3.5}$ atm.

5.3 Results

5.3.1 Characterization of synthesized solids

Initial identification of the synthesized solids was made based on X-ray diffraction results. As displayed in Figure 5.1, all three syntheses have the same six dominant peaks in the 2θ range $10\text{-}30^\circ$ and match well with reference card #43-0364, which is labeled as synthetic meta-schoepite (JCPDS-ICDD, 1999). The dominant peaks are located at 12.0° (7.39 Å), 24.2° (3.68 Å), 24.7° (3.60 Å), 25.3° (3.52 Å), 27.6° (3.23 Å), and 28.1° (3.17 Å). The reflections of the four dominant peaks in the reference pattern are indexed in Table 5.2 together with those of other reference patterns and calculated diffraction patterns for schoepite and clarkeite. The relative intensities of the peaks in the $23\text{-}29^\circ$ 2θ range are much higher in the TBA-synthesis than in either of the Na-syntheses, providing a better match to reference card #43-364. The dominant peak at 12° is narrowest for Na-synthesis #2, indicating that this material is the most crystalline

Table 5.2: X-ray diffraction reflections of synthetic uranyl oxide hydrate solids and reference data for related minerals.

Card #	Name/Formula	Dominant Diffraction Maxima (Å) (indexed reflection)			
Na-synthesis #1		7.38	3.67	3.58	3.22
Na-synthesis #2, aged 1 month		7.29	3.65	2.43	1.83
Na-synthesis #2, aged 10 months		7.35	3.67	3.23	3.17
Ripened Na-synthesis #2		7.36	5.12	3.67	3.23
Na-synthesis #2 residuals after long-term NaNO ₃ contact		5.86	4.12	3.39	
TBA-synthesis		7.39	3.68	3.60	3.23
13-241	Schoepite UO ₃ ·2H ₂ O	7.35 ₍₀₀₂₎	3.66 ₍₂₂₃₎	3.24 ₍₂₄₂₎	2.45 ₍₁₅₄₎
13-407	Schoepite UO ₃ ·2H ₂ O	7.28 ₍₀₂₁₎	5.08 ₍₂₂₁₎	3.66 ₍₂₂₃₎	3.44 ₍₄₁₁₎
29-1376	Schoepite, synthetic UO ₃ ·2H ₂ O	7.37 ₍₀₀₂₎	3.59 ₍₄₀₀₎	3.52 ₍₃₃₁₎	3.23 ₍₂₄₂₎
43-0364	Metaschoepite, synthetic UO ₃ ·2H ₂ O	7.33 ₍₀₀₂₎	3.67 ₍₀₀₄₎	3.58 ₍₂₄₀₎	3.22 ₍₂₄₂₎
calc. ^a	Schoepite (UO ₂) ₈ O ₂ (OH) ₁₂ ·12H ₂ O	7.37 ₍₀₀₂₎	3.63 ₍₂₄₀₎	3.25 ₍₂₄₂₎	3.22 ₍₄₀₂₎
calc. ^b	Clarkeite Na[(UO ₂)O(OH)]·H ₂ O	5.90 ₍₀₀₃₎	3.37 ₍₁₀₁₎	3.20 ₍₀₁₂₎	2.71 ₍₁₀₄₎

^a Pattern calculated from structure by Finch et al. (1997)

^b Pattern calculated by Finch and Ewing (1997)

of the three syntheses.

Additional confirmation of the identity of the stock material was provided by Raman and infrared spectra of the schoepite from Na-synthesis #2 (Fig. 5.2). Two dominant peaks in the Raman spectra are located at 852.9 and 841.1 cm⁻¹ and are assigned to the symmetric stretch of the uranyl ion in two different structural environments. The peak positions and interpretation are consistent with a previous study that measured peaks of equal intensity at 840 and 860 cm⁻¹ for schoepite (Maya and Begun, 1981). Two peaks were also observed in the Raman spectra of synthetic metaschoepite at 846 and 870 cm⁻¹ (Hoekstra and Siegel, 1973). Lower energy peaks are located at 544.9, 406.9, and 249.3 cm⁻¹ and are due to either uranyl bending modes or vibrations associated with uranium bonds to equatorial oxygen atoms. The symmetric

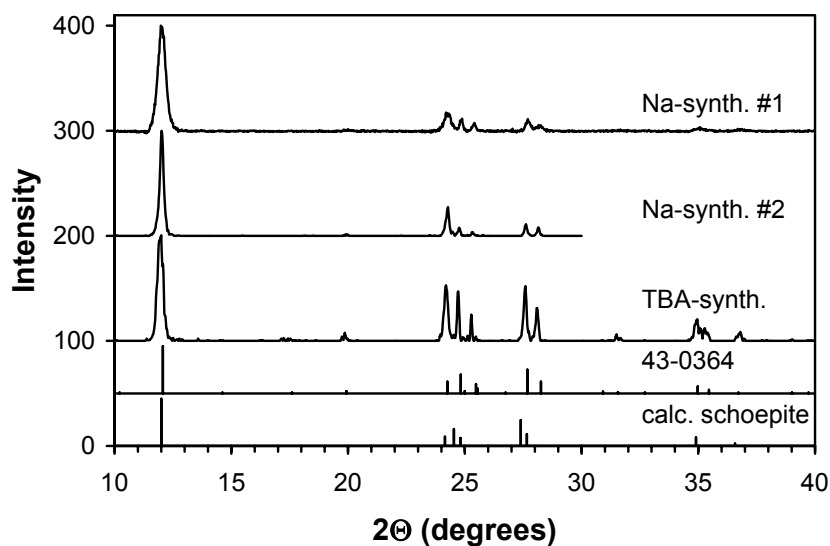


Figure 5.1: X-ray diffraction patterns of synthetic schoepite preparations (two prepared with sodium hydroxide and one prepared with tetrabutylammonium hydroxide). The measured diffraction patterns are presented above a reference pattern for synthetic metaschoepite (JCPDS card 43-0364) and a calculated diffraction pattern for schoepite (Finch et al., 1997).

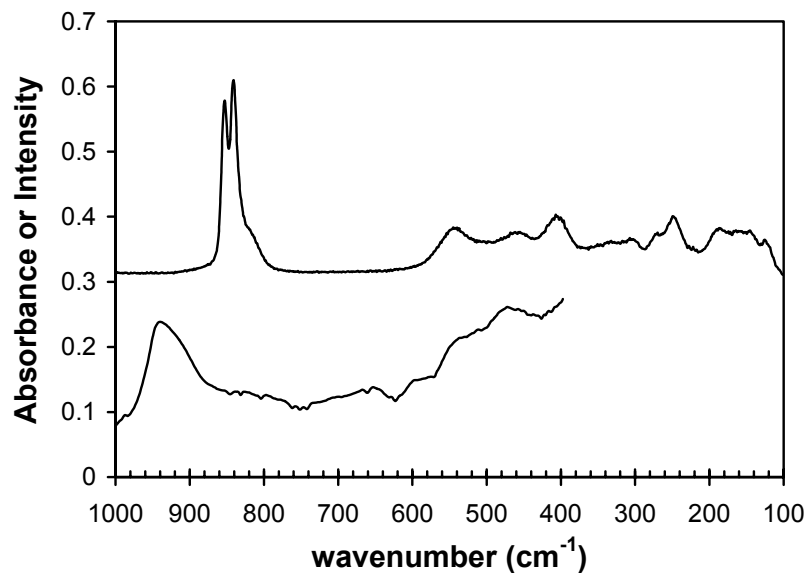


Figure 5.2: Raman (top) and infrared (bottom) spectra of schoepite from Na-synthesis #2. Infrared measurements were performed in DRIFTS mode and absorbance is presented. Raman intensity has been normalized to fit on the same scale. The symmetric uranyl ion stretch is only Raman active and appears in two discrete bands at 841.1 and 852.9 cm^{-1} , and the anti-symmetric uranyl ion stretch is only IR active and appears as a broad peak centered at 940 cm^{-1} .

stretch is only Raman active and does not appear in the IR spectrum, and conversely the anti-symmetric stretch is only IR active and appears as a broad peak at 939.9 cm^{-1} . The peak position has been measured at 930 cm^{-1} for natural schoepite (Cejka, 1999) and synthetic metaschoepite precipitated from uranyl nitrate solution with sodium hydroxide (Allen et al., 1996), but was measured at 958 cm^{-1} for metaschoepite synthesized by the hydration of anhydrous UO_3 (Hoekstra and Siegel, 1973). Cejka (1999) has suggested that such variations can result from differences in the conditions under which the solids are formed in the laboratory and environment and from the preparation of samples for IR measurements. The assignment of Raman versus IR active peaks and peak positions is consistent with a recent critical review (Cejka, 1999).

The surface areas of synthesized solids were determined by BET- N_2 adsorption. Material from Na-synthesis #2 and the TBA synthesis had specific surface areas of 12.9 and $8.8\text{ m}^2\text{ g}^{-1}$, respectively. Material synthesized by a method similar to that used for Na-synthesis #2 had a surface area of $13.3\text{ m}^2\text{ g}^{-1}$ (Sowder, 1998).

5.3.2 Batch Dissolution Experiments

5.3.2.1 Determining the Influence of Sodium

The dissolution and transformation of schoepite in batch reactors is a complicated story. In very few cases did experiments yield the expected results, and the completion of each set of experiments raised questions that were addressed in subsequent experiments. The results of the batch experiments are presented chronologically so as to follow the progression of understanding gained through the experiments. The conditions and some key results for each experiment are compiled in Table 5.3.

Table 5.3: Batch dissolution experiments performed.

Expt. (ID)	Starting Solid	Experiment Description	elec.	conc. (mM)	MES (mM)	[U] _{max} (μ M)	[U] _{max} (days)	[U] _{final} (μ M)	pH _{final}
A1	Na-syn. #1	dissolution	NaNO ₃	100	5	7.7	2	4.8	~6.0
A1R	A1 residual	dissolution	NaNO ₃	100	5	12.0	6	0.4	~6.0
A2	Na-syn. #1	dissolution	NaNO ₃	100	5	22.3	12	4.8	~6.0
B1	Na-syn. #2	dissolution	NaNO ₃	100	5	14.5	14	3.8	~6.0
B2	Na-syn. #2	dissolution	NaNO ₃	100	5	15.1	14	3.6	~6.0
B3	Na-syn. #2	dissolution	NaNO ₃	10	5	151.5	1	2.9	~6.0
B4	Na-syn. #2	dissolution	NaNO ₃	10	5	11.3	7	3.5	~6.0
B4R	B4 residual	dissolution	NaNO ₃	10	5	5.4	0.4	1.1	~6.0
B5	Na-syn. #2	dissolution	CsNO ₃	10	5	4.1	14	1.2	5.89
B6	Na-syn. #2	dissolution	CsNO ₃	100	5	2.9	54	0.9	5.93
B7	Na-syn. #2	dissolution	NaNO ₃	10	5	13.1	5	6.7	5.84
B8	ripe Na-syn. #2	dissolution	NaNO ₃	10	5	14.7	7	7.0	5.88
B9	ripe Na-syn. #2	dissolution	CsNO ₃	10	5	4.1	10	1.0	5.87
B10	Na-syn. #2	dissolution	dilute Na _{max} =35 μ M		0	25.9	3	2.1	6.03
B10R	B10 residual	dissolution	dilute		0	9.0	7	5.8	5.85
C1	TBA-syn.	dissolution	dilute		0	38.9	108	38.9	6.10
C2	TBA-syn.	fluoride-induced	NaF	1	0	107.3	3	100.8	5.96
C3	TBA-syn.	fluoride-induced	NaF	5	0	460.9	0.5	123.7	6.03
C4	TBA-syn.	post-equilibration electrolyte addition	NaNO ₃	1	0	44.5	0.01	20.9	5.88
C5	TBA-syn.	post-equilibration electrolyte addition	NaNO ₃	10	0	44.4	35	44.4	5.52
C6	TBA-syn.	post-equilibration electrolyte addition	CsNO ₃	1	0	49.3	28	48.8	5.12
C7	TBA-syn.	post-equilibration electrolyte addition	CsNO ₃	10	0	39.1	28	36.4	5.00

The first set of experiments (A1 and A2) examined the dissolution of schoepite ($[U]_{\text{tot}} = 230 \mu\text{M}$) in MES-buffered 0.1 M NaNO₃ solution. Sodium nitrate was originally included in order to simplify interpretation of surface electrostatics and for consistency with previous work on the uranium-goethite system (see Chapter 3). The

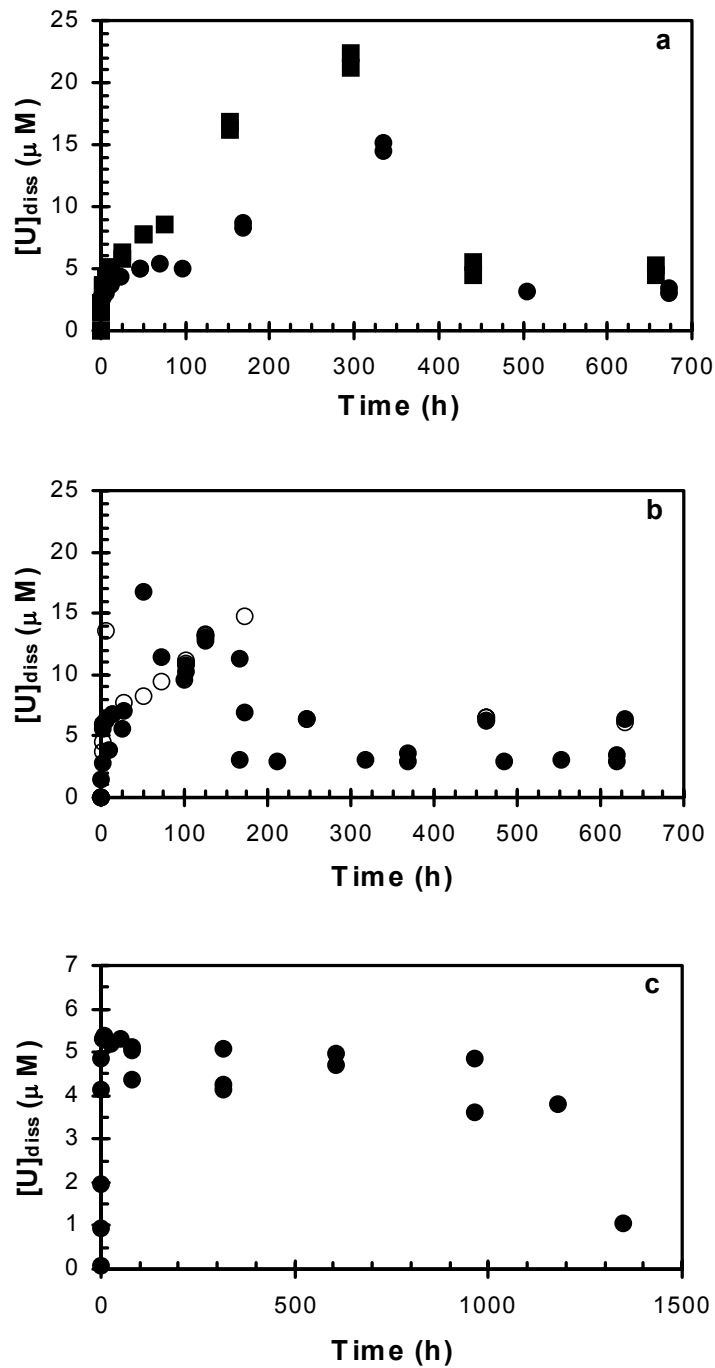


Figure 5.3: Batch schoepite dissolution at pH 6 in NaNO_3 : a) in 0.1 M NaNO_3 with schoepite from Na-synthesis #1 (\blacksquare) (experiments A1 and A2) and Na-synthesis #2 (\bullet) (experiments B1 and B2) b) in 0.01 M NaNO_3 with schoepite from Na-synthesis #2 (\bullet) (experiments B3, B4, and B7) and Parr-bomb ripened schoepite (\circ) (experiment B8) c) residual solids collected from conclusion of batch dissolution experiment at 0.01 M NaNO_3 and resuspended in fresh pH 6 solution with 0.01 M NaNO_3 (experiment B4R). Note that the axes for a and b are the same, but different for c.

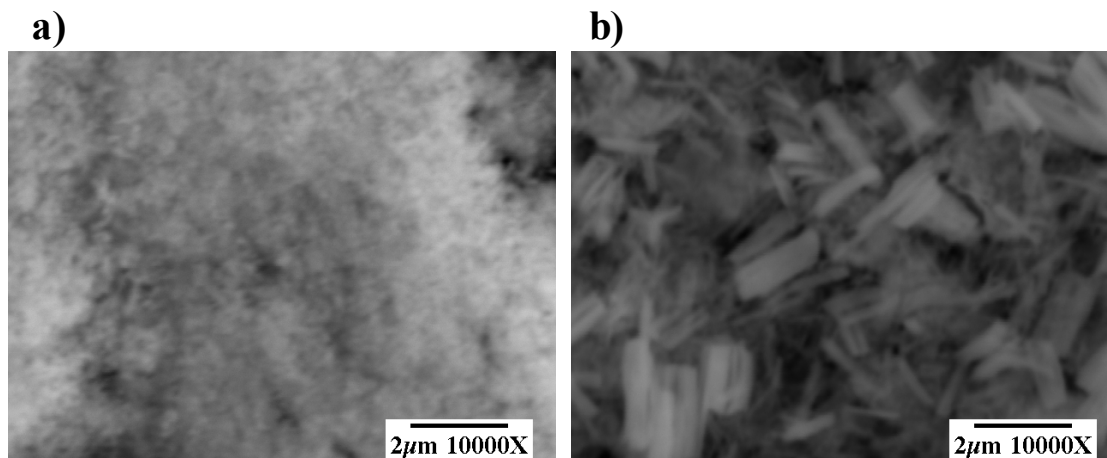


Figure 5.4: Scanning electron micrographs of a) the initial solid, b) the residual solids after the completion of a batch schoepite (Na-synthesis #1) dissolution experiment (A1) at pH 6 and 0.1 M NaNO_3 .

batch reaction progressed in three steps: rapid initial dissolution to 3-4 μM dissolved uranium within an hour, continuing and nearly-linear release of uranium to 22 μM at 296 hours, and ultimately a decrease and stabilization of the dissolved uranium concentration at 4-5 μM for the remainder of the experiment (944 h, but only first 700 h shown) (Fig. 5.3a). Scanning electron micrographs of the solids before and after the batch experiments (Fig. 5.4) show that the solid phase grew considerably over the course of the reaction from sub-micron size particles to 1-2 μm long rectangular crystals. The unreacted and reacted solids were also studied by X-ray diffraction (data not shown) and, with the exception of a small peak in the reacted solids at 15° , no changes were observed.

Based on the early results of becquerelite dissolution experiments (see Appendix D), it was thought that sodium might have been incorporated in the schoepite structure during the synthesis with sodium hydroxide producing a more soluble solid phase. It was hypothesized that, following the complete release of sodium from the structure, the solid might reorganize into a less soluble sodium-free phase, causing the reprecipitation of

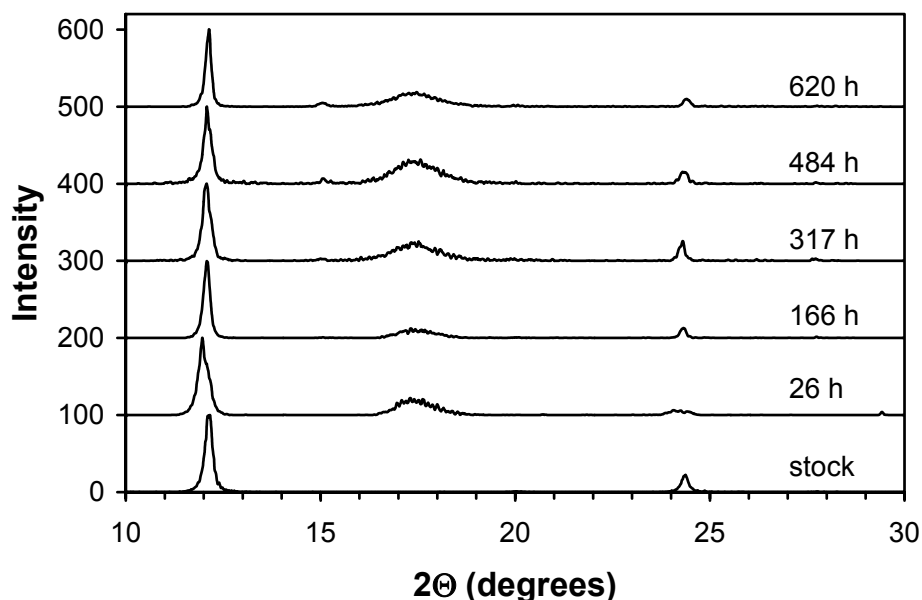


Figure 5.5: Time series of X-ray diffraction patterns following the dissolution of schoepite (Na-synthesis #2) in 0.01 M NaNO_3 solution at pH 6.0 (experiment B3).

uranium. A new batch of schoepite was prepared (Na-synthesis #2) and rinsed more rigorously than the first batch in an effort to remove as much sodium as possible from the synthesized solids.

Schoepite from Na-synthesis #2 was used as the starting material in pH-buffered dissolution experiments in 0.1 M (B1 and B2) and 0.01 M (B3, B4, and B7) NaNO_3 . The evolution of uranium in these experiments followed the same pattern as in the original experiments (Fig. 5.3a and b). In all five experiments, the final dissolved uranium concentration reached a steady value that persisted to the conclusion of the experiments (620-1080 h). This value, with the exception of experiment B7 (6.7 μM), was in the narrow range 2.9-3.8 μM . Reprecipitation occurred earlier for the lower sodium nitrate concentration, supporting the hypothesis that sodium release from the solid was the cause of the unusual pattern of dissolution followed by reprecipitation. A complete time-series

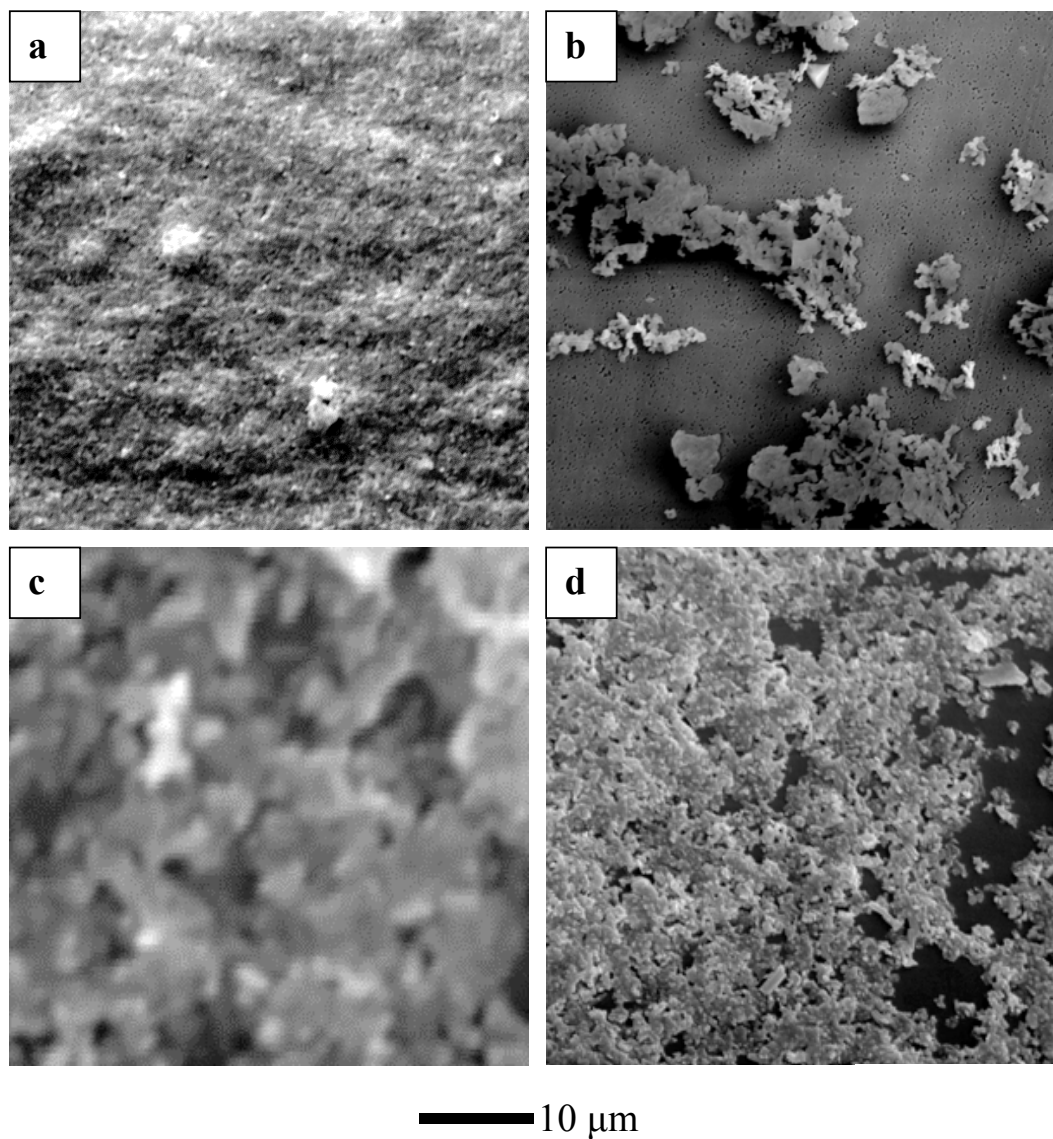


Figure 5.6: Scanning electron micrographs of a) stock schoepite from Na-synthesis #2 b) filtered solids after 2015 h in dilute solution c) filtered solids after 840 h in 0.01 M NaNO₃ (experiment B3) d) filtered solids after 1786 h in 0.01 M CsNO₃ (experiment B5).

of X-ray diffraction patterns was collected for experiment B3 (Fig. 5.5), and shows very little change over time with exception of a barely visible peak at 15° which first appeared after 317 hours. Scanning electron micrographs also show an increase in particle size from the original material (Fig. 5.6a) to the solids remaining at the conclusion of experiment B4 (Fig. 5.6c).

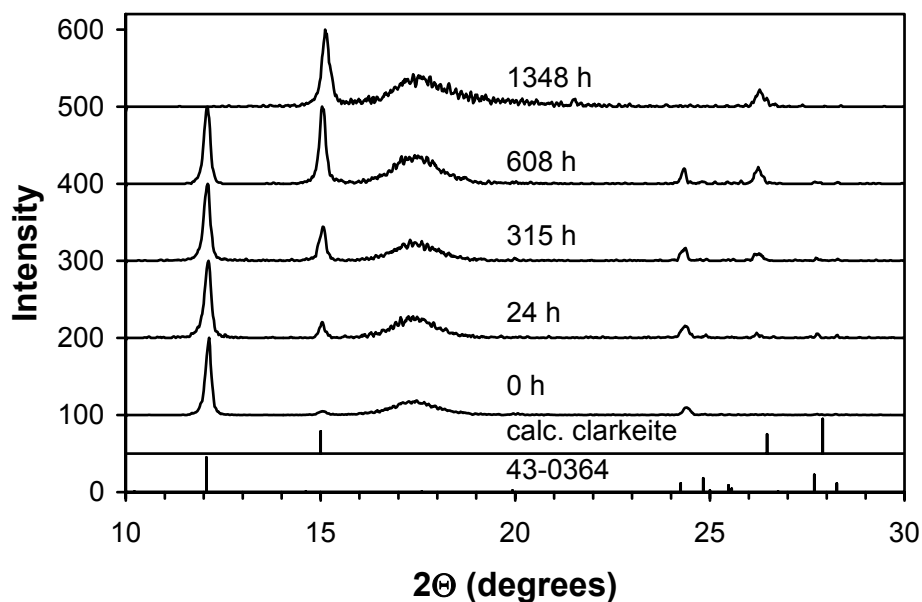


Figure 5.7 Time series of X-ray diffraction patterns of the transformation of residual solids from a batch dissolution experiment at pH 6 in 0.01 M NaNO_3 upon resuspension in solution also at pH 6 and 0.01 M NaNO_3 (experiment B4R). Shown below the measured patterns are the reference patterns for synthetic metaschoepite (JCPDS card 43-0364) and a calculated diffraction pattern for clarkeite (Finch and Ewing, 1997).

In order to examine the uranium release from a solid that had already undergone dissolution and reprecipitation, the solids remaining at the conclusion of experiment B4 were concentrated and resuspended in pH-buffered 0.01 M NaNO_3 solution (experiment B4R). The dissolved uranium concentration increased to 4.5-5.5 μM within 30 minutes and remained constant in that range until falling off towards a final concentration of 1.1 μM after 963 hours (Fig. 5.3c). While little change occurred in the solution chemistry, the structure of the solids in the reactor changed dramatically. An X-ray diffraction time series (Fig. 5.7) shows the gradual disappearance of the peaks at 12.0° (7.39\AA) and 24.4° (3.65\AA) and the in-growth of new peaks at 15.1° (5.86\AA) and 26.2° (3.39\AA). An examination of a recent review of X-ray diffraction patterns of uranyl minerals (Hill,

1999) indicated that clarkeite ($\text{Na}[(\text{UO}_2)\text{O}(\text{OH})]\cdot\text{H}_2\text{O}$) was the only possible phase that could have formed from the contents of the reactor and was consistent with the observed diffraction pattern. The two dominant peaks are in agreement with a calculated pattern for clarkeite (Finch and Ewing, 1997), but the dominant peak in the calculated pattern (3.20 Å) is absent in the observed patterns.

5.3.2.2 Experiments with Cesium, Ripened Schoepite, Dilute Solution, and Fluoride

The X-ray diffraction patterns of the reacted residual solids provided convincing evidence that sodium was not leaving the schoepite structure, but rather that it was being taken up by the solid phase, resulting ultimately in a phase transformation. Experiments were then designed to avoid the incorporation of sodium into the solid phase by using an alternate or no electrolyte, increasing the crystallinity of the starting schoepite, and including a uranyl complexing agent to stabilize uranium released from the solid in the dissolved phase and prevent precipitation.

Cesium nitrate was chosen as an alternative to sodium nitrate because of cesium's larger ionic radius (1.67-1.88 Å) compared with sodium's (0.99-1.39 Å) (the range of the radii are for different coordination numbers) (Klein and Hurlbut, 1993), since it was thought that ions with larger atomic radii might not be able to incorporate in the schoepite interlayers. Batch dissolution experiments using pH-buffered 0.01 (B5) and 0.10 M (B6) CsNO_3 still exhibited a dissolution-reprecipitation pattern, and reached final dissolved concentrations in the narrow range 0.9-1.2 μM (Fig. 5.8). The time-series of X-ray diffraction patterns for experiment B6 (Fig. 5.9) suggest that structural changes occurred. Over time, the dominant peak at 12.0° shifts to 11.9°, and new peaks appear at 23.9° and

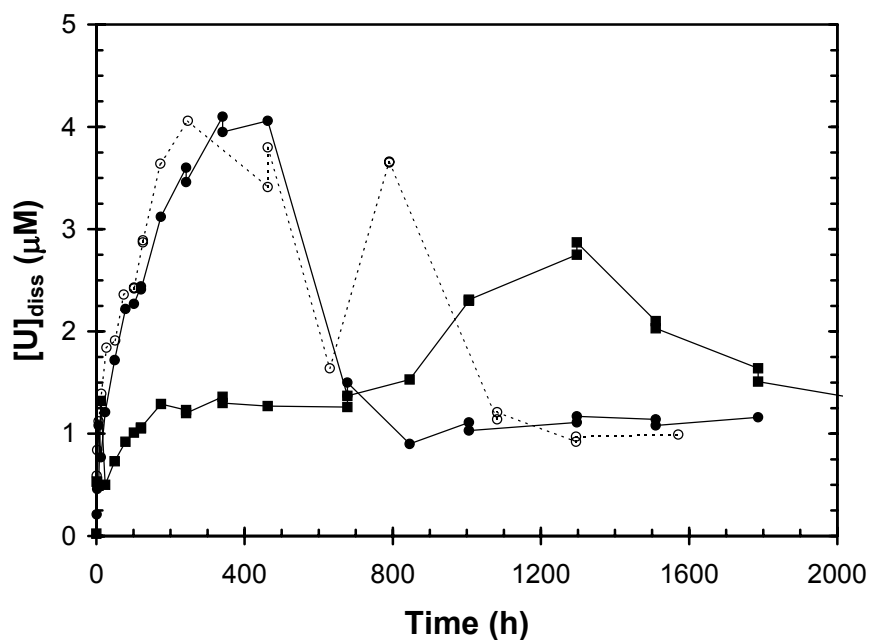


Figure 5.8 Batch schoepite dissolution at pH 6 with schoepite (Na-synthesis #2) in 0.01 M (●) and 0.1 M (■) CsNO_3 (experiments B5 and B6) and with Parr bomb-ripened schoepite in 0.01 M CsNO_3 (○) (experiment B9).

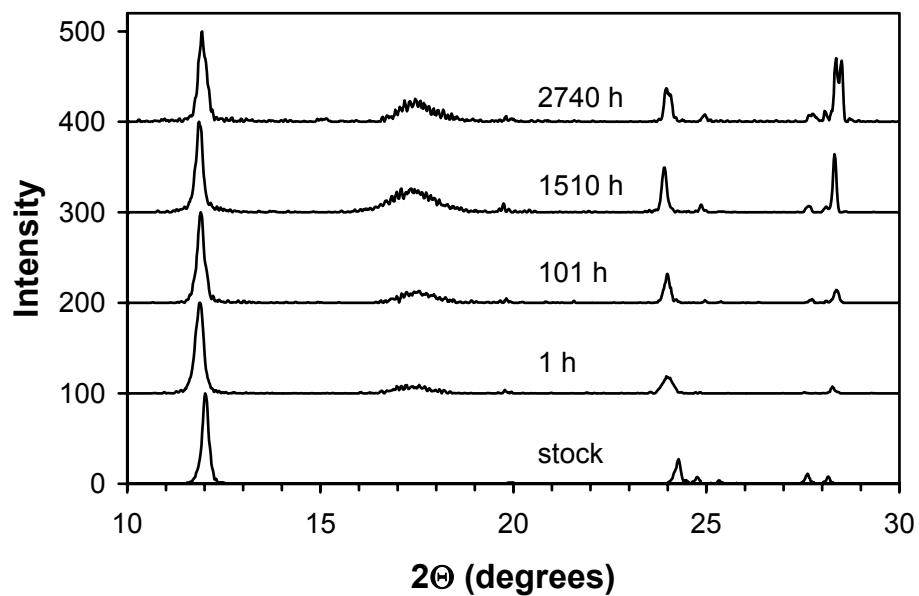


Figure 5.9: Time series of X-ray diffraction patterns following the dissolution of schoepite (Na-synthesis #2) at pH 6 in 0.1 M CsNO_3 (experiment B6).

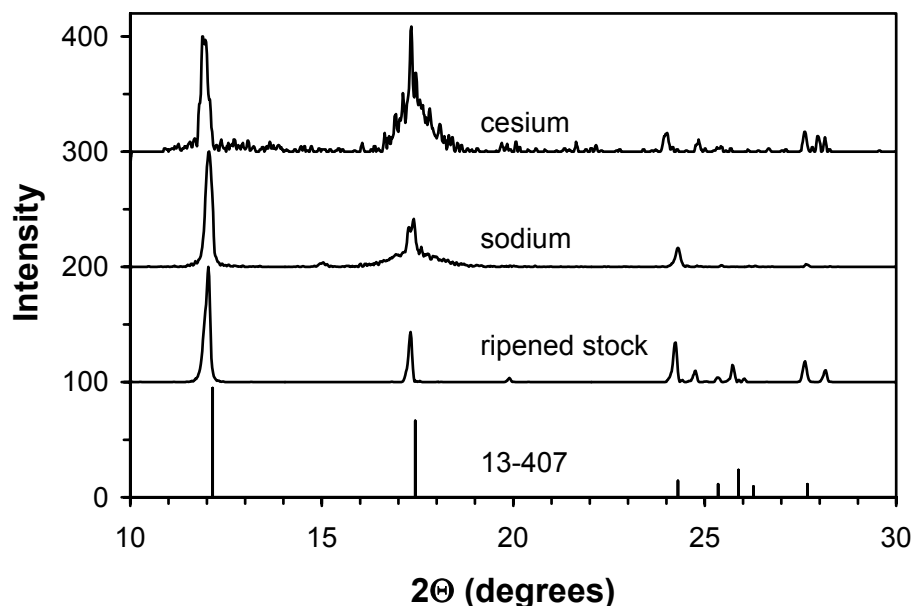


Figure 5.10 X-ray diffraction patterns of Parr bomb-ripened schoepite before and after being subjected to dissolution in either 0.01 M CsNO_3 or 0.01 M NaNO_3 for 463 hours (experiments B8 and B9). JCPDS reference card 13-407 (labeled as schoepite) is included for reference.

28.3°. Scanning electron microscopy also shows that the particles reacted in cesium nitrate solution (Fig. 5.6d) are larger than those present initially. Not only can cesium, as well as sodium, alter the original structure, but cesium lowers the solubility of the solid phase more effectively than does sodium.

Parr-bomb ripened schoepite was expected to have greater crystallinity and therefore be more resistant to the incorporation of monovalent cations. Batch dissolution patterns of ripened schoepite in 0.01 M NaNO_3 (Fig. 5.3b) and in 0.01 M CsNO_3 (Fig. 5.8) are essentially identical to the corresponding patterns with unripened material (in the case of sodium, datapoints after 200 h are obscured by corresponding unripened datapoints). X-ray diffraction indicates that schoepite was altered by the ripening process to a phase more consistent with JCPDS card 13-407 (Fig. 5.10 and Tab. 5.2), labeled as

schoepite (JCPDS-ICDD, 1999) but recently reinterpreted as a mixture of metaschoepite, ianthinite, and dehydrated schoepite (Finch et al., 1997). Ianthinite is a mixed oxidation state uranium phase and is unlikely in the present system, but dehydrated schoepite is a likely product of the ripening process. The diffraction patterns of ripened schoepite after reaction in sodium and cesium nitrate show the same alterations as for the reaction of unripened material (Fig. 5.10).

Once the influence, though not necessarily the mechanism, of cesium and sodium had been firmly established, the next logical experiment was dissolution in dilute solution. Batch dissolution of schoepite (Na-synthesis #2) was conducted with pH adjustments made by acid or base addition. During batch dissolution, the dissolved uranium concentration increased to more than 20 μM within the first ten minutes (Fig. 5.11a). In the first 20 minutes of the reaction, the pH increased; this was counteracted through the addition of nitric acid (the pH never rose above 6.62). After two hours the pH began dropping and sodium hydroxide was incrementally added. Between 75 and 126 hours the dissolved uranium concentration dropped markedly and thereafter remained in the range 1.5-3.3 μM (2015 h). At the point of uranium reprecipitation, the total sodium in the system was only 35 μM , well below the total uranium concentration in the reactor of 280 μM . The residual solids from the experiment were isolated and resuspended in deionized water, this time with no pH adjustment. The dissolved uranium concentration increased to more than 7 μM within 2 h, reached a maximum of 9.0 μM after 172 h, and eventually dropped and stabilized at 5.8 μM . No evidence for structural changes was apparent in X-ray diffraction time-series measured for either the original or

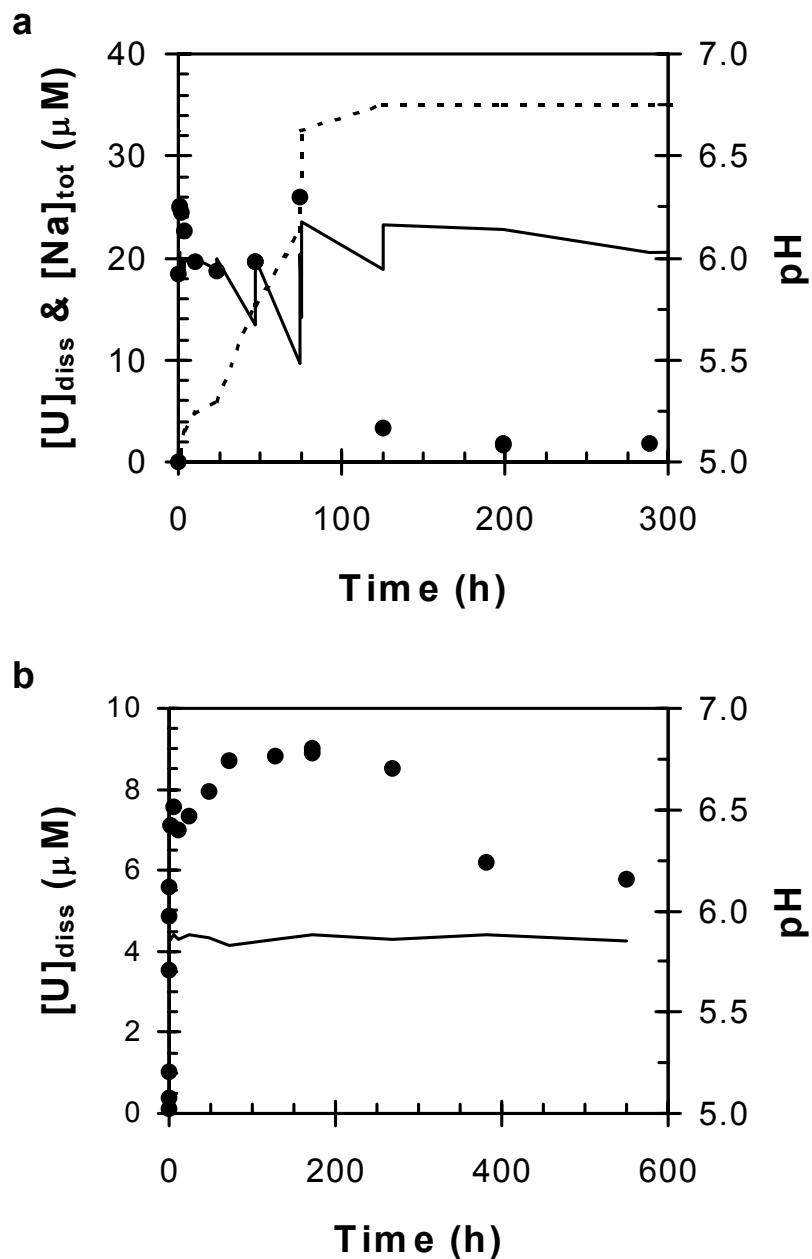


Figure 5.11: Batch schoepite (Na-synthesis #2) dissolution at pH 6 in dilute solution with pH adjustment using HNO₃ and NaOH : a) dissolved uranium (●), pH (solid line), and total sodium from NaOH (dashed line) in initial experiment (B10). Although only the first 300 hours are shown, the initial experiment was run for 2015 hours with no significant changes after 300 hours. b) dissolved uranium and pH upon resuspension of materials isolated from initial experiment (B10R).

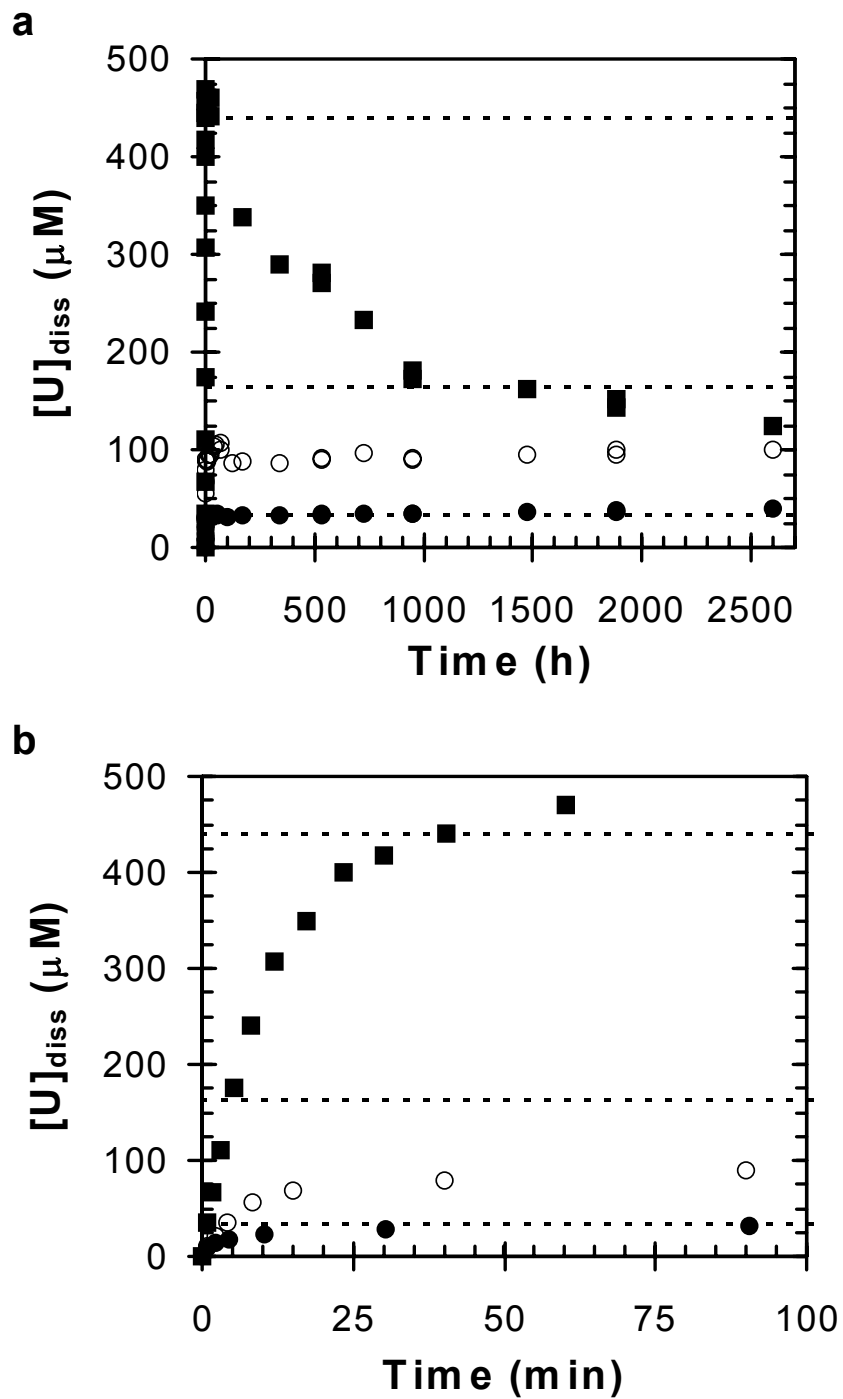


Figure 5.12: Batch dissolution of schoepite (TBA-synthesis) at pH 6 in dilute solution following the addition of 0 (\bullet), 1 mM (\circ), or 5 mM (\blacksquare) sodium fluoride (experiments C1-C3). Both long (a) and short (b) time-scales are shown. The dashed lines represent the dissolved uranium concentrations that would be in equilibrium with schoepite, calculated using the thermodynamic database for dissolved species and the average $\text{Log}K_{\text{sp}}$ for the TBA-synthesis schoepite of 5.52. The total uranium in each experiment is 440 μM .

residuals experiment (data not shown). Scanning electron microscopy suggests that the particle size did increase over the course of the original experiment (Fig. 5.6b).

At this point, the TBA-synthesis schoepite was prepared in an effort to examine the behavior of material that had never been exposed to sodium or cesium. This material was subjected to unbuffered batch dissolution in dilute solution and in sodium fluoride solution. Sodium fluoride solutions were used in an effort to stabilize the dissolved uranium as uranyl-fluoride complexes and prevent reprecipitation. In addition to fluoride, bicarbonate is also a strong complexing agent for uranium (VI), but fluoride could be used at pH 6 whereas bicarbonate would have required a higher pH. Batch dissolution results are presented for both long (Fig. 5.12a) and short (Fig. 5.12b) time-scales. Although the pH was unbuffered, the pH value stayed within the range 5.6-6.5 and was generally in the range 6.0-6.2. In the electrolyte-free system, schoepite dissolved rapidly to reach a dissolved concentration of about 30 μM which gradually increased to 38.9 μM over 2600 hours. The behavior is far more complex in the presence of sodium fluoride. With 1 mM sodium fluoride, the dissolved concentration increased rapidly in the first hour reaching a peak value of 107 μM at 71 h, then decreased to a value of 88 μM at 171 h, and ultimately increased again to a final value of 101 μM at 2600 hours. The dissolved uranium variations during the period from 71-2600 hours are consistent with the measured pH variations, with dissolved uranium decreasing with increasing pH and vice versa. In the presence of 5 mM NaF, the solid dissolved completely ($[\text{U}]_{\text{T}} = 440 \mu\text{M}$) within 1 hour and then uranium gradually reprecipitated until a final dissolved concentration of 124 μM was reached after 2600 hours. The X-ray

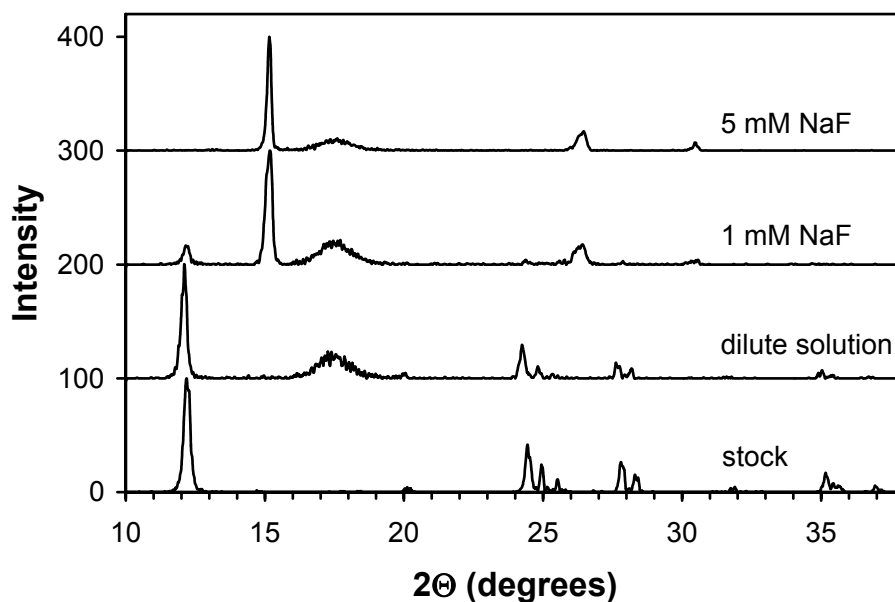


Figure 5.13: X-ray diffraction patterns of stock schoepite from the TBA-synthesis, and material subjected to batch dissolution in dilute solution, 1 mM NaF, or 5 mM NaF for 2599 hours (experiments C1-C3).

diffraction patterns obtained for solids collected after 2600 hours demonstrate no transformation for the dilute solution, and nearly complete and complete transformation to $\text{Na}(\text{UO}_2)\text{O}(\text{OH})_{(\text{s})}$ with 1 mM and 5 mM NaF respectively (Fig. 5.13). Scanning electron micrographs were also collected, but were too poorly resolved to yield useful information.

5.3.2.3 Post-equilibration Electrolyte Addition Experiments

To demonstrate definitively that the incorporation of sodium and cesium resulted in a lower solubility phase, suspensions of TBA-synthesis schoepite were equilibrated in dilute solution for 43 days and then spiked with electrolyte solutions. After 43 days of equilibration, the four suspensions were at pH 5.98-6.15 with 26.7-42.5 μM dissolved uranium. In all four experiments (C4-C7), the addition of either CsNO_3 or NaNO_3

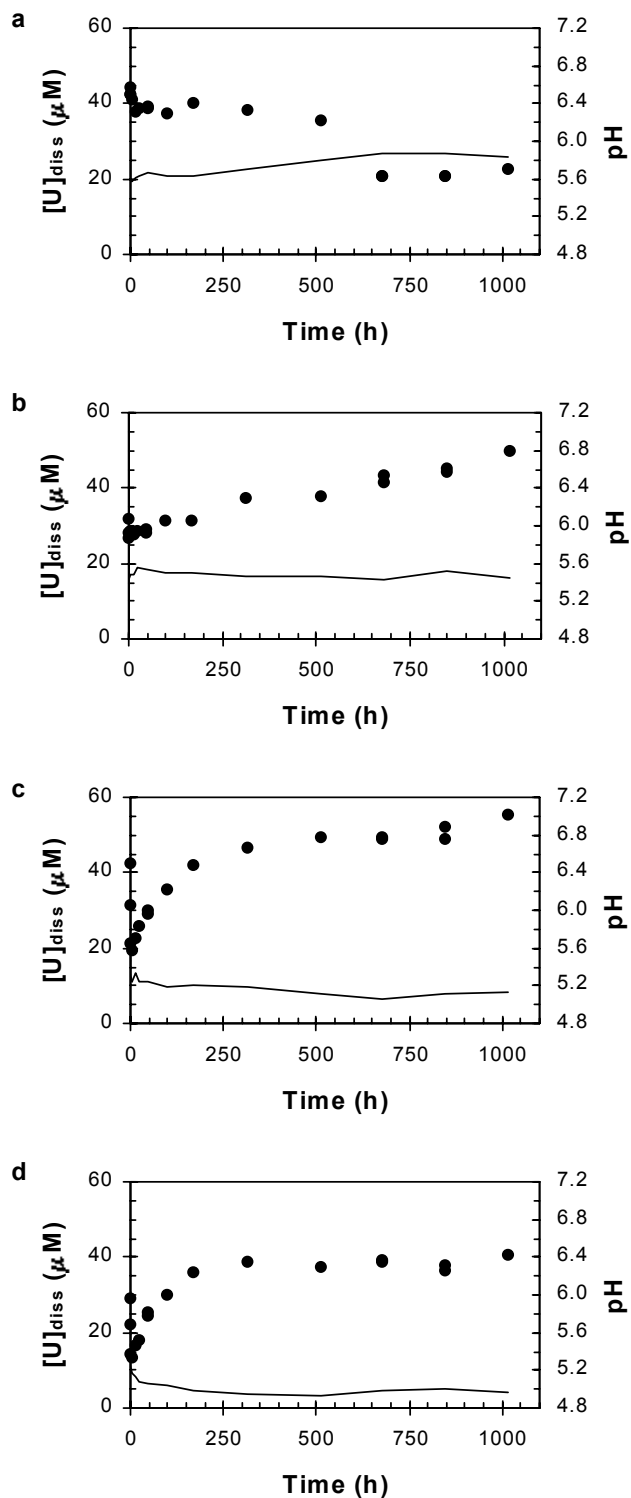


Figure 5.14: Evolution of dissolved uranium and pH following the addition of 1 mM NaNO_3 (a), 10 mM NaNO_3 (b), 1 mM CsNO_3 , or 10 mM CsNO_3 to schoepite (TBA-synthesis) pre-equilibrated at pH 5.98-6.15 for 43 days in dilute solution (experiments C4-C7).

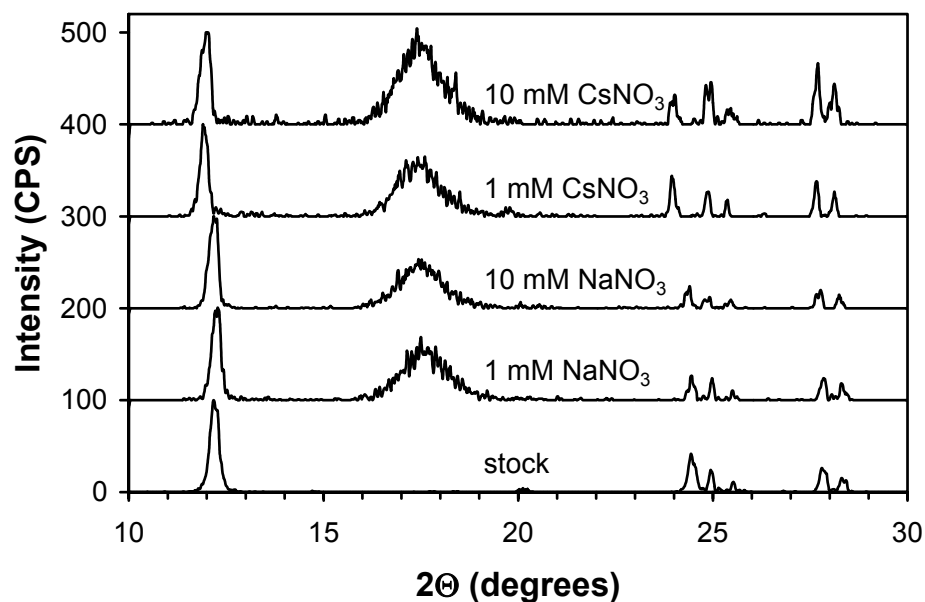


Figure 5.15: X-ray diffraction patterns of solids from suspensions originally pre-equilibrated with schoepite (TBA-synthesis) in dilute solution and then adjusted to 1 or 10 mM NaNO₃ or CsNO₃ (experiments C4-C7). Patterns are for solids 846 hours after electrolyte addition.

resulted in a significant decrease in pH (Fig. 5.14). Following the addition of 0.01 M NaNO₃ the dissolved uranium concentration gradually decreased from 42.3 to 20.9 μM, but the addition of 0.10 M NaNO₃ was followed by an increase from 26.7 to 44.4 μM. The addition of both 0.01 and 0.10 M CsNO₃ resulted in an initial decrease in the dissolved uranium concentration in the first 1 hour, followed by a gradual increase over the next several hundred hours. Both the depression of pH and initial decrease of the dissolved uranium concentration were more severe at the higher CsNO₃ concentration. The X-ray diffraction patterns of the pre-equilibrated solids spiked with NaNO₃ display no measurable changes, but those spiked with CsNO₃ show the same characteristic changes discussed earlier when schoepite was added to CsNO₃ solutions (Fig. 5.15).

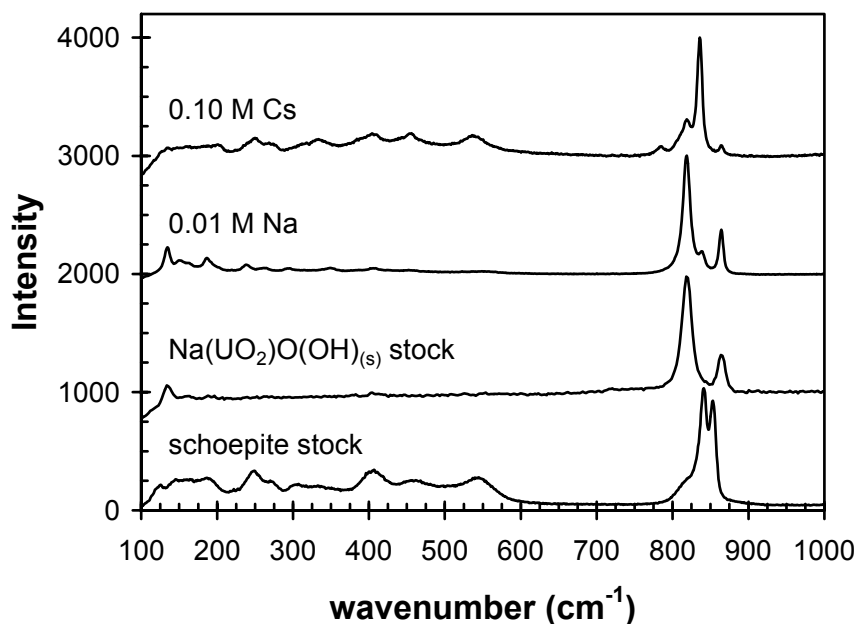


Figure 5.16: Raman spectra (from bottom to top) of stock schoepite from Na-synthesis #2, solids completely transformed to Na(UO₂)O(OH)_(s) after repeated exposure to 0.01 M NaNO₃ (experiment B4R), schoepite from Na-synthesis #2 subjected to batch dissolution in 0.01 M NaNO₃ (experiment B7), and to batch dissolution in 0.10 M CsNO₃ (experiment B6). The dominant peaks in the 800-900 cm⁻¹ region are all attributable to the symmetric uranyl stretch for uranyl ions in different structural environments.

5.3.2.4 Raman Spectroscopy

Raman spectra provide additional information regarding the transformations suggested by changes in solution chemistry, X-ray diffraction, and scanning electron microscopy. The Raman spectra of the solid that had been transformed completely to a clarkeite-like sodium uranyl oxide hydrate phase (hereafter referred to as Na(UO₂)O(OH)_(s)) in experiment B4R has a spectrum distinct from that of the original schoepite (Fig. 5.16). Two distinct uranyl environments are still evident as seen by the two peaks at 864.5 and 819.1 cm⁻¹, both corresponding to the symmetric uranyl stretch, but the positions are more separated than in the original schoepite stock. Schoepite

subjected to dissolution in 0.01 M NaNO₃ can be clearly seen as predominantly Na(UO₂)O(OH)_(s) with some remaining original schoepite. Material reacted in 0.10 M CsNO₃ also shows a splitting of the symmetric uranyl stretch into as many as four separate peaks.

5.3.3 Flow-through Dissolution Experiments

In addition to the extensive batch experiments just discussed, flow-through experiments with schoepite (Na-synthesis #1) provide complementary information. A summary of the experiments performed is given in Table 5.4. Experiments investigated the effect of changing either the influent dissolved uranium concentration or the reactor residence time. All influent solutions were pH-buffered and contained 0.1 M NaNO₃.

Ideally, in flow-through experiments, the effluent concentration will stabilize at some constant value, indicating that steady-state dissolution has been established. Dissolution rates ($\mu\text{mol m}^{-2} \text{h}^{-1}$) were calculated using equation 1, where C_{out} and C_{in} are the effluent and influent

$$\text{Rate} = \frac{(C_{\text{out}} - C_{\text{in}})}{t_{\text{res}}} \frac{1}{S \cdot A}, \quad (1)$$

uranium concentrations (μM) respectively, t_{res} is the hydraulic residence time of the reactor (h), S is the mass concentration of schoepite in the reactor (g L^{-1}), and A is the specific surface area ($\text{m}^2 \text{g}^{-1}$). Negative dissolution rates can be interpreted simply as (net) precipitation rates. The dissolution rate was calculated for each effluent sample, and the average and standard deviations for each experiment are listed in Table 5.4.

In experiments D1 (Fig. 5.17a), D5, and D6, influent solutions were uranium-free. Despite large variations in the residence time, the effluent uranium concentration only

Table 5.4: Flow-through dissolution experiments. Reactors loaded with 0.50-0.65 g L⁻¹ schoepite (Na-synthesis #1). All influents contained 0.1 M NaNO₃ and 5 mM MES pH buffer and were adjusted to pH 6.0.

Expt. (ID)	t_{res} (h)	[U]_{inf.} (μM)	[U]_{eff.} (μM)	R_{diss} (μmol m⁻² h⁻¹)
D1	1.03-1.32	0	3.13-3.42	0.42 ± 0.06
D2	3.34-3.65	5	5.79-7.44	0.05 ± 0.03
D3 ^a	3.27-3.59	10	5.85-12.63	-0.02 ± 0.12
D4 ^a	3.36-3.67	20-25	15.43-22.98	-0.07 ± 0.12
D5 ^b	0.25-0.26	0	2.96-3.41	1.58 ± 0.08
	0.51-0.52		2.59-2.73	0.70 ± 0.01
	1.02-1.05		2.78-2.92	0.41 ± 0.01
	2.07-2.10		3.00-3.16	0.24 ± 0.01
	4.23-4.41		3.04-3.16	0.13 ± 0.01
D6 ^b	0.48-0.50	0	2.70-2.84	0.65 ± 0.01
	0.98-1.01		2.90-2.98	0.37 ± 0.01
	1.97-2.02		3.02-3.19	0.21 ± 0.01
	4.01-4.23		3.21-3.36	0.09 ± 0.01

^a Flow-through reactors started with net dissolution but finished with net precipitation.

^b Flow-rates were incrementally changed and allowed to stabilize for at least 20 reactor volumes at each flow-rate.

varied from 2.59 to 3.42 μM (Table 5.4). This suggests that, even for very short reactor residence times, schoepite is dissolving sufficiently to approach saturation within one reactor residence time. If the reactors were operating far from saturation, a doubling of the reactor residence time should result in a doubling of the effluent concentration. The highest dissolution rate, 0.73 μmol m⁻² h⁻¹, was measured at the shortest residence time. Unfortunately, residence times shorter than 0.25 h could not be achieved, because, at the necessary flow-rate, the solid became completely impacted upon the filter and was no longer well stirred. At the 0.25 h residence time, the observed effluent concentrations correspond to a 1.58 μmol m⁻² h⁻¹ dissolution rate; however, this is only a lower limit because the actual solution contact time with schoepite (in the compacted layer on the filter) was less than the 0.25 h hydraulic residence time for the reactor.

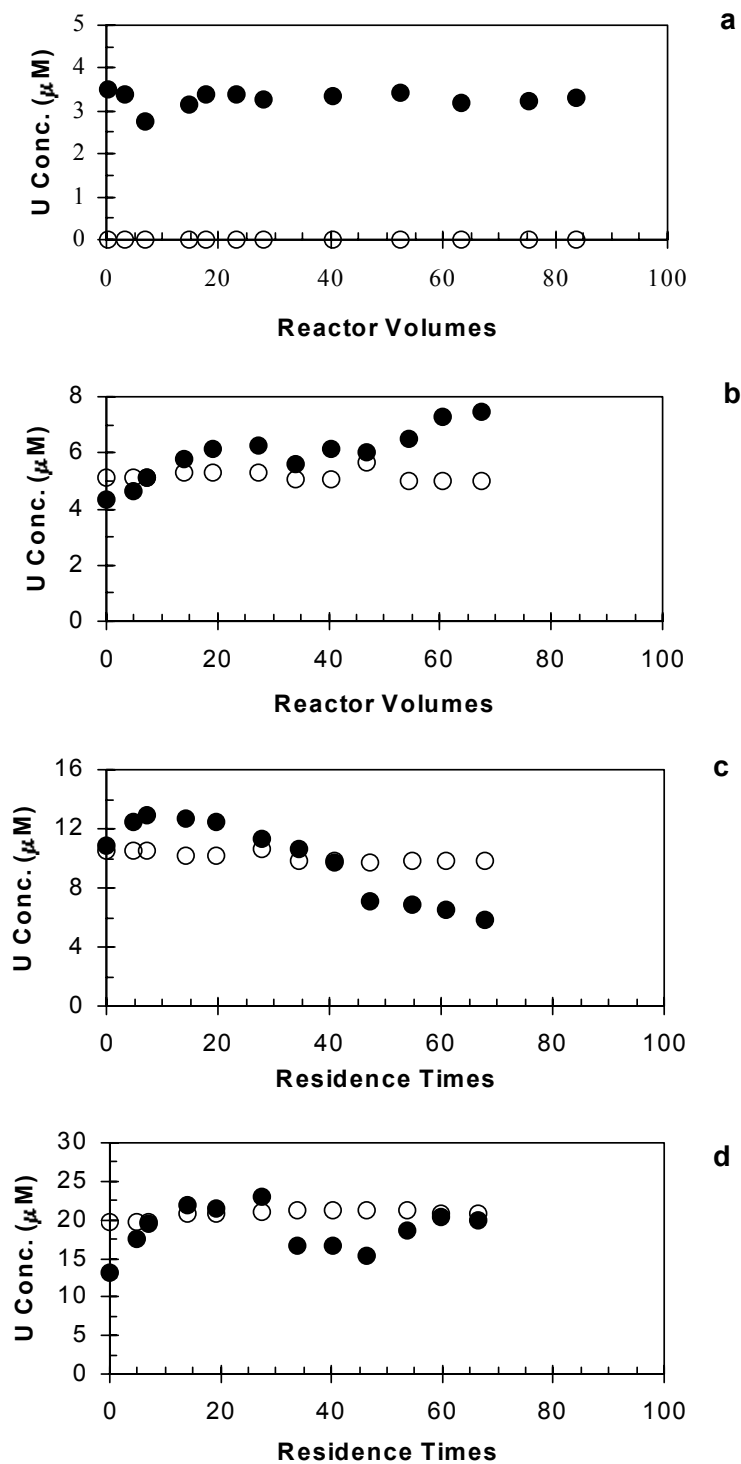


Figure 5.17: Influent (\circ) and effluent (\bullet) uranium concentrations in flow-through dissolution experiments a) D1 ($t_{\text{res}} = 1.0\text{-}1.3$ h, $[\text{U}]_{\text{inf.}} = 0$ μM) b) D2 ($t_{\text{res}} = 3.3\text{-}3.7$ h, $[\text{U}]_{\text{inf.}} = 5$ μM) c) D3 ($t_{\text{res}} = 3.3\text{-}3.6$ h, $[\text{U}]_{\text{inf.}} = 10$ μM) d) D4 ($t_{\text{res}} = 3.4\text{-}3.7$ h, $[\text{U}]_{\text{inf.}} = 20$ μM). All influents contain 0.01 M NaNO_3 and 5 mM MES buffer adjusted to pH 6.

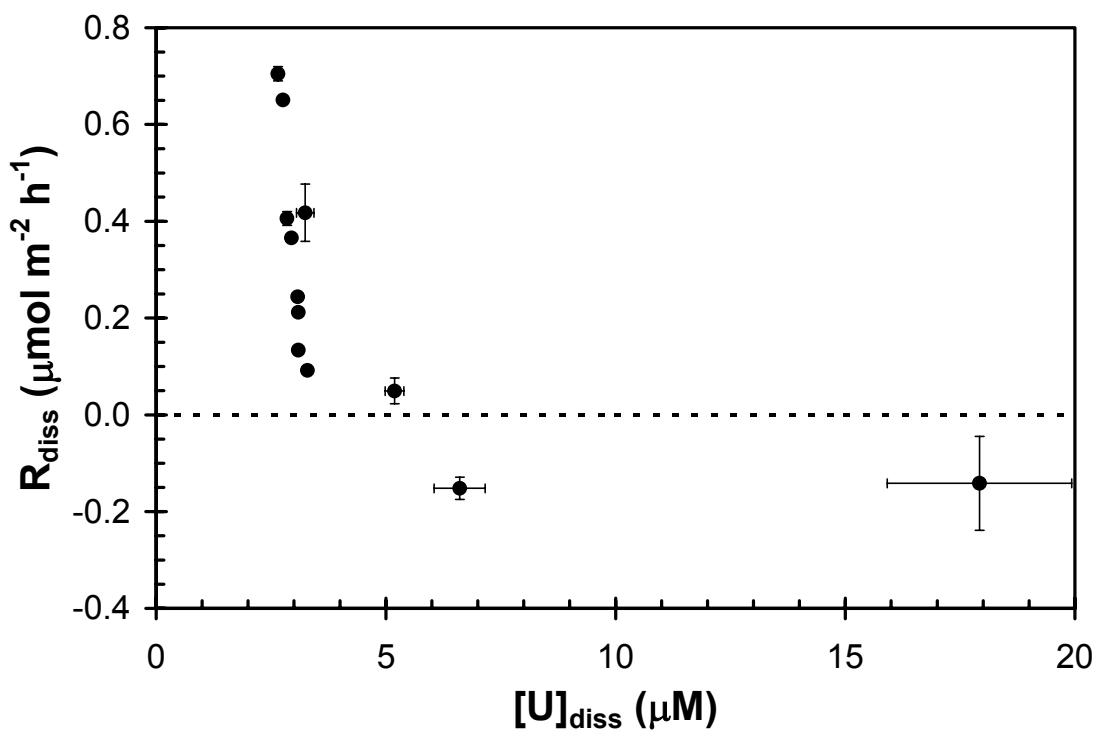


Figure 5.18: Schoepite (Na-synthesis #1) dissolution rate versus the dissolved uranium concentration from flow-through reactor data at pH 6 and 0.1 M NaNO_3 . Multiple samples were collected for each experiment, and average values and standard deviations (error bars) from each experiment are shown.

Experiments D2, D3, and D4 examined the effect of the influent uranium concentration on the dissolution rate. With 5 μM dissolved uranium in the influent, the effluent concentration increased over the course of the experiment (Fig. 5.17b), and an average dissolution rate of $0.05 \pm 0.03 \mu\text{mol m}^{-2} \text{h}^{-1}$ is calculated for samples with effluent uranium concentrations in excess of the influent concentration. With influent dissolved uranium concentrations of 10 and 20 μM , the effluent dissolved uranium concentrations dropped over the course of the experiments and were ultimately lower than the influent concentrations (Fig. 5.17c and d), indicating a switch from net dissolution to net precipitation.

The average values and ranges from all flow-through experiments are incorporated in a plot of the dissolution rate versus the dissolved uranium concentration (taken as the effluent uranium concentration) (Fig. 5.18). The concentration at which the data cross the line corresponding to zero (net) dissolution is the concentration in equilibrium with the solid phase. This value is between 3 and 7 μM . The y-intercept in Figure 5.18 corresponds to the maximum possible dissolution rate. The data show no significant inclination towards crossing the y-axis and even the $1.58 \mu\text{mol m}^{-2} \text{h}^{-1}$ dissolution rate mentioned earlier should only be considered a lower limit.

5.4 Discussion

5.4.1 Identification and Equilibrium Solubility of Endmember Phases

The first step in interpreting the large volume of data is to outline the equilibrium constraints on the system based on solubility products of the solid phases. Solubility products can only be determined from equilibrium data, and unfortunately very few of the experiments can be unambiguously interpreted as having reached equilibrium.

Identification of systems at equilibrium will be based on stable dissolved uranium concentrations and pH together with X-ray diffraction and Raman data indicating the presence of only one solid phase. The equilibrium behavior of schoepite will be investigated first and will be followed by an examination of $\text{Na}(\text{UO}_2)\text{O}(\text{OH})_{(\text{s})}$ and cesium uranyl oxide hydrate solubilities.

The equilibrium solubility of metaschoepite is described by the following reaction (which is the same for schoepite) and solubility product.



$$K_{\text{sp}} = \frac{\{\text{UO}_2^{2+}\}}{\{\text{H}^+\}^2} \quad (3)$$

Equilibrium calculations are made using the known pH, the dissolved uranium concentration, and ionic strength. Uranyl ion concentrations are calculated from total dissolved uranium concentrations with the database of constants given in Table A.1 and ionic strength corrections made with the Davies equation.

The best established equilibrium conditions are from experiments using schoepite from the TBA-synthesis. Stable concentrations are observed at the conclusion of batch dissolution in dilute solution (C1) and after the 43 day pre-equilibration at the beginning of the electrolyte spike experiments (C4-C7) and only peaks of the parent solid appear in the X-ray diffraction pattern. The $\text{Log}K_{\text{sp}}$ calculated using data from these four experiments only varies from 5.48 to 5.54 with an average of 5.52 and standard deviation of 0.03.

In all of the batch reactors using Na-synthesis #1, the solid underwent significant alteration, but the operation of the flow-through reactors gives insight into equilibrium (Fig. 5.18). The pH is strictly controlled at pH 6 in the system and zero (net) dissolution occurs at dissolved uranium concentrations of 3-7 μM ($[\text{UO}_2^{2+}] = 0.29\text{-}0.43 \mu\text{M}$), corresponding to $\text{Log}K_{\text{sp}}$ values of 5.0-5.2. The equilibrium constant could also be calculated from the solution conditions of the stock suspension, but unfortunately the pH of the stock suspension was never measured. The dissolved uranium concentration in the

Table 5.5: Equilibrium solubility constants for schoepite.

<i>Material</i>	Experimental Conditions			LogK _{sp} ^a	Ref. ^b
	pH	Electrolyte	Atmosphere		
Na-synthesis #1	6.0	0.1 M NaNO ₃	ambient	5.02-5.19	1
Na-synthesis #2	5.5-6.1	none	ambient	5.38-5.46	1
TBA-synthesis	6.0-6.2	none	ambient	5.48-5.54	1
Synthetic	4.7, 6.3	0.5 M NaClO ₄	argon	4.70	2
Synthetic	calorimetry with HF			4.81 ^c	3
Synthetic	2.8-4.6	0.1 M NaClO ₄	ambient	4.73-5.14	4, 5
Synthetic	4.5-5.5	0.1 M NaClO ₄	nitrogen	5.13	6
Synthetic	5.0-10.0	1 mM NaCl	argon	5.20	7
Synthetic	3.3, 8.4	1 M NaCl	oxygen/nitrogen	5.38	8
Formed on UO _{2(s)}	3.3, 8.4	1 M NaCl	oxygen/nitrogen	5.73	8
Crystalline	6.0-9.0	0.5 M NaClO ₄	nitrogen	5.97	9
Amorphous	6.0-9.0	0.5 M NaClO ₄	nitrogen	6.33	9

^a values extrapolated to zero ionic strength by authors.

^b 1) present work; 2) (Díaz Arocas and Grambow, 1998); 3) (Grenthe et al., 1992); 4) (Meinrath and Kimura, 1993); 5) (Meinrath et al., 1996); 6) (Kramer-Schnabel et al., 1992); 7) (Silva, 1992); 8) (Torrero et al., 1994); 9) (Sandino and Bruno, 1992).

^c Calculated from ΔG_f° values.

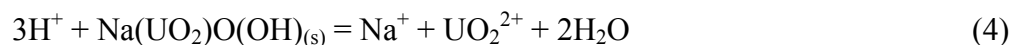
stock was 2.2 μ M, thus a pH of about 6 would be necessary for the solubility product to be comparable to that calculated from flow-through experiments.

The early operation (prior to NaOH addition) of a batch reactor with Na-synthesis #2 in dilute solution (B10) gives the best estimate of the solubility product for that phase. Before the onset of reprecipitation, the solution chemistry plateaued for 24 h, with dissolved concentrations of 18.4-25.9 μ M and pH fluctuations from 5.48 to 6.10. Although it is unclear whether the suspension reached equilibrium in only 24 hours, the stable dissolved uranium concentrations and short equilibration times observed in other experiments suggest that the suspension had reached equilibrium with respect to schoepite dissolution. Taking the most extreme data with sodium concentrations less than 10 μ M, a range for LogK_{sp} of 5.38-5.46 is calculated. The dissolved uranium

concentration of the Na-synthesis #2 stock suspension was measured as 4.7-5.7 μM , but corresponding pH measurements were not taken.

The solubility constants determined for the synthetic schoepite in the current work are in good agreement with several previous studies (Table 5.5). While a thorough review of previous work on schoepite solubility is presented in Appendix A, a brief discussion is included here. The results of the present study fall in the middle of the wide range of published $\text{Log}K_{\text{sp}}$ values (4.70-6.33). The constant determined for Na-synthesis #1 in 0.1 M NaNO_3 is very close to the values of 5.13 (Kramer-Schnabel et al., 1992) and 5.14 (Meinrath et al., 1996) determined in 0.1 M NaClO_4 . The higher solubility products of Na-synthesis #2 and TBA-synthesis are best matched by values determined by Silva (1992) and Torrero et al. (1994). The differences in equilibrium solubility among the synthetic solids in the current work may arise from differences in particle sizes. Several authors have discussed qualitatively the effect of increasing solubility with decreasing particle size but have not dealt with the phenomenon quantitatively (Meinrath et al., 1996; Sandino and Bruno, 1992; Torrero et al., 1994).

The equilibrium solubility of $\text{Na}(\text{UO}_2)\text{O}(\text{OH})_{(\text{s})}$ was also estimated from batch experiment data. The X-ray diffraction pattern of the final sample of residuals dissolution experiment B4R in 0.01 M NaNO_3 exhibits only the peaks of a clarkeite-like phase. The following reaction and solubility product correspond to the stoichiometry of clarkeite:

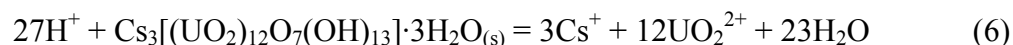


$$K_{\text{sp}} = \frac{\{\text{UO}_2^{2+}\}\{\text{Na}^+\}}{\{\text{H}^+\}^3} \quad (5)$$

The system was buffered at pH 6 and open to the atmosphere, had approximately 0.01 M ionic strength, and contained 12.3 mM dissolved sodium. Using the final dissolved uranium concentration of 1.05 μM , a $\log K_{\text{sp}}$ value of 8.81 is calculated. A $\log K_{\text{sp}}$ value of 7.65 is calculated from the final conditions of the 5 mM NaF fluoride-induced dissolution experiment (C3), which also contained a solid displaying only the XRD peaks of $\text{Na}(\text{UO}_2)\text{O}(\text{OH})_{(\text{s})}$. There are very few published data for comparison with the calculated values. Using free energies of formation for the anhydrous sodium uranate $\text{Na}_2\text{U}_2\text{O}_7$, a solubility constant of $10^{22.6}$ is calculated (Grenthe et al., 1992). If such a phase were the solubility-controlling solid, the uranyl ion concentration at pH 6 in 0.01 M NaNO_3 solution would be 16 μM (total dissolved uranium more than 1 M), orders of magnitude higher than observed in current experiments. Diaz Arocas and Grambow (1998) determined a $\log K_{\text{sp}}$ for the sodium uranyl oxide hydrate $\text{Na}_{0.33}\text{UO}_{3.16}\cdot 2\text{H}_2\text{O}$ of 7.13, but because of the relatively low sodium content of the reactor, the conditions of experiment B4R are undersaturated with respect to this phase. The XRD pattern of the solid investigated by Diaz Arocas and Grambow is also unlike that determined in the current work.

The identification of a pure cesium uranyl oxide hydrate phase is a challenge because the X-ray diffraction pattern has only minor differences in the 12° peak of the parent schoepite material, and no matches with reference database XRD patterns can be made. Recently a cesium uranyl oxide hydrate with the formula $\text{Cs}_3[(\text{UO}_2)_{12}\text{O}_7(\text{OH})_{13}]\cdot 3\text{H}_2\text{O}_{(\text{s})}$ was synthesized at high temperature and pressure. Using single-crystal XRD, the structure was determined to consist of sheets of pentagonal uranyl bipyramids with cesium located in interlayer spaces (Hill and Burns, 1999). The

exact lattice spacings of the solid were not published, and therefore are not directly available for comparison with the solid formed in batch reactors. Nevertheless, by using the final conditions of cesium batch reactors (experiments B5 and B6) and the stoichiometry of the solid synthesized by Hill and Burns, a solubility product for the following reaction can be calculated.



$$K_{\text{sp}} = \frac{\{\text{UO}_2^{2+}\}^{12} \{\text{Cs}^+\}^3}{\{\text{H}^+\}^{27}} \quad (7)$$

The $\text{Log}K_{\text{sp}}$ values extrapolated to zero ionic strength are 68.7 and 67.8 for experiments B5 and B6 respectively. Remarkably, the average value of 68.3 successfully predicts the dissolved uranium concentrations at the conclusion of experiments involving the post-equilibration addition of 1 mM and 10 mM CsNO_3 . For the 1 mM and 10 mM CsNO_3 experiments respectively, dissolved concentrations of 50.8 and 39.0 μM are calculated for the given pH and total concentrations of cesium and uranium, in agreement with measured concentrations of 55.2 and 40.7 μM after 43 days.

5.4.2 Role of Monovalent Cations

Clearly sodium and cesium do not behave as background cations (as originally intended) but rather play key roles in the alteration of schoepite. The interlayer space in schoepite is capable of incorporating many different types of cations. The proposed alteration mechanism is the exchange of sodium or cesium with structural interlayer water molecules in pure schoepite, accompanied by the expulsion of protons or uranyl

ions to maintain charge balance. For the sodium system this reaction is expressed by the following reaction:



This mechanism is consistent with the results of isotope exchange experiments with ^{22}Na , which showed that dissolved sodium can exchange with solid-associated sodium without bulk recrystallization (Bilgin, 1989). However, sodium incorporation does appear to be assisted by bulk dissolution of the original phase, as demonstrated by the faster transformation of schoepite in 1 mM NaF than in 1 mM NaNO_3 . The transformation of metaschoepite to becquerelite in calcium-rich solution was also faster for metaschoepite that had been dehydrated and rehydrated than for the original metaschoepite (Sowder et al., 1999). The presence of defects in the schoepite structure appears to facilitate the transformation to phases with interlayer cations.

Reaction 8 provides a method for calculating the amount of sodium or cesium incorporated into the solid phase during post-equilibration electrolyte addition experiments (C4-C7), despite the drift in both dissolved uranium and pH. To maintain charge balance the protons released (net change in alkalinity) during alteration are balanced by sodium or cesium taken up by the solid. The net change in alkalinity is calculated by following the Tableau method (Morel and Hering, 1993) to determine the value of the mole balance equation for H^+ at different steps during the reactions. Using water, H^+ , $\text{CO}_{2(\text{g})}$, and $\text{UO}_2(\text{OH})_2 \cdot \text{H}_2\text{O}_{(\text{s})}$ as components, the mole balance equation (only significant species are included) is as follows:

$$\begin{aligned} \text{TOT H} = & [\text{H}^+] - [\text{OH}^-] - [\text{HCO}_3^-] + 2[\text{UO}_2^{2+}] + [\text{UO}_2\text{OH}^+] + 2[(\text{UO}_2)_2(\text{OH})_2^{2+}] \\ & + 2[(\text{UO}_2)_3(\text{OH})_4^{2+}] + [(\text{UO}_2)_3(\text{OH})_5^+] + [(\text{UO}_2)_4(\text{OH})_7^+] \quad (9) \end{aligned}$$

Table 5.6: Evolution of solution chemistry and the net change in alkalinity during post-equilibration electrolyte spike experiments.

Expt.	Electrolyte	Time	pH	[U] _{diss} (μM)	TOTH (μM)
B4	1 mM NaNO ₃	0 min	5.98	42.3	12.3
B4	1 mM NaNO ₃	10 min	5.60	44.5	21.9
B4	1 mM NaNO ₃	42 d	5.84	22.6	8.0
B5	10 mM NaNO ₃	0 min	6.15	26.7	3.3
B5	10 mM NaNO ₃	10 min	5.51	32.1	21.0
B5	10 mM NaNO ₃	42 d	5.44	49.7	32.0
B6	1 mM NaNO ₃	0 min	6.05	42.5	10.8
B6	1 mM NaNO ₃	10 min	5.46	31.4	21.0
B6	1 mM NaNO ₃	42 d	5.13	55.2	52.2
B7	10 mM NaNO ₃	0 min	6.04	28.9	6.5
B7	10 mM NaNO ₃	10 min	5.44	22.1	18.7
B7	10 mM NaNO ₃	42 d	4.97	40.7	55.6

The results of calculations with equation 9 are applied to experiments C4-C7 for time zero, ten minutes, and 42 days after electrolyte addition (Table 5.6). With the addition of only 1 mM NaNO₃, there is no uptake of sodium, but with 10 mM NaNO₃, 28.7 (32.0 - 3.3) μM Na⁺ was incorporated in the solid ([U]_{tot} = 440 μM). The solid incorporated cesium more effectively than it did sodium with 41.3 and 49.1 μM Cs⁺ taken up following the addition of 1 and 10 mM CsNO₃ respectively. The greater incorporation of cesium than sodium is consistent with the observations that cesium alters the schoepite structure more rapidly.

The decrease in the solubility of the solids following the incorporation of monovalent cations may be attributed to two possible phenomena. In the first case, the incorporation of monovalent cations into the interlayer space leads to a new crystal structure, which is inherently more stable. This explanation is consistent with the formation of the lower solubility minerals becquerelite and compreignacite following the formation of schoepite in natural and laboratory weathering of UO_{2(s)} (Finch and

Murakami, 1999; Wronkiewicz and Buck, 1999). In the second case, the incorporation of monovalent cations accelerates crystal growth and leads to the formation of larger crystals which are less soluble because of surface area effects.

Particle size can affect the equilibrium solubility of particles smaller than 1 μm or with a specific surface area greater than a few $\text{m}^2 \text{g}^{-1}$. By combining the free energy of the bulk solid with the interfacial free energy, the effect on the solubility product is expressed as follows:

$$\log K_{\text{sp}(s)} = \log K_{\text{sp}(s=\infty)} + \frac{\frac{2}{3} \bar{\gamma}}{RT} s \quad (10)$$

where $\bar{\gamma}$ is the interfacial energy of the solid-liquid interface (J m^{-2}) and s is the molar surface area ($\text{m}^2 \text{mol}^{-1}$) (Stumm and Morgan, 1996). The interfacial energy is generally determined from experimentally measured relationships between K_{sp} and s , though a semi-theoretical approach provided comparable estimates to experimentally determined values for ZnO, Cu(OH)₂, and CuO (Schindler, 1967). Interfacial energies range from 26 mJ m^{-2} for gypsum to 1600 mJ m^{-2} for goethite (Stumm and Morgan, 1996). The effect of surface area on solubility has also been measured for the iron oxyhydroxides goethite and hematite (Langmuir and Whittemore, 1971). If the critically reviewed value (also one of the lowest available) of $10^{4.81}$ is taken as the surface area independent solubility product, then an interfacial energy of 930 mJ m^{-2} is calculated with the solubility product and molar surface area ($2800 \text{m}^2 \text{mol}^{-1}$) of TBA-synthesis schoepite. For this interfacial energy, if the particles were to only double in size and assuming an associated decrease in the specific surface area (i.e., area over volume), then the solubility product would

decrease from $10^{5.52}$ to $10^{5.16}$, which corresponds to a decrease in the equilibrium dissolved uranium concentration from 46.1 to 5.1 μM at pH 6 and 0.01 M ionic strength.

5.4.3 Schoepite Dissolution Rate

The rate of schoepite dissolution can be determined from both batch and flow-through experiments. Dissolution rates are quantified with data from the steady-state operation of flow-through reactors. As discussed in the results section, the lower limit of the schoepite dissolution rate at pH 6 is $1.58 \mu\text{mol m}^{-2} \text{h}^{-1}$. Flow-through experiments also show that the dissolution rate decreases (even becoming negative) as the reaction reaches or exceeds saturation.

The time-scales for schoepite dissolution can also be estimated from dissolution experiments during periods when reprecipitation was not yet significant. In the presence of NaNO_3 , dissolution experiments display a rapid initial increase in the dissolved uranium concentration during the first hour(s), followed by a slower increase extending for tens or hundreds of hours. It is unclear whether the slower uranium phase is determined only by schoepite dissolution, or instead by a balance between schoepite dissolution and secondary phase precipitation. In the complete absence of sodium or cesium (experiments B10, B10R, C1), dissolution is very fast, nearly reaching maximum values within one hour. A similarly rapid time-scale is observed in the early portions of fluoride-induced dissolution experiments (C2 and C3).

In a previous study, rapid dissolution was also measured for dehydrated schoepite with rates higher than $3.5 \mu\text{mol m}^{-2} \text{h}^{-1}$ in bicarbonate solution at pH 8-10. Dissolution rates increased with increasing pH, inorganic carbon concentration, and temperature

(Steward and Mones, 1997). The dissolution of airborne $\text{UO}_{3(s)}$ dust in aqueous solution at pH 7.2-7.4 and 37° C occurred with a half-time of 1-2 hours (Heffernan et al., 2001). The dissolution of natural schoepite in oxic synthetic groundwater at pH 7.7-8.0 was dramatically slower, displaying biphasic kinetics with two zero-order dissolution periods. The initial dissolution period extended for the first 500 hours with a uranium release rate of $0.023 \mu\text{mol h}^{-1}$, and a second period extended for 13,000 hours with a release rate of $0.0014 \mu\text{mol h}^{-1}$ (Casas et al., 1994). Casas et al. did not measure the surface area of the natural schoepite, but using their 0.27 g L^{-1} schoepite concentration and 450 mL reactor volume and the surface area measured in this work ($8.8 \text{ m}^2 \text{ g}^{-1}$ for TBA-synthesis), their dissolution rates can be normalized to surface area to give rates of 0.021 and $0.0013 \mu\text{mol m}^{-2} \text{ h}^{-1}$. The slower dissolution of the natural sample may be due to the higher crystallinity of natural versus synthetic phases. Marked differences in the dissolution behavior of natural and synthetic becquerelite have previously been observed, with solubility products differing by 14 orders of magnitude (Casas et al., 1997), and the solubility of $\text{UO}_2(s)$ depends upon crystallinity (Neck and Kim, 2000). The schoepite dissolution rate observed by Casas et al. (1994) may also be limited by the formation of secondary phases, but unfortunately the composition of the synthetic groundwater was not specified.

Synthetic schoepite dissolution is also fast relative to the other synthetic uranyl phases studied in this work. The maximum observed dissolution rate of the uranyl silicate soddyite (Chapter 6) is $0.70 \mu\text{mol m}^{-2} \text{ h}^{-1}$, and the dissolution rate of a uranyl phosphate phase (Chapter 7) is even lower at $0.46 \mu\text{mol m}^{-2} \text{ h}^{-1}$.

5.4.4 Schoepite Transformation Rate

Only a small number of the experiments conducted can be interpreted by considering schoepite dissolution alone. The remainder should be interpreted by considering the transformation of a single phase system to a different single phase or multi-phase system. For a complete understanding of the system, dissolution and precipitation rates of both schoepite and the secondary phase must be known.

Conceptually, this is represented by the following equation:

$$\frac{d[U]_{\text{diss}}}{dt} = R_{\text{diss,schpt}} - R_{\text{pptn,schpt}} + R_{\text{diss,XUOH}} - R_{\text{pptn,XUOH}} \quad (11)$$

where subscripts “schpt” and “XUOH” denote schoepite and either sodium or cesium uranyl oxide hydrate. Initially the only non-zero term in equation 11 is $R_{\text{diss,schpt}}$, but as the reaction progresses, other terms become important. When the sum of terms in equation 11 equals zero, the system is either at equilibrium with the solid phase(s) or the dissolved uranium concentration is held at a steady-state value balanced by the release of uranium from schoepite and the uptake by the secondary phase. The latter is most likely the case for experiment B4R, in which the dissolved concentration remains constant while the XRD observations indicate ongoing growth of $\text{Na}(\text{UO}_2)\text{O}(\text{OH})_{(\text{s})}$.

The evolution of the dissolved uranium concentration in batch experiments with initial dissolution followed by reprecipitation of uranium can be rationalized by equation 11. Initially the dissolved uranium concentration increases according only to $R_{\text{diss,schpt}}$. If no secondary phase were formed, then $R_{\text{diss,schpt}}$ would eventually be balanced by $R_{\text{pptn,schpt}}$ and equilibrium with schoepite would be attained. However, as the new secondary solid phase forms, $R_{\text{pptn,XUOH}}$ also increases. If the growth of the secondary phase is dependent upon the surface area or volume of the secondary phase, then $R_{\text{pptn,XUOH}}$ increases as the

secondary phase grows until equilibrium with the secondary phase is approached. Initially the precipitation of the secondary phase retards the net increase of dissolved uranium in the system, and when $R_{\text{pptn,XUOH}}$ exceeds $R_{\text{diss,schpt}}$, the dissolved uranium concentration starts to decrease. Over time $R_{\text{diss,XUOH}}$ increases until it balances $R_{\text{pptn,XUOH}}$ and the dissolved uranium concentration in the system becomes controlled by the solubility of the secondary phase. The effect of surface area on the solubility of fine particles can lead to a continuing decrease in the dissolved uranium concentration as the crystals grow. At equilibrium the system may contain exclusively the secondary phase, but it is also possible for schoepite to coexist with the secondary phase. A similarly unusual dissolution-reprecipitation pattern was previously observed during the dissolution of uranophane in dilute solution. Initially the dissolved uranium concentration increased as uranophane dissolved, but when soddyite began precipitating because of the low calcium concentration in the system, the uranium concentration decreased as uranium was taken up by the new phase (Casas et al., 1994).

The observations of fast schoepite dissolution and subsequent formation of lower solubility secondary phases are consistent with the chronology of secondary mineral formation during the weathering of uraninite and corrosion of spent nuclear fuel. In long-term unsaturated corrosion tests of $\text{UO}_{2(s)}$ pellets, schoepite was the first phase to form. With a lifetime of about two years in the system, schoepite was replaced by lower solubility uranyl oxide hydrates, primarily becquerelite and compreignacite, which also persisted for about two years. Ultimately uranyl alkaline silicate hydrate minerals formed (Wronkiewicz and Buck, 1999). The precipitation of the most soluble species first in a consecutive precipitation reaction is a well documented phenomenon known as the

Ostwald Step Rule. Because of the inverse relationship between solubility and the solid-solution interfacial energy, higher solubility phases have lower interfacial energies and therefore higher nucleation rates, making them kinetically favorable (Stumm and Morgan, 1996).

The rates of schoepite transformation to sodium or cesium uranyl oxide hydrate can be compared with the transformation rates of schoepite upon exposure to other cations. When contacted with calcium solutions of 10 mM or greater, schoepite was transformed to becquerelite within 1-3 months (Sandino and Grambow, 1994; Sowder et al., 1996; Sowder et al., 1999; Vochten and Van Haverbeke, 1990), a time-scale comparable to that of the present work. Exposure of schoepite to 1 M potassium chloride completely transformed the solid to compregnacite within three months (Sandino and Grambow, 1994), and exposure to barium and lead at 60° C yielded billietite and wölsendorfitite respectively within one week (Vochten and Van Haverbeke, 1990). Synthetic magnesium, manganese, and nickel uranyl oxide hydrates were also formed from synthetic schoepite through contact with 0.5 M metal salt solutions at 60° C for two weeks (Vochten et al., 1991).

5.5 Conclusions

5.5.1 Summary of Observations

An array of batch experiments has enabled the determination of equilibrium solubility products which contribute to the existing database. The solubility product of synthetic schoepite was $10^{5.02} - 10^{5.54}$, in the middle of the published range of values, and

was systematically lower for solids synthesized with NaOH instead of TBAOH. The determination of solubility products for sodium and cesium uranyl oxide hydrates is a new contribution to the thermodynamic database. A clarkeite-like sodium uranyl oxide hydrate ($\text{Na}(\text{UO}_2)\text{O}(\text{OH})_{(s)}$) has a solubility product of $10^{8.81}$ (eqn. 5), and equilibrium uranium concentrations in systems with cesium were successfully fit with a solubility product of $10^{68.4}$ for a cesium uranyl oxide hydrate ($\text{Cs}_3[(\text{UO}_2)_{12}\text{O}_7(\text{OH})_{13}] \cdot 3\text{H}_2\text{O}_{(s)}$) (eqn. 7) with the composition of a recently synthesized phase.

Schoepite dissolved rapidly at rates of $1.58 \mu\text{mol m}^{-2} \text{h}^{-1}$ or greater in flow-through systems, and dissolution reactions neared completion within one hour in batch experiments in which dissolved uranium was observed only to increase (i.e., no reprecipitation was observed). In the presence of even 1 mM electrolyte concentrations, simple dissolution was not observed. In many batch experiments the dissolved uranium concentration initially increased as schoepite dissolved, but later decreased as a secondary phase formed. The evolution of the dissolved uranium concentration was controlled by the balance between precipitation and dissolution rates of both schoepite and the secondary phase. The formation of the secondary phase was accompanied by changes in lattice parameters and crystal growth. Cesium was more effective than sodium at inducing phase transformations and depressing the dissolved uranium concentration.

5.5.2 Environmental Implications

The experimental data are consistent with the observation of schoepite as an initial weathering product of uraninite corrosion. While schoepite may form first, its

ongoing dissolution supplies uranium for incorporation into more stable secondary phases. If the dissolution and precipitation rates of all of the minerals in the paragenetic weathering sequence of uraninite were known, it might be possible to relate their steady-state dissolution and precipitation to the spatial and mass distribution of uranium among various secondary phases. Although sodium uranyl oxide hydrates are uncommon in the environment and no natural cesium uranyl oxide hydrates have been observed, the formation of these phases following the disposal of spent nuclear fuel will depend upon the composition of the infiltrating solution. The presence of cesium as a fission product makes it a particularly apt candidate for interlayer incorporation. Sodium and cesium uranyl oxide hydrate solids may become the solubility-controlling phases.

In predicting the mobility of uranium at contaminated sites or designing remediation strategies for contaminated soils, reaction rates as well as long-term equilibrium should be considered. The overall release of uranium from fine grained uranyl oxide hydrates may be dominated by a transient period of high dissolved uranium concentrations. Calculations of the release of uranium from such phases will underpredict actual releases if only the long-term equilibrium behavior is considered.

Chapter 6

SODDYITE DISSOLUTION AND TRANSFORMATION RATES

* draft of submission to *Geochimica et Cosmochimica Acta*, March 2001

6.1 Introduction

Uranyl (UO_2^{2+}) minerals are formed as secondary phases during the oxidative weathering of uraninite (UO_2) (Finch and Murakami, 1999) and the uranium (IV) oxides that are the dominant component of spent nuclear fuel (Wronkiewicz and Buck, 1999). The dissolution of uranium (IV) oxides and spent nuclear fuel controls the initial release of uranium and associated radionuclides (Shoesmith, 2000). Subsequently, the dissolved concentrations, and hence the mobility, of uranium and associated radionuclides may be limited by the solubility of secondary uranyl phases (Finn et al., 1996; Trocellier et al., 1998).

The uranyl orthosilicate mineral soddyite, $(\text{UO}_2)_2(\text{SiO}_4)\cdot 2\text{H}_2\text{O}$, has a framework structure, consisting of chains of pentagonal uranyl bipyramids cross-linked by silicate tetrahedra, that is uncommon among uranyl minerals (Burns, 1999). In natural environments, soddyite is stable when in contact with waters high in dissolved silica, low in carbonate, and with a pH below 7 (Finch and Murakami, 1999). Soddyite can be

formed by the alteration of previously precipitated uranophane ($\text{Ca}(\text{UO}_2)_2(\text{SiO}_3\text{OH})_2(\text{H}_2\text{O})_5$) upon exposure to dilute meteoric waters (Finch and Murakami, 1999). Soddyite is one of the secondary phases identified in the yellow rim of solids surrounding the uraninite core of the Nopal I deposit in Mexico (Ildefonse et al., 1990). Seepage waters from uranium mines in Germany contain elevated dissolved concentrations of both uranium and silica and the solubility of uranyl silicates may be important in controlling uranium mobility (Moll et al., 1996). In corrosion tests of both uraninite and spent nuclear fuel, soddyite was identified in the paragenetic sequence of alteration phases (Wronkiewicz and Buck, 1999; Wronkiewicz et al., 1992, 1996). A simple thermodynamic model of the dissolution of uranium(IV) oxide in granitic groundwater suggested that, under oxidizing conditions, the solubility of uranium may be controlled by several uranyl phases including soddyite (Trocellier et al., 1998).

While the dissolution of uraninite has been studied under a variety of conditions (Casas et al., 1998; de Pablo et al., 1999; Steward and Mones, 1997; Torrero et al., 1994), information on the solubilities and dissolution rates of secondary uranyl minerals is limited. Some laboratory studies of synthetic soddyite phases have been performed in recent years. Synthesis methods and the physicochemical characterization of synthesized phases are discussed by Moll et al. (1995) and Vochten et al. (1995). The solubility of soddyite has been determined in dilute aqueous solution (Nguyen et al., 1992), 0.1 M NaClO_4 (Moll et al., 1996), and in the presence of dissolved silicon, sodium and bicarbonate (Perez et al., 1997). However, the solubility products determined for soddyite in these various studies are not in agreement.

The evolution of dissolved uranium concentrations over time has been measured in batch studies of soddyite dissolution (Moll et al., 1996; Perez et al., 1997). Based on the observation of a transient peak in dissolved uranium concentrations, Moll et al. (1996) suggested that some alteration phases might have formed in systems open to the atmosphere even though soddyite remained the most abundant phase during dissolution. In the batch dissolution studies of Perez et al. (1999), the formation of secondary solid phases was prevented by the inclusion of bicarbonate, which stabilizes dissolved uranium in solution through the formation of uranyl-carbonate species.

In the current study, the dissolution rate of soddyite in aqueous suspension at near neutral pH has been investigated. The dissolution and transformation of soddyite in batch studies were tracked by characterizing the dissolving solids over time as well as by following the dissolved concentrations of uranium and silicon. Dissolution rates were also quantified in flow-through experiments to avoid the accumulation of reaction products.

6.2 Experimental Materials and Methods

6.2.1 Soddyite Synthesis

Soddyite was synthesized by the method of Moll et al. (1995) optimized for yield and phase purity. Two separate batches (syntheses #1 and #2) were synthesized by combining stoichiometric amounts of 0.1 M uranyl acetate (Alfa Aesar) and 0.1 M sodium metasilicate (Alfa Aesar) solutions in the Teflon liner of a 23 mL Parr bomb. The Parr bomb was heated to 110°C for ten days and then cooled. The precipitated solids

were filtered with a 0.2 μm polycarbonate filter membrane (Millipore Corp.) and then washed with boiling deionized water to remove any excess reactants. The remaining solids were rinsed off of each filter and diluted to a suspension volume of approximately 20 mL with deionized water. The mass concentration of soddyite in each suspension was determined gravimetrically by filtering an aliquot of the suspension through pre-weighed polycarbonate filter membranes, drying, and weighing the filter and solids.

6.2.2 Dissolution Experiments

Soddyite dissolution was investigated in both batch and flow-through modes. All dissolution experiments were conducted at the ambient temperature of the laboratory ($22 \pm 2^\circ\text{C}$). Duplicate batch experiments were initiated by adding a volume of stock soddyite suspension to a polycarbonate flask containing a magnetically-stirred solution of 5 mM 2-(n-morpholino)ethanesulfonic acid (MES) buffer (Avocado Research Chemicals) in 0.01 M sodium nitrate (Mallinckrodt). The pH of the solutions was adjusted to 6.00 with sodium hydroxide prior to the soddyite addition, contributing an additional 2.3 mM sodium to the system. The flasks were capped to minimize evaporation, but no effort was made to exclude carbon dioxide from the suspensions. The soddyite suspensions were periodically sampled to determine dissolved concentrations of uranium and silicon and total uranium concentrations, and to collect solids for subsequent analyses. Samples for dissolved uranium were collected by filtering 5 mL of suspension through 0.2 μm polycarbonate filter membranes (Millipore Corp.), collecting the last 1 mL of filtrate, and diluting 0.5 mL of the collected filtrate to 5 mL in 1% nitric acid. The filter membranes were removed from their filter holders, mounted on glass slides, air dried and saved for

X-ray diffraction and scanning electron microscopy analyses. Samples for total uranium determination were obtained by diluting 0.5 mL of the suspension to 10 mL with 10% nitric acid to dissolve the soddyite particles.

In flow-through experiments, stock soddyite suspension was added to two approximately 50 mL polymethylmethacrylate stirred flow-through reactors with outlets sealed by 0.2 μm polycarbonate filter membranes to yield a soddyite concentration of 0.41-0.42 g L^{-1} . The exact volumes of the flow-through reactors were determined gravimetrically by filling them with water. The influent solutions for both flow-through reactors were 0.01 M sodium nitrate, 5 mM MES at pH 6.00, amended for one reactor to 100 μM silicon (1 g L^{-1} Si standard, Aldrich). Flow to the reactors was controlled by a peristaltic pump and stirring was provided by a magnetic stir bar and stir plate. The residence times in the flow-through reactors were 1.14 to 1.26 h for the reactor without added silicon and 1.22 to 1.88 h (but mostly 1.22 to 1.44 h) for the reactor with added silicon.

6.2.3 Analytical Methods

Uranium and silicon concentrations in solution were determined by inductively coupled plasma mass spectrometry (ICP-MS) with a Hewlett Packard HP4500 instrument. Thallium was used as an internal standard in ICP-MS analyses in order to compensate for drift in instrument sensitivity. Calibration was performed with commercially available standard solutions for uranium (Alfa Aesar), silicon (Aldrich), and thallium (SPEX Chemical). Solution pH was measured with a Ross glass electrode and Orion 720A pH meter.

The synthesized and partially-reacted solids were characterized and identified by X-ray powder diffraction (XRD), diffuse reflectance infrared spectroscopy (DRIFTS), scanning electron microscopy (SEM), Raman spectroscopy, and BET surface area analysis. XRD analyses were performed on a Scintag Pad V X-ray powder diffractometer with a Cu k-alpha X-ray source and germanium detector. A Bio-Rad FTS-45 Fourier Transform Infrared spectrometer was used with a DRIFTS sample stage for infrared spectroscopy. Powdered soddyite was diluted with potassium bromide before DRIFTS analysis. SEM images were collected on gold-coated samples with a Camscan Series II scanning electron microscope. Raman spectra were measured with a 514.5 nm argon ion laser on a Renishaw MicroRaman Spectrometer with a spectral resolution of 1 cm^{-1} . Samples for Raman analysis were prepared by evaporating an aliquot of concentrated suspension on glass microscope slides. The surface area was determined on freeze-dried samples by BET N_2 adsorption using a Micromeritics Gemini surface area analyzer.

6.2.4 Equilibrium Calculations

Equilibrium calculations were performed using the aquatic chemical equilibrium software program MINEQL+ (Environmental Research Software, 1998). Ionic strength corrections in MINEQL+ are made using the Davies equation. The thermodynamic constants of dissolved uranyl species used in calculations are taken from the critical review of Grenthe et al. (1992) amended to use the $\text{UO}_2(\text{OH})_{2(\text{aq})}$ formation constant of Silva (1992) (Table 6.1).

Table 6.1: Aqueous phase uranium reactions and thermodynamic stability constants that are significant at pH 6.0, $P_{\text{CO}_2} = 10^{-3.5}$ atm, and total uranium concentrations less than 10 μM (T=25°C, I=0).

Reaction	Log K
$\text{UO}_2^{2+} + \text{H}_2\text{O} = \text{UO}_2\text{OH}^+ + \text{H}^+$	-5.20
$\text{UO}_2^{2+} + 2\text{H}_2\text{O} = \text{UO}_2(\text{OH})_2 + 2\text{H}^+$	-11.5*
$2\text{UO}_2^{2+} + 2\text{H}_2\text{O} = (\text{UO}_2)_2(\text{OH})_2^{2+} + 2\text{H}^+$	-5.62
$3\text{UO}_2^{2+} + 5\text{H}_2\text{O} = (\text{UO}_2)_3(\text{OH})_5^+ + 5\text{H}^+$	-15.55
$4\text{UO}_2^{2+} + 7\text{H}_2\text{O} = (\text{UO}_2)_4(\text{OH})_7^+ + 7\text{H}^+$	-21.9
$\text{UO}_2^{2+} + \text{CO}_3^{2-} = \text{UO}_2\text{CO}_3(\text{aq})$	9.68

Source: Grenthe et al., 1992, with the exception of * Silva et al., 1992

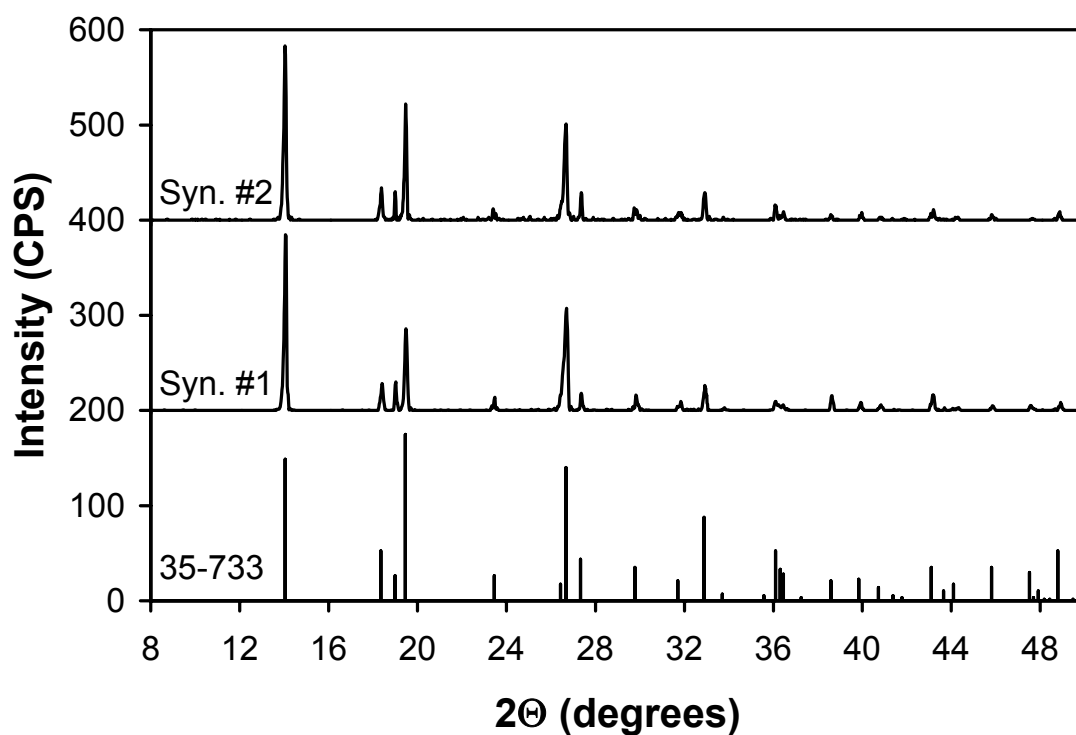


Figure 6.1: X-ray diffraction patterns of synthetic soddyite and the JCPDS-ICDD reference file (card no. 35-733) for soddyite.

6.3 Results

6.3.1 Soddyite Characterization

The powder XRD patterns of the synthesized solids are matched best by card 35-733 of the JCPDS database (Fig. 6.1), which is labeled as soddyite (JCPDS-ICDD, 1999). The DRIFTS spectrum obtained for the synthesized solids (Fig. 6.2) agrees very well with previously collected and interpreted spectra for synthetic soddyite (Moll et al., 1995; Cejka, 1999). Symmetric and antisymmetric stretching vibrations are observed at 834 and 912 cm^{-1} respectively for the uranyl ion and at 879 and 962 cm^{-1} respectively for the silicate ion. The sharp absorption peak at 1583 cm^{-1} is due to the bending vibration of water. The specific surface area of the synthesized soddyite was 3.15 $\text{m}^2 \text{g}^{-1}$.

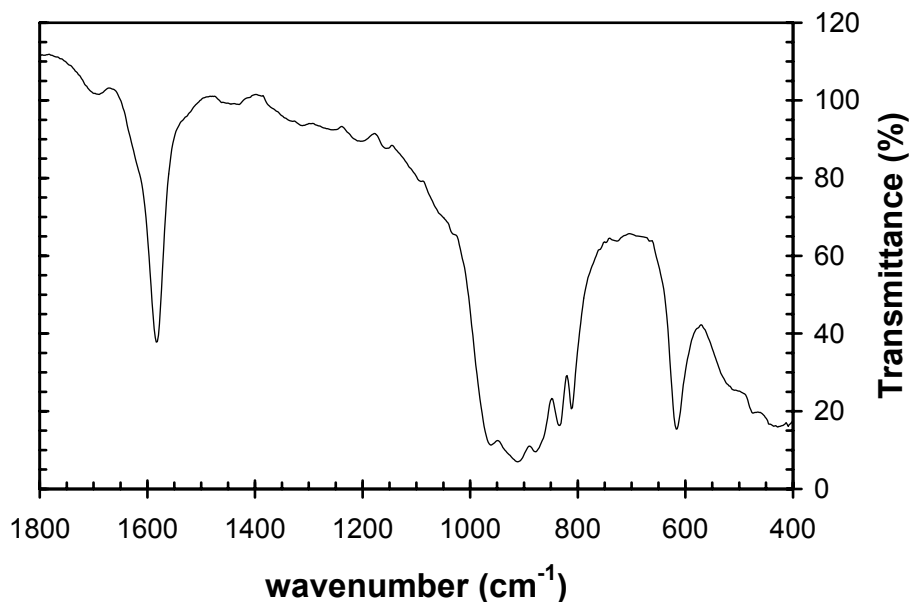


Figure 6.2: DRIFTS spectrum of synthetic soddyite. Uranyl vibrations are observed at 834 cm^{-1} (symmetric) and 912 cm^{-1} (antisymmetric). Silicate vibrations are observed at 879, 960, and 619 cm^{-1} . The bending vibration of water gives rise to the strong peak at 1583 cm^{-1} .

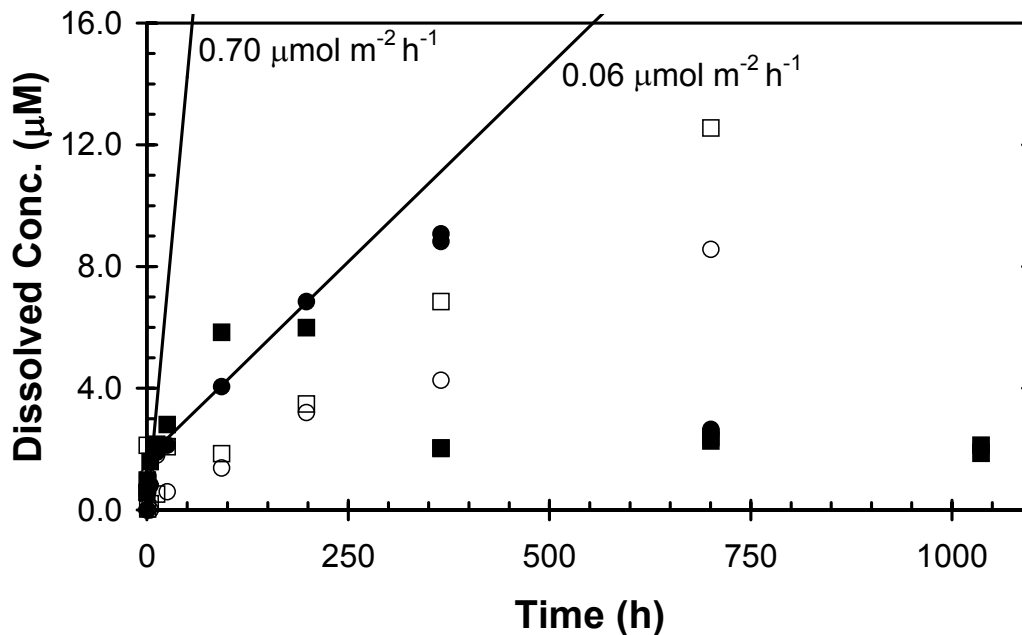


Figure 6.3: Batch dissolution of soddyite (~ 0.125 g/L) at pH 6 (5 mM MES) and $I = 0.01$ M (NaNO_3). Dissolved concentrations of uranium (\bullet , \blacksquare) and silicon (\circ , \square) for both synthesis #1 (\bullet , \circ) and #2 (\blacksquare , \square). Plotted lines represent the uranium concentration for dissolution rates of 0.06 and 0.70 $\mu\text{mol m}^{-2} \text{h}^{-1}$ from batch and flow-through experiments respectively.

6.3.2 Batch Dissolution Experiments

6.3.2.1 Solution Chemistry

The evolution of the dissolved uranium and silicon concentrations during batch soddyite dissolution is presented in Fig. 6.3. Data was collected in two duplicate experiments, one with 0.13 g L^{-1} of soddyite from synthesis #1 and the other with 0.12 g L^{-1} of soddyite from synthesis #2. The dissolved uranium concentration reached 1 μM after only 4 h, and then increased at a slower rate from 4 h until 365 or 200 h for the soddyite from syntheses #1 and #2 respectively. A linear fit of the uranium data from 4-198 hours ($r^2 = 0.88$) gives a uranium release rate of 0.20 $\mu\text{mol U g soddyite}^{-1} \text{h}^{-1}$ or

$0.064 \mu\text{mol m}^{-2} \text{h}^{-1}$ normalized to the $3.15 \text{ m}^2 \text{ g}^{-1}$ specific surface area (shown by the line applied to the 0.13 g L^{-1} flask in Fig. 6.3).

The increase in the dissolved uranium concentration in the batch reaction flasks ceased some time between 365 and 700 hours for synthesis #1 and between 198 and 365 hours for synthesis #2. The dissolved uranium concentration then decreased and remained constant in the range $1.9\text{-}2.5 \mu\text{M}$ for the remainder of the experiment (1683 hours). The decrease and stabilization of the dissolved uranium concentration suggest the precipitation of a new solubility-controlling phase.

In addition to the dissolved uranium concentrations, the dissolved silicon concentrations were also measured for the first 365 hours of the experiment. Samples were also collected after 365 hours, but were lost during an unsuccessful ICP-MS run. The silicon data can be fit linearly ($r^2 = 0.89$) for the data from 90-700 hours to yield a silicon release rate of $0.11 \mu\text{mol Si g soddyite}^{-1} \text{ h}^{-1}$, which is $0.035 \mu\text{mol m}^{-2} \text{ h}^{-1}$ normalized to surface area. For samples obtained prior to the precipitation event, the ratio of dissolved uranium to silicon is approximately two (Fig. 6.4), consistent with congruent dissolution.

The total uranium concentration of the suspension was monitored to check for the loss of the solid phase to the container walls. The total uranium concentration remained near its expected value of $390 \mu\text{M}$ for synthesis #1 for the first 365 hours, and to the expected value of $360 \mu\text{M}$ for synthesis #2 for the first 198 hours. After those times, the concentration began dropping, which indicates that the solid phase was adhering to the walls of the flasks. This phenomenon was also observed by visual examination of the reaction flasks.

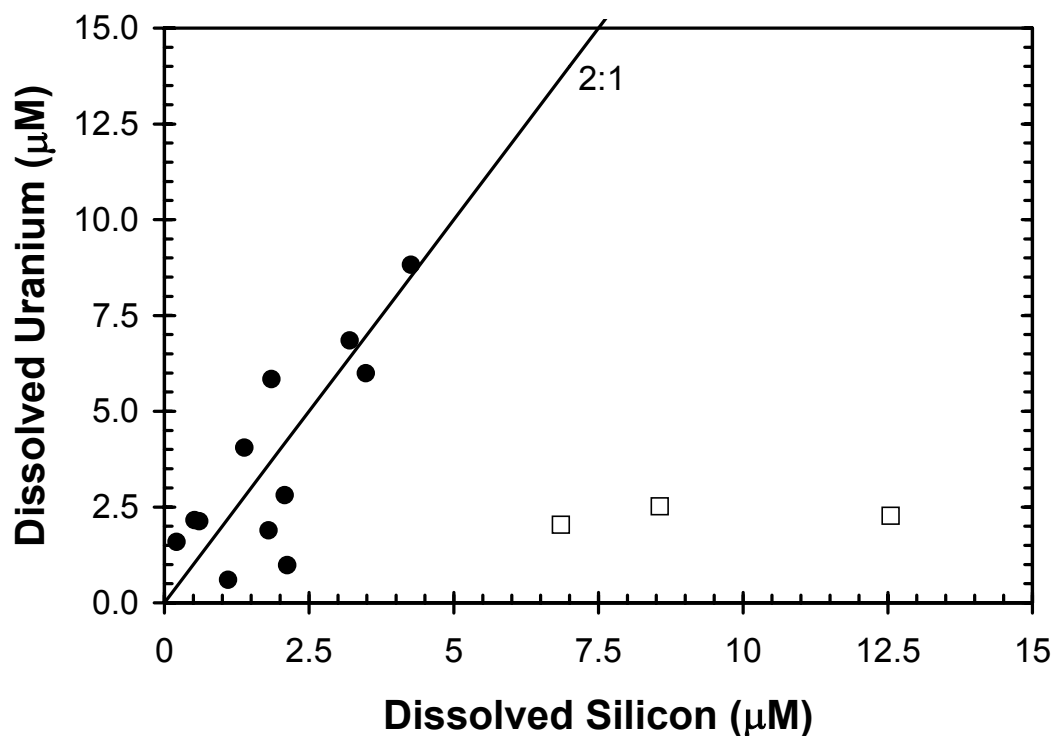


Figure 6.4: Dissolved uranium versus silicon concentrations during batch soddyite dissolution. Data are shown for the period before (●) and after (□) the uranium reprecipitation event. The line corresponding to a 2:1 ratio of the uranium to silicon concentrations represents ideal congruent dissolution.

6.3.2.2 Characterization of Partly-reacted Solids

Solids were retained at each sampling point and analyzed. XRD patterns for the stock soddyite (synthesis #1) and for the solids in the reactor at several sampling times are shown in Fig. 6.5. XRD patterns were collected for solids retained on 0.2 μm polycarbonate filter membranes, which produce a broad peak observed at 16-19°. The dominant peaks of the stock soddyite are present in all of the samples of solids collected during batch dissolution. A peak at 15°, not seen for the stock soddyite, appears in the 1040 hour sample and grows in intensity for the 1680 hour sample. This peak is a dominant peak in the spectrum of the sodium-uranyl oxide hydrate mineral clarkeite

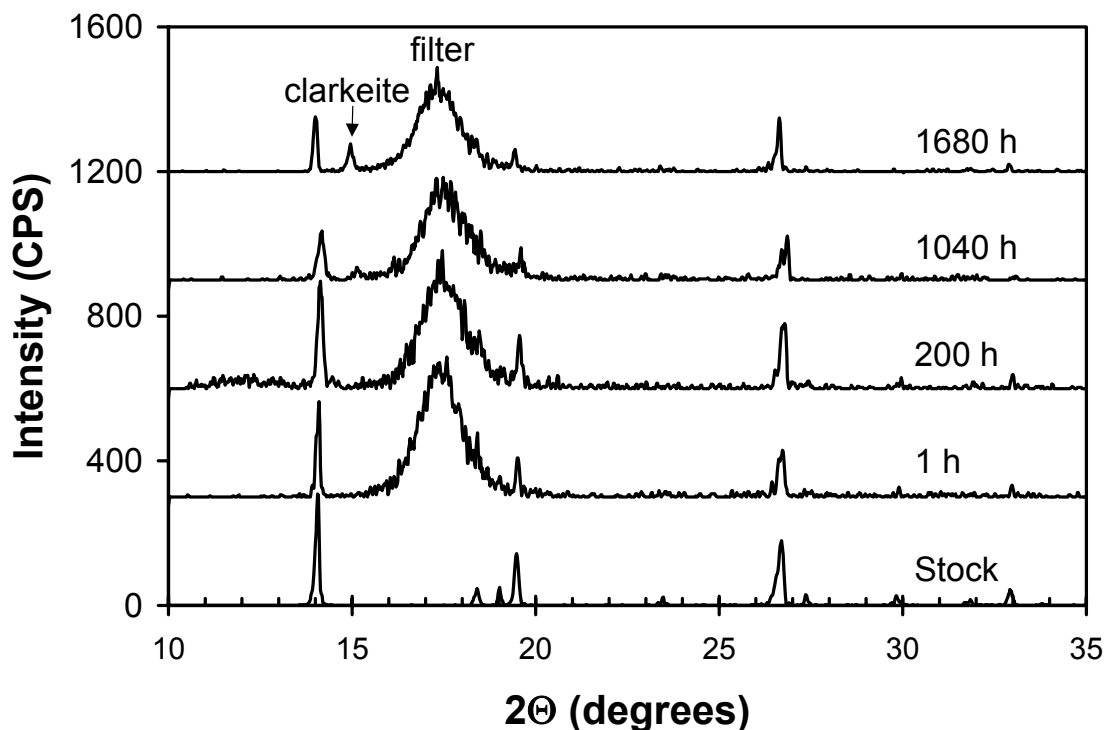


Figure 6.5: Time series of X-ray diffraction patterns for solids collected from batch soddyite dissolution experiments. The three dominant peaks in the pattern for the stock soddyite (bottom pattern) are located at 14.1° , 19.5° , and 26.7° . The solids collected from 1-1680 hours are impacted on polycarbonate filter membranes, which give rise to a broad peak from 16 - 19° . The peak appearing at 15.0° in the 1040 and 1680 hour samples is a strong peak in the diffraction pattern of clarkeite.

$(\text{Na}[(\text{UO}_2)\text{O}(\text{OH})](\text{H}_2\text{O})_{0.1})$. Clarkeite is isostructural with the synthetic anhydrous sodium uranates $\text{Na}_2\text{U}_2\text{O}_7$ and $\text{Na}_6\text{U}_7\text{O}_{24}$ and these phases are difficult to distinguish from one another with powder XRD (Finch and Ewing, 1997). Clarkeite, or one of the sodium uranates, was the only phase with an XRD peak at 15° that could have formed from the contents of the reaction flasks. The uranyl oxide hydrate schoepite $((\text{UO}_2)_8\text{O}_2(\text{OH})_{12}\cdot 12\text{H}_2\text{O})$ is a common secondary phase that might have been expected to form; however, the XRD patterns of the collected solids lack the characteristic schoepite peak at 12° .

The precipitation of a new solid phase following initial soddyite dissolution was also observed by scanning electron microscopy. In the electron micrographs taken after 1 hour (Fig. 6.6a) and 365 hours (Fig 6.6b), blocky crystals of soddyite about 1 μm by 2 μm are the only solids observed. After 1683 hours, a new phase in addition to soddyite is observed by SEM (Fig. 6.6c). The new phase consists of 1-2 μm long needle-like crystals.

The Raman spectra of solids from both the stock soddyite suspension and the conclusion of the batch dissolution experiment for synthesis #1 are presented in Fig. 6.7a. The spectrum of the stock soddyite is consistent with a published spectrum, in which the dominant peak at 829 cm^{-1} was assigned to the symmetric uranyl ion stretch, the peak at 457 cm^{-1} to the equatorial U-O stretch, and peaks at 222, 288, and 308 cm^{-1} to U-O bending modes (Biwer et al., 1990). The spectrum of the solids from the batch dissolution reactor contains the same peaks as the spectrum of the stock soddyite, but the dominant peak at 829 cm^{-1} is broader and additional peaks are observed at 136 and 866 cm^{-1} . A weighted value of the stock soddyite spectrum was subtracted from the spectrum of the solids from the batch dissolution reactor; the difference spectrum, which exhibits peaks at 136, 820, and 866 cm^{-1} , is displayed in Fig. 6.7b. These peaks match perfectly with those from a separately synthesized solid phase that was identified as a clarkeite-like phase by X-ray diffraction (Giammar, 2001).

6.3.3 Flow-through Dissolution Experiments

Rates of soddyite dissolution were also determined in flow-through dissolution experiments. The effluent uranium concentrations from the flow-through reactors over

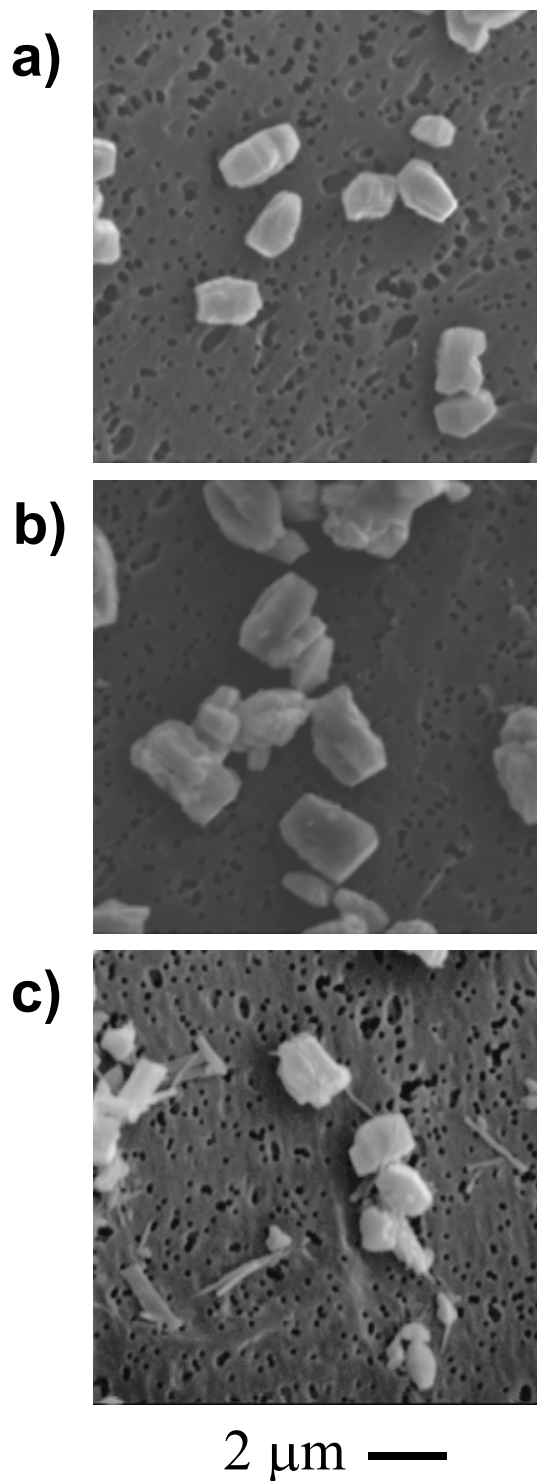


Figure 6.6: Scanning electron micrographs of solids collected from batch dissolution experiments after 1 hour (a), 365 hours (b), and 1683 hours (c) of reaction in batch reactors. Only the blocky soddyite crystals are observed after 1 and 365 hour(s), but a new needle-shaped phase is apparent after 1683 hours.

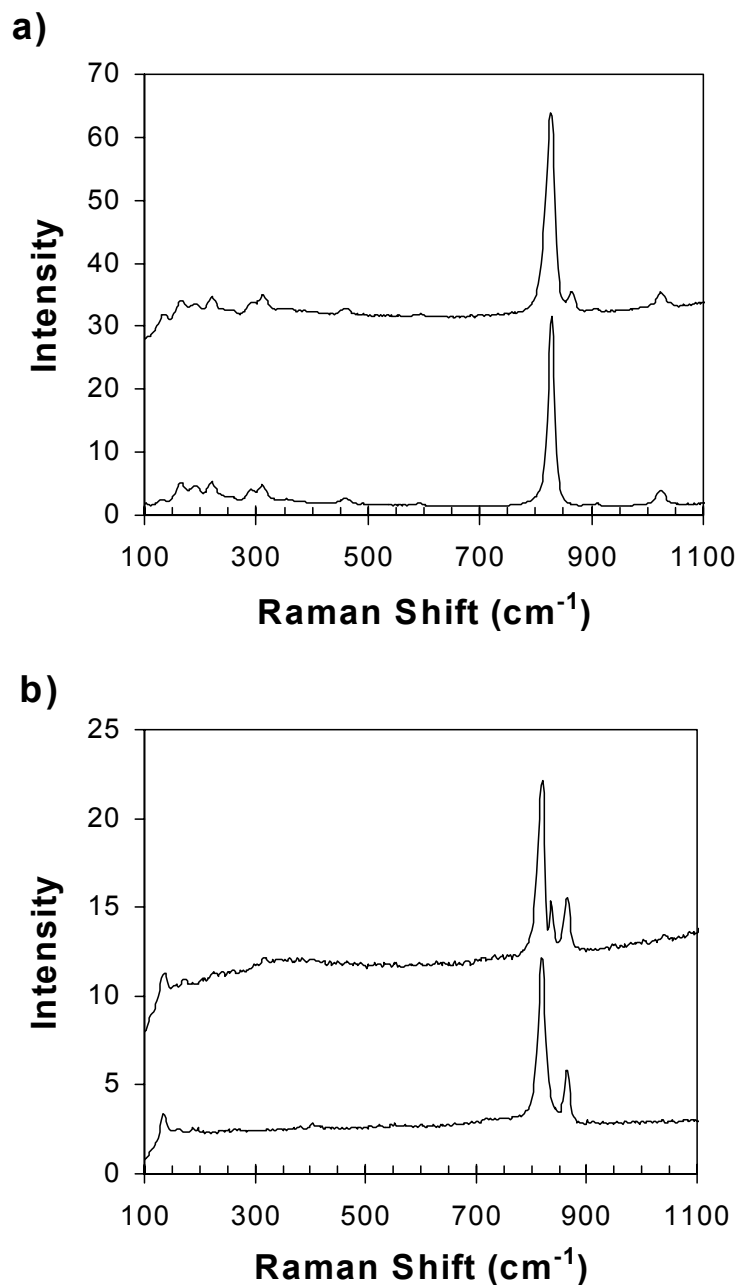


Figure 6.7: Raman spectra of a) solids at conclusion of batch dissolution (top) and synthetic soddyite stock (bottom) b) difference spectrum of batch solids – soddyite stock (top) and a synthetic sodium uranyl oxide hydrate (bottom). The dominant peak(s) in all spectra correspond to the symmetric stretch of the uranyl ion. In soddyite the vibration occurs at 829 cm^{-1} , and in the synthetic uranyl oxide hydrate two distinct uranium environments give rise to two energies for the same stretch at 820 and 866 cm^{-1} . Peaks below 500 cm^{-1} correspond to equatorial U-O stretches and U-O bending modes.

the course of the experiment were in the range 0.91-1.27 μM for the reactor without added silicon and in the range 0.59-0.87 μM for the reactor with 100 μM dissolved silicon in the influent (Fig. 6.8). The effluent pH from the reactors was consistently 6.00-6.06. Stability of the effluent uranium concentrations is an indication that steady-state dissolution has been reached. Very stable effluent uranium concentrations are observed for the reactor without added silica for the first 80 reactor volumes, but then the effluent concentrations increase. For the reactor with 100 μM dissolved silicon in the influent, the effluent uranium concentrations remain stable for about 50 reactor volumes and then gradually decrease. As dissolved products were flushed from the reactors, the total uranium concentration remaining in the reactors decreased by 11.7 and 7.4% for the zero silicon and 100 μM silicon reactors, respectively. Neither the flow-rate variations nor loss of material from the reactor can account for the variations in effluent concentrations. Despite the variations, the effluent concentrations are still sufficiently stable to allow for flow-rate quantification.

The steady-state dissolution rate ($\mu\text{mol m}^{-2} \text{ h}^{-1}$) was calculated using equation 1,

$$\text{Rate} = \frac{C}{t_{\text{res}}} \frac{1}{S \cdot A}, \quad (1)$$

where C is the effluent uranium concentration (μM), t_{res} is the hydraulic residence time of the reactor (h), S is the mass concentration of soddyite in the reactor (g L^{-1}), and A is the specific surface area ($\text{m}^2 \text{ g}^{-1}$). Note that the dissolution rate is calculated as the uranium release rate, and not as the soddyite loss rate (one mole of soddyite contains two moles of uranium). The dissolution rate was calculated for each effluent sample collected and these values were averaged. The average dissolution rate for the reactor without added

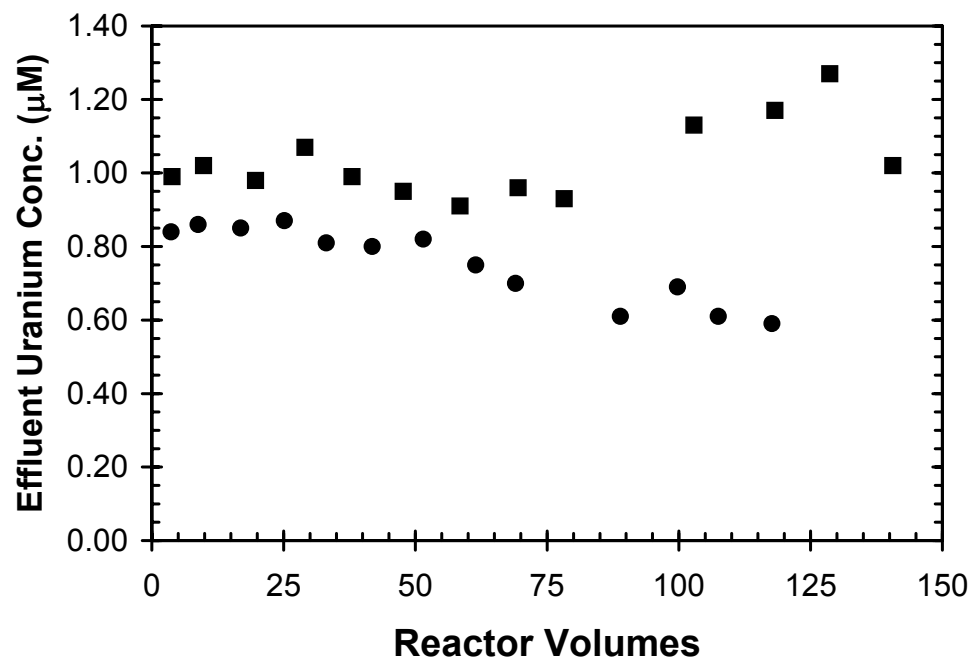


Figure 6.8: Effluent uranium concentrations from flow-through reactors at pH 6 (5 mM MES), $0.41\text{-}0.42\text{ g L}^{-1}$ soddyite ($[\text{U}]_{\text{tot}} = 1.25\text{ mM}$), ~ 1.3 hour residence time, and with either $0\text{ }\mu\text{M}$ (■) or $100\text{ }\mu\text{M}$ (●) dissolved silicon in the reactor influent.

silicon is $0.70 \pm 0.11\text{ }\mu\text{mol m}^{-2}\text{ h}^{-1}$. A line corresponding to this dissolution rate is plotted with batch dissolution data in Fig. 6.3. For the reactor with $100\text{ }\mu\text{M}$ silicon in the influent, the average rate is $0.45 \pm 0.06\text{ }\mu\text{mol m}^{-2}\text{ h}^{-1}$.

6.4 DISCUSSION

6.4.1 Equilibrium Soddyite Solubility

Before examining the formation of secondary phase(s) and rates of dissolution, it is useful to examine the predicted dissolved concentrations of uranium and silicon at equilibrium with soddyite. This equilibrium is calculated assuming stoichiometric

Table 6.2: Conditions and results of previous determinations of the solubility product for soddyite.

pH	atm.	Experimental Conditions			Added Solutes	U species considered ^a	LogK _{sp} ^b	ref. ^c
		I (M)	[U] _{diss} (mM)	[Si] _{diss} (mM)				
3.0	Ar	0.08	19.3	5.12		UO ₂ ²⁺ (UO ₂) ₂ (OH) ₂ ²⁺	5.74±0.21	1
3.0	N ₂	0.14	18.0	9.0	0.1 M NaClO ₄	UO ₂ ²⁺	6.03±0.45 6.15±0.53	2
3.0	air	0.14	19.5	10.0	0.1 M NaClO ₄			
8.54 - 9.11	air	calc.	0.29- 2.24	calc. ^d	NaHCO ₃ ≥5mM 1 mM Na ₂ SiO ₃ 7 mM NaClO ₄	SKB Database ^e	3.9±0.7	3

^a Only species present as more than 1% of dissolved uranium are listed.

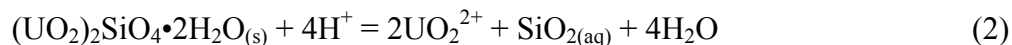
^b All of the authors adjusted conditional constants to I = 0 using the specific ion interaction theory discussed in Grenthe et al. (1992).

^c (1) Nguyen et al., 1992; (2) Moll et al., 1996; (3) Perez et al., 1997

^d Calculated as the sum of the initial dissolved silicon and an amount released following congruent dissolution of the soddyite (i.e., 0.5[U]_{diss})

^e Puigdomenech and Bruno, 1988

dissolution of the solid (reaction 2) with an associated solubility product constant (equation 3) (Nguyen et al., 1992).



$$K_{sp} = \frac{\{\text{UO}_2^{2+}\}^2 \{\text{SiO}_{2(aq)}\}}{\{\text{H}^+\}^4} \quad (3)$$

Several solubility constants have been reported for soddyite (Nguyen et al., 1992; Moll et al., 1996; Perez et al., 1997). Interpretation and application of these constants is complicated by the difficulty in relating the activity of UO₂²⁺ to the measured dissolved uranium concentration. Above pH 4, the hydrolysis species of uranyl contribute significantly to the total dissolved uranium, and in systems open to atmospheric carbon dioxide, dissolved uranyl carbonate species become important above pH 7. Although a compilation of thermodynamic data for uranium has been published (Grenthe et al.,

1992), the set of solution reactions considered since then varies from study to study. The solubility constants and the conditions for which they were determined are compiled in Table 6.2.

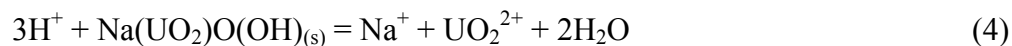
A solubility product of $\log K_{sp} = 5.74 \pm 0.21$ was determined after the equilibration of soddyite at pH 3, under argon and by using the Nuclear Energy Agency database (Grenthe et al., 1990) to calculate uranyl speciation (Nguyen et al., 1992). Under a wider range of pH and under both air and nitrogen atmospheres, Moll et al. were unable to model their complete data set using a single solubility product. At pH 3, a solubility product of $\log K_{sp} = 6.15 \pm 0.53$ was calculated (Moll et al., 1996). Another study investigated the solubility of soddyite at higher pH and in the presence of dissolved carbonate, using the SKBU database (Puigdomenech and Bruno, 1988) to calculate dissolved uranyl speciation. The solubility product determination was highly sensitive to the bicarbonate concentration and $\log K_{sp}$ ranged from 2.58-6.30. The authors report a value of $\log K_{sp} = 3.9 \pm 0.7$ for bicarbonate concentrations greater than 2 mM (Perez et al., 1997).

For the sake of comparison with the published solubility products, the reaction quotient was calculated for the conditions immediately prior to the reprecipitation event. For the batch dissolution of synthesis #1, these conditions are pH 6, 0.01 M ionic strength, 4.3 μM dissolved silicon, and 9.1 μM dissolved uranium ($[\text{UO}_2^{2+}] = 0.28 \mu\text{M}$). Using the solubility product of $\log K_{sp} = 5.74$, a reaction quotient of $\log Q = 5.52$ was calculated, indicating that the batch dissolution suspensions were still slightly undersaturated with respect to soddyite at the time of the sodium uranyl oxide hydrate precipitation. For congruent dissolution and a solubility product of $\log K_{sp} = 5.74$, the

expected dissolved uranium concentration in equilibrium with soddyite is 19 μM in the absence of any secondary phases. In the other published study of soddyite solubility at pH 6 in an open system (in 0.1 M NaClO_4), the dissolved uranium concentration was approximately 10 μM at equilibrium (Moll et al., 1996).

6.4.2 Predicted Equilibrium of Mixed Solid System

Since spectroscopic evidence suggests the formation of a clarkeite-like sodium uranyl oxide hydrate as a secondary phase, it is instructive to calculate the solution composition in equilibrium with both soddyite and the secondary phase (which we will refer to as $\text{Na}(\text{UO}_2)\text{O}(\text{OH})_{(\text{s})}$ omitting waters of hydration for convenience). Although no published value for the solubility product of this secondary phase is available, one can be estimated based on dissolution experiments in which schoepite, a uranyl oxide hydrate phase, was transformed completely to $\text{Na}(\text{UO}_2)\text{O}(\text{OH})_{(\text{s})}$ as determined by X-ray diffraction (Giammar, 2001). In the presence of 12.3 mM sodium at pH 6.00, the dissolved uranium concentration in equilibrium with $\text{Na}(\text{UO}_2)\text{O}(\text{OH})_{(\text{s})}$ was 1.1 μM ($[\text{UO}_2^{2+}] = 0.097 \mu\text{M}$) corresponding to a solubility constant for the reaction:



$$K_{\text{sp}} = \frac{\{\text{UO}_2^{2+}\}\{\text{Na}^+\}}{\{\text{H}^+\}^3} \quad (5)$$

with a value of $\log K_{\text{sp}} = 8.81$. This solubility product may then be used with that for soddyite ($\log K_{\text{sp}} = 5.74$) and the constants in Table 6.1 to calculate the equilibrium speciation for total concentrations of 360 μM uranium, 180 μM silicon, 12.3 mM sodium, at pH 6 in equilibrium with the atmosphere ($P_{\text{CO}_2} = 10^{-3.5}$ atm). Under these conditions,

coexistence of $\text{Na}(\text{UO}_2)\text{O}(\text{OH})_{(\text{s})}$ and soddyite is predicted. The calculated distribution of the total uranium is 16.1% as soddyite, 83.6% as $\text{Na}(\text{UO}_2)\text{O}(\text{OH})_{(\text{s})}$, and 0.3% dissolved. The calculated dissolved concentrations of uranium and silicon are 1.2 μM and 151 μM respectively. The results of the equilibrium calculation are highly sensitive to the solubility product assumed for $\text{Na}(\text{UO}_2)\text{O}(\text{OH})_{(\text{s})}$. A dissolved uranium concentration of 2.2 μM can be obtained by changing the $\log K_{\text{sp}}$ from 8.81 to 9.00, which is in better agreement with the final measurements of the experiments. In this case, 35.4% of the total uranium is $\text{Na}(\text{UO}_2)\text{O}(\text{OH})_{(\text{s})}$, 64% is soddyite, and the dissolved silicon concentration is 65 μM .

6.4.3 Evolution of Solid Phases and Dissolved Concentrations

The dominant feature of long-term batch soddyite dissolution is the precipitation of $\text{Na}(\text{UO}_2)\text{O}(\text{OH})_{(\text{s})}$ as a secondary, solubility-controlling phase. Although this phase was barely detectable by XRD after even 1040 hours, it was already influencing the dissolved uranium concentration at 680 hours. The XRD patterns and Raman spectra suggest that, even at the conclusion of the batch dissolution experiment, the solubility-controlling phase is present as only a minor component. The structure of clarkeite is based on sheets of edge sharing uranyl bipyramidal polyhedra with sodium ions occupying the interlayer positions (Finch and Ewing, 1997). This structure is very distinct from the framework structure of soddyite; therefore, it is likely that the precipitation of the $\text{Na}(\text{UO}_2)\text{O}(\text{OH})_{(\text{s})}$ occurs by homogeneous nucleation and not by reordering of the soddyite structure. This interpretation is supported by the observation of precipitated crystals distinct from soddyite crystals in the electron micrographs.

In the batch dissolution experiments, the onset of precipitation of $\text{Na}(\text{UO}_2)\text{O}(\text{OH})_{(\text{s})}$ is indicated by the decrease in the dissolved uranium concentration. Even after this point, the dissolved silicon concentrations continue to increase indicating continued dissolution of soddyite and implying continued release of uranium from that solid. However, the uranium released from soddyite must be rapidly taken up by the growing $\text{Na}(\text{UO}_2)\text{O}(\text{OH})_{(\text{s})}$. Since dissolved uranium is being removed by precipitation of the secondary phase and yet does not decrease to undetectable levels, dissolution of this phase must also be occurring. Thus, $\text{Na}(\text{UO}_2)\text{O}(\text{OH})_{(\text{s})}$ appears to be in pseudo-equilibrium as the dissolution of soddyite proceeds. Eventually, the dissolved concentration of silicon should reach its equilibrium value and the (net) dissolution of soddyite should cease. Unfortunately, silicon concentrations were not determined after 700 h because of analytical problems and these data are not available to compare with the predicted equilibrium concentrations of between 65 and 151 μM (depending on the K_{sp} used for the secondary phase).

The precipitation of $\text{Na}(\text{UO}_2)\text{O}(\text{OH})_{(\text{s})}$ was not observed in flow-through experiments because dissolved uranium was flushed from the reactors before it could reach a critical concentration required for precipitation. The soddyite dissolution experiments of Perez et al. (1997) in the presence of bicarbonate also show no evidence of phase transformation. Reprecipitation would not be favored under such conditions because the dissolved uranium is stabilized in solution through the formation of complexes with carbonate. Moll et al. (1996) do not report any reprecipitation in their soddyite dissolution experiments conducted at pH 6 in a 0.1 M NaClO_4 solution;

however, their measured dissolved uranium concentration did decline from approximately 10 μM at 60 days to 4 μM at 120 days.

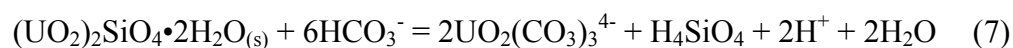
6.4.4 Soddyite Dissolution Rate Quantification

The dissolution rate calculated from the flow-through experiment without added silicon is 0.70 $\mu\text{mol U m}^{-2} \text{ h}^{-1}$ (or $10^{-10.0} \text{ mol Si m}^{-2} \text{ s}^{-1}$), which falls toward the high end of the range ($10^{-8.0}$ to $10^{-13.4} \text{ mol m}^{-2} \text{ s}^{-1}$) reported for silicate and aluminosilicate minerals at pH 5, and is comparable to the weathering rate of forsterite, Mg_2SiO_4 (Langmuir, 1997). The dissolution rate calculated from the linear increase in dissolved uranium in the batch experiments is slower by an order of magnitude, which may be attributable to the accumulation of the reaction products in the batch experiments. Similarly the introduction of silicon to the flow-through reactors decreases the dissolution rate from 0.70 to 0.45 $\mu\text{mol m}^{-2} \text{ h}^{-1}$.

In the flow-through reactor without added silicon, soddyite dissolution occurs under conditions that are very undersaturated with respect to the solid. Based on the measured pH of 6.0 and average dissolved uranium concentration of 1.0 μM and assuming a stoichiometric dissolved silicon concentration of 0.5 μM , the saturation index ($\log Q/K_{\text{sp}}$) is -2.15. The flow-through reactor with 100 μM added silicon is much closer to equilibrium, with an average dissolved uranium concentration of 0.75 μM and a saturation index of -0.53. The 100 μM dissolved silicon concentration is somewhat lower than the median value ($\sim 270 \mu\text{M}$) for groundwater (Langmuir, 1997). The 100 μM silicon flow-through reactor conditions are actually slightly less favorable for (net) soddyite dissolution than those in the batch experiments after the onset of precipitation of

the secondary phase. Under the batch conditions, with 2 μM dissolved uranium and 10 μM dissolved silicon, the saturation index (for soddyite) is -0.82. However, the dissolution rate in the batch reactor is only $0.035 \mu\text{mol Si m}^{-2} \text{h}^{-1}$ corresponding to $0.07 \mu\text{mol U m}^{-2} \text{h}^{-1}$ while the rate in the flow-through reactor with added silicon is $0.45 \mu\text{mol U m}^{-2} \text{h}^{-1}$. This discrepancy suggests that dissolution in the batch reactor may be transport-limited.

The only other study that has examined the kinetics of soddyite dissolution was performed in bicarbonate solution (Perez et al., 1997). Perez et al. determined an average dissolution rate of $2.45 \pm 1.58 \mu\text{mol m}^{-2} \text{h}^{-1}$, approximately four times greater than that determined in the current work. They modeled the dissolution rate by fitting a rate law to the following reaction:



Although rate constants were determined for each separate dissolution experiment, they were unique to that particular experiment and no general dissolution rate equation was determined.

6.5 Conclusions

Although the solubility of soddyite has been examined in several studies under a wide range of conditions, the kinetics of soddyite dissolution have received less attention. Here, we report a steady-state dissolution rate for soddyite, obtained in a flow-through reactor at pH 6, of $0.70 \mu\text{mol m}^{-2} \text{h}^{-1}$, comparable to that of the silicate mineral forsterite, Mg_2SiO_4 . Introduction of 100 μM silicon into the influent of the flow-through reactor

decreased the observed (net) dissolution rate by a factor of 1.6. In this experiment, the conditions were much closer to soddyite saturation, which is reflected in the decreased (net) dissolution rate. In batch experiments conducted at a similar degree of (under)saturation, substantially slower (net) dissolution rates were observed suggesting that the reaction may be subject to transport limitation in this system.

The most striking feature of the batch experiments, however, was the precipitation of a clarkeite-like sodium uranyl oxide hydrate (identified by XRD and Raman spectroscopy) as a secondary phase. The onset of precipitation of this secondary phase occurred as soddyite dissolution progressed (as indicated by increasing dissolved silicon concentrations) and was accompanied by a significant decrease in the dissolved uranium concentration. Thus the dissolved uranium concentrations in the batch experiments exhibited a transient maximum value in approximately five-fold excess of the steady-state value controlled by the solubility of the secondary phase.

Soddyite has been identified as a product of the oxidative weathering of uraninite and spent nuclear fuel and its weathering may, in turn, influence the release of dissolved uranium to soil- or groundwater. The results reported here suggest that soddyite dissolution could be significantly inhibited in groundwater due to ambient dissolved silicon concentrations (though this does not account for the possible effects of bicarbonate). Further, our results indicate that sodium uranyl oxide hydrates should be considered as potential solubility-limiting phases.

Acknowledgments

The Raman measurements were suggested by George Rossman and performed on an instrument in his laboratory. The assistance of Liz Arredondo in the acquisition of Raman spectra is greatly appreciated.

Chapter 7

URANYL PHOSPHATE DISSOLUTION AND TRANSFORMATION

7.1 Introduction and Background

Uranium (VI) minerals play important roles in uranium fate and transport at both contaminated sites and natural ore bodies. Generally uranyl minerals are formed as secondary minerals during the weathering of uranium (IV) oxide, which occurs in nature as the mineral uraninite (UO_2) (Finch and Murakami, 1999). Proposed geologic repositories for nuclear waste will contain large amounts of spent nuclear fuel which is greater than 96% UO_2 . The paragenetic sequence of phases formed during the corrosion of spent nuclear fuel in a high silica synthetic groundwater was identical to that observed in natural uraninite weathering environments (Wronkiewicz and Buck, 1999). The weathering of uraninite has been widely studied, and the solubility is a function of pH, redox potential, and the presence of other ions in the weathering solution (Casas et al., 1998). When secondary uranium (VI) minerals form, they can become the solubility-controlling phases (Finn et al., 1996; Trocellier et al., 1998).

The uranyl phosphates are a large family within the larger group of uranium (VI) minerals. Uranyl phosphates form following the weathering of uranium (IV) and other uranium (VI) minerals in high phosphate environments (Finch and Murakami, 1999). In some locations, uranyl phosphates are so abundant that they are the principal ore minerals

Table 7.1: Composition of environmentally significant uranyl phosphate minerals.

Name	Composition
autunite	$\text{Ca}(\text{UO}_2)_2(\text{PO}_4)_2 \cdot 10\text{H}_2\text{O}$
meta-autunite	$\text{Ca}(\text{UO}_2)_2(\text{PO}_4)_2 \cdot (2-6)\text{H}_2\text{O}$
uranyl orthophosphate	$(\text{UO}_2)_3(\text{PO}_4)_2 \cdot 4\text{H}_2\text{O}$
chernikovite	$(\text{H}_3\text{O})_2(\text{UO}_2)_3(\text{PO}_4)_2 \cdot 4\text{H}_2\text{O}$
sodium meta-autunite	$\text{Na}_2(\text{UO}_2)_2(\text{PO}_4)_2 \cdot 8\text{H}_2\text{O}$
meta-ankoleite	$\text{K}_2(\text{UO}_2)_2(\text{PO}_4)_2 \cdot 6\text{H}_2\text{O}$
phosphuranylite	$\text{Ca}(\text{UO}_2)_3(\text{PO}_4)_2(\text{OH})_2 \cdot 6\text{H}_2\text{O}$
saleeite	$\text{Mg}(\text{UO}_2)_2(\text{PO}_4)_2 \cdot 10\text{H}_2\text{O}$
lehnerite	$\text{Mn}(\text{UO}_2)_2(\text{PO}_4)_2 \cdot 10\text{H}_2\text{O}$

(Finch and Murakami, 1999)

(Vochten and Van Doorselaer, 1984). Table 7.1 lists several of the most commonly observed uranyl phosphate minerals. As with most uranium (VI) minerals, the structures of uranyl phosphates are sheet structures consisting of edge- and corner-sharing uranyl bipyramids with cross-linking phosphate groups. Additional cations occupy the interlayer spaces in the sheet structure (Burns, 1999).

Uranyl phosphates are very insoluble (Finch and Murakami, 1999), a characteristic that has generated considerable interest in their behavior in the environment. Autunite-like uranyl phosphate phases have been identified in contaminated soils at the Fernald Environmental Management Project (FEMP) in Ohio (Buck et al., 1996; Morris et al., 1996), and their presence was suggested as the factor controlling the concentration of dissolved uranium in the underlying aquifer (Elless and Lee, 1998). Calcium uranyl phosphate phases have also been identified in contaminated soils at Oak Ridge National Laboratory (Roh et al., 2000). Because of the low solubility of uranyl phosphates, the addition of apatite ($\text{Ca}_5(\text{PO}_4)_3(\text{OH})$) to contaminated soils has been proposed as a remediation strategy (Arey et al., 1999). Microcrystalline uranyl phosphates have also been observed in association with iron oxide surfaces downgradient

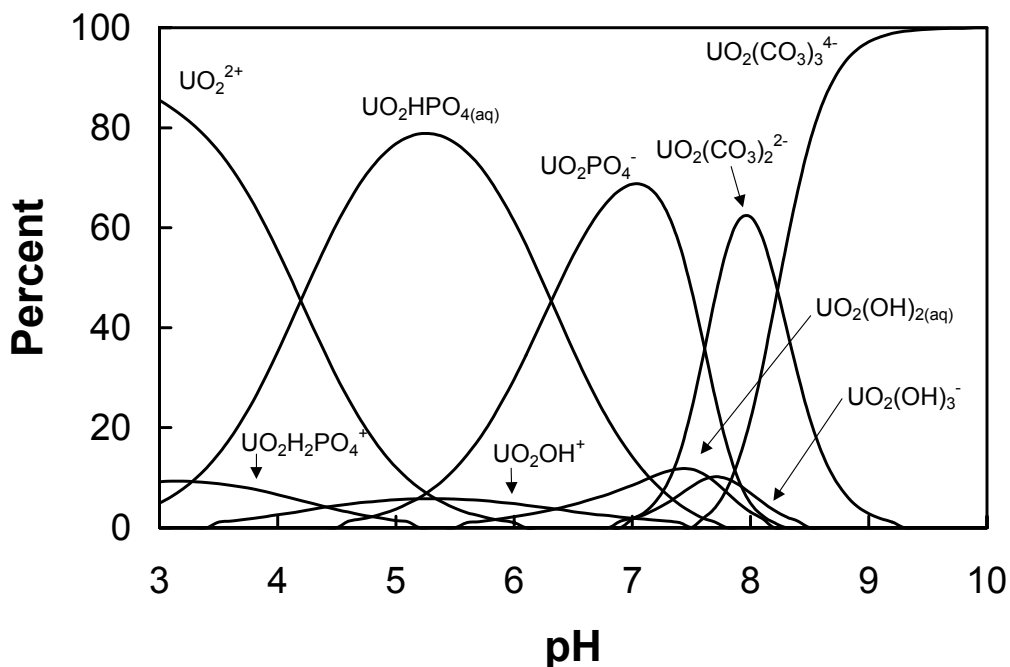


Figure 7.1: Uranium speciation in a system open to the atmosphere ($P_{\text{CO}_2} = 10^{-3.5}$ atm), at 0.01 M ionic strength, and with an excess of phosphate ($[P]_{\text{diss}} = 100 \mu\text{M}$) over uranium ($[U]_{\text{diss}} = 1 \mu\text{M}$). Calculations were made with the complete set of uranyl complexation reactions with hydroxide, carbonate, and phosphate compiled in Table A.1. No solid phases were considered in the calculation, and species that are never greater than 5% of total uranium are not included.

of the Koongarra ore body in Australia (Murakami, 1997; Sato et al., 1997) and the Bangombé deposit in Gabon (Del Nero et al., 1999).

The solubility of uranyl phosphate phases depends on the speciation of dissolved uranium. A review of dissolved uranyl species is presented in Appendix A, and a table including formation constants for dissolved complexes of the uranyl ion with hydroxide, carbonate, and phosphate is given in Table A.1. The speciation of dissolved uranium in an open system with total concentrations of $1 \mu\text{M}$ uranium (VI) and $100 \mu\text{M}$ phosphate is presented in Figure 7.1. For the given excess of phosphate over uranium, uranyl phosphate complexes are dominant at neutral pH until uranyl carbonate complexes form

Table 7.2: Dissolution reactions and associated solubility products found in the literature.

Reaction	Log K_{sp}	Ref. ^a
$(\text{UO}_2)_3(\text{PO}_4)_2 \cdot 4\text{H}_2\text{O}_{(s)} = 4\text{H}_2\text{O}_{(l)} + 2\text{PO}_4^{3-} + 3\text{UO}_2^{2+}$	-49.37	1
$(\text{UO}_2)_3(\text{PO}_4)_2 \cdot 4\text{H}_2\text{O}_{(s)} = 4\text{H}_2\text{O}_{(l)} + 2\text{PO}_4^{3-} + 3\text{UO}_2^{2+}$	-53.32	2
$\text{UO}_2\text{HPO}_4 \cdot 4\text{H}_2\text{O}_{(s)} = 4\text{H}_2\text{O}_{(l)} + \text{H}^+ + \text{PO}_4^{3-} + \text{UO}_2^{2+}$	-24.20	1
$(\text{H}_3\text{O})\text{UO}_2\text{PO}_4 \cdot 3\text{H}_2\text{O}_{(s)} = 4\text{H}_2\text{O}_{(l)} + \text{H}^+ + \text{PO}_4^{3-} + \text{UO}_2^{2+}$	-22.73 ^b	3
$\text{Ca}(\text{UO}_2)_2(\text{PO}_4)_2 \cdot x\text{H}_2\text{O}_{(s)} = x\text{H}_2\text{O}_{(l)} + \text{Ca}^{2+} + 2\text{PO}_4^{3-} + 2\text{UO}_2^{2+}$	-44.70	4

^a (1) Grenthe et al. (1992), (2) Sandino and Bruno (1992), (3) Van Haverbeke et al. (1996), (4) Langmuir (1997).

^b Value is for $\text{Log}K_{sp}^c$ (at $I = 0.5 \text{ M}$) because no ionic strength corrections were made.

at higher pH values. The solubility products of several uranyl phosphate minerals have been determined and compiled in a recent review (Grenthe et al., 1992). Table 7.2 lists the reactions and corresponding solubility products for those phases which are relevant to the current study. The solubility of uranyl phosphate hydrate was most recently studied by Sandino and Bruno (1992), and the solubility constant that they determined is listed in addition to the critical review value of Grenthe et al. (1992).

The formation and dissolution of uranyl phosphate phases is a function of the solution composition. Sowder et al. (1996) found that the uranyl oxide hydrate schoepite was slowly transformed to autunite when exposed to a solution with 10 mM calcium and phosphate. Chernikovite, also referred to as hydrogen autunite, is transformed to autunite by reaction with calcium (Sowder, 1998), meta-ankoleite by reaction with potassium (Van Haverbeke et al., 1996), sodium-autunite by reaction with sodium, and lehnerite by reaction with manganese(II) (Vochten, 1990).

Sowder (1998) investigated the dissolution of autunite in a variety of leaching solutions. The autunite concentration during dissolution experiments was at or below 1 g L^{-1} ($\sim 2.5 \text{ mM}$ uranium). Less than 1% of the total uranium in autunite suspensions was released on time-scales of 10-100 days in deionized water and 1mM acetic acid or

sodium bicarbonate. Dissolution in 1 and 100 mM EDTA and 100 mM acetic acid resulted in release of 5-25% of the total uranium after 2 weeks. Dissolution in 100 mM sodium bicarbonate was complete after only 8 hours. The solubility of uranium solid phases, including uranyl phosphates, was also crucial to the performance of soil-washing processes with contaminated soils from FEMP using citrate and bicarbonate as extractants (Francis and Dodge, 1998; Francis et al., 1999).

In the current investigation, a synthetic uranyl phosphate phase was prepared and investigated in dissolution experiments. The goal of the synthesis was the formation of autunite; however, the autunite synthesis was incomplete and, as discussed in the following sections, the synthesized solids were a mixture of three phases. The synthesized solids were thoroughly characterized, and subsequent characterization of solids removed from dissolution experiments was also performed. Batch dissolution studies probed the evolution of aqueous uranyl phosphate suspensions toward equilibrium. Flow-through experiments were used to quantify dissolution rates as a function of the solution chemistry.

7.2 Experimental

7.2.1 Synthesis of Solid Phases

Hydrogen uranyl phosphate hydrate $((\text{UO}_2)(\text{HPO}_4)\cdot 4\text{H}_2\text{O})$ was used as the starting uranyl phosphate phase for subsequent syntheses. Hydrogen uranyl phosphate hydrate was synthesized following the published methods (Sandino and Bruno, 1992; Sowder et al., 1996), in which a solution of 1 M uranyl nitrate (Alfa Aesar) and 1.1 M phosphoric

acid (Mallinckrodt) was mixed in order to precipitate the solid. The suspension was aged at room temperature for 3 months to improve crystallinity. The transformation of hydrogen uranyl phosphate hydrate to autunite was attempted by mixing 10 mL of the hydrogen uranyl phosphate hydrate suspension with 40 mL of 1 M calcium nitrate (Alfa Aesar) and aging for 39 days at room temperature and at 80°C for 7 days. The resulting solid suspension was dialyzed to remove excess reactants. A dialysis bag containing the solid suspension was placed in deionized water; the external volume of deionized water was frequently exchanged until the solution conductivity remained constant at 8-10 $\mu\text{S cm}^{-1}$. The washed stock suspension was stored in a polycarbonate centrifuge tube. The mass concentration of the stock suspension was determined gravimetrically by drying a portion of filtered solids at 105° C, and the chemical composition of the stock suspension was determined for an aliquot of whole suspension digested in concentrated hydrochloric acid in a Parr bomb at 105° C.

7.2.2 Dissolution Experiments

Dissolution was investigated in both batch and flow-through modes. All dissolution experiments were conducted at the ambient temperature of the laboratory (22° \pm 2°C). Two batch experiments were initiated by adding a volume of stock suspension from the autunite synthesis to a flask containing a magnetically stirred solution of 5 mM 2-(n-morpholino)ethanesulfonic acid (MES) buffer (Avocado Research Chemicals) in 0.01 M sodium nitrate (Mallinckrodt). Before addition of the solid, the pH of the solutions was adjusted to 6.00 with sodium hydroxide, which contributed an additional 2.3 mM sodium to the system. The flasks were sealed with parafilm to minimize

evaporation, but no effort was made to exclude carbon dioxide from the suspensions. The batch dissolution reactors were periodically sampled to determine dissolved concentrations of uranium, calcium, and phosphorus and to collect solids for subsequent analyses. The two batch experiments were designed to provide resolution of both short- and long-term dissolution with overlap between the two experiments to yield some duplicate analyses; the short-term experiment was run for 21 days and the long-term experiment for 56 days. While the initial pH was adjusted to 6 and buffered with 5 mM MES, no subsequent adjustments or measurements of the pH were made. It is regrettable that no pH measurements of the batch reactors were made, because, even in a buffered system, some pH drift would be expected as the solids dissolve and transform.

Samples for dissolved concentrations were collected by filtering 10 mL of suspension through 0.2 μm polycarbonate filter membranes (Millipore Corp.), collecting the last 5 mL of filtrate, and acidifying to 1% nitric acid. The filter membranes were removed from their filter holders, mounted on glass slides, air dried and saved for X-ray diffraction and scanning electron microscopy analyses.

In flow-through experiments, stock uranyl phosphate suspension was added to approximately 50 mL stirred, flow-through polymethylmethacrylate reactors with outlets sealed by 0.2 μm polycarbonate filter membranes. The exact volumes of the flow-through reactors were determined gravimetrically by filling them with water. The influent solutions for all flow-through reactors contained 0.01 M sodium nitrate and 5 mM MES at pH 6.00. For three experiments conducted with an approximately one hour reactor residence time, calcium nitrate was also included in the influent solutions at 0, 10, or 100 μM concentrations. Experiments with the 0 and 100 μM influent calcium

concentrations were also performed with half hour reactor residence times. If autunite were the solid that was dissolving in the reactors, then the presence of calcium in the influent solution would decrease the dissolution rate. Flow to the reactors was controlled by a peristaltic pump and stirring was provided by a magnetic stir bar and stir plate.

7.2.3 Analytical Methods

Uranium, calcium and phosphorus concentrations in solution were determined by inductively coupled plasma mass spectrometry (ICP-MS) with a Hewlett Packard HP4500 instrument. Thallium was used as an internal standard in ICP-MS analysis in order to compensate for drift in instrument sensitivity. Calibration was performed with commercially available standard solutions for uranium (Alfa Aesar), calcium (Fisher), and thallium (SPEX Chemical) and with a phosphorus standard prepared from sodium phosphate dibasic ($\text{Na}_2\text{HPO}_4 \cdot 7\text{H}_2\text{O}$) (EM Science). Solution pH was measured with a Ross glass electrode and Orion 720A pH meter.

The synthesized and partly-reacted solids were characterized and identified by X-ray powder diffraction (XRD), scanning electron microscopy (SEM), Raman spectroscopy, and BET surface area analysis. XRD analyses were performed on a Scintag Pad V X-ray powder diffractometer with a Cu k-alpha X-ray source and germanium detector. SEM images were collected on gold-coated samples with a Camscan Series II scanning electron microscope. Raman spectra were measured with a 782 nm diode laser on a Renishaw MicroRaman Spectrometer with a spectral resolution of 1 cm^{-1} . Samples for Raman analysis were prepared by evaporating an aliquot of concentrated suspension on glass microscope slides. The surface area was determined on

freeze-dried samples by BET N₂ adsorption using a Micromeritics Gemini surface area analyzer.

7.3 Results

7.3.1 Characterization of Synthesized Solids

The synthesis yielded a suspension of readily settleable pale yellow particles. A trace amount of much larger translucent yellow-green crystals was also visible. The suspension was divided between two bottles, with one of them containing no visible crystals of the larger phase. The more visibly homogenous suspension was used in all dissolution experiments. Total concentrations of 74.3 mM uranium, 70.4 mM phosphorus, and 11.1 mM calcium were measured on digested solids from the stock suspension, and dissolved concentrations of 0.03 mM uranium, 2.10 mM phosphorus, and 0.14 mM calcium were measured for filtered stock suspension. The elemental composition of the solid was determined by taking the difference between total and dissolved concentrations, yielding a molar ratio of uranium to phosphorus to calcium of 6.8:6.3:1. Both autunite and hydrogen uranyl phosphate have a uranium to phosphorus ratio of 1:1, and uranyl phosphate has a ratio of 3:2. By assuming that all of the calcium is present as autunite and distributing the remaining uranium and phosphorus between hydrogen uranyl phosphate and uranyl phosphate, the distribution of uranium among the three phases can be calculated. On a uranium molar basis the ratio of autunite to hydrogen uranyl phosphate to uranyl phosphate is 0.63:1.00:0.52. Clearly the autunite synthesis was incomplete.

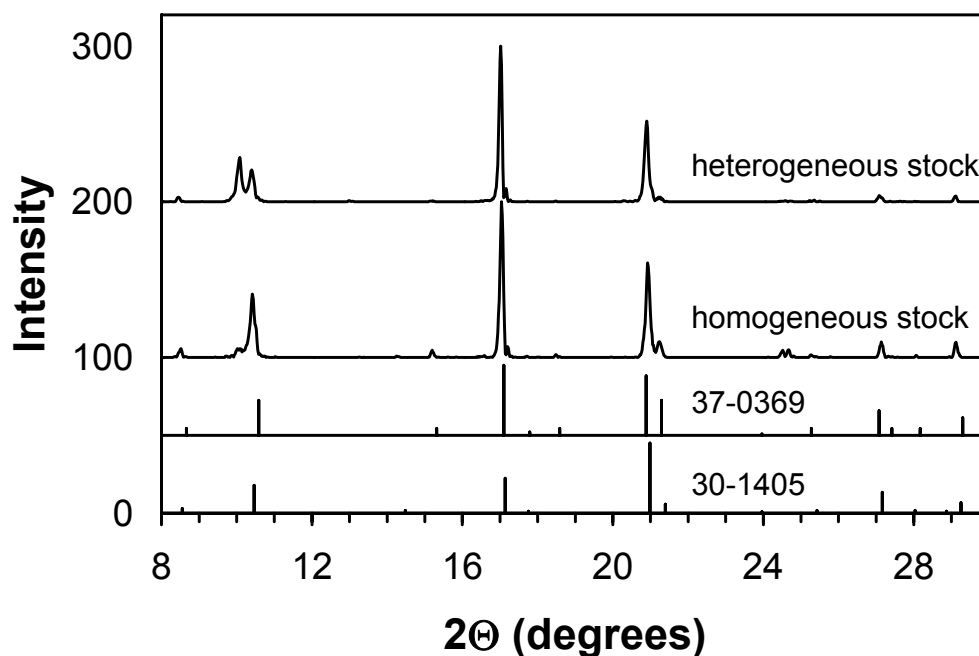


Figure 7.2: X-ray diffraction patterns of the synthesized uranyl phosphate solids and the reference patterns that provide the closest matches. The stock suspension of synthesized solids was split into one batch containing similarly sized and colored particles (homogeneous), and another containing a minor component of larger and greener particles (heterogeneous). Both reference cards 37-0369 and 30-1405 are identified as uranyl phosphate hydrate $((\text{UO}_2)_3(\text{PO}_4)_2 \cdot (4-4.8)\text{H}_2\text{O})$.

X-ray diffraction patterns (Fig. 7.2) of the synthesized solids from both the homogeneous stock suspension and the suspension with trace amounts of the larger yellow-green crystals were collected to identify the synthesized solids. Solids from the homogeneous suspension have X-ray diffraction patterns with three dominant peaks at 2θ values of 10.4° , 17.0° , and 20.9° , corresponding to lattice spacings of 8.50, 5.20, and 4.24 Å. The same peaks are seen for the heterogeneous suspension, but with an additional significant peak at 10.1° (8.78 Å). The large number of reference patterns in the JCPDS database (JCPDS-ICDD, 1999) makes identification a challenge. Of the more than forty reference cards of phases consisting of uranium, oxygen, hydrogen,

Table 7.3: Experimental and reference X-ray diffraction lattice spacings.

Card #	Name/Formula	Dominant Diffraction Maxima (Å) (indexed reflection)			
	Homogeneous stock suspension	8.48	5.20	4.24	3.28
	Heterogeneous stock suspension	8.78	8.50	5.21	4.25
	Batch dissolution residual solids	8.63	5.20	4.32	4.24
13-0061	hydrogen uranyl phosphate hydrate $\text{UO}_2\text{HPO}_4 \cdot x\text{H}_2\text{O}$	8.64	5.19	4.22	3.26
29-0670	chernikovite, synthetic $\text{H}_2(\text{UO}_2)_2(\text{PO}_4)_2 \cdot 8\text{H}_2\text{O}$	8.57 ₍₀₀₁₎	3.68 ₍₁₀₂₎	3.50 ₍₂₀₀₎	3.25 ₍₂₀₁₎
30-1405	uranyl phosphate hydrate $(\text{UO}_2)_3(\text{PO}_4)_2 \cdot 4.8\text{H}_2\text{O}$	8.45 ₍₀₀₂₎	5.17 ₍₁₀₃₎	4.23 ₍₃₀₁₎	3.28 ₍₄₀₀₎
33-1428	hydrogen uranyl phosphate hydrate $\text{UO}_2\text{HPO}_4 \cdot x\text{H}_2\text{O}$	5.22	4.25	4.20	3.54
37-0284	uranyl phosphate hydrate $(\text{UO}_2)_3(\text{PO}_4)_2 \cdot 4\text{H}_2\text{O}$	8.75 ₍₀₀₂₎	3.71 ₍₁₀₄₎	3.51 ₍₂₀₀₎	3.25 ₍₂₀₂₎
37-0369	uranyl phosphate hydrate $(\text{UO}_2)_3(\text{PO}_4)_2 \cdot 4\text{H}_2\text{O}$	5.18	4.25	4.17	3.29
39-1351	meta-autunite 9Å $\text{Ca}(\text{UO}_2)_2(\text{PO}_4)_2 \cdot 3\text{H}_2\text{O}$	8.46 ₍₀₀₁₎	5.39 ₍₁₀₁₎	4.23 ₍₀₀₂₎	3.62 ₍₁₀₂₎

phosphorus, calcium, or sodium, eighteen of them have significant diffraction peaks corresponding to at least one of the four dominant peaks of the synthesized solids. The best matches to the homogeneous suspension are for uranyl phosphate hydrate phases referenced by cards 30-1405 and 37-0369. The 8.78 Å peak found at low intensity for the homogeneous suspension and at higher intensity for the heterogeneous suspension is only found for card 37-0284, another uranyl phosphate hydrate. The next best matches for the material are for cards 39-1351 (meta-autunite 9Å) and 33-1428 (hydrogen uranyl phosphate hydrate). Table 7.3 presents the locations of the diffraction maxima for the collected and referenced patterns discussed above.

Four references in the database are labeled as synthetic chernikovite, but none match the collected diffraction patterns. The stoichiometries of chernikovite and hydrogen uranyl phosphate hydrate are identical, and no structural basis is available for

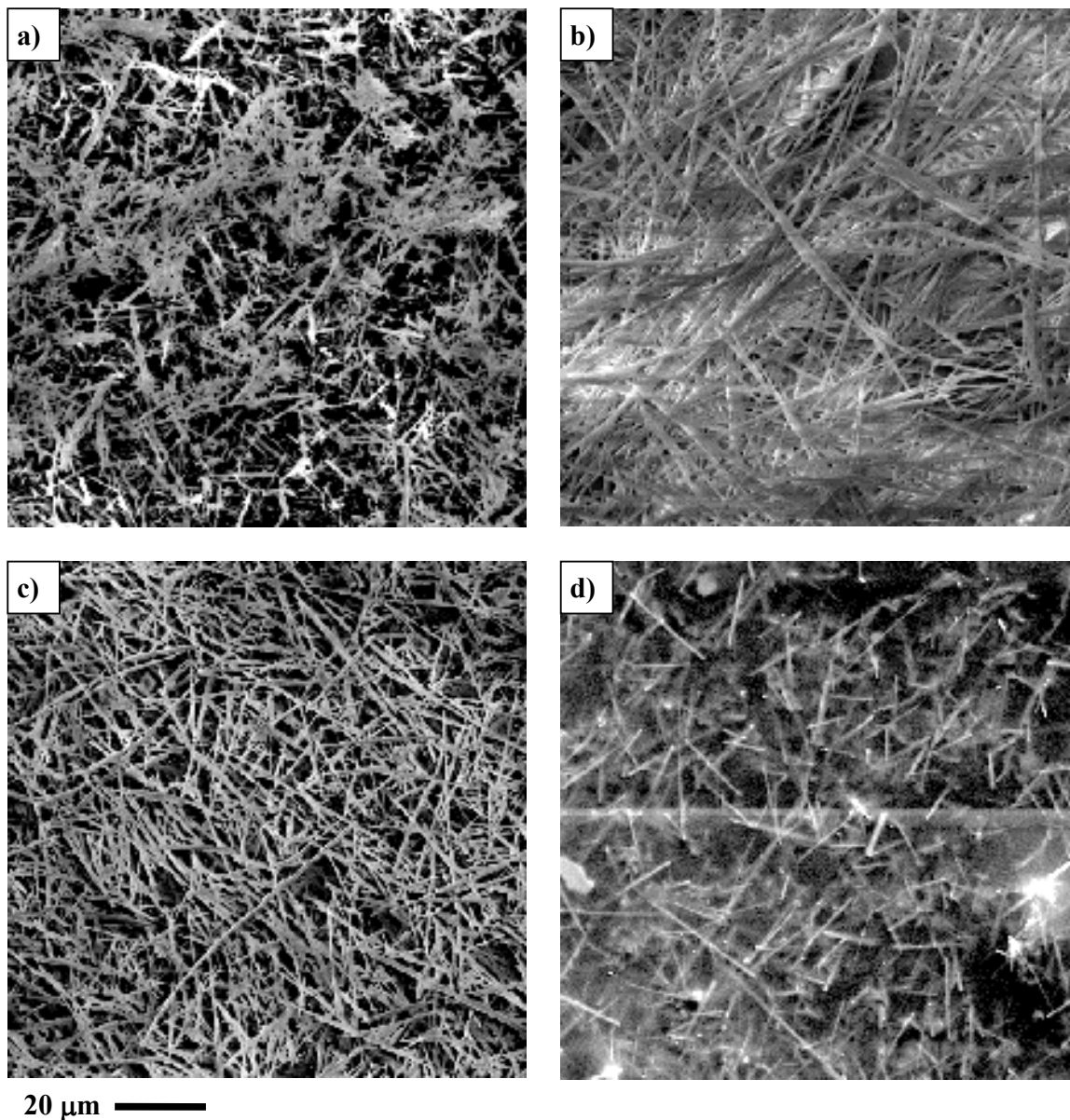


Figure 7.3: Scanning electron micrographs of visibly homogeneous uranyl phosphate stock suspension (see p. 7-9) (a) and solids subjected to batch dissolution conditions after 1 hour (b), 193 hours (c), and 1350 hours (d).

distinguishing between the two phases or determining whether the phases are actually different. There is a large variation for the XRD patterns between phases labeled as synthetic chernikovite and phases labeled as hydrogen uranyl phosphate as well as variation among patterns for phases with the same label. This range of XRD patterns

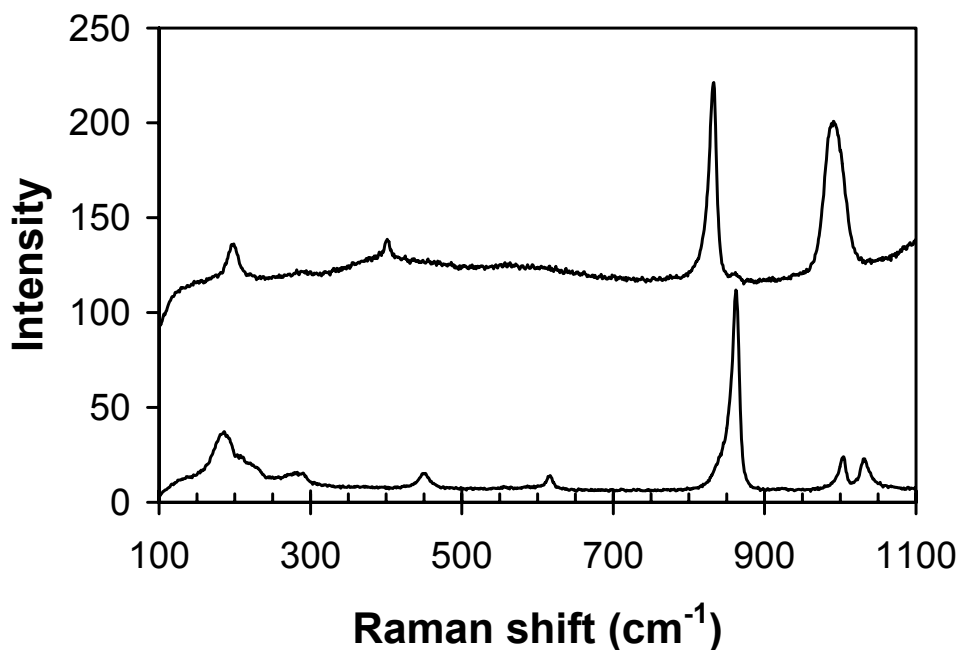


Figure 7.4: Raman spectra of solids from the visibly homogeneous uranyl phosphate stock suspension (bottom) and of residual solids five months after the conclusion of batch dissolution experiments (top). The dominant peak between 800-900 cm^{-1} is from the symmetric stretch of the uranyl ion. The peak(s) between 950-1050⁻¹ are either the ν_3 phosphate stretch and/or the uranyl symmetric stretch.

suggests that a variety of structures are possible for hydrogen uranyl phosphate phases.

Differences among phases may arise from differences in the formation temperature, pressure, and pH.

The crystals formed during the synthesis are long needle-like crystals. Scanning electron micrographs of the stock material and solids subjected to batch dissolution experiment conditions are presented in Figure 7.3. The highest quality images are those collected 1 hour and 193 hours into batch dissolution, and these show crystals about 20-40 μm long. The poor quality of the image of the stock material may be due to the presence of some amorphous phase, or simply to a higher loading of solids which would

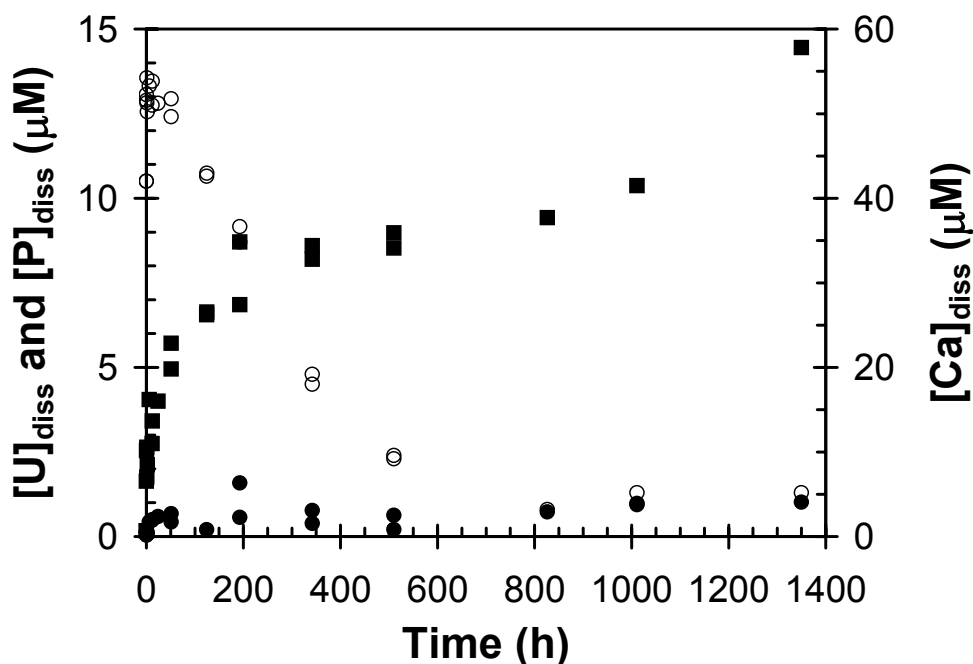


Figure 7.5: The evolution of dissolved concentrations of uranium (●), phosphorus (○), and calcium (■) in two batch dissolution experiments. Dissolution experiments were open to the atmosphere, buffered at pH 6.0 through the inclusion of 5 mM MES buffer, and with 0.01 M NaNO₃. The batch reactors contained total concentrations of 370 μM uranium, 350 μM phosphorus, and 55 μM calcium.

lead to a decreased ability to resolve individual crystals. The surface area of the freeze-dried solids from the homogeneous stock suspension is 2.11 m² g⁻¹.

The Raman spectrum of the solids from the homogeneous stock suspension (Fig. 7.4 lower curve) contains peaks corresponding to both uranyl and phosphate peaks. The strong peak at 862.3 cm⁻¹ is attributed to the symmetric stretch of the uranyl ion. Uranyl bending vibrations are also associated with the lower energy peaks at 185.9, 282.8, and 290.2 cm⁻¹. Phosphate vibrations are assigned to the peaks at 415.8, 1004.5, and 1031.5 cm⁻¹. Peak assignments are consistent with those of other uranyl phosphate minerals (Cejka, 1999).

7.3.2 Batch Dissolution

The evolution of dissolved concentrations of uranium, phosphorus and calcium in duplicate batch experiments is presented in Figure 7.5. The dissolved concentrations in the stock suspension were measured immediately before the stock aliquots were added to batch reactors, and can be used to calculate instantaneous dissolved concentrations at the beginning of the experiments of $0.13 \mu\text{M}$ uranium, $10.5 \mu\text{M}$ phosphorus, and $0.67 \mu\text{M}$ calcium. The dissolved concentrations then evolved from these initial values. Uranium release to solution was small with dissolved concentrations varying over the course of the experiment from 0.04 to $1.58 \mu\text{M}$. In both experiments, the highest uranium concentrations occurred after 8 days of dissolution and decreased from there. The final dissolved uranium concentration in the long-term (56 day) reactor was $1.02 \mu\text{M}$.

Calcium was completely released over the duration of the experiments, culminating at a dissolved concentration of $57.8 \mu\text{M}$ after 1350 hours. The final dissolved calcium concentration was approximately equal to the total concentration of $55.3 \mu\text{M}$, which was estimated from the measured calcium content of the stock suspension. Coincident with the release of calcium from the solid was the uptake of phosphorus by the solid. The dissolved concentration of phosphorus was highest ($13\text{-}14 \mu\text{M}$) in the first hour of the experiment and gradually decreased until a stable value of approximately $1 \mu\text{M}$ ($0.8\text{-}1.3 \mu\text{M}$) was reached after 826 hours. The initial pH was buffered at pH 6, but was not subsequently measured or adjusted. In order to maintain electroneutrality, protons were probably removed from solution as calcium was released to and phosphate (H_2PO_4^- is the dominant species at pH 6) was removed from solution, thereby resulting in an increase in the pH.

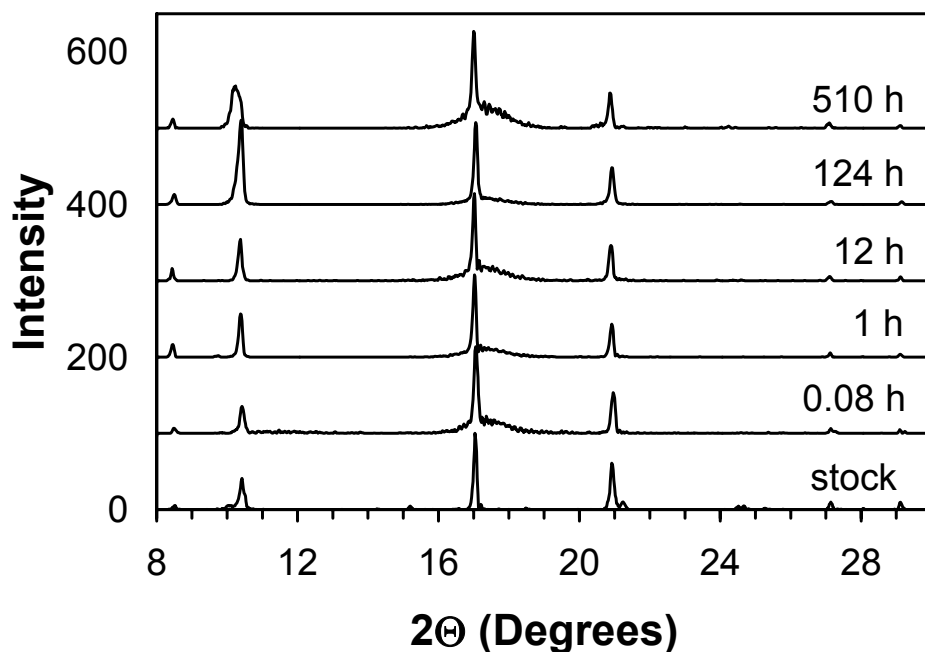


Figure 7.6: Time-series of X-ray diffraction patterns of filtered solids collected during the batch dissolution process and a reference pattern for hydrogen uranyl phosphate. The broad peak from 17-19° is due to the polycarbonate filter membranes.

Remarkably, the dramatic changes in the dissolved phosphorus and calcium changes were not associated with major changes in the morphology of the solid. Scanning electron micrographs of the material subjected to dissolution (Fig. 7.3) for varying amounts of time show no changes in the general shape or length of the needle-like crystals. Although the resolution is poor for the image of the material that had undergone dissolution for 1350 h, this is not likely to be the result of structural changes in the material.

A time-series of X-ray diffraction patterns (Fig. 7.6) of the solids collected from the batch reactors displays only minor changes. Dominant peaks at 8.44° (10.37 Å), 17.01° (5.21 Å), and 20.89° (4.24 Å) persisted throughout the dissolution process. The broad peak centered at 17.4° is generated by the polycarbonate filter membranes upon

which the analyzed solids are loaded. The most significant change is the shift and growth of a peak from 10.4° (8.50 Å) to 10.2° (8.63 Å), which is quite apparent in the 510 hour sample. This shift is even more pronounced in an XRD pattern of residual solids from the batch reactors analyzed after 9 months of storage in a concentrated suspension. Other changes are the disappearances of the small shoulder peaks in the stock suspension at 10.09° (8.76 Å) and 21.24° (4.18 Å) upon initiation of the dissolution experiment.

In contrast to the SEM and XRD data, the Raman spectrum of residual solids from the experiment is dramatically different from the spectrum of the stock suspension. The symmetric stretch of the uranyl moiety shifts from 862.3 to 832.6 cm^{-1} , and the two discrete phosphate bands around 1000 cm^{-1} in the stock suspension appear to have merged into a single broad peak at 990 cm^{-1} . The position and width of the peak at 990 cm^{-1} suggest that it might also be due to the antisymmetric stretch of the uranyl moiety, which could have become activated by symmetry lowering as the solid phase transformed. It should be noted that the Raman spectrum of the solids from the batch reactor was collected six months after the conclusion of the batch experiments, and may reflect structural changes during that period that were not probed by SEM or XRD.

7.3.3 Flow-through Dissolution

The objective of flow-through experiments was to quantify dissolution rates under steady-state conditions. In all five flow-through experiments, the dissolved concentrations of uranium and phosphorus stabilized at constant values within 10-20 reactor volumes (Fig. 7.7). While the pH and ionic strength in the reactors were the same for all five reactors, the influent calcium concentration and the reactor residence time

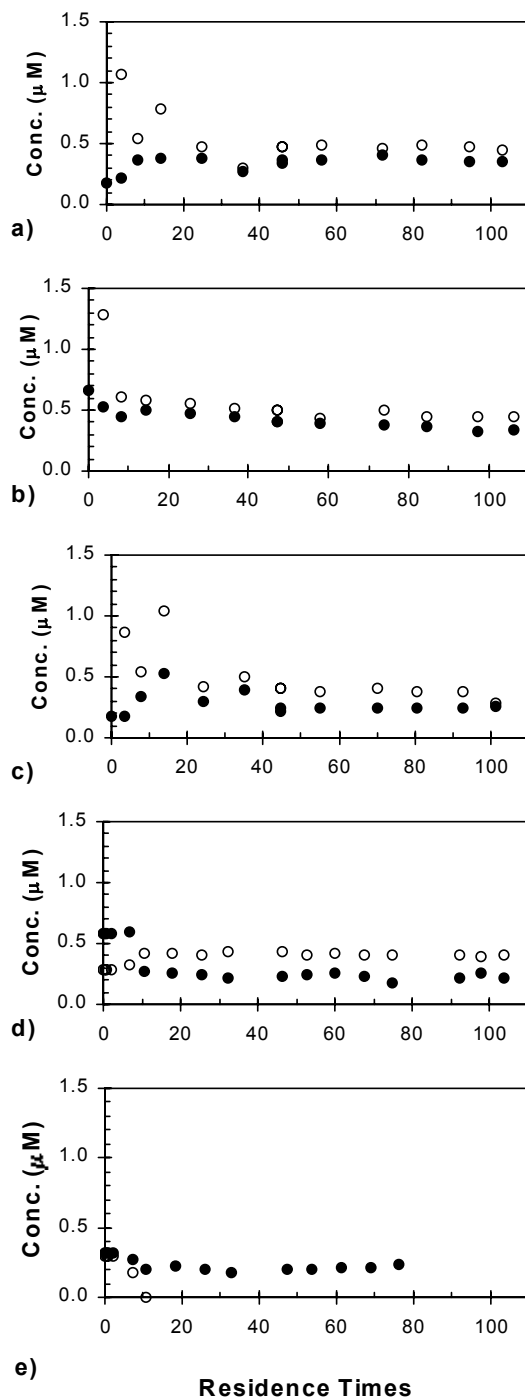


Figure 7.7: Effluent uranium (●) and phosphorus (○) concentrations from flow-through dissolution reactors. Influent to all reactors contained 0.01 M NaNO_3 and were buffered at pH 6 with 5 mM MES buffer. The influent calcium concentration and reactor residence time varied for each experiment (numbered as in Table 7.4): a) Expt. 3: $[\text{Ca}]_{\text{inf}} = 0 \mu\text{M}$, $t_{\text{res}} = 1 \text{ h}$; b) Expt. 4: $[\text{Ca}]_{\text{inf}} = 10 \mu\text{M}$, $t_{\text{res}} = 1 \text{ h}$; c) Expt. 5: $[\text{Ca}]_{\text{inf}} = 100 \mu\text{M}$, $t_{\text{res}} = 1 \text{ h}$; d) Expt. 6: $[\text{Ca}]_{\text{inf}} = 0 \mu\text{M}$, $t_{\text{res}} = 0.5 \text{ h}$; e) Expt. 7: $[\text{Ca}]_{\text{inf}} = 100 \mu\text{M}$, $t_{\text{res}} = 0.5 \text{ h}$.

Table 7.4: Conditions and calculated dissolution rates of flow-through dissolution experiments. All reactors were operated at pH 6.00 and with an influent containing 0.01 M NaNO₃ and 5 mM MES buffer. The total uranium concentration in each reactor was 1.26-1.36 mM, primarily associated with the solid phase.

Expt. (#)	[Ca] _{inf} (μM)	t _{res} (h)	Avg. Steady-state Conc.		Avg. Release Rates	
			[U] _{eff} (μM)	[P] _{eff} (μM)	U	P
					(μmol m ⁻² h ⁻¹)	
3	0	1.01-1.04	0.27-0.40	0.30-0.78	0.34 ± 0.03	0.44 ± 0.06
4	10	0.98-1.01	0.33-0.50	0.44-0.61	0.42 ± 0.05	0.49 ± 0.04
5	100	1.02-1.05	0.22-0.39	0.28-0.50	0.26 ± 0.05	0.38 ± 0.06
6 ^a	0	0.51-0.53	0.17-0.27	0.39-0.42	0.46 ± 0.06	0.81 ± 0.03
7 ^b	100	0.50-0.51	0.18-0.22	0.00-0.00	0.43 ± 0.03	≤ 0.40

^a continuation of experiment #3; ^b continuation of experiment #5

varied. The conditions for the five experiments and the corresponding steady-state effluent concentrations and dissolution rates are given in Table 7.4. The dissolved phosphorus concentration in experiment #7 (Fig 7.7) fell below the detection limit (0.2 μM) after ten residence times. Calcium concentrations were also measured and matched influent concentrations (data not shown). For experiment #3 (Fig. 7a; 0 μM influent calcium), the effluent calcium concentration had dropped below the detection limit (1 μM) within 4 residence times.

Dissolution rates are calculated from the steady-state reactor conditions using the following equation:

$$\text{Rate} = \frac{C}{t_{\text{res}}} \frac{1}{S \cdot A}, \quad (1)$$

where C is the effluent uranium concentration (μM), t_{res} is the hydraulic residence time of the reactor (h), S is the mass concentration of solid in the reactor (g L⁻¹), and A is the specific surface area of the solid (m² g⁻¹). The dissolution rate was calculated at each sampling point, and the average value and standard deviation in each experiment for the period corresponding to steady-state are reported.

The uranium release rates (for corresponding experiments) increase as the residence time is decreased from 1 to 0.5 h, suggesting that the dissolution reaction is inhibited by the accumulation of dissolution products in the reactor for experiments with a 1-h residence time (and probably for those with a 0.5 h residence time as well). No systematic effect of calcium in the reactor influent on dissolution rates was observed. With a 1-h residence time, dissolution rates (based either on U or P release) were higher with 10 mM Ca than without Ca in the influent but lower with 100 mM Ca. With a 0.5-h residence time, the U release rate was the same with 100 mM Ca as without Ca while the P release rate was lower with 100 mM Ca. The release rates of P (which ranged from 0.38 to 0.81 $\mu\text{mol m}^{-2} \text{h}^{-1}$) were more variable than those of U (which ranged from 0.26 to 0.46 $\mu\text{mol m}^{-2} \text{h}^{-1}$). Roughly congruent dissolution was observed in experiments 3-5 but, in experiment 6, the release rate of P was approximately double that of U.

7.4 Discussion

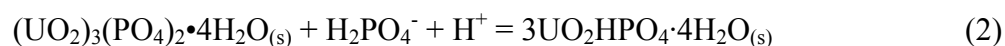
7.4.1 Evolution of Calcium-Uranyl-Phosphate Solid Toward Equilibrium

The peculiar evolution of the dissolved concentrations of calcium, phosphorus, and uranium over the eight weeks of batch dissolution will first be examined based on equilibrium constraints of the system. This approach may yield insights into the identity of the phase or phases present initially and those present at the conclusion of the experiment.

The most striking feature of batch dissolution is the complete release of calcium from the solid phase and the concurrent uptake of phosphorus. The release of calcium

occurs on a time-scale of days, and the mechanism of release is probably the dissolution of a trace calcium-containing phase or the diffusion of calcium from interlayer spaces, perhaps by exchange with sodium or hydronium ions. The final phase present must be a uranyl phosphate hydrate, hydrogen uranyl phosphate hydrate, or sodium uranyl phosphate hydrate because the calcium has been leached entirely from the solid. While calcium is released completely, the bulk of both uranium and phosphorus in the system is associated with the solid phase. By difference between the total and dissolved concentrations of uranium and phosphorus, the elemental composition of the solid phase can be determined. The solid phase present at the initiation of batch dissolution experiments had a uranium:phosphorus ratio of 1:0.92 and the ratio of the solids at the conclusion of the experiments had a ratio of 1:0.95. The distribution of uranium among autunite, hydrogen uranyl phosphate, and uranyl phosphate in the stock suspension was previously determined with a molar ratio of 0.63:1.00:0.52. Following the same approach for the solids in the batch reactor at the conclusion of the experiments, the ratio is calculated as 0.00:1.00:0.18. The final phase is most consistent with a hydrogen uranyl phosphate hydrate, and the XRD pattern is in good agreement with a reference pattern identified as such (card 13-0061). No good matches are found with reference patterns for sodium autunite.

The XRD and solution data indicate that the hydrogen uranyl phosphate hydrate was present initially and grew as uranyl phosphate hydrate and autunite were transformed by the following reactions:



Reaction 2 accounts for the uptake of phosphorus by the solid, while reaction 3 offers a mechanism for calcium release to solution. The batch system was strongly buffered at pH 6 with 5 mM MES, but some pH drift probably occurred as protons were consumed in both reactions 2 and 3. The uptake of approximately 10 μM dissolved inorganic phosphorus (H_2PO_4^- at pH 6) and the release of 55 μM Ca^{2+} should consume 120 μM of protons. In 5 mM MES ($\text{pK}_a = 6.1$) solution, this consumption of acid would increase the pH from 6.00 to 6.04.

If the solubility-controlling solid is indeed a hydrogen uranyl phosphate hydrate, the equilibrium solubility product (eqn. 5) for the following reaction can be calculated:



$$K_{sp} = \{\text{H}^+\} \{\text{PO}_4^{3-}\} \{\text{UO}_2^{2+}\} \quad (5)$$

Where K_{sp} is the solubility product in terms of activities (i.e., extrapolated to zero ionic strength) at 25°C and 1 atm pressure. Values for K_{sp} are calculated for the final pH of 6.0 and dissolved uranium and phosphorus concentrations of 1.02 and 1.30 μM respectively. By using the database for dissolved species given in Table A.1, the phosphate and uranyl ion concentrations are calculated to be $7.48 \cdot 10^{-14}$ and $8.61 \cdot 10^{-8}$ M respectively. Using those values and correcting for the ionic strength of 0.01 M with the Davies equation, a $\log K_{sp}$ of -26.8 is calculated. This value is markedly lower than the published values of -24.2 (Grenthe et al., 1992) and -22.7 (Van Haverbeke et al., 1996). The value of -22.7 was determined from measurements exclusively below pH 1.5, and the XRD pattern and crystal morphology of the material are completely dissimilar to that of the solid used in the current work (Van Haverbeke et al., 1996). The studies used for obtaining the -24.2 value were also conducted in acidic media. No reliable published solubility product is

available near the conditions studied in this work. No attempt to model the equilibrium with either of the uranyl phosphate hydrate solubility products has been attempted because the composition of the solid is not consistent with such a phase.

7.4.2 Dissolution Rate Quantification

Flow-through dissolution experiments are complementary to batch experiments and allow a better quantification of dissolution rates when undersaturated conditions can not be maintained in batch experiments. The calcium release and phosphate uptake are well resolved in the batch dissolution experiments, but the changes in the dissolved uranium concentrations with time are far too small to allow for rate calculations. In flow-through experiments, the dissolution rate of the solid was calculated using the release of either uranium or phosphorus from the solid phase. For congruent dissolution of hydrogen uranyl phosphate hydrate, the release rates of uranium and phosphorus would be identical, and for uranyl phosphate hydrate the uranium release rate would be 1.5 times that of phosphorus. In all but one of the flow-through dissolution experiments, the phosphorus release rate is actually higher than that of uranium. This observation can not be explained by any form of congruent dissolution; however, it should be emphasized that in several cases the uranium and phosphorus release rates were in agreement when considering the error estimates for the release rates. No simple explanation is available for the phosphorus release rate that is nearly double the uranium release rate in experiment #6. It is possible that the phosphate was released from the solid and that the uranium was retained in a uranyl oxide hydrate phase; however, the uranyl oxyhydroxides are generally more soluble than the uranyl phosphates.

Little or no effect of the influent calcium concentration on the uranium release rate was observed. This observation is consistent with the identification of the dissolving solid as a calcium-free uranyl phosphate or hydrogen uranyl phosphate phase. There is also no effect of calcium on the phosphate release rate for one hour residence experiments. The detection limit for phosphorus makes it difficult to determine phosphorus release rates at the shorter half hour residence time.

The maximum dissolution rate as measured by uranium release is $0.46 \mu\text{mol m}^{-2} \text{h}^{-1}$, but this may only be a lower limit. The accumulation of dissolution products in the flow-through reactors decreases the driving force of the dissolution reaction, and consequently decreases the dissolution rate. If dissolution were occurring far from equilibrium and dissolution were surface-controlled, then the dissolution rates would be equal for the two different reactor residence times. Using the average values for experiment #6 ($[\text{U}]_{\text{diss}} = 0.235 \mu\text{M}$; $[\text{P}]_{\text{diss}} = 0.411 \mu\text{M}$), the reaction quotient for reaction 4 is $10^{-27.79}$. Relating this reaction quotient to the equilibrium solubility constant determined in batch dissolution experiments yields a free energy for the dissolution reaction of only -5.8 kJ mol^{-1} . In a similar calculation, the free energy of the dissolution reaction in experiment #3 (rate = $0.34 \mu\text{mol m}^{-2} \text{h}^{-1}$) is only -4.4 kJ mol^{-1} . For conditions further from saturation than those of experiment #6, the free energy of the reaction would be greater than -5.8 kJ mol^{-1} and the dissolution rate would correspondingly be higher. The current experimental approach is limited by the minimum flow-through reactor residence time of 30 minutes.

Despite providing only a conservative estimate for the dissolution rate, the rate of uranyl phosphate dissolution is convincingly slower than for a uranyl silicate and a uranyl

oxide hydrate studied in related experiments. On a mass basis, the maximum uranyl phosphate dissolution rate of $0.97 \mu\text{mol g}^{-1} \text{h}^{-1}$ is significantly lower than that of the uranyl silicate soddyite ($2.07 \mu\text{mol g}^{-1} \text{h}^{-1}$) or uranyl oxide hydrate schoepite (rate $> 9 \mu\text{mol g}^{-1} \text{h}^{-1}$). When normalized to surface area, the difference among the minerals is not as striking but the dissolution rate of uranyl phosphate is still the lowest of the three phases.

7.4.3. Environmental Implications

Uranyl phosphates have both low solubilities and low dissolution rates as compared to other uranyl minerals. These two properties make uranyl phosphates important phases for sequestering uranium when sufficient phosphate concentrations are present. The formation of uranyl phosphates at contaminated sites may maintain both the uranium concentration in the porewater and the rate of uranium release to the porewater at values that are low enough to mitigate the problem of uranium contamination. The removal of uranium from contaminated soils by soil-washing processes is expected to be considerably slower in soils with high phosphate levels than in soils with low phosphate levels. Nonetheless, bicarbonate has been demonstrated as an effective extractant for both contaminated soils (Francis et al., 1999) and a synthetic meta-autunite (Sowder, 1998).

As expected, the solution chemistry dictates the formation of specific phases; however, the formation of certain phases may be kinetically hindered. Despite the exposure of the originally synthesized hydrogen uranyl phosphate hydrate to high calcium concentrations at elevated temperatures, only a small portion of the solid was

converted to an autunite-like calcium uranyl phosphate phase. The transition between hydrogen uranyl phosphate hydrate and uranyl phosphate hydrate phases is also ill-defined. It is likely that uranyl phosphates in contaminated environments may be transformed from one uranyl phosphate phase to another depending on the solution pH and cation composition. The distinction between phases may not be important if different uranyl phosphate phases have comparable solubilities and are all relatively insoluble compared with other uranyl minerals.

Chapter 8

Conclusions

8.1 Summary of Experimental Work

8.1.1 Uranium Uptake on Mineral Surfaces

Adsorption and desorption of uranium to goethite was rapid, occurring on time-scales shorter than a minute. Rapid sorption rates of uranium on goethite were independent of the method of investigation: adsorption following uranium addition, dilution-induced desorption, fluoride-induced desorption, and near-equilibrium surface-solution isotope exchange. Rapid rates of adsorption and desorption of uranium to montmorillonite were also observed.

Uranium sorption on goethite at pH 6 and relatively high ionic strength (0.1 M) was modeled with the Langmuir isotherm, using a maximum sorbed uranium concentration of $114 \mu\text{mol g}^{-1}$. Sorption was generally reversible though some irreversibility was observed with aged uranium-goethite suspensions. Sorption on montmorillonite was consistent with a Langmuir isotherm at pH 6 and high ionic strength but, at lower pH and ionic strength, the data were better fit with a Freundlich isotherm.

Metastable uranium sorption on goethite was observed, in which the dissolved uranium concentration was controlled by sorption even when supersaturated with respect to a uranium-containing precipitate. The metastable sorption-control of dissolved uranium concentrations in excess of a solubility limit persisted for as long as 30 days. Ultimately, metastable sorption was followed by the formation of a precipitated phase,

which subsequently controlled the dissolved uranium concentration. The uranium-containing precipitate was identified as a schoepite-like uranyl oxide hydrate phase by X-ray diffraction, and its spatial relationship to goethite was studied with scanning electron microscopy (SEM) and transmission electron microscopy (TEM). SEM showed an increasingly heterogeneous uranium spatial distribution with both increasing contact time and increasing uranium content. Uranium-containing precipitates and goethite particles were observed in close proximity with TEM. Discrete uranium-containing particles were observed for high uranium contents and long contact times, and low-crystallinity uranium clusters on goethite particles were observed for a shorter contact time.

8.1.2 Dissolution and Transformation of Uranyl Minerals

The rates of dissolution of schoepite, soddyite, and hydrogen uranyl phosphate were quantified in flow-through reactors. The maximum soddyite dissolution rate ($0.70 \mu\text{mol U m}^{-2} \text{ h}^{-1}$) is somewhat faster than the maximum rate for hydrogen uranyl phosphate ($0.46 \mu\text{mol m}^{-2} \text{ h}^{-1}$) when normalized to surface area. Schoepite dissolution is much faster, nearing equilibrium within one hour in batch experiments; a lower limit for the rate ($1.58 \mu\text{mol m}^{-2} \text{ h}^{-1}$) is provided by flow-through experiments.

In batch dissolution experiments, dissolution of a single solid phase to equilibrium with the starting solid was the exception and dissolution followed by precipitation of a secondary phase was the rule. In both schoepite and soddyite systems with as little as 10 mM sodium, a sodium uranyl oxide hydrate ($\text{Na}(\text{UO}_2)\text{O}(\text{OH})_{(s)}$) formed as a secondary phase and, in schoepite suspensions with as little as 1 mM cesium, a cesium uranyl oxide hydrate ($\text{Cs}_3[(\text{UO}_2)_{12}\text{O}_7(\text{OH})_{13}] \cdot 3\text{H}_2\text{O}_{(s)}$) formed. The layered structure of schoepite and

the affinity of schoepite for alkali and alkaline earth cations favor secondary phase formation through the solid-state transformation of the original solid. The transformation mechanism in systems with soddyite, a phase with a compact framework structure, probably proceeds by release of uranium from soddyite to solution and the subsequent precipitation of uranium from solution as $\text{Na}(\text{UO}_2)\text{O}(\text{OH})_{(\text{s})}$. The dissolution of hydrogen uranyl phosphate (which remained after the attempted synthesis of autunite) involved the release of calcium from either sorption sites or a minor autunite phase and the concurrent uptake of phosphate from solution.

The sequential formation of solids of increasing stability is consistent with the Ostwald Step Rule, which postulates that the most soluble solids precipitate first because of their lower interfacial surface energies. The equilibrium solubility of the fine particles studied, particularly in schoepite suspensions, may also be affected by the interfacial surface energy. The growth of particles over the course of experiments (enhanced in the presence of sodium or cesium) coincided with a decrease in the dissolved uranium concentration.

Characterization of systems undergoing dissolution and transformation was only fully accomplished through the integration of analytical techniques offering information at a variety of spatial scales. The best example of this integrated analytical approach is the identification of $\text{Na}(\text{UO}_2)\text{O}(\text{OH})_{(\text{s})}$ formation in soddyite suspensions. X-ray diffraction initially suggested the formation of a crystalline phase distinct from soddyite, SEM images showed the formation over time of needle-like crystals different than the blocky soddyite crystals, and Raman spectra confirmed XRD identification of the solid as

$\text{Na}(\text{UO}_2)\text{O}(\text{OH})_{(s)}$. Raman spectra also proved particularly diagnostic in identifying changes in the hydrogen uranyl phosphate solid, which were not observed with XRD.

Sufficient experiments were conducted to allow for the determination of the equilibrium solubilities of the synthetic phases and of some secondary products. The schoepite solubility product of $10^{5.02} - 10^{5.54}$ is within the range of published values. Sodydite solubility is consistent with a previously published solubility product of $10^{5.74}$. The hydrogen uranyl phosphate solid has a solubility product of $10^{-26.77}$, which does not agree with published values for both uranyl phosphate and hydrogen uranyl phosphate solids. The sodium and cesium uranyl oxide hydrates $\text{Na}(\text{UO}_2)\text{O}(\text{OH})_{(s)}$ and $\text{Cs}_3[(\text{UO}_2)_{12}\text{O}_7(\text{OH})_{13}] \cdot 3\text{H}_2\text{O}_{(s)}$ formed in schoepite experiments have solubility products of $10^{7.65}$ - $10^{9.00}$ and $10^{68.3}$ respectively.

8.2 Environmental Implications

8.2.1 Mobility of Uranium at Contaminated Sites

The primary hypothesis of the project, that the rate of uranium release to solution is governed by the speciation of uranium in the solid phase, has been verified. The first distinction is between sorbed and precipitated phases, with uranium release from sorbed phases operating on shorter time-scales. Rapid release from sorbed phases is independent of desorption mechanism or sorption site type; however, in natural environments the occlusion of uranium during mineral diagenesis may lead to slow desorption governed by physical (i.e., diffusive) mass transfer processes. When uranium-containing minerals are present, they will control dissolved uranium concentrations and uranium mobility, and it

is important to identify such mineral phase(s). Uranyl phosphates are well known for their low solubilities, and this work has determined that they also have low dissolution rates. Uranyl silicates may be more soluble than phosphates, but have comparably low dissolution rates. Because schoepite is more soluble and dissolves more readily than other uranyl minerals, it is unlikely that the presence of schoepite would appreciably limit uranium mobility.

The composition of the aqueous phase will determine which solid phases may form, although the most thermodynamically favored phases may not form first. Common groundwater cations, including sodium, can become incorporated in mineral phases and may actually facilitate the formation of lower solubility solids. The presence of fluoride as a strong complexing agent for uranium (VI) in experiments led to rapid desorption of uranium from goethite and rapid dissolution of schoepite, and similar effects are expected in environmental settings with high concentrations of dissolved carbonate, another strong uranium(VI) complexing agent.

In reactive transport modeling, sorption occurs on sufficiently fast time-scales with respect to hydrodynamic processes so that local equilibrium may be assumed at each modeling step. Dissolution and precipitation reactions, however, occur on slower time-scales and reactive transport modeling must account for equilibrium solubilities as well as dissolution and precipitation rates.

The distribution of uranium among various sorbed and precipitated phases will affect the performance of various remediation strategies. Soil washing technologies will be most effective on soils containing only sorbed uranium or uranyl oxide hydrate solid phases, and additional chemicals (e.g., carbonate) should be included if the solubilization

of crystalline uranyl silicates or phosphates is required. Taking advantage of the low solubility and dissolution rate of uranyl phosphate solids, addition of phosphate minerals (e.g., apatite) to contaminated soils may effectively immobilize uranium and control the dissolved uranium concentration at acceptable levels.

8.2.2 Long-term Behavior of Geologic Repositories

The long-term behavior of uranium in a repository will be determined by the dissolution equilibrium and kinetics of $\text{UO}_{2(s)}$ and secondary uranium(VI) phases. Ideally, knowledge of the equilibrium solubilities and dissolution rate laws will enable the construction of a model capable of fitting observed paragenetic sequences and forecasting the long-term distribution of uranium among the dissolved phase and various solid phases. In a similar manner, equilibrium and dissolution rate information can be applied to the interpretation of the distribution of uranium at natural ore deposits.

In either a constructed repository or natural ore deposit, the infiltrating solution will dictate which solid phases form. Dissolved phosphate should lead to the formation of highly insoluble uranyl phosphates, but high phosphate concentrations are not encountered in many systems. Dissolved silica is abundant in essentially all geologic waters, and ultimately uranyl silicates are expected to form. Alkali and alkaline earth cations from solution can incorporate in the interlayer spaces first of schoepite and later of uranyl silicates to form phases like uranophane and boltwoodite. Expected dissolved cations in a repository include fission and decay products (e.g., cesium and strontium) as well as those present naturally. Uranyl minerals may be important phases for the

sequestration of fission products through both sorption and structural incorporation at interlayer positions.

8.3 Suggestions for Future Research

8.3.1 Extension to Different Materials and Solution Compositions

New information and trends would be uncovered by extending the approach used in this work to different mineral sorbents, uranium-containing precipitates, and solution compositions. Studying sorption equilibrium and kinetics of uranium on other iron oxyhydroxides would determine which features are common to all iron oxyhydroxides and which are unique to goethite. Clay minerals other than Na-montmorillonite could be studied to determine general trends and differences among phases.

By studying schoepite, soddyite, and uranyl phosphate, representative phases of three important groups of uranyl minerals were examined, but these three phases are only a fraction of the possible uranyl minerals that may be encountered at contaminated sites and geologic repositories for nuclear waste. Studying a larger set of uranyl oxide hydrate phases with interlayer cations would allow a more mechanistic understanding of schoepite alteration by interlayer cation incorporation. Equilibrium solubility and dissolution rate laws for compregnacite, uranophane, boltwoodite, sklodowskite, and weeksite are crucial to attempts to model the paragenetic sequence. The attempted synthesis of autunite fell far short of completion, and it would be instructive to complete the autunite synthesis and to investigate its dissolution kinetics.

For reasons of consistency and simplicity of interpretation, nearly this entire body of work was conducted at pH 6, rather than over the range of pH values of natural waters (or the wider pH range of contaminated environments). Related to the issue of pH is the concentration of dissolved inorganic carbon, a major factor in uranium mobility in the environment that was not addressed in the current work. By working over a wider range of pH and carbonate concentration, data would be obtained for development of more broadly applicable interpretations of reaction rates and mechanisms.

8.3.2 Phenomena in Aquatic Chemistry

Certain experiments offered insights into interesting general phenomena in aquatic chemistry. The transition from a sorption to a surface precipitation regime in uranium-goethite suspensions is an interesting illustration of non-equilibrium behavior. An understanding and quantification of the reactions and factors governing the transition from sorption to precipitation could be pursued in further research. Uranium-loaded mineral suspensions could be formed under different conditions, for example by evaporative concentration analogous to vadose zone operation. More information about the nature of the solid-associated uranium would allow for distinctions between monomeric surface complexes, polymeric surface complexes, amorphous uranium clusters, and crystalline surface precipitates. Various spectroscopic techniques could be used to probe the surface-association of uranium in hydrated systems, as opposed to the SEM and TEM analyses performed under vacuum. These spectroscopic techniques include Raman and infrared spectroscopy, extended X-ray absorption fine structure

spectroscopy, and luminescence spectroscopy, a technique that may soon be applied to existing samples.

The behavior of multi-solid systems as solid solutions is a remaining frontier in aquatic chemistry, and the uranyl oxide hydrates could be used as a model system for investigating solid solutions. In the current work, sodium and cesium were found to be readily incorporated into the interlayer spaces of the schoepite structure; even with only partial incorporation of the interlayer cation, the solubility of the solid phase dropped precipitously. As a first step in further investigation, better defined alkaline uranyl oxide hydrates should be synthesized and characterized, perhaps by direct precipitation with the appropriate alkaline hydroxide base (e.g., with calcium hydroxide to form becquerelite). Once the endmembers are defined, various mixtures could be studied and interpreted as part of a solid solution. Measuring changes in the concentrations of the alkaline cations in the current work was difficult, nearly impossible in the case of sodium, because of their high background concentrations. By selecting less abundant cations or working with isotopically labeled cations, systems could be evaluated on the basis of overall solution composition and not just on dissolved uranium concentrations.

Effects of interfacial surface energy on the solubility of small particles are suspected in schoepite suspensions. Data relating particle size to solubility for schoepite would be a useful contribution to the existing data available for generalizing the effect. Information on particle size during dissolution experiments would have been useful in the current work, and in future experiments this information could be gained by dynamic light scattering analysis and measurement of the surface area of solids isolated from

dissolution experiments. Ideally, methods for preparing monodisperse suspensions of uranyl mineral particles would also be developed.

8.3.3 Extension to the Field Environment

Because the current project has been exclusively laboratory-based experimentation, direct application of the results to environmental systems is limited. By working with natural materials instead of pure mineral sorbents and synthetic uranyl minerals, aspects of environmental complexity could be addressed. The equilibrium sorption of uranium to heterogeneous natural materials has been interpreted through component additivity and composite approaches, and a similar approach could be followed for sorption rates. Field measurements of the mobility of uranium contamination could serve to constrain reactive transport models. The solid phase characterization techniques applied in the current work could also be applied to the characterization of environmental solids.

The unsaturated conditions and microbial activity in many environmental systems are additional layers of complexity. Uranium contamination frequently occurs in unsaturated soils which are subjected to repeated wetting and drying cycles. Such conditions may lead to redistribution of uranium and formation of uranium-containing precipitates by evaporative concentration. The mobility of uranium in unsaturated systems can be studied in the field and also in analog laboratory systems. The operation of microbial processes in natural systems adds another layer of complexity. A variety of iron reducing and sulfate reducing bacteria are able to reduce uranium(VI) enzymatically to the less soluble uranium(IV). Investigation of the concurrent operation of abiotic

sorption and dissolution processes with microbially mediated redox processes would provide a more comprehensive understanding of the environmental fate and transport of uranium.

References

- Abdelouas A., Lutze W., Gong W., Nuttall E. H., Strietelmeier B. A., and Travis B. J. (2000) Biological reduction of uranium in groundwater and subsurface soil. *The Science of the Total Environment* **250**, 21-35.
- Abdelouas A., Lutze W., and Nuttall H. E. (1999) Uranium Contamination in the Subsurface: Characterization and Remediation. In *Uranium: mineralogy, geochemistry and the environment*, Vol. 38 (ed. P. C. Burns and R. Finch), pp. 433-474. Mineralogical Society of America.
- Allard T., Ildefonse P., Beaucaire C., and Calas G. (1999) Structural chemistry of uranium associated with Si, Al, Fe gels in a granitic uranium mine. *Chemical Geology* **158**, 81-103.
- Allen P. G., Shuh D. K., Bucher J. J., Edelstein N. M., Palmer C. E. A., Silva R. J., Nguyen S. N., Marquez L. N., and Hudson E. A. (1996) Determination of uranium structures by EXAFS: schoepite and other U(VI) oxide precipitates. *Radiochimica Acta* **75**, 47-53.
- Andersson P. S., Porcelli D., Gustafsson Ö., Ingri J., and Wasserburg G. J. (2001) The importance of colloids for the behavior of uranium isotopes in the low-salinity zone of a stable estuary. *Geochimica et Cosmochimica Acta* **65**(1), 13-25.
- Andersson P. S., Porcelli D., Wasserburg G. J., and Ingri J. (1998) Particle transport of U-234-U-238 in the Kalix River and in the Baltic Sea. *Geochimica et Cosmochimica Acta* **62**(3), 385-392.
- Arey J. S., Seaman J. C., and Bertsch P. (1999) Immobilization of uranium in contaminated sediments by hydroxyapatite addition. *Environmental Science and Technology* **33**(2), 337-342.
- Arnold T., Zorn T., Bernhard G., and H. N. (1998) Sorption of uranium(VI) onto phyllite. *Chemical Geology* **151**, 129-141.
- Arnold T., Zorn T., Zänker H., Bernhard G., and Nitsche H. (2001) Sorption behavior of U(VI) on phyllite: experiments and modeling. *Journal of Contaminant Hydrology* **47**(2-4), 219-231.
- Ball J. W. and Nordstrom D. K. (1991) User's manual for WATEQ4F, with revised thermodynamic data base and test cases for calculating speciation of major, trace, and redox elements in natural waters. U.S. Geo. Sur.

- Baran V. (1988) Relation between precipitated and high-temperature sodium uranates. *Journal of Radioanalytical and Nuclear Chemistry, Letters* **128**(2), 155-163.
- Bargar J. R., Reitmeyer R., and Davis J. A. (1999) Spectroscopic confirmation of uranium(VI)-carbonato complexes on hematite. *Environmental Science and Technology* **33**(14), 2481-2484.
- Bargar J. R., Reitmeyer R., Lenhart J. J., and Davis J. A. (2000) Characterization of U(VI)-carbonato ternary complexes on hematite: EXAFS and electrophoretic mobility measurements. *Geochimica et Cosmochimica Acta* **64**(16), 2737-2749.
- Barnett M. O., Jardine P. M., Brooks S. C., and Selim H. M. (2000) Adsorption and transport of uranium(VI) in subsurface media. *Soil Science Society of America Journal* **64**, 908-917.
- Barrow N. J., Gerth J., and Brümmer G. W. (1989) Reaction kinetics of the adsorption and desorption of nickel, zinc and cadmium by goethite. II. Modelling the extent and rate of reaction. *Journal of Soil Science* **40**, 437-450.
- Batson V. L., Bertsch P. M., and Herbert B. E. (1996) Transport of anthropogenic uranium from sediments to surface waters during episodic storm events. *Journal of Environmental Quality* **25**, 1129-1137.
- Beasley T. M., Dixon P. R., and Mann L. J. (1998) ⁹⁹Tc, ²³⁶U, and ²³⁷Np in the Snake River plaining aquifer at the Idaho National Engineering and Environmental Laboratory, Idaho Falls, Idaho. *Environmental Science and Technology* **32**, 3875-3881.
- Bender J., Duff M. C., Phillips P., and Hill M. (2000) Bioremediation and bioreduction of dissolved U(VI) by microbial mat consortium supported on silica gel particles. *Environmental Science and Technology* **34**, 3235-3241.
- Bertsch P. M., Hunter D. B., Sutton S. R., Bajt S., and Rivers M. L. (1994) In situ chemical speciation of uranium in soils and sediments by micro X-ray absorption spectroscopy. *Environmental Science and Technology* **28**(5), 980-984.
- Biehler D. and Falck W. E. (1999) Simulation of the effects of geochemical reactions on groundwater quality during planned flooding of the Königstein uranium mine, Saxony, Germany. *Hydrogeology Journal* **7**, 284-293.
- Bilgin B. G. (1989) Isotopic exchange between precipitated sodium polyuranates and sodium ions in aqueous solution. *Chimica Acta Turcica* **17**, 205-210.
- Biwer B. M., Ebert W. L., and Bates J. K. (1990) The Raman spectra of several uranyl-containing minerals using a microprobe. *Journal of Nuclear Materials* **175**, 188-193.

- Braithwaite A., Livens F. R., Richardson S., Howe M. T., and Goulding K. W. T. (1997) Kinetically controlled-release of uranium from soils. *European Journal of Soil Science* **48**(4), 661-673.
- Braithwaite A., Richardson S., Moyes L. N., Livens F. R., Bunker D. J., Hughes C. R., Smith J. T., and Hilton J. (2000) Sorption kinetics of uranium-238 and neptunium-237 on a glacial sediment. *Czechoslovak Journal of Physics* **50**(2), 265-269.
- Brümmer G. W., Gerth J., and Tiller K. G. (1988) Reaction kinetics of the adsorption and desorption of nickel, zinc and cadmium by goethite. I. Adsorption and diffusion of metals. *Journal of Soil Science* **39**, 23-28.
- Bruno J., de Pablo J., Duro L., and Figuerola E. (1995) Experimental study and modeling of the U(VI)-Fe(OH)₃ surface precipitation coprecipitation equilibria. *Geochimica et Cosmochimica Acta* **59**(20), 4113-4123.
- Bruno J. and Puigdomenech I. (1989) Validation of the SKBU1 Uranium Thermodynamic Data Base for its use in geochemical calculations with EQ3/6. *Materials Research Society Symposium Proceedings* **127**, 887-896.
- Buck E. C., Brown N. R., and Dietz N. L. (1996) Contaminant uranium phases and leaching at the Fernald site in Ohio. *Environmental Science and Technology* **30**(1), 81-88.
- Burns P. C. (1999) The Crystal Chemistry of Uranium. In *Uranium: mineralogy, geochemistry and the environment*, Vol. 38 (ed. P. C. Burns and R. Finch), pp. 23-90. Mineralogical Society of America.
- Burns P. C. and Hill F. C. (2000a) Implications of the synthesis and structure of the Sr analogue of curite. *The Canadian Mineralogist* **38**, 175-181.
- Burns P. C. and Hill F. C. (2000b) A new uranyl sheet in K₅[(UO₂)₁₀O₈(OH)₉](H₂O): new insight into sheet anion-topologies. *The Canadian Mineralogist* **38**, 163-173.
- Cahill C. L. and Burns P. C. (2000) The structure of agrinierite: a Sr-containing uranyl oxide hydrate mineral. *American Mineralogist* **85**, 1294-1297.
- Casas I., Bruno J., Cera E., Finch R. J., and Ewing R. C. (1994a) Kinetic and thermodynamic studies of uranium minerals: assessment of the long-term evolution of spent nuclear fuel, pp. 73. SKB.
- Casas I., Bruno J., Cera E., Finch R. J., and Ewing R. C. (1997) Characterization and dissolution behavior of a becquerelite from Shinkolobwe, Zaire. *Geochimica et Cosmochimica Acta* **61**(18), 3879-3884.

- Casas I., Casabona D., Duro L., and J. d. P. (1994b) The influence of hematite on the sorption of uranium(VI) onto granite filling fractures. *Chemical Geology* **113**(3-4), 319-326.
- Casas I., De Pablo J., Gimenez J., Torrero M. E., Bruno J., Cera E., Finch R. J., and Ewing R. C. (1998) The role of pe, pH, and carbonate on the solubility of UO₂ and uraninite under nominally reducing conditions. *Geochimica et Cosmochimica Acta* **62**, 2223-2231.
- Cejka J. (1999) Infrared Spectroscopy and Thermal Analysis of the Uranyl Minerals. In *Uranium: mineralogy, geochemistry and the environment*, Vol. 38 (ed. P. C. Burns and R. Finch), pp. 521-620. Mineralogical Society of America.
- Chen F., Burns P. C., and Ewing R. C. (2000) Near-field behavior of ⁹⁹Tc during the oxidative alteration of spent nuclear fuel. *Journal of Nuclear Materials* **278**, 225-232.
- Chen F., Ewing R. C., and Clark S. B. (1999) The Gibbs free energies and enthalpies of formation of U6⁺ phases: an empirical method of prediction. *American Mineralogist* **84**, 650-664.
- Chisholm-Brause C., Conradson C. D., Buscher C. T., Eller P. G., and Morris D. E. (1994) Speciation of uranyl sorbed at multiple binding sites on montmorillonite. *Geochimica et Cosmochimica Acta* **58**(17), 3625-3631.
- Chisholm-Brause C. J., Berg J. M., Matzner R. A., and Morris D. E. (2001) Uranium(VI) sorption complexes on montmorillonite as a function of solution chemistry. *Journal of Colloid and Interface Science* **233**, 38-49.
- Choppin G. R. (1988) Humics and radionuclide migration. *Radiochimica Acta* **44/45**, 23-28.
- Choppin G. R. and Mathur J. N. (1991) Hydrolysis of actinyl(VI) cations. *Radiochimica Acta* **52/53**, 25-28.
- Clark S. B., Johnson W. H., Malek M. A., Serkiz S. M., and Hinton T. G. (1996) A comparison of sequential extraction techniques to estimate geochemical controls on the mobility of fission product, actinide, and heavy metal contaminants in soils. *Radiochimica Acta* **74**, 173-179.
- Copenhaver S. A., Krishnaswami S., Turekian K. K., Epler N., and Cochran J. K. (1992) ²³⁸U and ²³²Th series nuclides in groundwater from the J-13 well at the Nevada Test Site: implications for ion retardation. *Geophysical Research Letters* **19**(13), 1383-1386.
- Cordfunke E. H. P. and Loopstra B. O. (1971) Sodium uranates: preparation and thermochemical properties. *Journal of Inorganic and Nuclear Chemistry* **33**, 2427-2436.

- Coston J. A., Fuller C. C., and Davis J. A. (1995) Pb²⁺ and Zn²⁺ adsorption by a natural aluminum- and iron-bearing surface coating on an aquifer sand. *Geochimica et Cosmochimica Acta* **59**(17), 3535-3547.
- Crespo M. T., Perez Del Villar L., Jimenez A., Pelayo M., Quejido A., and Sanchez M. (1996) Uranium isotopic distribution in the mineral phases of granitic fracture fillings by a sequential extraction procedure. *Applied Radiation and Isotopes* **47**(9/10), 113-126.
- Cross J. E., Haworth A., Neretnieks I., Sharland S. M., and Tweed C. J. (1991) Modelling of redox front and uranium movement in a uranium mine at Pocos de Caldas. *Radiochimica Acta* **52/53**, 445-451.
- Davis J. A., Coston J. A., Kent D. B., and Fuller C. C. (1998) Application of the surface complexation concept to complex mineral assemblages. *Environmental Science and Technology* **32**, 2820-2828.
- Davis J. A. and Kent D. B. (1990) Surface complexation modeling in aqueous geochemistry. In *Mineral-Water Interface Geochemistry*, Vol. 23 (ed. M. F. Hochella and A. F. White), pp. 177-260. Mineralogical Society of America.
- De Pablo J., Casas I., Gimenez J., Molera M., Rovira M., Duro L., and Bruno J. (1999) The oxidative dissolution mechanism of uranium dioxide. I. The effect of temperature in hydrogen carbonate medium. *Geochimica et Cosmochimica Acta* **63**(19/20), 3097-3103.
- Debets P. C. and Loopstra B. O. (1963) On the uranates of ammonium - II. X-ray investigation of the compounds in the system NH₃-UO₃-H₂O. *Journal of Inorganic and Nuclear Chemistry* **25**, 945-953.
- Del Nero M., Salah S., Miura T., Clement A., and Gauthier-Lafaye F. (1999) Sorption/desorption processes of uranium in clayey samples of the Bangombe natural reactor zone, Gabon. *Radiochimica Acta* **87**, 135-149.
- Dent A. J., Ramsay J. D., and Swanton S. W. (1992) An EXAFS study of uranyl ion in solution and sorbed onto silica and montmorillonite clay colloids. *Journal of Colloid and Interface Science* **150**(1), 45-60.
- Dhoum R. T. and Evans G. J. (1998) Evaluation of uranium and arsenic retention by soil from low level radioactive waste management site using sequential extraction. *Applied Geochemistry* **13**(4), 109-114.
- Díaz Arocas P. and Grambow B. (1998) Solid-liquid equilibria of U(VI) in NaCl solutions. *Geochimica et Cosmochimica Acta* **62**(2), 245-263.
- Dowdall M. and O'Dea J. (1999) Speciation of ²²⁶Ra, ²³⁸U and ²²⁸Ra in an upland organic soil overlying uraniumiferous granite. *Radiochimica Acta* **87**, 109-114.

- Duff M. C. and Amrhein C. (1996) Uranium(VI) adsorption on goethite and soil in carbonate solutions. *Soil Science Society of America Journal* **60**, 1393-1400.
- Duff M. C., Amrhein C., Bertsch P. M., and Hunter D. B. (1997) The chemistry of uranium in evaporation pond sediment in the San Joaquin Valley, California, USA, using X-ray fluorescence and XANES techniques. *Geochimica et Cosmochimica Acta* **61**(1), 73-81.
- Duff M. C., Hunter D. B., Bertsch P. M., and Amrhein C. (1999) Factors influencing uranium reduction and solubility in evaporation pond sediments. *Biogeochemistry* **45**, 95-114.
- Duff M. C., Hunter D. B., Triay I. R., Bertsch P. M., Kitten J., and Vaniman D. T. (2001) Comparison of two micro-analytical methods for detecting the spatial distribution of sorbed Pu on geologic materials. *Journal of Contaminant Hydrology* **47**(2-4), 211-218.
- Duff M. C., Mason C. F. V., and Hunter D. B. (1998) Comparison of acid and base leach for the removal of uranium from contaminated soil and catch-box media. *Canadian Journal of Soil Science* **78**, 675-683.
- Duff M. C., Morris D. E., Hunter D. B., and Bertsch P. M. (2000) Spectroscopic characterization of uranium in evaporation pond sediments. *Geochimica et Cosmochimica Acta* **64**(9), 1535-1550.
- Echevarria G., Sheppard M. I., and Morel J. (2001) Effect of pH on the sorption of uranium in soils. *Journal of Environmental Radioactivity* **53**, 257-264.
- Elless M. P. and Lee S. Y. (1998) Uranium solubility of carbonate-rich uranium-contaminated soils. *Water, Air, and Soil Pollution* **107**, 147-162.
- Fayek M., Burns P., Guo Y.-X., and Ewing R. C. (2000) Micro-structures associated with uraninite alteration. *Journal of Nuclear Materials* **277**, 204-210.
- Fenton B. R. and Waite T. D. (1996) A kinetic study of cation release from a mixed mineral assemblage: implications for determination of uranium uptake. *Radiochimica Acta* **74**, 251-256.
- Fiedor J. N., Bostick W. D., Jarabek R. J., and Farrell J. (1998) Understanding the mechanism of uranium removal from groundwater by zero-valent iron using X-ray photoelectron spectroscopy. *Environmental Science and Technology* **32**, 1466-1473.
- Finch R. and Murakami T. (1999) Systematics and Paragenesis of Uranium Minerals. In *Uranium: mineralogy, geochemistry and the environment*, Vol. 38 (ed. P. C. Burns and R. Finch), pp. 91-180. Mineralogical Society of America.

Finch R. J. (1997) Thermodynamic stabilities of U(VI) minerals: estimated and observed relationships. In *Scientific basis for nuclear waste management XX: symposium held December 2-6, 1996, Boston, Massachusetts, U.S.A.*, Vol. 465 (ed. W. J. Gray and I. R. Triay), pp. 1185-1192. Materials Research Society.

Finch R. J., Cooper M. A., Hawthorne F. C., and Ewing R. C. (1996) The crystal structure of schoepite, $[(UO_2)_8O_2(OH)_{12}](H_2O)_{12}$. *The Canadian Mineralogist* **34**, 1071-1088.

Finch R. J. and Ewing R. C. (1997) Clarkeite: new chemical and structural data. *American Mineralogist* **82**, 607-619.

Finch R. J., Hawthorne F. C., and Ewing R. C. (1998) Structural relations among schoepite, metaschoepite and "dehydrated schoepite." *The Canadian Mineralogist* **36**, 831-845.

Finch R. J., Hawthorne F. C., Miller M. L., and Ewing R. C. (1997) Distinguishing among schoepite and related minerals by X-ray powder diffraction. *Powder Diffraction* **12**, 230-238.

Finch R. J., Miller M. L., and Ewing R. C. (1992) Weathering of natural uranyl oxide hydrates: schoepite polytypes and dehydration effects. *Radiochimica Acta* **58/59**, 433-443.

Finn P. A., Hoh J. C., Wolf S. F., Slater S. A., and Bates J. K. (1996) The release of uranium, plutonium, cesium, strontium, technetium and iodine from spent fuel under unsaturated conditions. *Radiochimica Acta* **74**, 65-71.

Fowle D. A., Fein J. B., and Martin A. M. (2000) Experimental study of uranyl adsorption onto *Bacillus subtilis*. *Environmental Science and Technology* **34**, 3737-3741.

Francis A. J. and Dodge C. J. (1998) Remediation of soils and wastes contaminated with uranium and toxic metals. *Environmental Science and Technology* **32**, 3993-3998.

Francis C. W., Timpson M. E., and Wilson J. H. (1999) Bench- and pilot-scale studies relating to the removal of uranium from uranium-contaminated soils using carbonate and citrate lixiviants. *Journal of Hazardous Materials* **66**, 67-87.

Fredrickson J. K., Zachara J. M., Kennedy D. W., Duff M. C., Gorby Y. A., Li S.-M. W., and Krupka K. M. (2000) Reduction of U(VI) in goethite (α -FeOOH) suspensions by a dissimilatory metal-reducing bacterium. *Geochimica et Cosmochimica Acta* **64**(18), 3085-3098.

Fröhlich K. and Gellermann R. (1987) On the potential use of uranium isotopes for groundwater dating. *Chemical Geology* **65**, 67-77.

Fröhlich K., Ivanovich M., Hendry M. J., Andrews J. N., Davis S. N., Drimmie R. J., Fabryka-Martin J., T. F., Fritz P., Lehrmann B., Loosli H. H., and Nolte E. (1991) Application of isotopic methods to dating very old groundwater. *Applied Geochemistry* **6**, 465-472.

Gabriel U., Gaudet J.-P., Spadini L., and Charlet L. (1998) Reactive transport of uranyl in a goethite column: an experimental and modelling study. *Chemical Geology* **151**, 107-128.

Gascoyne M. (1992) Geochemistry of the actinides and their daughters. In *Uranium-series Disequilibrium: Applications to Earth, Marine, and Environmental Science* (ed. M. Ivanovich and R. S. Harmon), pp. 34-61. Clarendon Press.

Geipel G., Bernhard G., Brendler V., and Nitsche H. (1996) Sorption of uranium(VI) on rock material of a mine tailing pile: solution speciation by fluorescence spectroscopy. *Radiochimica Acta* **74**, 235-238.

Giammar D. E. (2001) Geochemistry of uranium at mineral-water interfaces: Rates of sorption-desorption and dissolution-precipitation reactions, California Institute of Technology.

Grenthe I., Fuger J., Konings R. J. M., Lemire R. J., Mueller A. B., Nguyen-Trung C., and Wanner H. (1992) *Chemical Thermodynamics of Uranium*. Elsevier.

Gu B., Liang L., Dickey M. J., Yin X., and Dai S. (1998) Reductive precipitation of uranium(VI) by zero-valent iron. *Environmental Science and Technology* **32**, 3366-3373.

Guilbert S., Guittet M. J., Barré N., Gautier-Soyer M., Trocellier P., Gosset D., and Andriambololona Z. (2000) Dissolution of UO₂ in Boom clay water in oxidizing conditions: an XPS study. *Journal of Nuclear Materials* **282**, 75-82.

Heffernan, T.E., Lodwick J. C., Spitz H., Neton J., and Soldano M. (2001) Solubility of airborne uranium compounds at the Fernald Environmental Management Project. *Health Physics* **80**(3), 255-262.

Hill F. C. (1999) Identification of Uranium-bearing Minerals and Inorganic Phases by X-ray Powder Diffraction. In *Uranium: mineralogy, geochemistry and the environment*, Vol. 38 (ed. P. C. Burns and R. Finch), pp. 653-679. Mineralogical Society of America.

Hill F. C. and Burns P. C. (1999) The structure of a synthetic Cs uranyl oxide hydrate and its relationship to compreignacite. *The Canadian Mineralogist* **37**, 1283-1288.

Ho C. H. and Doern D. C. (1985) The sorption of uranyl species on a hematite sol. *Canadian Journal of Chemistry* **63**, 1100-1104.

Ho C. H. and Miller N. H. (1986) Adsorption of uranyl species from bicarbonate solution onto hematite particles. *Journal of Colloid and Interface Science* **110**(1), 165-170.

Hoekstra H. R. and Siegel S. (1973) The uranium trioxide-water system. *Journal of Inorganic and Nuclear Chemistry* **35**, 761-779.

Hsi C.-K. D. and Langmuir D. (1985) Adsorption of uranyl onto ferric oxyhydroxides: application of the surface complexation site-binding model. *Geochimica et Cosmochimica Acta* **49**, 1931-1941.

Hudson E. A., Terminello L. J., Viani B. E., Denecke M., Reich T., Allen P. G., Bucher J. J., Shuh D. K., and Edelstein N. M. (1999) The structure of U⁶⁺ sorption complexes on vermiculite and hydrobiotite. *Clays and Clay Minerals* **47**(4), 439-457.

Hunter D. B. and Bertsch P. M. (1998) In situ examination of uranium contaminated soil particles by micro-X-ray absorption and micro-fluorescence spectroscopies. *Journal of Radioanalytical and Nuclear Chemistry* **234**(1), 237-242.

Ildefonse P., Muller J.-P., Clozel B., and Calas G. (1990) Study of two alteration systems as natural analogues for radionuclide release and migration. *Engineering Geology* **29**, 413-429.

Ivanovich M., Fröhlich K., and Hendry M. J. (1991) Uranium-series radionuclides in fluids and solids, Milk River Aquifer, Alberta, Canada. *Applied Geochemistry* **6**, 405-418.

Ivanovich M., Latham A. G., and Ku. T.-L. (1992a) Uranium-series disequilibrium applications in geochronology. In *Uranium-series Disequilibrium: Applications to Earth, Marine, and Environmental Science* (ed. M. Ivanovich and R. S. Harmon), pp. 62-94. Clarendon Press.

Ivanovich M., Latham A. G., Longworth G., and Gascoyne M. (1992b) Applications to radioactive waste disposal studies. In *Uranium-series Disequilibrium: Applications to Earth, Marine, and Environmental Science* (ed. M. Ivanovich and R. S. Harmon), pp. 583-630. Clarendon Press.

JCPDS-ICDD. (1999) Powder diffraction file. International Centre for Diffraction Data.

Jung J., Hyun S. P., Lee J. K., Cho Y. H., and Hahn P. S. (1999) Adsorption of UO₂²⁺ on natural composite materials. *Journal of Radioanalytical and Nuclear Chemistry* **242**(2), 405-412.

Kaplan D. I., Bertsch P. M., Adriano D. C., and Orlandini K. A. (1994a) Actinide association with groundwater colloids in a coastal plain aquifer. *Radiochimica Acta* **66/67**, 181-187.

- Kaplan D. I., Hunter D. B., Bertsch P. M., Bajt S., and Adriano D. C. (1994b) Application of synchrotron X-ray fluorescence spectroscopy and energy dispersive X-ray analysis to identify contaminant metals on groundwater colloids. *Environmental Science and Technology* **28**, 1186-1189.
- Kaplan D. I., Serne R. J., Owen A. T., Conca J., Wietsma T. W., and Gervais T. L. (1996) Radionuclide adsorption distribution coefficients measured in Hanford sediments for the Low Level Waste Performance Assessment project. Pacific Northwest National Laboratory.
- Kelly S. D., Boyanov M. I., Bunker B. A., Fein J. B., Fowle D. A., Yee N., and Kemner K. M. (2001) XAFS determination of the bacterial cell wall functional groups responsible for complexation of Cd and U as a function of pH. *Journal of Synchrotron Radiation* **8**, 946-948.
- Killough G. G., Rope S. K., Shleien B., and Voilleque P. G. (1999) Nonlinear estimation of weathering rate parameters for uranium in surface soil near a nuclear facility. *Journal of Environmental Radioactivity* **45**, 95-118.
- Klein C. and Hurlbut J., C.S. (1993) *Manual of mineralogy*. John Wiley & Sons, Inc.
- Kohler M., Curtis G. P., Kent D. B., and Davis J. A. (1996) Experimental investigation and modeling of uranium(VI) transport under variable chemical conditions. *Water Resources Research* **32**(12), 3539-3551.
- Kramer-Schnabel H., Bischoff H., Xi R. H., and Marx G. (1992) Solubility products and complex formation equilibria in the systems uranyl hydroxide and uranyl carbonate at 25°C and I = 0.1 M. *Radiochimica Acta* **56**, 183-188.
- Landa E. R. and Gray J. R. (1995) US Geological Survey research on the environmental fate of uranium mining and milling wastes. *Environmental Geology* **26**, 19-31.
- Langmuir D. (1997) *Aqueous environmental chemistry*. Prentice Hall.
- Langmuir D. and Whittemore D. O. (1971) Variations in the Stability of Precipitated Ferric Oxyhydroxides. In *Nonequilibrium Systems in Natural Water*, Vol. 106 (ed. J. D. Hem), pp. 209-224. American Chemical Society.
- Lenhart J. J., Cabaniss S. E., MacCarthy P., and Honeyman B. D. (2000) Uranium(VI) complexation with citric, humic and fulvic acids. *Radiochimica Acta* **88**, 345-353.
- Lenhart J. J. and Honeyman B. D. (1999) Uranium(VI) sorption to hematite in the presence of humic acid. *Geochimica et Cosmochimica Acta* **63**(19/20), 2891-2901.

- Lichtner P. C. (1996) Continuum formulation of multicomponent-multiphase reactive transport. In *Reactive transport in porous media*, Vol. 34 (ed. P. C. Lichtner, C. I. Steefel, and E. H. Oelkers). Mineralogical Society of America.
- Liger E., Charlet L., and Van Cappellen P. (1999) Surface catalysis of uranium(VI) reduction by iron(II). *Geochimica et Cosmochimica Acta* **63**(19/20), 2939-2955.
- Litaor I. (1995) Uranium isotopes distribution in soils at the Rocky-Flats Plant, Colorado. *Journal of Environmental Quality* **25**(2), 314-323.
- Lovley D. and Phillips E. J. P. (1992) Reduction of uranium by *Desulfovibrio desulfuricans*. *Applied and Environmental Microbiology* **58**(3), 850-856.
- Lovley D. R., Phillips E. J. P., Gorby Y. A., and Landa E. R. (1991) Microbial reduction of uranium. *Nature* **350**, 413-416.
- Lowson R. T., Short S. A., Davey B. G., and Gray D. J. (1986) $^{234}\text{U}/^{238}\text{U}$ and $^{230}\text{Th}/^{234}\text{U}$ activity ratios in mineral phases of a lateritic weathered zone. *Geochimica et Cosmochimica Acta* **50**, 1697-1702.
- Loyland S. M., LaMont S. P., Herbison S. E., and Clark S. B. (2000) Actinide partitioning to an acidic, sandy lake sediment. *Radiochimica Acta* **88**, 793-798.
- Lubal P., Fetsch D., Siroky D., Lubalova M., Senkyr J., and Havel J. (2000) Potentiometric and spectroscopic study of uranyl complexation with humic acids. *Talanta* **51**, 977-991.
- Lumpkin G. R., Payne T. E., Fenton B. R., and Waite T. D. (1999) Preferential association of adsorbed uranium with mineral surfaces: a study using analytical electron microscopy. *Materials Research Society Symposium Proceedings* **556**, 1067-1074.
- Luo S., Ku T.-L., Roback R., Murrell M., and McLing T. L. (2000) In-situ radionuclide transport and preferential groundwater flows at INEEL (Idaho): Decay-series disequilibrium studies. *Geochimica et Cosmochimica Acta* **64**(5), 867-881.
- MacDonald J. A. (1999) Cleaning up the nuclear weapons. *Environmental Science and Technology* **33**, 314A-319A.
- Malý J. and Veselý V. (1958) A contribution to sodium polyuranate chemistry. *Journal of Inorganic and Nuclear Chemistry* **7**, 119-128.
- Mann H. and Fyfe W. S. (1985) Uranium uptake by algae: experimental and natural environments. *Canadian Journal of Earth Science* **22**, 1899.

- Mason C. F. V., Turney W. R. J. R., Thomson B. M., Lu N., Longmire P. A., and Chisholm-Brause C. J. (1997) Carbonate leaching of uranium from contaminated soils. *Environmental Science and Technology* **31**, 2707-2711.
- Maya L. (1982) Sorbed uranium(VI) species on hydrous titania, zirconia, and silica gel. *Radiochimica Acta* **31**, 147-151.
- Maya L. and Begun G. M. (1981) A Raman spectroscopy study of hydroxo and carbonate species of the uranyl (VI) ion. *Journal of Inorganic and Nuclear Chemistry* **43**(11), 2827-2832.
- McKinley J. P., Zachara J. M., Smith S. C., and Turner G. D. (1995) The influence of uranyl hydrolysis and multiple site-binding reactions on adsorption of U(VI) to montmorillonite. *Clays and Clay Minerals* **43**(5), 586-598.
- Megumi K. (1979) Radioactive disequilibrium of uranium and actinium series nuclides in soil. *Journal of Geophysical Research* **84**(B7), 3677-3682.
- Meinrath G. (1998) Direct spectroscopic speciation of schoepite-aqueous phase equilibria. *Journal of Radioanalytical and Nuclear Chemistry* **232**(1-2), 179-188.
- Meinrath G., Kato Y., Kimura T., and Yoshida Z. (1996a) Solid-aqueous phase equilibria of uranium(VI) under ambient conditions. *Radiochimica Acta* **75**, 159-167.
- Meinrath G. and Kimura T. (1993) Behaviour of U(VI) solids under conditions of natural aquatic systems. *Inorganica Chimica Acta* **204**, 79-85.
- Meinrath G., Klenze R., and Kim J. I. (1996b) Direct spectroscopic speciation of uranium(VI) in carbonate solutions. *Radiochimica Acta* **75**, 81-86.
- Moll H., Geipel G., Matz W., Bernhard G., and Nitsche H. (1996) Solubility and speciation of $(\text{UO}_2)_2\text{SiO}_4\text{-H}_2\text{O}$. *Radiochimica Acta* **74**, 3-7.
- Moll H., Matz W., Schuster G., Brendler E., Bernhard G., and Nitsche H. (1995) Synthesis and characterization of uranyl orthosilicate $(\text{UO}_2)_2\text{SiO}_4\text{-H}_2\text{O}$. *Journal of Nuclear Materials* **227**, 40-49.
- Moll H., Reich T., and Szabó Z. (2000) The hydrolysis of dioxouranium(VI) investigated using EXAFS and ^{17}O -NMR. *Radiochimica Acta* **88**, 411-415.
- Montavon G., Mansel A., Seibert A., Keller H., Kratz J. V., and Trautmann N. (2000) Complexation studies of UO_2^{2+} with humic acid at low metal ion concentrations by indirect speciation methods. *Radiochimica Acta* **88**, 17-24.

Morel F. M. M. and Hering J. G. (1993) *Principles and applications of aquatic chemistry*. Wiley Inter-science.

Morris D. E., Allen P. G., Berg J. M., Chisholm-Brause C. J., Conradson S. D., Donohoe R. J., Hess N. J., Musgrave J. A., and Tait C. D. (1996) Speciation of uranium in Fernald soils by molecular spectroscopic methods: characterization of untreated soils. *Environmental Science and Technology* **30**(7), 2322-2331.

Morris D. E., Chisholm-Brause C. J., Barr M. E., Conradson S. D., and Eller P. G. (1994) Optical spectroscopic studies of the sorption of UO_2^{2+} species on a reference smectite. *Geochimica et Cosmochimica Acta* **58**(17), 3613-3623.

Morrison S. J., Metzler D. R., and Carpenter C. E. (2001) Uranium precipitation in a permeable reactive barrier by progressive irreversible dissolution of zerovalent iron. *Environmental Science and Technology*.

Morrison S. J., Spangler R. R., and Tripathi V. S. (1995) Adsorption of uranium(VI) on amorphous ferric oxyhydroxide at high concentrations of dissolved carbon(IV) and sulfur(VI). *Journal of Contaminant Hydrology* **17**(4), 333-346.

Moyes L. N., Parkman R. H., Charnock J. M., Vaughan D. J., Livens F. R., Hughes C. R., and Braithwaite A. (2000) Uranium uptake from aqueous solution by interaction with goethite, lepidocrocite, muscovite, and mackinawite: an X-ray absorption spectroscopy study. *Environmental Science and Technology* **34**, 1062-1068.

Murakami T., Ohnuki, T., Isobe, H. and Sato, T. (1997) Mobility of uranium during weathering. *American Mineralogist* **82**, 888-8999.

Murphy R. J., Lenhart J. J., and Honeyman B. D. (1999) The sorption of thromium (IV) and uranium (VI) to hematite in the presence of natural organic matter. *Colloids and Surfaces A* **157**, 47-62.

Murphy W. M. and Shock E. L. (1999) Environmental Aqueous Geochemistry of Actinides. In *Uranium: mineralogy, geochemistry and the environment*, Vol. 38 (ed. P. C. Burns and R. Finch), pp. 221-254. Mineralogical Society of America.

Neck V. and Kim J. I. (2000) Solubility and hydrolysis of tetravalent actinides. *Radiochimica Acta* **88**(9/11).

Nguyen S. N., Silva R. J., Weed H. C., and Andrews J., J.E. (1992) Standard Gibbs free energies of formation at the temperature 303.15K of four uranyl silicates: soddyite, uranophane, sodium boltwoodite, and sodium weeksite. *Journal of Chemical Thermodynamics* **24**, 359-376.

Nitzsche O., Meinrath G., and Merkel B. (2000) Database uncertainty as a limiting factor in reactive transport prognosis. *Journal of Contaminant Hydrology* **44**, 223-237.

Nitzsche O. and Merkel B. (1999) Reactive transport modeling of uranium 238 and radium 226 in groundwater of the Königstein uranium mine, Germany. *Hydrogeology Journal* **44**, 423-430.

O'Hare P. A. G., Lewis B. M., and Nguyen S. N. (1988) Thermochemistry of uranium compounds XVII. Standard molar enthalpy of formation at 298.15 K of dehydrated schoepite $\text{UO}_3 \cdot 0.9\text{H}_2\text{O}$. Thermodynamics of (schoepite + dehydrated schoepite + water). *Journal of Chemical Thermodynamics* **20**, 1287-1296.

Ohnuki T., Isobe H., Yanase N., Nagano T., Sakamoto Y., and Sekine K. (1997) Change in sorption characteristics of uranium during crystallization of amorphous iron minerals. *Journal of Nuclear Science and Technology* **34**(12), 1153-1158.

Olguin M. T., Solacherios M., Acosta D., Bosch P., and Bulbulian S. (1997) UO_2^{2+} sorption on bentonite. *Journal of Radioanalytical and Nuclear Chemistry* **218**(1), 65-69.

Osmond J. K. and Cowart J. B. (1992) Ground water. In *Uranium-series Disequilibrium: Applications to Earth, Marine, and Environmental Science* (ed. M. Ivanovich and R. S. Harmon), pp. 290-333. Clarendon Press.

Pabalan R. T. and Turner D. R. (1997) Uranium(6+) sorption on montmorillonite: experimental and surface complexation modeling study. *Aquatic Geochemistry* **2**, 203-226.

Panak P. J., Raff J., Selenska-Pobell S., Geipel G., Bernhard G., and Nitsche H. (2000) Complex formation of U(VI) with *Bacillus*-isolates from a uranium mining waste pile. *Radiochimica Acta* **88**, 71-76.

Payne T. E., Davis J. A., and Waite T. D. (1994) Uranium retention by weathered schists - the role of iron minerals. *Radiochimica Acta* **66/67**, 297-303.

Payne T. E. and Harries J. R. (2000) Adsorption of Cs and U(VI) on soils of the Australian arid zone. *Radiochimica Acta* **88**(9/11), 799.

Payne T. E., Lumpkin G. R., and Waite T. D. (1998) Uranium^{VI} adsorption on model minerals: Controlling factors and surface complexation. In *Adsorption of Metals by Geomedia* (ed. E. A. Jenne), pp. 75-97. Academic Press.

Payne T. E. and Waite T. D. (1991) Surface complexation modelling of uranium sorption data obtained by isotope exchange techniques. *Radiochimica Acta* **52/53**, 487-493.

Pérez I., Casas I., Martín M., and Bruno J. (2000) The thermodynamics and kinetics of uranophane dissolution in bicarbonate test solutions. *Geochimica et Cosmochimica Acta* **64**(4), 603-608.

Pérez I., Casas I., Torrero M. E., Cera E., Duro L., and Bruno J. (1997) Dissolution studies of soddyite as a long-term analogue of the oxidative alteration of the spent nuclear fuel matrix. In *Scientific basis for nuclear waste management XX: symposium held December 2-6, 1996, Boston, Massachusetts, U.S.A.*, Vol. 465 (ed. W. J. Gray and I. R. Triay), pp. 565-572. Materials Research Society.

Porcelli D., Andersson P. S., Wasserburg G. J., Ingri J., and Baskaran M. (1997) The importance of colloids and mires for the transport of uranium isotopes through the Kalix River watershed and Baltic Sea. *Geochimica et Cosmochimica Acta* **61**, 4095-4113.

Prikryl J. D., Jain A., Turner D. R., and Pabalan R. T. (2001) Uranium^{VI} sorption behavior on silicate mineral mixtures. *Journal of Contaminant Hydrology* **47**(2-4), 241-253.

Puigdomenech I. and Bruno J. (1988) SKB.

Ramebäck H., Albinsson Y., Skålberg M., Eklund U. B., Kjellberg L., and Werme L. (2000) Transport and leaching of technetium and uranium from spent UO₂ fuel in compacted bentonite clay. *Journal of Nuclear Materials* **277**, 288-294.

Redden G. R., Li J., and Leckie J. (1998) Adsorption of UVI and citric acid on goethite, gibbsite, and kaolinite: Comparing results for binary and ternary systems. In *Adsorption of Metals by Geomedia* (ed. E. A. Jenne), pp. 291-315. Academic Press.

Ricci J. E. and Loprest F. J. (1955) Phase relations in the system sodium oxide - uranium trioxide - water at 50 and 75°. *Journal of the American Chemical Society* **77**, 2119-2129.

Riley R. G. and Zachara J. M. (1992) Chemical contaminants on DOE lands and selection of contaminant mixtures for subsurface science research. U.S. Dept. of Energy, Office of Energy Research.

Roh Y., Lee S. R., Choi S.-K., Elless M. P., and Lee S. Y. (2000) Physicochemical and mineralogical characterization of uranium-contaminated soils. *Soil and Sediment Contamination* **9**(5), 463-486.

Rosentreter J. J., Quarder H. S., Smith R. W., and McLing T. (1998) Uranium sorption onto natural sands as a function of sediment characteristics and solution pH. In *Adsorption of Metals by Geomedia* (ed. E. A. Jenne), pp. 181-192. Academic Press.

Sandino A. and Bruno J. (1992) The solubility of (UO₂)₃(PO₄)₂·4H₂O(s) and the formation of U(VI) phosphate complexes: Their influence in uranium speciation in natural waters. *Geochimica et Cosmochimica Acta* **56**, 4135-4145.

Sandino M. C. A. and Grambow B. (1994) Solubility equilibrium in the U(VI)-Ca-K-Cl-H₂O system: Transformation of schoepite into becquerelite and compregnacite. *Radiochimica Acta* **66/67**, 37-43.

- Sato T., Murakami T., Yanase N., Isobe H., Payne T. E., and Airey P. L. (1997) Iron nodules scavenging uranium from groundwater. *Environmental Science and Technology* **31**(10), 2854-2858.
- Schecher W. D. and McAvoy D. C. (1998) MINEQL+: A chemical equilibrium modeling system, version 4.0. Environmental Research Software.
- Scheinost A. C., Abend, S., Pandya, K.I., and Sparks, D.L. (2001) Kinetic controls on Cu and Pb sorption by ferrihydrite. *Environmental Science and Technology* **35**(6), 1090-1096.
- Schimmack W., Klotz D., Kretner R., and Bunzl K. (2000) Longterm leaching of natural radionuclides from uranium mill tailings material: comparison of indoor and outdoor column experiments. *Radiochimica Acta* **88**, 77-81.
- Schindler P. W. (1967) Heterogeneous Equilibria Involving Oxides, Hydroxides, Carbonates, and Hydroxide Carbonates. In *Equilibrium Concepts in Natural Water System*, Vol. 67 (ed. W. Stumm), pp. 196-221. American Chemical Society.
- Schnoor J. L. (1990) Kinetics of chemical weathering: A comparison of laboratory and field weathering rates. In *Aquatic Chemical Kinetics* (ed. W. Stumm), pp. 475-504. Wiley-Interscience.
- Schwertmann U. and Cornell R. M. (1991) *Iron Oxides in the Laboratory*. VCH.
- Sheppard J. C., Campbell M. J., Cheng T., and Kittrick J. A. (1980) Retention of radionuclides by mobile humic compounds and soil particles. *Environmental Science and Technology* **14**, 1349-1353.
- Shoesmith D. W. (2000) Fuel corrosion processes under waste disposal conditions. *Journal of Nuclear Materials* **282**, 1-31.
- Shriver D. F., Atkins P., and Langford C. H. (1994) *Inorganic Chemistry*. W.H. Freeman and Company.
- Side W. C. and Lee P. Y. (1996) Uranium contamination in the Great Miami aquifer at the Fernald Environmental Management Project, Fernald, Ohio. *Ground Water* **5**, 876-882.
- Silva R. J. (1992) Mechanisms for the retardation of uranium (VI) migration. *Materials Research Society Symposium Proceedings* **257**, 323-330.
- Sowder A. G. (1998) Assessing the impact of uranyl mineralogy in the U-Ca-PO₄ system on the environmental availability of uranium. Ph.D. Dissertation, Clemson University.

- Sowder A. G., Clark S. B., and Fjeld R. A. (1996) The effect of silica and phosphate on the transformation of schoepite to becquerelite and other uranyl phases. *Radiochimica Acta* **74**, 45-49.
- Sowder A. G., Clark S. B., and Fjeld R. A. (1999) The transformation of uranyl oxide hydrates: the effect of dehydration on synthetic metaschoepite and its alteration to becquerelite. *Environmental Science and Technology* **33**, 3552-3557.
- Sparks D. L. (1999) Kinetics and mechanisms of chemical reactions at the soil mineral/water interface. In *Soil Physical Chemistry* (ed. D. L. Sparks). CRC Press.
- Spear J. R., Figueroa L. A., and Honeyman B. D. (1999) Modeling the removal of uranium U(VI) from aqueous solutions in the presence of sulfate reducing bacteria. *Environmental Science and Technology* **33**, 2667-2675.
- Spear J. R., Figueroa L. A., and Honeyman B. D. (2000) Modeling reduction of uranium U(VI) under variable sulfate concentrations by sulfate-reducing bacteria. *Applied and Environmental Microbiology* **66**(9), 3711-3721.
- Steeffel C. I. and MacQuarrie K. T. B. (1996) Approaches to modeling of reactive transport in porous media. In *Reactive transport in porous media*, Vol. 34 (ed. P. C. Lichtner, C. I. Steefel, and E. H. Oelkers). Mineralogical Society of America.
- Steward S. A. and Mones E. T. (1997) Comparison and modeling of aqueous dissolution rates of various uranium oxides. In *Scientific basis for nuclear waste management XX : symposium held December 2-6, 1996, Boston, Massachusetts, U.S.A.*, Vol. 465 (ed. W. J. Gray and I. R. Triay), pp. 557-564. Materials Research Society.
- Stohl F. V. and Smith D. K. (1981) The crystal chemistry of the uranyl silicate minerals. *American Mineralogist* **66**, 610-625.
- Stumm W. (1992) *Chemistry of the solid-water interface*. John Wiley & Sons, Inc.
- Stumm W. and Morgan J. J. (1996) *Aquatic chemistry*. John Wiley & Sons, Inc.
- Suzuki Y. and Banfield J. (1999) Geomicrobiology of Uranium. In *Uranium: mineralogy, geochemistry and the environment*, Vol. 38 (ed. P. C. Burns and R. Finch), pp. 393-432. Mineralogical Society of America.
- Syed H. S. (1999) Comparison studies adsorption of thorium and uranium on pure clay minerals and local Malaysian soil sediments. *Journal of Radioanalytical and Nuclear Chemistry* **241**(1), 11-14.
- Sylwester E. R., Hudson E. A., and Allen P. G. (2000) The structure of uranium (VI) sorption complexes on silica, alumina, and montmorillonite. *Geochimica et Cosmochimica Acta* **64**(14), 2431-2438.

Szecsody J. E., Krupka K. M., Williams M. D., Cantrell K. J., Resch C. T., and Fruchter J. S. (1998) Uranium mobility during in situ redox manipulation of the 100 Areas of the Hanford Site. Pacific Northwest National Laboratory.

Tasker I. R., O'Hare P. A. G., Lewis B. M., Johnson G. K., and Cordfunke E. H. P. (1988) Thermochemistry of uranium compounds. XVI. Calorimetric determination of the standard molar enthalpy of formation at 298.15 K, low-temperature heat capacity, and high-temperature enthalpy increments of $\text{UO}_2(\text{OH})_2 \cdot \text{H}_2\text{O}$ (schoepite). *Canadian Journal of Chemistry* **66**, 620-625.

Thomas P. A. (2000a) Radionuclides in the terrestrial ecosystem near a Canadian uranium mill - Part I: Distribution and doses. *Health Physics* **78**(6), 614-624.

Thomas P. A. (2000b) Radionuclides in the terrestrial ecosystem near a Canadian uranium mill - Part II: Small mammal food chains and bioavailability. *Health Physics* **78**(6), 625-632.

Thomas P. A. (2000c) Radionuclides in the terrestrial ecosystem near a Canadian uranium mill - Part III: Atmospheric deposition rates (pilot test). *Health Physics* **78**(6), 633-640.

Thompson H. A., Parks G. A., and Brown Jr. G. E. (1998) Structure and composition of uranium(VI) sorption complexes at the kaolinite-water interface. In *Adsorption of Metals by Geomedia* (ed. E. A. Jenne), pp. 349-370. Academic Press.

Torrero M. E., Depablo J., Sandino M. C. A., and Grambow B. (1994) A comparison between unirradiated $\text{UO}_2(\text{s})$ and schoepite solubilities in 1M NaCl medium. *Radiochimica Acta* **66/67**, 29-35.

Tricca A., Porcelli D., and Wasserburg G. J. (2000) Factors controlling the groundwater transport of U, Th, Ra, and Rn. *Proceedings of the Indian Academy of Science (Earth and Planetary Science)* **109**(1), 95-108.

Tripathi V. S. (1984) Uranium(VI) transport modeling: geochemical data and submodels. Ph.D. Dissertation, Stanford University.

Trivedi P. and Axe L. (2000) Modeling Cd and Zn sorption to hydrous metal oxides. *Environmental Science and Technology* **34**, 2215-2223.

Trocellier P., Cachoir C., and Guilbert S. (1998) Dissolution of uranium dioxide in granitic groundwater by secondary phase formation. *Journal of Nuclear Materials* **256**, 197-206.

Turner G. D., Zachara J. M., McKinley J. P., and Smith S. C. (1996) Surface-charge properties and UO_2^{2+} adsorption of a subsurface smectite. *Geochimica et Cosmochimica Acta* **60**(18), 3399-3414.

U.S.DOE. (1997) *Linking legacies: connecting Cold War nuclear weapons processes to their environmental consequences*. U.S. Department of Energy, Office of Environmental Management.

U.S.DOE. (1998) GW/VZ Integration Project Specification. DOE/RL-98-48.

U.S.DOE. (1999) Permeable Reactive Barriers. U.S. Department of Energy Grand Junction Office.

U.S.EPA. (2000) Final rule for (non-radon) radionuclides in drinking water, pp. 1-6. U.S. Environmental Protection Agency, Office of Water.

Van Haverbeke L., Vochten R., and Van Springel K. (1996) Solubility and spectrochemical characteristics of synthetic chernikovite and meta-ankoleite. *Mineralogical Magazine* **60**, 759-766.

Van Olphen H. and Fripiat J. J. (1979) *Data handbook for clay minerals and other non-metallic materials*. Pergamon Press.

Vochten R. (1990) Transformation of chernikovite and sodium autunite into lehnerite. *American Mineralogist* **75**, 221-225.

Vochten R., Blaton N., and Peeters O. (1997a) Synthesis of sodium weeksite and its transformation into weeksite. *Neues Jahrbuch für Mineralogie Monatshefte* **12**, 569-576.

Vochten R., Blaton N., Peeters O., Van Springel K., and Van Haverbeke L. (1997b) A new method of synthesis of boltwoodite and of formation of sodium boltwoodite, uranophane, sklodowskite and kasolite from boltwoodite. *The Canadian Mineralogist* **35**, 735-741.

Vochten R. and Van Doorselaer M. (1984) Secondary uranium minerals of the Cunha Baixa mine. *The Mineralogical Record*, 293-297.

Vochten R. and Van Haverbeke L. (1990) Transformation of schoepite into the uranyl oxide hydrates: becquerelite, billietite and wölsendorffite. *Mineralogy and Petrology* **43**, 65-72.

Vochten R., Van Haverbeke L., and Sobry R. (1991) Transformation of schoepite into uranyl oxide hydrates of the bivalent cations Mg^{2+} , Mn^{2+} and Ni^{2+} . *Journal of Materials Chemistry* **1**(4), 637-642.

- Vochten R., Van Haverbeke L., Van Springel K., and De Grave E. (1995) Soddyite: synthesis under elevated temperature and pressure, and study of some physicochemical characteristics. *Neues Jahrbuch für Mineralogie Monatshefte* **10**, 470-480.
- Vochten R. F. C., van Haverbeke L., and Goovaerts F. (1990) External surface adsorption of uranyl-hydroxo complexes on zeolite particles in relation to the double-layer potential. *Journal of the Chemical Society - Faraday Transactions I* **86**(24), 4095-4099.
- Waite T. D., Davis J. A., Fenton B. R., and Payne T. E. (2000) Approaches to modelling uranium(VI) adsorption on natural mineral assemblages. *Radiochimica Acta*, 687-693.
- Waite T. D., Davis J. A., Payne T. E., Waychunas G. A., and Xu N. (1994) Uranium(VI) adsorption to ferrihydrite: application of a surface complexation model. *Geochimica et Cosmochimica Acta* **58**(24), 5465-5478.
- Wamser C. A., Belle J., Bernsohn E., and Williamson B. (1952) The constitution of the uranates of sodium. *Journal of the American Chemical Society* **74**, 1020-1022.
- Wehrli B., Ibric S., and Stumm W. (1990) Adsorption kinetics of vanadyl (IV) and chromium (III) to aluminum oxide: Evidence for a two-step mechanism. *Colloids and Surfaces* **51**, 77-88.
- Wong C. T., Okamoto H. S., Milea A. M., Perera S. K., and Baumann F. J. (1999) Isotopic uranium activity ratios in California groundwater. *Journal of the American Water Works Association* **91**(4), 171-185.
- Wronkiewicz D. and Buck E. (1999) Uranium Mineralogy and the Geologic Disposal of Spent Nuclear Fuel. In *Uranium: mineralogy, geochemistry and the environment*, Vol. 38 (ed. P. C. Burns and R. Finch), pp. 475-498. Mineralogical Society of America.
- Wronkiewicz D. J., Bates J. K., Gerding T. J., Veleckis E., and Tani B. S. (1992) Uranium release and secondary phase formation during unsaturated testing of UO₂ at 90°C. *Journal of Nuclear Materials* **190**, 107-127.
- Wronkiewicz D. J., Bates J. K., Wolf S. F., and Buck E. C. (1996) Ten-year results from unsaturated drip tests with UO₂ at 90°C: implications for the corrosion of spent nuclear fuel. *Journal of Nuclear Materials* **238**, 78-95.
- Yanase N., Nightingale T., Payne T., and Duerden P. (1991) Uranium distribution in mineral phases of rock by sequential extraction procedure. *Radiochimica Acta* **52/53**, 387-393.
- Yang J. and Volesky B. (1999) Modeling uranium-proton ion exchange in biosorption. *Environmental Science and Technology* **33**, 4079-4085.

Yinjie S., Hui Z., Fuliang L., and Qiaolin Y. (1995) The sorption of uranyl ions on silica-titania mixed-hydroxide gels. *Journal of Radioanalytical and Nuclear Chemistry* **190**(1), 155-166.

Zachara J. M. and McKinley J. P. (1993) Influence of hydrolysis on the sorption of metal cations by smectites: Importance of edge coordination reactions. *Aquatic Sciences* **55**(4), 250-261.

Zänker H., Richter W., Brendler V., and Nitsche H. (2000) Colloid-borne uranium and other heavy metals in the water of a mine drainage gallery. *Radiochimica Acta* **88**, 619-624.

Zhao D. and Ewing R. C. (2000) Alteration products of uraninite from the Colorado Plateau. *Radiochimica Acta* **88**, 739-749.

Appendix A

THERMODYNAMIC DATABASE REVIEW

A.1 Introduction

The aquatic chemistry of uranium is remarkably complex, and unfortunately the available thermodynamic database is still subject to considerable uncertainty. The uncertainty of the thermodynamic database has been considered the limiting factor in reactive transport modeling (Nitzsche et al., 2000). For the purpose of comparing the results from multiple independent studies, a consistent database of thermodynamic constants is essential. In this appendix, the databases of three recent reviews and experimental work published subsequent to those reviews are discussed. In the first section, the formation constants for dissolved species are discussed, and in the second section, the published solubility products for schoepite are reviewed. Frequently, formation constants of dissolved species were determined from equilibrium with schoepite (so as to fix $[\text{UO}_2^{2+}]$ as a function of pH), so the formation constants for the dissolved species and the solubility products are not strictly independent of each other.

A.2 Dissolved Species

A.2.1 Selected Databases

The selected database of formation constants for dissolved species used in this work is presented in Table A.1. Only constants for uranium (VI) complexation with species encountered in the present work (i.e., hydroxide, carbonate, fluoride, phosphate) are listed. The relevant constants from the Organisation for Economic Co-operation and Development (OECD) Nuclear Energy Agency (NEA) database (Grenthe et al., 1992), the Swedish Nuclear Fuel and Waste Management Co. (SKB) database (Bruno and Puigdomenech, 1989), and the most recent review available (Langmuir, 1997) are also presented in Table A.1. The constants selected for use in calculations in the present work are from the NEA database with the exception of the constant for $\text{UO}_2(\text{OH})_{2(\text{aq})}$, which was taken from Silva (1992). Additional reactions (e.g., acid-base) used in equilibrium calculations are listed in Table A.2 with equilibrium constants from the database of the chemical equilibrium software application MINEQL⁺ (Schecher and McAvoy, 1998), which primarily uses constants from the thermodynamic database of the WATEQ4F software application (Ball and Nordstrom, 1991).

A.2.2 Calculation of Activity Coefficients

In order to compare the constants determined in different experimental systems, it is important to correct for ionic strength effects. Constants are extrapolated to zero ionic strength by using activity coefficients for dissolved ionic species. In this work, activity coefficients have been calculated using the Davies equation (1) as part of calculations made using the chemical equilibrium software program MINEQL⁺ (Schecher and

$$\log \gamma_j = -Az_j^2 \left(\frac{\sqrt{I}}{1 + \sqrt{I}} - bI \right) \quad (1)$$

McAvoy, 1998) where z_j is the charge of the ionic species and A and b are constants. Calculations used values of 1.17 (at 25°C) for A and 0.24 for b (the values used in MINEQL+). Several authors report constants extrapolated from experimental conditions using the specific ion interaction theory (SIT), discussed in detail in the critical review by Grenthe et al. (1992). In the SIT, activity coefficients are calculated by

$$\log \gamma_j = -Az_j^2 \left(\frac{\sqrt{I}}{1 + Ba_j\sqrt{I}} \right) + \sum_k \varepsilon(j,k,I)m_k \quad (2)$$

where A and B are constants 0.509 and $3.28 \cdot 10^7$ respectively, a_j is the effective diameter of the hydrated ion (the product Ba_j is usually assigned a constant value of 1.5), $\varepsilon(j,k,I)$ is the ion interaction coefficient for ions j and k , and m_k is the molality of ion k . Ion interaction coefficients for many relevant species are tabulated in the NEA database.

A.2.3 Hydrolysis Species

As many as ten monomeric and polymeric uranyl hydrolysis species have been proposed; however, some hydrolysis species may be the result of overfitting experimental data (Meinrath, 1998). While the entire set of ten species has been considered in this work, only a subset of species are significant for specific experimental conditions. In most determinations of formation constants for hydrolysis species, a parsimonious approach has sought the best fit to experimental data with the fewest reactions. The most convincing determinations combine concentration measurements with spectroscopic evidence for the presence of the proposed species.

Table A.1: Aqueous phase uranium complexation reactions and thermodynamic stability constants (T=25°C, I=0).

Reaction	Log K			
	This Work	NEA ^a	SKB ^b	Langmuir ^c
Hydrolysis:				
$\text{UO}_2^{2+} + \text{H}_2\text{O} = \text{UO}_2\text{OH}^+ + \text{H}^+$	-5.20	-5.20 ± 0.30	-5.24	-5.20
$\text{UO}_2^{2+} + 2\text{H}_2\text{O} = \text{UO}_2(\text{OH})_2 + 2\text{H}^+$	-11.50	≤ -10.30	-12.05	-12.00
$\text{UO}_2^{2+} + 3\text{H}_2\text{O} = \text{UO}_2(\text{OH})_3^- + 3\text{H}^+$	-19.20	-19.20 ± 0.40	-19.97	-19.20
$\text{UO}_2^{2+} + 4\text{H}_2\text{O} = \text{UO}_2(\text{OH})_4^{2-} + 4\text{H}^+$	-33.00	-33.00 ± 0.40	-31.77	
$2\text{UO}_2^{2+} + \text{H}_2\text{O} = (\text{UO}_2)_2\text{OH}^{3+} + \text{H}^+$	-2.70	-2.70 ± 1.00	-2.79	
$2\text{UO}_2^{2+} + 2\text{H}_2\text{O} = (\text{UO}_2)_2(\text{OH})_2^{2+} + 2\text{H}^+$	-5.62	-5.62 ± 0.04	-5.64	-5.62
$3\text{UO}_2^{2+} + 4\text{H}_2\text{O} = (\text{UO}_2)_3(\text{OH})_4^{2+} + 4\text{H}^+$	-11.90	-11.90 ± 0.30	-11.97	
$3\text{UO}_2^{2+} + 5\text{H}_2\text{O} = (\text{UO}_2)_3(\text{OH})_5^+ + 5\text{H}^+$	-15.55	-15.55 ± 0.12	-15.63	-15.55
$3\text{UO}_2^{2+} + 7\text{H}_2\text{O} = (\text{UO}_2)_3(\text{OH})_7^- + 7\text{H}^+$	-31.00	-31.00 ± 2.00	-31.7	-31.00
$4\text{UO}_2^{2+} + 7\text{H}_2\text{O} = (\text{UO}_2)_4(\text{OH})_7^+ + 7\text{H}^+$	-21.90	-21.90 ± 1.00	-21.89	-21.90
Inorganic Anions:				
$\text{UO}_2^{2+} + \text{F}^- = \text{UO}_2\text{F}^+$	5.09	5.09 ± 0.13		5.09
$\text{UO}_2^{2+} + 2\text{F}^- = \text{UO}_2\text{F}_2(\text{aq})$	8.62	8.62 ± 0.04		8.62
$\text{UO}_2^{2+} + 3\text{F}^- = \text{UO}_2\text{F}_3^-$	10.90	10.90 ± 0.40		10.90
$\text{UO}_2^{2+} + 4\text{F}^- = \text{UO}_2\text{F}_4^{2-}$	11.70	11.70 ± 0.70		11.70
$\text{UO}_2^{2+} + \text{PO}_4^{3-} = \text{UO}_2\text{PO}_4^-$	13.23	13.23 ± 0.15		13.69
$\text{UO}_2^{2+} + \text{H}^+ + \text{PO}_4^{3-} = \text{UO}_2\text{HPO}_4(\text{aq})$	19.59	19.59 ± 0.26		20.06
$\text{UO}_2^{2+} + 2\text{H}^+ + \text{PO}_4^{3-} = \text{UO}_2\text{H}_2\text{PO}_4^+$	22.82	22.82 ± 0.06		22.81
$\text{UO}_2^{2+} + 3\text{H}^+ + \text{PO}_4^{3-} = \text{UO}_2\text{H}_3\text{PO}_4^{2+}$	22.46	22.46 ± 0.15		22.45
$\text{UO}_2^{2+} + 4\text{H}^+ + 2\text{PO}_4^{3-} = \text{UO}_2(\text{H}_2\text{PO}_4)_2(\text{aq})$	44.04	44.04 ± 0.11		44.26
$\text{UO}_2^{2+} + 5\text{H}^+ + 2\text{PO}_4^{3-} = \text{UO}_2(\text{H}_2\text{PO}_4)(\text{H}_3\text{PO}_4)^+$	45.05	45.05 ± 0.11		
$\text{UO}_2^{2+} + \text{NO}_3^- = \text{UO}_2\text{NO}_3^+$	0.26	0.30 ± 0.15		
$\text{UO}_2^{2+} + \text{H}_4\text{SiO}_4(\text{aq}) = \text{UO}_2\text{H}_3\text{SiO}_4^+ + \text{H}^+$	-2.40 ^d			
$\text{UO}_2^{2+} + \text{CO}_3^{2-} = \text{UO}_2\text{CO}_3(\text{aq})$	9.68	9.68 ± 0.04	9.52	9.67
$\text{UO}_2^{2+} + 2\text{CO}_3^{2-} = \text{UO}_2(\text{CO}_3)_2^{2-}$	16.94	16.94 ± 0.12	16.65	17.00
$\text{UO}_2^{2+} + 3\text{CO}_3^{2-} = \text{UO}_2(\text{CO}_3)_3^{4-}$	21.60	21.60 ± 0.05	21.37	21.63
$3\text{UO}_2^{2+} + 6\text{CO}_3^{2-} = (\text{UO}_2)_3(\text{CO}_3)_6^{6-}$	54.00	54.00 ± 1.00	53.41	

^a (Grenthe et al., 1992)^b (Bruno and Puigdomenech, 1989)^c (Langmuir, 1997); ^d (Schecher and McAvoy, 1998)

Table A.2: Thermodynamic stability constants for auxiliary reactions (T=25°C, I=0).

Reaction	Log K
$\text{H}_2\text{O} = \text{OH}^- + \text{H}^+$	-14.00
$\text{CO}_{2(\text{g})} + \text{H}_2\text{O} = \text{H}_2\text{CO}_3^*{}^{\text{a}}$	1.48
$\text{CO}_3^{2-} + 2\text{H}^+ = \text{H}_2\text{CO}_3^*$	16.68
$\text{CO}_3^{2-} + \text{H}^+ = \text{HCO}_3^-$	10.33
$2\text{F}^- + 2\text{H}^+ = \text{H}_2\text{F}_{2(\text{aq})}$	6.77
$2\text{F}^- + \text{H}^+ = \text{HF}_2^-$	3.75
$\text{F}^- + \text{H}^+ = \text{HF}_{(\text{aq})}$	3.17
$\text{H}_4\text{SiO}_{4(\text{aq})} = \text{H}_3\text{SiO}_4^- + \text{H}^+$	-9.93
$\text{H}_4\text{SiO}_{4(\text{aq})} = \text{H}_2\text{SiO}_4^{2-} + 2\text{H}^+$	-21.62
$\text{PO}_4^{3-} + 3\text{H}^+ = \text{H}_3\text{PO}_{4(\text{aq})}$	21.71
$\text{PO}_4^{3-} + 2\text{H}^+ = \text{H}_2\text{PO}_4^-$	19.55
$\text{PO}_4^{3-} + \text{H}^+ = \text{HPO}_4^{2-}$	12.35
$\text{Na}^+ + \text{CO}_3^{2-} + \text{H}^+ = \text{NaHCO}_{3(\text{aq})}$	10.08
$\text{Na}^+ + \text{CO}_3^{2-} = \text{NaCO}_3^-$	1.27
$\text{Ca}^{2+} + \text{H}_2\text{O} = \text{CaOH}^+$	-12.60
$\text{Ca}^{2+} + \text{CO}_3^{2-} + \text{H}^+ = \text{CaHCO}_3^+$	11.33
$\text{Ca}^{2+} + \text{CO}_3^{2-} = \text{CaCO}_{3(\text{aq})}$	3.15
$\text{Ca}^{2+} + \text{PO}_4^{3-} + \text{H}^+ = \text{CaHPO}_{4(\text{aq})}$	15.09

^a $\text{H}_2\text{CO}_3^* = \text{H}_2\text{CO}_{3(\text{aq})} + \text{CO}_{2(\text{aq})}$
(Schecher and McAvoy, 1998)

UO_2OH^+ . Evidence for the existence of the simplest monomeric species is quite robust. A value of $10^{-5.20}$ for the formation constant is consistent with both the NEA and SKB databases. Those values as well as others determined more recently are listed in Table A.3. A value of $10^{-5.91}$ (I = 0.1 M) was determined through competitive complexation with diglycolate followed by extraction of the organic complex into

dibenzoylmethane (Choppin and Mathur, 1991). In the fitting of schoepite solubility data, a value of $10^{-6.08}$ ($I = 0.1$ M) in combination with adjustments to other hydrolysis species gave the best fit to experimental data (Meinrath et al., 1996a).

Table A.3: Published formation constants for UO_2OH^+ .

Method	I (M)	$\text{LogK}'_{1,1}$	$\text{LogK}_{1,1}^a$	Ref.
critical review			-5.20 ± 0.30	Grenthe et al., 1992
critical review			-5.24	Bruno and Puigdomenech, 1989
solvent extraction	0.1	-5.91 ± 0.08	-5.69	Choppin and Mathur, 1991
solubility	0.1	-6.08 ± 0.04	-5.86	Meinrath et al., 1996a

^a If the value were not reported for zero ionic strength, the conditional formation constant was extrapolated to zero ionic strength with activity coefficients calculated with the Davies equation.

$\text{UO}_2(\text{OH})_{2(\text{aq})}$. In addition to the constants in the NEA and SKB databases, values for the formation constant of the neutral $\text{UO}_2(\text{OH})_{2(\text{aq})}$ species have been calculated by competitive complexation and solvent extraction (Choppin and Mathur, 1991) and fitting of schoepite solubility data (Silva, 1992) (Tab. A.4). Silva fit schoepite solubility results with the complete NEA database with only the adjustment of the $\text{UO}_2(\text{OH})_{2(\text{aq})}$ constant.

Table A.4: Published formation constants for $\text{UO}_2(\text{OH})_{2(\text{aq})}$.

Method	I (M)	$\text{LogK}'_{1,2}$	$\text{LogK}^o_{1,2}^a$	Ref.
critical review			≤ -10.30	Grenthe et al., 1992
critical review			-12.05	Bruno and Puigdomenech, 1989
solvent extraction	0.1	-12.43 ± 0.09	-12.21	Choppin and Mathur, 1991
solubility	0		-11.50	Silva, 1992

^a If the value was not reported for zero ionic strength, the conditional formation constant was extrapolated to zero ionic strength with activity coefficients calculated with the Davies equation.

$\text{UO}_2(\text{OH})_3^-$. In addition to the critically reviewed values in the databases, the constant was optimized in a study of schoepite solubility at pH 6-9 along with other hydrolysis species (Sandino and Bruno, 1992). At even higher pH, extended X-ray

absorption fine structure spectroscopy provides evidence for $\text{UO}_2(\text{OH})_4^{2-}$ and $\text{UO}_2(\text{OH})_5^{3-}$ species (Moll et al., 2000).

Table A.5: Published formation constants for $\text{UO}_2(\text{OH})_3^-$.

Method	I (M)	LogK _{1,3} '	LogK _{1,3} ^a	Ref.
critical review			-19.20 ± 0.40	Grenthe et al., 1992
critical review			-19.97	Bruno and Puigdomenech, 1989
solubility	0.1	-20.00 ± 0.50	-20.10 ± 0.50	Sandino and Bruno, 1992

^a Sandino and Bruno extrapolated their value at 0.5 M ionic strength to zero ionic strength with the specific ion interaction theory.

$(\text{UO}_2)_2(\text{OH})_2^{2+}$. The binuclear dihydrolysis species is one of the most important and widely accepted uranyl species. A constant was determined by simultaneously fitting the solubility product and two hydrolysis constants for schoepite solubility at slightly acidic pH (Kramer-Schnabel et al., 1992). Another solubility study determined a mean value for the formation constant based on several previously published studies (Meinrath et al., 1996a). A subsequent spectroscopic investigation of dissolved uranium at pH 2.4-4.8 directly observed the species and a formation constant was used to fit the results of 26 spectra (Meinrath, 1997).

Table A.6: Published formation constants for $(\text{UO}_2)_2(\text{OH})_2^{2+}$.

Method	I (M)	LogK _{2,2} '	LogK _{2,2} ^a	Ref.
critical review			-5.62 ± 0.04	Grenthe et al., 1992
critical review			-5.64	Bruno and Puigdomenech, 1989
solubility	0.1	-5.42 ± 0.04	-5.31	Kramer-Schnabel et al., 1992
critical review	0.1	-6.00 ± 0.06	-5.89	Meinrath et al., 1996a
spectroscopic	0.1	-6.14 ± 0.08	-6.03	Meinrath, 1997

^a If the value were not reported for zero ionic strength, the conditional formation constant was extrapolated to zero ionic strength with activity coefficients calculated with the Davies equation.

$(\text{UO}_2)_3(\text{OH})_5^+$. The trinuclear pentahydrolysis species is widely observed and probably dominates speciation over much of the pH range. The value of the formation

constant was optimized in solubility studies (Kramer-Schnabel et al., 1992; Meinrath, 1998; Meinrath et al., 1996a) and also spectroscopically (Meinrath, 1997). Values determined by both methods for the same experimental system are in good agreement, and the value determined from fitting the solubility data is considered the better quantitative estimate (Meinrath, 1998).

Table A.7: Published formation constants for $(\text{UO}_2)_3(\text{OH})_5^+$.

Method	I (M)	LogK' _{3,5}	LogK _{3,5} ^a	Ref.
critical review			-15.55 ± 0.12	Grenthe et al., 1992
critical review			-15.63	Bruno and Puigdomenech, 1989
solubility	0.1	-15.90 ± 0.04	-15.24	Kramer-Schnabel et al., 1992
critical review	0.1	-17.14 ± 0.13	-16.48	Meinrath et al., 1996a
spectroscopic	0.1	-17.14 ± 0.13	-16.48	Meinrath, 1997
solubility	0.1	-17.16 ± 0.17	-16.50	Meinrath, 1998

^a If the value were not reported for zero ionic strength, the conditional formation constant was extrapolated to zero ionic strength with activity coefficients calculated with the Davies equation.

$(\text{UO}_2)_3(\text{OH})_7^-$. In addition to the critically reviewed values in the databases, the constant was optimized in a study of schoepite solubility at pH 6-9 along with other hydrolysis species (Sandino and Bruno, 1992).

Table A.8: Published formation constants for $(\text{UO}_2)_3(\text{OH})_7^-$.

Method	I (M)	LogK' _{3,7}	LogK _{3,7} ^a	Ref.
critical review			-31.00 ± 2.00	Grenthe et al., 1992
critical review			-31.70	Bruno and Puigdomenech, 1989
solubility	0.1	-32.87 ± 0.80	-32.20 ± 0.80	Sandino and Bruno, 1992

^a Sandino and Bruno extrapolated their value at 0.5 M ionic strength to zero ionic strength with the specific ion interaction theory.

A.2.4 Uranyl Carbonate Complexes

It is generally accepted that three mononuclear uranyl carbonate complexes exist. In addition to the values published in the critically reviewed database, the constants have also been optimized in fitting solubility data of rutherfordine ($\text{UO}_2\text{CO}_3(\text{s})$) (Kramer-

Schnabel et al., 1992) and by spectroscopic investigation of solutions in equilibrium with a pure carbon dioxide atmosphere (Meinrath et al., 1996b).

Table A.9: Published formation constants for uranyl carbonate complexes.

	Reference ^a			
	NEA	SKB	Kramer-Schnabel	Meinrath
LogK^o			I = 0.1 M	
UO ₂ CO _{3(aq)}			8.70 ± 0.04	8.81 ± 0.04
UO ₂ (CO ₃) ₂ ²⁻			16.33 ± 0.07	15.50 ± 0.40
UO ₂ (CO ₃) ₃ ⁴⁻			23.92 ± 0.03	21.74 ± 0.22
LogK	Reported for I = 0, or extrapolated to I = 0 with Davies equation			
UO ₂ CO _{3(aq)}	9.68 ± 0.04	9.52	10.34	10.45
UO ₂ (CO ₃) ₂ ²⁻	16.94 ± 0.12	16.65	17.97	17.14
UO ₂ (CO ₃) ₃ ⁴⁻	21.60 ± 0.05	21.37	23.50	21.32

^a NEA database of Grenthe et al., 1992; SKB database of Bruno and Puigdomenech, 1989; Kramer-Schnabel et al., 1992; Meinrath et al., 1996b.

A.2.5 Uranyl Phosphate Complexes

The NEA database has formation constants for six uranyl phosphate complexes (Tab. A.1).

Experimental data of the solubility of uranyl phosphate hydrate as a function of pH in the range 6-9 was fit by optimizing the solubility product, one hydrolysis species (another was included but not optimized), and two uranyl phosphate complexes (Sandino and Bruno, 1992).

Table A.10: Published formation constants for uranyl phosphate complexes.

Method	LogK ^a		Ref.
	UO ₂ PO ₄ ⁻	UO ₂ HPO _{4(aq)}	
critical review	13.23 ± 0.15	19.59 ± 0.26	Grenthe et al., 1992
critical review	13.69	20.06	Langmuir, 1997
solubility	13.25 ± 0.09	19.63 ± 0.10	Sandino and Bruno, 1992

^a Sandino and Bruno extrapolated constants for zero ionic strength from measurements at 0.5 M ionic strength with activity coefficients determined using the specific ion interaction theory.

A.3 Schoepite Solubility

The solubility of schoepite has been investigated under a wide variety of conditions in numerous previous studies. The solubility product for schoepite is:

$$K_{\text{sp}} = \frac{\{\text{UO}_2^{2+}\}}{\{\text{H}^+\}^2} \quad (3)$$

The challenges in determining solubility products arise from the selection of dissolved species (i.e., hydrolysis and carbonate complexes) for determining the uranyl ion concentration and in the method of extrapolating values to zero ionic strength. The uranyl ion concentration must be calculated from the total dissolved uranium, which is the sum of multiple species as discussed in the preceding section.

The critically reviewed databases are a good starting point for discussing the solubility of schoepite. Using the suggested free energies of the NEA database, a $\text{Log}K_{\text{sp}}$ of 4.78 to 4.81 is calculated. The NEA free energies are taken from a calorimetry study of synthetic schoepite ($\text{UO}_3 \cdot 2\text{H}_2\text{O}$) dissolution in hydrofluoric acid (O'Hare et al., 1988; Tasker et al., 1988). The $\text{Log}K_{\text{sp}}$ is 5.58 in the SKB database and 5.20 in the review by Langmuir (1997), but the sources of those values are unclear. In addition to reporting a free energy for schoepite, Grenthe et al. (1992) present a thorough discussion of schoepite solubility studies conducted prior to 1992. The following discussion will be limited to experiments conducted during or after 1992.

For ten separate investigations, the experimental conditions, solubility products, and dissolved species considered together with their formation constants are compiled in Table A.11. The schoepite solubility product ranges from $10^{4.70}$ to $10^{6.33}$. The actual

Table A.11: Previous investigations of schoepite solubility.

Reference ^a	1	2	3	4	5	6	7	8	9	6	10	10
Conditions:												
Electrolyte		NaClO ₄	NaClO ₄	NaClO ₄	NaClO ₄	NaCl	NaCl	NaClO ₄	natural water	NaCl	NaClO ₄	NaClO ₄
I (M)		0.5	0.1	0.1	0.1	0.001	1	0.1	0.0077	1	0.5	0.5
pH		4.7, 6.3	2.8-4.6	3.8-7.0	4.5-5.5	5.0-10.0	3.3, 8.4	4.07-5.92	7.9-8.52	3.3, 8.4	6.0-9.0	6.0-9.0
Atmosphere	critical review	Ar	0.03% CO ₂	0.03-0.3% CO ₂	N ₂	Ar	5% O ₂ /N ₂	0.03% CO ₂	0.04-2.34% CO ₂	5% O ₂ /N ₂	N ₂	N ₂
Temperature (°C)		25	24	25	25	25	25	24	96	25	25	25
Solid Comments									UO ₃ ·H ₂ O	on UO _{2(s)}	crystalline	amorphous
L·logK_{sp} (I = 0)		4.81	4.70 ^b	5.02 ^c	5.01-5.50 ^c	5.13	5.20	5.38	5.53 ^c	5.66 ^d	5.73	6.33
L·logK_r (I = 0)												
UO ₂ OH ⁺		-5.20	-5.20	NC	-5.88 ^c	NC	-5.20	-5.20	NC	-5.20	-5.20	NC
UO ₂ (OH) _{2(aq)}		< -10.30	NC	NC	NC	NC	-11.50	-11.50	NC	< -10.30	-11.50	NC
UO ₂ (OH) ₃ ⁻		-19.20	-19.20	NC	NC	NC	-19.20	-19.74	NC	NC	-19.74	-19.83
UO ₂ (OH) ₄ ²⁻		-33.00	NC	NC	NC	NC	NC	NC	NC	NC	NC	NC
(UO ₂) ₂ OH ³⁺		-2.70	-2.70	NC	NC	NC	-2.70	NC	NC	NC	NC	NC
(UO ₂) ₂ (OH) ₂ ²⁺		-5.62	-5.62	-5.76 ^c	-5.79 ^c	-5.18	-5.62	-5.62	-5.93 ^c	NC	-5.62	NC
(UO ₂) ₃ (OH) ₄ ²⁺		-11.90	-11.90	NC	NC	NC	-11.90	-11.90	NC	NC	-11.90	NC
(UO ₂) ₃ (OH) ₅ ⁺		-15.55	-15.55	NC	-16.52 ^c	-15.19	-15.55	-15.55	-16.52 ^c	-15.55	-15.55	-15.55
(UO ₂) ₃ (OH) ₇ ⁻		-31.00	NC	NC	NC	NC	-31.00	-32.20	NC	NC	-32.20	-32.00
(UO ₂) ₄ (OH) ₇ ⁺		-21.90	-21.90	NC	NC	NC	-21.90	-21.90	NC	NC	-21.90	NC
UO ₂ CO _{3(aq)}		9.68	NA	NA	10.12 ^c	9.58	9.68	NA	NC	9.68	NA	NA
UO ₂ (CO ₃) ₂ ²⁻		16.94	NA	NA	NC	17.21	16.94	NA	NC	16.94	NA	NA
UO ₂ (CO ₃) ₃ ⁴⁻		21.60	NA	NA	NC	23.92	21.60	NA	NC	21.60	NA	NA

NC - not considered; NA - not applicable

^a 1) Grenthe et al., 1992; 2) Diaz Arocas and Grambow, 1998; 3) Meinrath and Kimura, 1993; 4) Meinrath et al., 1996a; 5) Kramer-Schnabel et al., 1992; 6) Silva, 1992; 7) Torero et al., 1994; 8) Meinrath, 1997; 9) Trocellier et al., 1998; 10) Sandino and Bruno, 1992.

^b Extrapolated by the authors to zero ionic strength from experimental ionic strength using the specific ion interaction theory.

^c Extrapolated to zero ionic strength with activity coefficients determined with the Davies equation.

^d Extrapolated to zero ionic strength and 25°C by the authors.

dissolved uranium concentration in equilibrium with schoepite is both a function of the solubility product and the formation constants of the dissolved species. Studies conducted at low pH values minimized the number of hydrolysis species required for fitting experimental data, and studies of suspensions purged with nitrogen or argon avoided the influence of uranyl carbonate complexes.

The solubility of schoepite is plotted as a function of pH for an open system according to the sets of thermodynamic constants from four studies conducted at pH

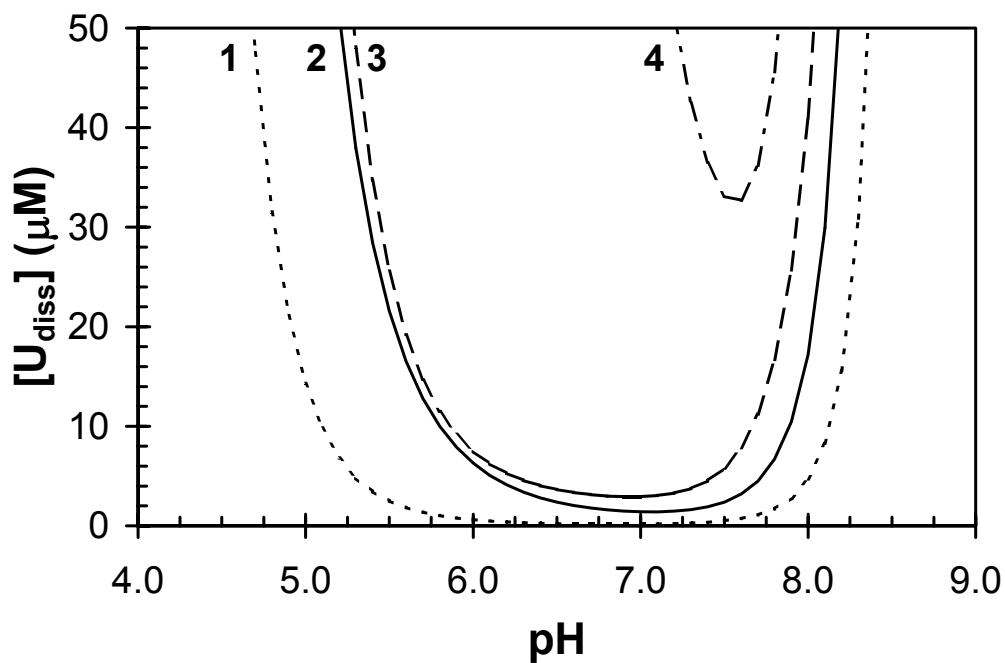


Figure A.1: Schoepite solubility at $I = 0.01 \text{ M}$, $P_{\text{CO}_2} = 10^{-3.5} \text{ atm}$, and 25°C calculated using the constants and dissolved species listed in Table A.11 for the following previous studies: 1) Diaz Arocas and Grambow, 1998, 2) Silva, 1992, 3) Meinrath, 1997, and 4) crystalline schoepite of Sandino and Bruno, 1992. Uranyl carbonate complex formation constants for the curves 1 and 4 were taken from the NEA database (Table A.1), and for curve 3 from the constants determined by Meinrath et al. (1996b) (Table A.9).

values and/or carbon dioxide partial pressures similar to those of the present work (Fig. A.1). The dissolved uranium concentrations observed at equilibrium in the current study

are consistent with calculations based on studies with schoepite solubility products in the range $10^{5.0}$ to $10^{5.5}$. The pH range and ionic strength used by Silva (1992) are the most comparable to those of the current work. It is also convenient that Silva considered the full set of dissolved species in determining the schoepite solubility product, just as was done in the current investigation (see Chapter 5). The contribution of various dissolved species to the solubility of schoepite in an open system is illustrated in a LogC-pH solubility diagram (Fig. A.2) calculated with the set of constants used by Silva (1992).

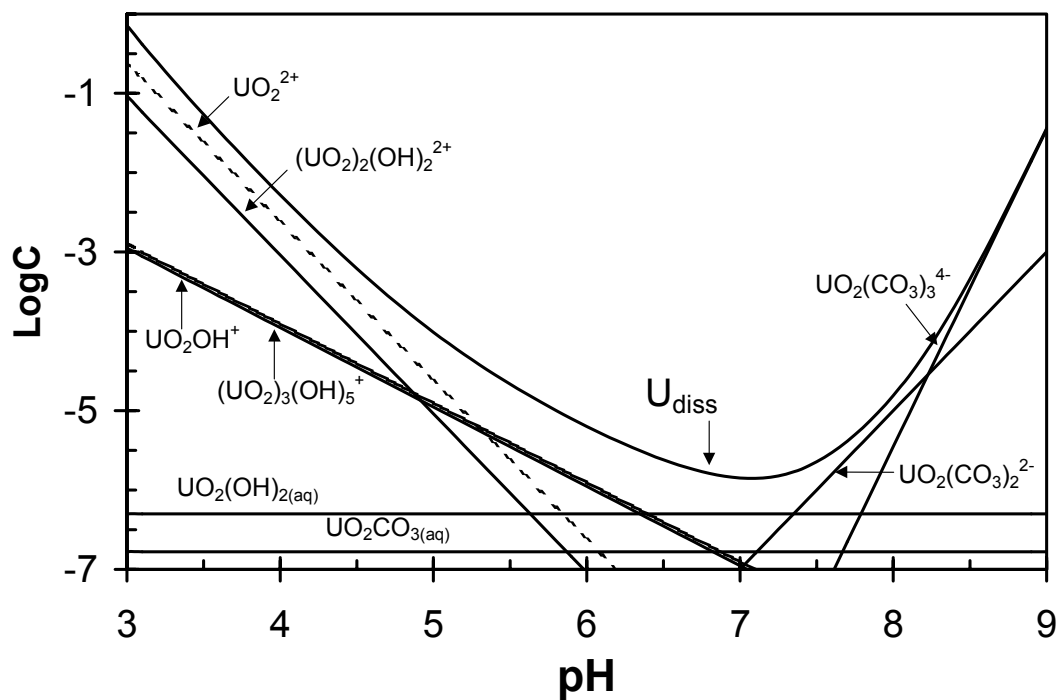


Figure A.2: Schoepite solubility and dissolved speciation as a function of pH for the thermodynamic data of Silva (1992) at $I = 0.01$ M, $P_{\text{CO}_2} = 10^{-3.5}$ atm, and 25°C .

Appendix B

Rates of Uranium(VI) Sorption on Montmorillonite

* performed as part of Helen Claudio's 1999 SURF research

B.1 Introduction

Clay minerals as well as iron oxyhydroxides are important mineral sorbents for heavy metals and radionuclides. Like iron oxyhydroxides, clay minerals have high specific surface areas and reactive surface groups for binding metals and radionuclides. The ubiquitous presence of clay minerals makes them important phases to consider in many contaminated systems. In the iron-poor sediments at the Savannah River Site, uranium transport is facilitated by mobile kaolinite colloids (Kaplan et al., 1994a; Kaplan et al., 1994b). Kaolinite is also the dominant sorbent in the weathered zones of uranium ore deposits in Mexico and Cameroon (Ildefonse et al., 1990).

Montmorillonite is a member of the smectite group of clay minerals, minerals composed of tetrahedral-octahedral-tetrahedral (*t-o-t*) layers, in which a sheet of octahedrally coordinated aluminum is sandwiched between two sheets of tetrahedrally coordinated silicon layers. Montmorillonite has the characteristic of swelling during hydration because of expansion of the interlayer spaces (Klein and Hurlbut, 1993). The ideal composition of montmorillonite is $\text{Al}_8(\text{Si}_4\text{O}_{10})_4(\text{OH})_8 \cdot 12\text{H}_2\text{O}$, but the substitution of divalent cations for aluminum in the octahedral site and of aluminum for silicon in the

tetrahedral site gives rise to a negative charge on the *t-o-t* layers which is balanced by the incorporation of cations in the interlayer. The cation exchange capacity (CEC) of a clay mineral is a measure of the cations needed in the interlayer space to neutralize the fixed charge of the aluminosilicate sheets (Langmuir, 1997).

The unique structures of clay minerals allow for sorption of metals and radionuclides through two different mechanisms. Sorption can occur either in the interlayer space (fixed-charge sites) between sheets by an ion-exchange mechanism, or at the edges of the sheets through specific coordination with hydroxylated silanol ($\equiv\text{SiOH}$) or aluminol ($\equiv\text{AlOH}$) functional groups. Surface complexation modeling of uranium sorption on sodium montmorillonite (McKinley et al., 1995; Zachara and McKinley, 1993) and a subsurface smectite mineral isolate (Turner et al., 1996) incorporated both ion-exchange and specific coordination mechanisms. At low ionic strength, significant sorption occurred at fixed-charge interlayer sites even at low pH, but at higher ionic strength uranium sorption decreased because sodium and calcium ions occupied the fixed-charge sites. Specific coordination at edge-sites was dominated by aluminol functional groups and increased across a pH-edge centered around pH 5. A study conducted at high ionic strength to block uranium access to fixed-charge sites confirmed the pH-dependence of uranium sorption and modeled the sorption with surface complexation at aluminol and silanol sites (Pabalan and Turner, 1997). Figure B.1 illustrates the pH and ionic strength dependence of uranium sorption on montmorillonite that were exploited in this study.

Spectroscopic measurements of uranium sorbed on montmorillonite support the sorption mechanisms used in surface complexation models. Extended X-ray absorption fine structure spectroscopy measurements suggest the formation of inner-sphere surface

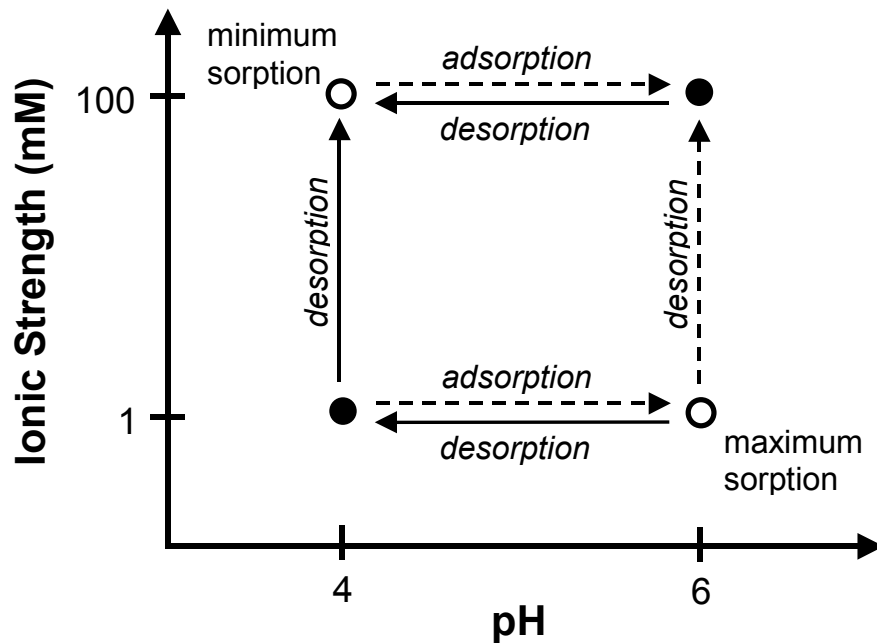


Figure B.1: Effects of pH and ionic strength on uranium sorption on montmorillonite. Sorption isotherms were determined at the conditions of the filled circles. Solid arrows represent processes investigated experimentally in this work, and dashed arrows represent processes not studied.

complexes at edge sites for low uranium loading and outer-sphere complexes at fixed-charge sites for higher loading (Chisholm-Brause et al., 1994; Dent et al., 1992). Using optical spectroscopic techniques, multiple surface complexes have been observed: two highly hydrated surface complexes indicative of outer-sphere coordination at fixed-charge sites, a bidentate inner-sphere surface complex coordinated by aluminol surface groups, and an inner-sphere polymeric surface complex observed at the highest uranium concentrations (Chisholm-Brause et al., 2001; Morris et al., 1994).

While the equilibrium sorption of uranium on montmorillonite has been attributed to multiple mechanisms and surface complexes, the kinetics of uranium sorption and desorption have not been studied. The rates of uranium uptake and release by different sorption mechanisms (i.e., specific coordination vs. ion-exchange) may be expected to be different. In this work, the rates of uranium adsorption and desorption were studied for systems with sorption dominated by either specific coordination or ion exchange. Desorption rates were examined following perturbations of total uranium concentration, ionic strength, or pH.

B.2 Experimental

B.2.1 Materials

The reference clay SWy-2 was obtained from the Source Clays Repository at the University of Missouri. SWy-2 is a montmorillonite from Crook County, Wyoming, with a BET surface area of $31.82 \text{ m}^2 \text{ g}^{-1}$ and a CEC of 0.76 meq g^{-1} . The exact composition of Swy-2 is given as

$(\text{Ca}_{0.12}\text{Na}_{0.32}\text{K}_{0.05})[\text{Al}_{3.01}\text{Fe(III)}_{0.41}\text{Mn}_{0.01}\text{Mg}_{0.54}\text{Ti}_{0.02}][\text{Si}_{7.98}\text{Al}_{0.02}]\text{O}_{20}(\text{OH})_4$ (Van Olphen and Fripiat, 1979). Particles larger than $2 \mu\text{m}$ were removed from the received clay by suspending a portion of the clay in pH 9.5 sodium bicarbonate solution and allowing the solids to settle through the water column for a prescribed length of time calculated with Stoke's Law. Solids smaller than $2 \mu\text{m}$ (remaining in suspension after sedimentation) were then subjected to sequential chemical washing following a published procedure (McKinley et al., 1995). First the sodium bicarbonate solution was removed by centrifugation and decantation and the clay was concentrated into six polycarbonate

bottles. To each bottle, 50 mL of 1 M sodium acetate was added and mixed with the clay for at least one hour to remove carbonates. The sodium acetate was removed by centrifugation and decantation and the clay was rinsed several times with deionized water. This process was then repeated using 10 mM nitric acid to dissolve fine particulate matter and 1% hydrogen peroxide to remove organic matter.

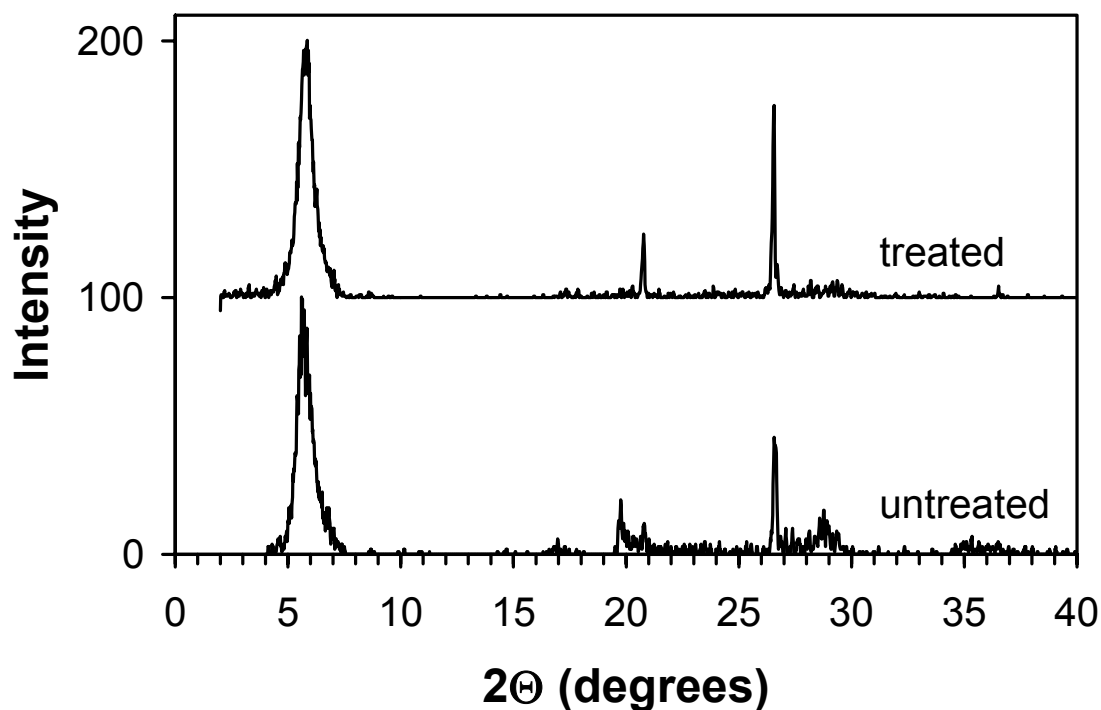


Figure B.2: X-ray diffraction patterns of untreated montmorillonite and montmorillonite pretreated by washing and size fractionation.

The X-ray diffraction pattern of the size fractionated and chemically washed material contains fewer and sharper peaks than the pattern of the untreated clay, indicating that the washing procedure removed some impurities (Fig. B.2). In a previous study using the same pre-treatment procedure for SWy-1 (SWy-2 is from the same geologic source as SWy-1), the surface area was confirmed as $31 \text{ m}^2 \text{ g}^{-1}$, the CEC was measured as $0.6\text{-}0.8 \text{ meq g}^{-1}$, and elemental analysis yielded the composition

(Ca_{0.001}Na_{0.707}K_{0.003})[Al_{3.04}Fe(III)_{0.41}Mg_{0.532}][Si_{7.85}Al_{0.147}]O₂₀(OH)₄ (McKinley et al., 1995). In the current work the BET surface area was measured for the received clay as 28.4 m² g⁻¹, but insufficient material was available to determine the surface area of the treated material accurately.

Additional reagents have been discussed in previous sections of this work. The X-ray diffraction and BET surface area analyses have also been discussed previously (Chapter 3).

B.2.2 Sorption Equilibrium

Before investigating the rates of adsorption and desorption, it was necessary to understand the equilibrium sorption of uranium on montmorillonite. Batch sorption experiments were carried out at two solution conditions: 1) 100 mM NaNO₃ at pH 6, and 2) 1 mM NaNO₃ at pH 4. Uranium-free clay suspensions were pre-equilibrated in polycarbonate centrifuge bottles at the specific pH and ionic strength for at least 48 hours with periodic pH adjustment with 1 mM nitric acid or sodium hydroxide if necessary. Following pre-equilibration of the clay suspensions, uranium was added to the suspensions from a uranyl nitrate stock solution, the pH was measured and adjusted if necessary, and the uranium-montmorillonite suspensions were mixed for at least 48 hours on a wrist action shaker. Samples for dissolved uranium were obtained by collecting and acidifying the last 5 mL of 10 mL of filtrate passed through 0.025 μm mixed cellulose ester membranes (Millipore). Unfiltered samples of whole suspension were also periodically collected and diluted 1:10 in 10% nitric acid to determine the total uranium concentration of the suspension, providing a check for uranium sorption to the centrifuge

bottle walls. Uranium concentrations were measured by inductively coupled plasma mass spectrometry (ICP-MS) as discussed in previous sections.

B.2.3 Sorption Kinetics

Sorption rates were investigated following a variety of perturbations of the solution chemistry, but the general methodology was consistent for all experiments. Suspensions were equilibrated for at least 48 hours before a perturbation of the solution chemistry. Samples for total and dissolved uranium concentrations in the pre-equilibrated suspensions were collected immediately prior to the perturbation. Following the perturbation, four samples were collected as quickly as possible in the first 15 minutes of the experiment and subsequent samples were collected over the next two days. Sampling techniques for total and dissolved uranium were the same as those discussed previously for batch equilibrium experiments.

Table B.1: Batch sorption kinetics experiments performed.

Expected Reaction	Pre-equilibration conditions				Perturbation
	pH	I (mM)	[U] _{tot} (μM)	[clay] (mg L ⁻¹)	
adsorption	6	100	0	50	Add 2 μM total uranium
adsorption	4	1	0	50	Add 20 μM total uranium
desorption	6	100	10	1000	1:10 dilution in U-free solution
desorption	4	1	150	1000	1:10 dilution in U-free solution
desorption	6	100	2	50	Add HNO ₃ to pH 4
adsorption	4	1	20	50	Add NaOH to pH 6
desorption	4	1	20	50	Add NaNO ₃ to 100 mM

Table B.1 lists the sorption kinetics experiments conducted. Adsorption rates were determined for both 100 mM NaNO₃ at pH 6 and 1 mM NaNO₃ at pH 4 by adding uranium to montmorillonite suspension and monitoring the decrease in the dissolved uranium concentration over time. In dilution-induced desorption experiments, pre-

equilibrated uranium-montmorillonite suspensions were diluted 1:10 in uranium-free solution. The responses of pre-equilibrated uranium-montmorillonite suspensions to changes in pH were investigated by both increasing the pH from 4 to 6 with sodium hydroxide and by decreasing the pH from 6 to 4 with nitric acid. The effect of ionic strength on sorption at pH 4 was studied by increasing the ionic strength of a pre-equilibrated uranium-montmorillonite suspension from 1 to 100 mM with sodium nitrate.

B.3 Results and Discussion

B.3.1 Equilibrium Sorption

At pH 6 and 100 mM ionic strength, the equilibrium sorption data fit the characteristic shape of a Langmuir isotherm (Fig. B.3a). Data included on the isotherm are from batch equilibrium sorption experiments, pre-equilibrated suspensions prior to initiating sorption kinetics experiments, and from the last samples collected in kinetics experiments. The data were fit to a Langmuir isotherm (1) with a sorption constant K_L of $2.5 \mu\text{M}^{-1}$ and maximum sorbed density Γ_{max} of $9.4 \mu\text{mol g}^{-1}$, where C and Γ are the dissolved and sorbed uranium concentrations respectively.

$$\Gamma = \frac{\Gamma_{\text{max}} K_L C}{1 + K_L C} \quad (1)$$

The data were fit by trial and error with visual optimization, though clearly a non-linear optimization procedure would have provided a more quantitative fit. The Langmuir isotherm assumes a single sorption site with a finite concentration, and at the high 100 mM ionic strength this is consistent with sorption occurring only at aluminol or silanol edge sites by inner-sphere complexation.

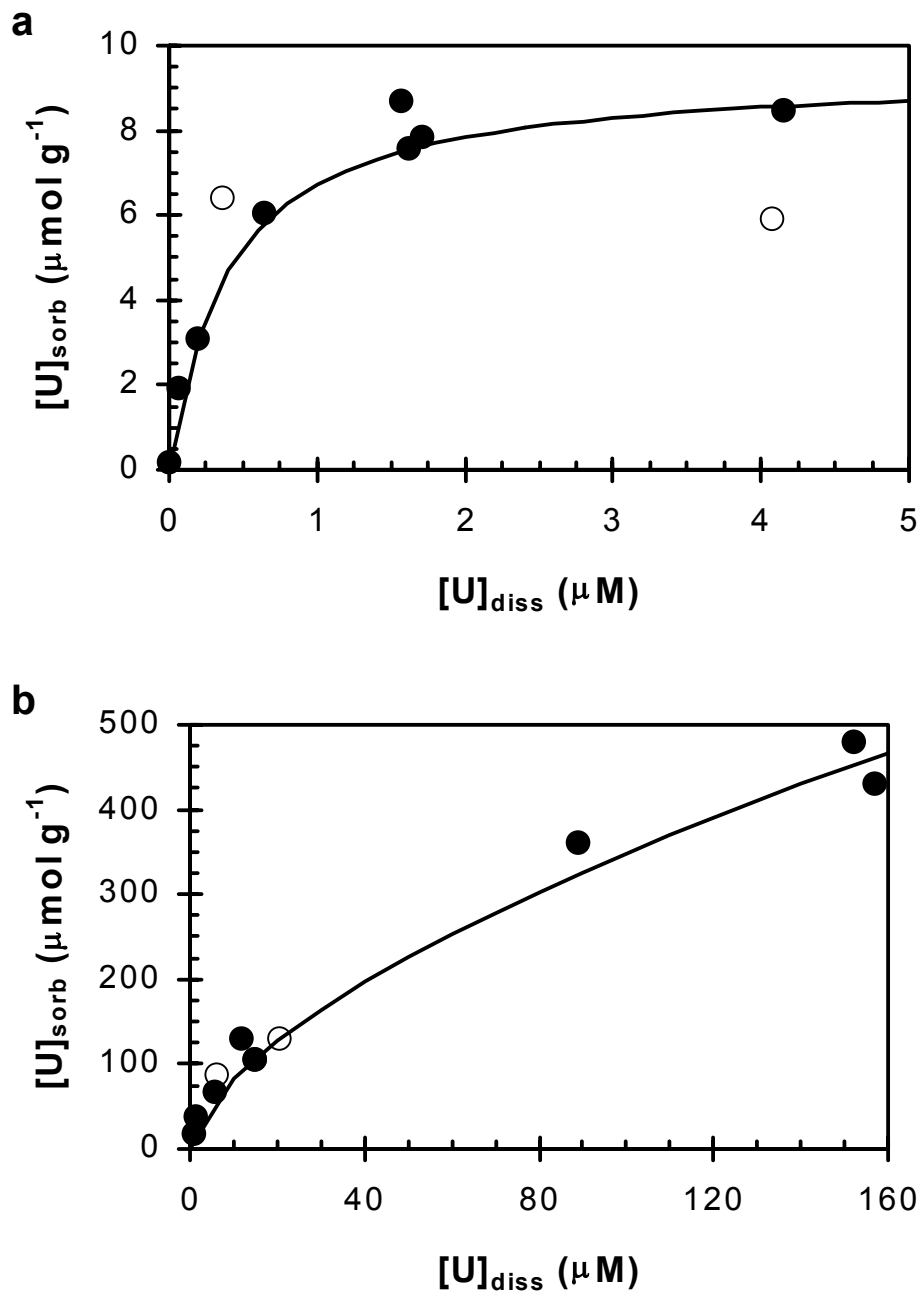


Figure B.3: Equilibrium sorption of uranium on montmorillonite at a) pH 6 and 100 mM NaNO₃ and b) pH 4 and 1 mM NaNO₃. Data are from batch equilibrium experiments (●) and dilution-induced desorption experiments (○). The lines are Langmuir (a) and Freundlich (b) isotherms fit to the experimental data.

At pH 4 and a lower ionic strength (1 mM), equilibrium sorption does not have the saturation behavior associated with the Langmuir isotherm, indicating that sorption is not occurring at sites with a finite concentration (Fig. B.3b). The sorption data are instead fit to a Freundlich isotherm (2) with values of $19.5 \mu\text{mol}^{1-n} \text{L}^n \text{g}^{-1}$ and 0.63 for K_F and n respectively, where C and Γ are the dissolved and sorbed uranium concentrations respectively.

$$\Gamma = K_F C^n \quad (2)$$

As seen in Figure B.3b and by the n value less than one, sorption becomes less favorable as the sorbed concentration increases. Sorption for pH 4 and 1 mM ionic strength is considered to be occurring only at fixed-charge sites, and the CEC should represent an upper limit for sorption to these sites. The highest sorbed uranium concentration measured was $480 \mu\text{mol g}^{-1}$ (0.48 mmol g^{-1} , 0.96 meq g^{-1} for UO_2^{2+} sorption) which is comparable to the CEC of $0.60\text{-}0.80 \text{ meq g}^{-1}$. The curvature of the isotherm at the highest sorbed concentration suggests that the interlayer was becoming saturated.

B.3.2 Adsorption Kinetics

Uranium adsorption to montmorillonite occurs rapidly for both solution conditions examined (Figure B.4). Following the addition of uranium to the montmorillonite suspensions, the dissolved concentration decreased dramatically within three minutes and then varied by less than 5% for the duration of the experiments. The sorbed concentration was calculated as the difference between the known total and measured dissolved concentrations, and the scatter in the sorbed concentration data is simply the result of subtracting one large number ($[\text{U}]_{\text{diss}}$) from another ($[\text{U}]_{\text{tot}}$). There

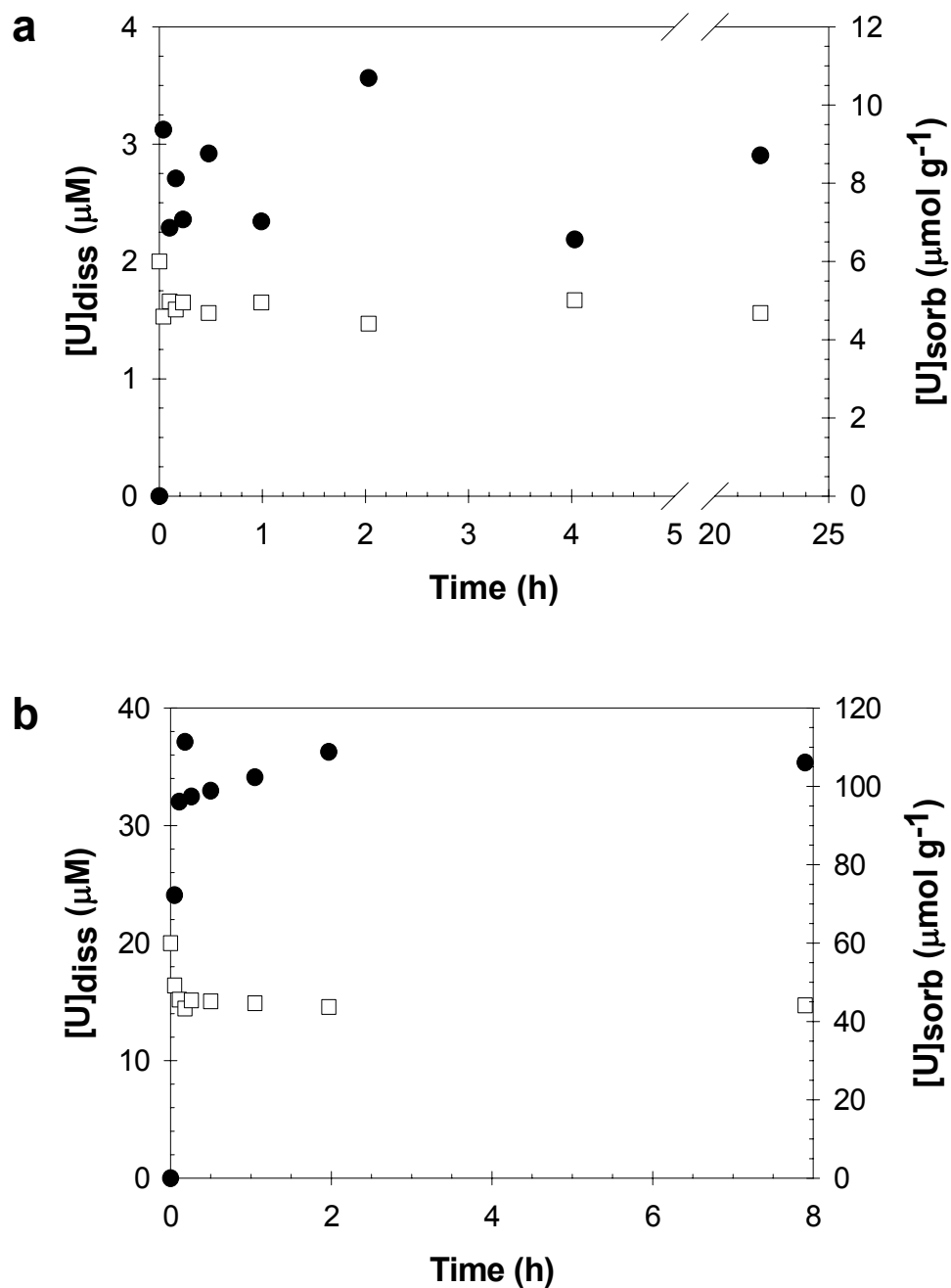


Figure B.4: Dissolved (\square) and adsorbed (\bullet) uranium concentrations during adsorption on montmorillonite: a) $[U]_{\text{tot}} = 2 \mu\text{M}$, 50 mg L^{-1} montmorillonite, pH 6.0 (buffered by 5 mM MES), and 100 mM NaNO_3 ; b) $[U]_{\text{tot}} = 20 \mu\text{M}$, 50 mg L^{-1} montmorillonite, pH 4.0, and 1 mM NaNO_3 .

does not appear to be any effect of the sorption mechanism on the rate of sorption for time-scales of minutes to hours. Sorption by ion exchange at fixed-charge sites might be

expected to occur more rapidly than by inner-sphere complex formation at edge sites because ion exchange does not require dehydration of the solvation shell of the sorbing uranyl species. Conversely, if diffusion into the interlayer of the montmorillonite clay were slow, then sorption by ion-exchange might be slower than by coordination to the more accessible edge sites.

B.3.3 Responses of Pre-equilibrated Suspensions to Dilution

After the dilution of uranium-loaded montmorillonite suspensions in uranium-free solution, the dissolved concentration decreases instantaneously, but the sorbed concentration in $\mu\text{mol g}^{-1}$ remains constant. As the diluted (in terms of both total uranium and clay) suspension moves towards a new equilibrium state, it is expected that uranium will desorb from the montmorillonite and the associated increase in the dissolved uranium concentration can be measured over time.

After diluting the suspension pre-equilibrated at pH 6 and 100 mM ionic strength in uranium-free solution, the sorbed uranium concentration actually increased slightly (Fig. B.5a). The conditions of the pre-equilibrated suspension ($[\text{U}]_{\text{diss}} = 4.08 \mu\text{M}$, $[\text{U}]_{\text{sorb}} = 5.92 \mu\text{mol g}^{-1}$) fall on the saturated plateau portion of the Langmuir isotherm (Fig. B.3a) and were not ideal for monitoring desorption. The equilibrium conditions established following the dilution ($[\text{U}]_{\text{diss}} = 0.36 \mu\text{M}$, $[\text{U}]_{\text{sorb}} = 6.41 \mu\text{mol g}^{-1}$) also fit reasonably well on the isotherm. The increase in the sorbed concentration may be an effect of the decrease in the clay concentration upon dilution. As the clay concentration decreased, the particles may have become more dispersed and the surface area available for sorption may have increased. Ideal conditions of a pre-equilibrated suspension for

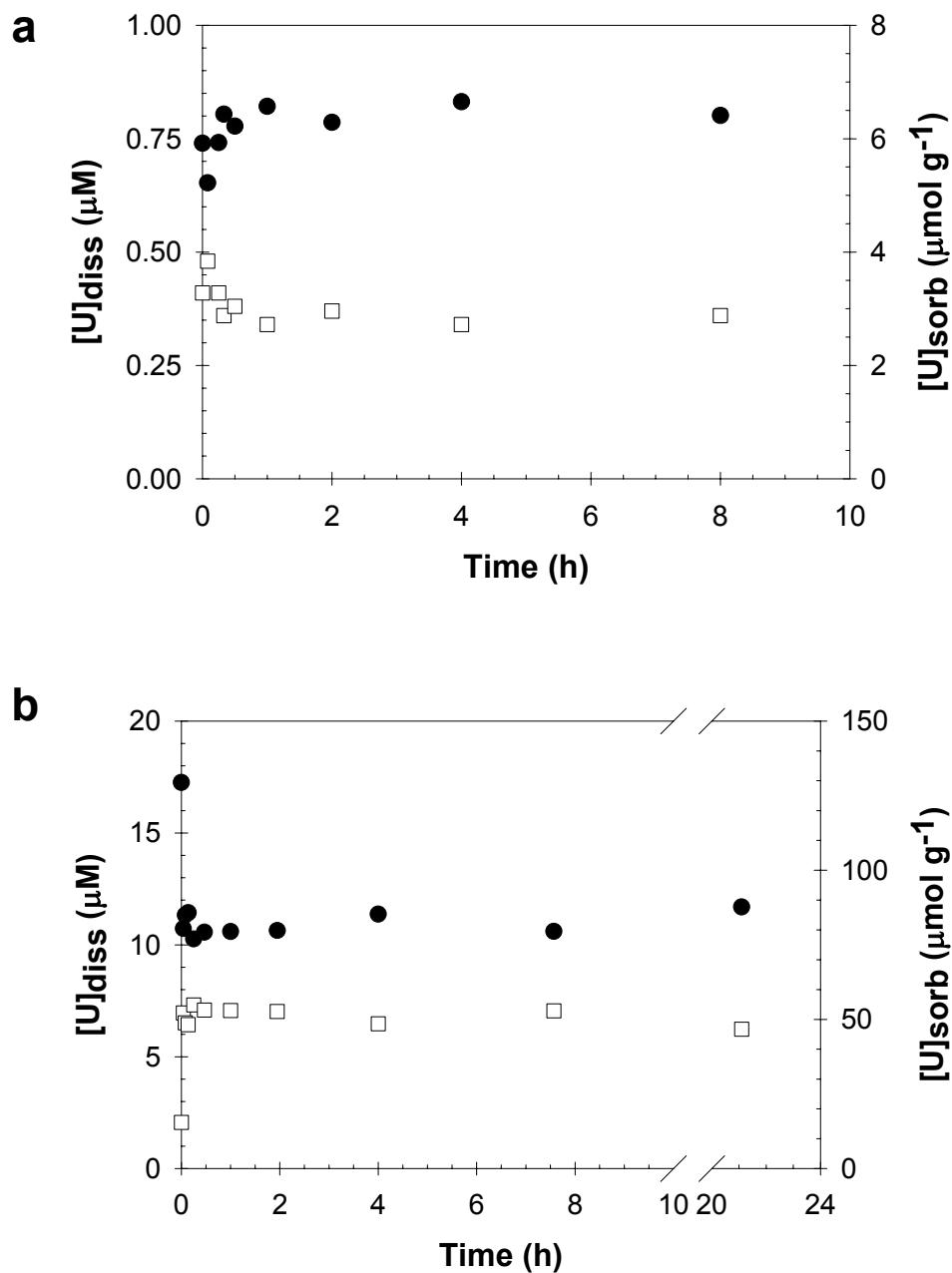


Figure B.5: Dissolved (\square) and adsorbed (\bullet) uranium concentrations following the 1:10 dilution of pre-equilibrated uranium-montmorillonite suspensions in uranium-free solution. Pre-equilibrated suspensions contained: a) $[U]_{\text{tot}} = 10 \mu\text{M}$, $[U]_{\text{diss}} = 4.08 \mu\text{M}$, $[U]_{\text{sorb}} = 5.92 \mu\text{mol g}^{-1}$, 1 g L^{-1} montmorillonite, pH 6.0 (buffered by 5 mM MES), and 100 mM NaNO_3 ; b) $[U]_{\text{tot}} = 150 \mu\text{M}$, $[U]_{\text{diss}} = 20.6 \mu\text{M}$, $[U]_{\text{sorb}} = 129 \mu\text{mol g}^{-1}$, 1 g L^{-1} montmorillonite, pH 4.0, and 1 mM NaNO_3 . The uranium-free solutions were at the same pH and ionic strength as the uranium-montmorillonite suspensions added to them.

dilution-induced desorption would fall near the top of the linear portion of the Langmuir isotherm.

The response of the suspension pre-equilibrated at pH 4 and 1 mM ionic strength to dilution was more in accord with expected behavior. Following the dilution, uranium desorbed rapidly from the montmorillonite, and a new equilibrium state was established on a time-scale faster than that of the earliest sample (2.5 minutes) (Fig. B.5b). Both the pre-equilibrated and post-dilution conditions fit the Freundlich isotherm quite well (Fig. B.3b).

B.3.4 Rates of Response to pH Adjustment

Uranium desorbed from a uranium-montmorillonite suspension pre-equilibrated at pH 6 and 100 mM ionic strength when nitric acid was added to decrease the pH to 4 (Fig. B.6a). The sorbed concentration appeared to initially drop rapidly and rebound, and then follow a slower decrease for the remainder of the experiment. The initial decrease may be the result of errors made in preparing samples for ICP-MS analysis. Other problems were found for samples analyzed during the same ICP-MS analysis session. Based on previously published work and results discussed in the next section, acidification of the suspension to pH 4 should have led to complete desorption of uranium from the montmorillonite. The pH was measured initially but was not monitored over the course of the experiment, and it is possible that the suspension was not sufficiently acidified to sustain pH 4 conditions. Clearly this experiment should be repeated to obtain better results which would allow an interpretation of the desorption rate following acidification.

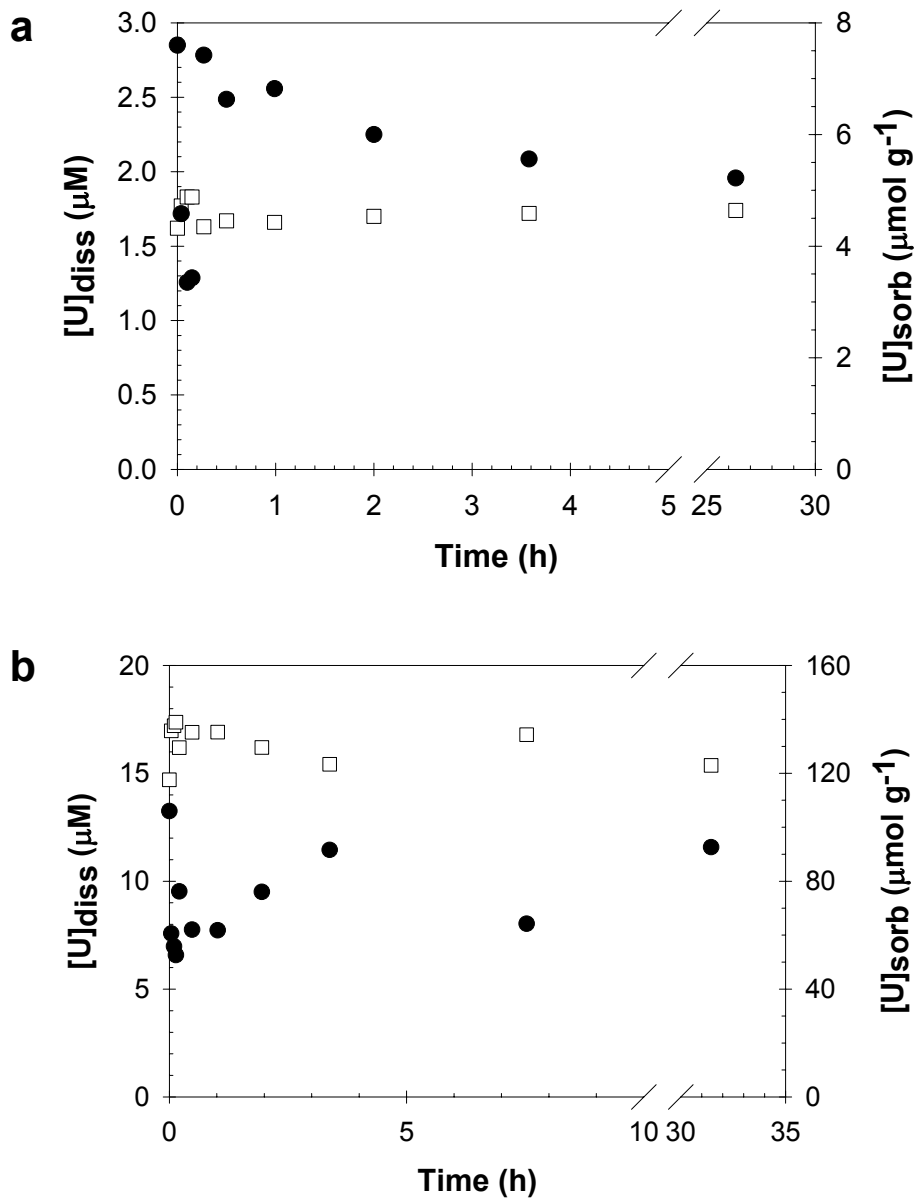


Figure B.6: Dissolved (\square) and adsorbed (\bullet) uranium concentrations following the pH adjustment of pre-equilibrated uranium-montmorillonite suspensions. a) pH adjusted from 6.0 to 4.0 with nitric acid for a pre-equilibrated suspension with $[U]_{\text{tot}} = 2.0 \mu\text{M}$, $[U]_{\text{diss}} = 1.62 \mu\text{M}$, $[U]_{\text{sorb}} = 7.60 \mu\text{mol g}^{-1}$, 50 mg L^{-1} montmorillonite, pH 6.0 (buffered by 5 mM MES), and 100 mM NaNO_3 ; b) pH adjusted from 4.0 to 6.0 with sodium hydroxide for a pre-equilibrated suspension with $[U]_{\text{tot}} = 20.0 \mu\text{M}$, $[U]_{\text{diss}} = 14.7 \mu\text{M}$, $[U]_{\text{sorb}} = 106 \mu\text{mol g}^{-1}$, 50 mg L^{-1} montmorillonite, pH 4.0 (with 5 mM MES), and 1 mM NaNO_3 .

When a suspension at pH 4 and 1 mM ionic strength was increased to pH 6 by addition of sodium hydroxide, the dissolved and sorbed concentrations changed only

slightly (Fig. B.6b). As the pH increased from 4 to 6 and the ionic strength remained low, sorption at edge-sites should have become more favorable and uranium previously sorbed at fixed-charge exchange sites may have redistributed to the edge-sites. An initial increase in the dissolved uranium concentration may be the result of the sodium from the sodium hydroxide displacing uranium from fixed-charge sites. The final dissolved uranium concentration of 15 μM may be supersaturated with respect to schoepite (Chapter 5), but for only a few days of contact this dissolved concentration may reasonably be controlled by a metastable sorption state similar to that observed for goethite (Chapter 3).

B.3.5 Rates of Ion-exchange

The addition of sodium nitrate to a pre-equilibrated suspension at pH 4 and initially 1 mM ionic strength leads to the ion exchange of sodium ions for uranium ions at the fixed-charge sites in the interlayer. This ion-exchange was rapid and led to nearly-complete desorption of uranium from the montmorillonite (Fig. B.7). This rapid rate of ion-exchange is consistent with the earlier observation of rapid adsorption of uranium to fixed-charge sites at pH 4 and 1 mM ionic strength. The montmorillonite interlayers are readily accessible to ions in solution and there are no apparent diffusion limitations to uptake or release.

B.3.6 Environmental Implications

As was also the case with goethite, uranium adsorption and desorption on montmorillonite are very rapid processes. In reactive transport modeling, local

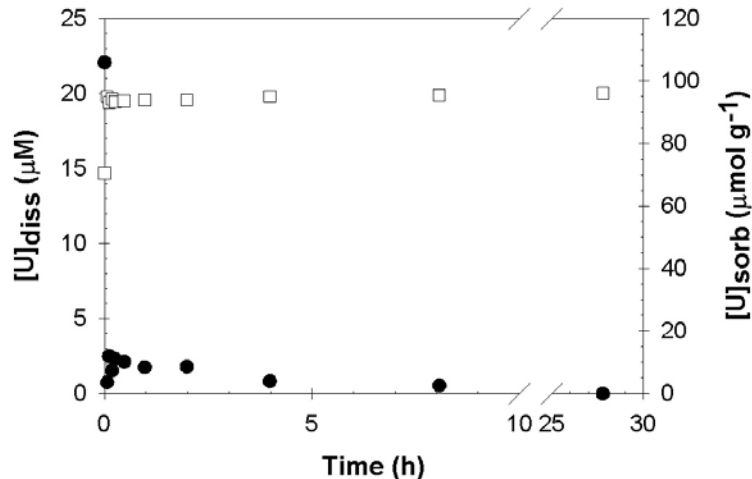


Figure B.7: Dissolved (\square) and adsorbed (\bullet) uranium concentrations following the addition of sodium nitrate to adjust the ionic strength of a pre-equilibrated uranium-montmorillonite suspension from 1 mM to 100 mM. The pre-equilibrated suspension contained $[U]_{\text{tot}} = 20.0 \mu\text{M}$, $[U]_{\text{diss}} = 14.7 \mu\text{M}$, $[U]_{\text{sorb}} = 106 \mu\text{mol g}^{-1}$, 50 mg L^{-1} montmorillonite, pH 4.0 (with 5 mM MES), and 1 mM NaNO_3 .

equilibrium can be assumed and sorption rate constants do not need to be incorporated in models. In soil-washing technologies, chemical desorption from mineral surfaces should not be a rate-limiting step. However, slow release from actual soils may result from physical mass transfer processes. For example, the low hydraulic conductivity of clays may make sorbed uranium inaccessible to infiltrating solutions.

Equilibrium sorption experiments have demonstrated the high sorption capacity of montmorillonite, especially when interlayer exchange sites are accessible. In groundwaters, the dissolved ion composition can have a large influence on the extent of uranium sorption on montmorillonite. In the current study, only sodium has been considered as an exchanging ion for uranium, but in natural systems potassium, magnesium, and calcium may also be important. These additional cations can both displace uranium from fixed-charge sites and may, especially in the case of divalent or trivalent cations, alter the sorption behavior by compressing the interlayer spacing.

Appendix C

URANIUM RELEASE FROM MIXED GOETHITE-SCHOEPITE SYSTEMS

* performed as part of Yi-Ping Liu's 1999 SURF research

C.1 Introduction

The iron oxyhydroxide goethite (α -FeOOH) is a common soil mineral and important sorbent for heavy metals and radionuclides in the environment. The rates of uranium sorption and surface-precipitation on goethite were discussed in Chapter 3, and the characterization of highly loaded uranium-goethite suspensions by electron microscopy was presented in Chapter 4. Schoepite $((\text{UO}_2)_8\text{O}_8(\text{OH})_{12}\cdot 12\text{H}_2\text{O})$ is a uranyl oxide hydrate with a structure consisting of sheets of edge- and corner-sharing pentagonal uranyl bipyramids with water molecules occupying the interlayer space. The rates of schoepite dissolution and transformation were discussed in Chapter 5.

As discussed in Chapter 1, uranium in porous media is distributed among dissolved, sorbed, and precipitated phases. At low dissolved uranium concentrations, uranium may be adsorbed to mineral surfaces and the precipitation of uranium-containing minerals is unlikely. At higher dissolved uranium concentrations, solid-associated uranium may occur as both sorbed and precipitated phases. Sorbed and precipitated

phases were observed following the incremental loading of goethite suspensions with uranium as examined in Chapters 3 and 4. During the drying of soils in the vadose zone, the dissolved uranium concentration in the porewater will increase due to evaporative concentration and uranium-containing precipitates like schoepite may form.

The central hypothesis guiding this overall work is that the rate of uranium release from solid phases is governed by the solid phase speciation (i.e., sorbed versus precipitated). This hypothesis was verified by work showing the rapid desorption of uranium from mineral surfaces (Chapter 3 and Appendix B) and the slower time-scales for dissolution of uranium-containing minerals (Chapters 5-7). A natural next step is an investigation of the rates of uranium release from solids containing both sorbed and precipitated uranium. Such solids could be prepared by incrementally adding uranium to a sorbent suspension as in Chapter 3, evaporatively concentrating uranium-sorbent suspensions, or by directly mixing a mineral sorbent and a uranium-containing mineral. The last method, by far the simplest, was employed in preparing the mixed goethite-schoepite suspensions examined in this Appendix.

The work discussed presently was actually performed before the surface-precipitation studies and systematic investigations of mineral dissolution rates. The simple mixed goethite-schoepite suspensions allowed a quick check of the central hypothesis that different time-scales should be observed for desorption and dissolution. By working with samples with known distributions of uranium between sorbed and precipitated phases, the utility of analytical techniques for characterizing solid-associated uranium was also evaluated.

C.2 Materials and Methods

Goethite was prepared as discussed in Chapter 3 by the hydrolysis of a ferric salt solution with strong base to precipitate amorphous ferric hydroxide, which was subsequently heated to transform the solid to goethite. The solid was identified as goethite by X-ray diffraction and its surface area was measured by BET nitrogen adsorption. Schoepite was prepared as discussed in Chapter 5 by the addition of a strong base to a uranyl nitrate solution to reach pH 6. The schoepite used in the work discussed here is referred to as Na-synthesis #2 in Chapter 5. Other reagents used in this work include sodium nitrate and the pH buffer 2-(n-morpholino)ethanesulfonic acid (MES). A laboratory purification system (Millipore) supplied water with 18.2 M Ω -cm resistivity.

Mixed goethite-schoepite suspensions were prepared by adding aliquots of schoepite stock suspension to goethite suspensions with 0.1 M NaNO₃ and buffered at pH 6 with 5 mM MES. The goethite and total uranium concentrations of the mixed suspensions prepared in this work are compiled in Table C.1. The stock goethite-schoepite suspensions were aged for two weeks to allow the schoepite to dissolve partially, leading to a redistribution of uranium among the dissolved, sorbed, and precipitated phases. Uranium release experiments were initiated by diluting aliquots of the goethite-schoepite stock suspensions into volumes of 0.1 M NaNO₃ solution buffered at pH 6. In addition to collecting samples over the course of an experiment, the stock goethite-schoepite suspensions were sampled immediately before portions were diluted in uranium-free solution. Samples were collected for both dissolved and total uranium concentrations. For measurements of dissolved uranium, samples were filtered through

0.2 μm polycarbonate membrane filters (Millipore) and acidified to 1% nitric acid. For measurements of total uranium, samples were first acidified with nitric acid to completely dissolve and desorb uranium and then filtered to remove goethite particles. Uranium concentrations were determined by inductively coupled plasma mass spectrometry (ICP-MS) on an HP4500 instrument.

Table C.1: Goethite-schoepite mixed suspensions. Equilibrated at pH 6 (buffered with 5 mM MES) in 0.1 M NaNO_3 solution.

Mixture (#)	[goethite] (g L^{-1})	TOTU (μM)	U_{diss} (μM)	Uranium Distribution (%)		
				Diss.	Sorb. ^a	Precip. ^b
1	5.05	5360	23.0	0.4	10.1	89.5
2	5.05	1060	7.4	0.7	45.2	54.1
3	5.05	622	1.3	0.2	42.6	57.2
4	5.05	7140	11.6	0.2	7.1	92.7

^a calculated using equation 2

^b calculated using equation 3

In addition to measuring the dissolved and total uranium concentrations in the stock goethite-schoepite suspensions, the filtered solids present from the suspensions were air-dried at room temperature and characterized. Solids were examined with X-ray diffraction (XRD) to look for the relative intensities of schoepite and goethite diffraction patterns. Imaging and elemental analysis of some carbon-coated solids were performed by scanning electron microscopy (SEM) with energy dispersive X-ray analysis (EDX). Details of the techniques and instruments used for XRD and SEM-EDX have been presented earlier.

C.3 Results and Discussion

C.3.1 Characterization of Stock Goethite-Schoepite Suspensions

The total and dissolved uranium concentrations in the goethite-schoepite stock suspensions were determined immediately before the initiation of dilution-induced release experiments (Table C.1). Table C.1 also lists the distribution of uranium between the dissolved, sorbed, and precipitated phases. The dissolved uranium concentration was measured and the total uranium concentration was known from analysis of the stock schoepite suspension used to add uranium to the mixed suspensions. The sorbed uranium concentration was calculated with the Langmuir Isotherm (1 and 2) determined in Chapter 3 and assuming that the dissolved and sorbed phases were in equilibrium, a reasonable assumption considering the rapid adsorption kinetics observed in Chapter 3.

$$\Gamma = \frac{114.4 \cdot 0.653 \cdot C_{\text{diss}}}{1 + 0.653 \cdot C_{\text{diss}}} = \text{Sorbed Concentration, } [\mu\text{mol} \cdot \text{g}^{-1}] \quad (1)$$

$$C_{\text{sorb}} = \Gamma \cdot [\text{goethite}] = \text{Sorbed Concentration, } [\mu\text{M}] \quad (2)$$

$$C_{\text{ppt}} = C_{\text{tot}} - C_{\text{diss}} - C_{\text{sorb}} = \text{Precipitated Concentration, } [\mu\text{M}] \quad (3)$$

The precipitated uranium concentration was then calculated by difference (3).

The equilibrium dissolved uranium concentration in all of the suspensions should be controlled by the solubility of the schoepite precipitate. This dissolved concentration should be the same for all of the goethite-schoepite suspensions regardless of the distribution among the dissolved, sorbed, and precipitated phases. The dissolved uranium concentrations of the stock suspensions ranged from 1.3 to 23 μM , indicating that at least some of the mixtures were probably undersaturated with respect to schoepite. An exact definition of undersaturated conditions can not be made, because an equally broad range

of dissolved concentrations has been observed in equilibrium with schoepite at pH 6: 2-3 μM for surface-precipitated schoepite (Chapter 3) and 3-42 μM for pure schoepite (Chapter 5).

The solids in the mixed goethite-schoepite stock suspensions were also analyzed by XRD and SEM-EDX. Diffraction maxima corresponding to both goethite and schoepite are visible in the XRD patterns (Fig. C.1), and the relative intensities of the dominant goethite (21.5°) and schoepite (12°) peaks scale according to the relative concentrations of goethite and schoepite in the systems. This simple experiment demonstrates that XRD is an effective technique for phase identification, and that XRD can be used to qualitatively examine the relative abundances of goethite and schoepite in a sample. Two distinct phases were also observed in scanning electron microscope images (Fig. C.2b) of solids from a mixed goethite-schoepite suspension (mixture 2). Using EDX, the bright particles were identified as uranium-rich particles, presumably schoepite, and the fine-grained material was identified as iron-rich goethite. In a uranium-loaded sample with solid-associated uranium present only as a sorbed phase, only the fine-grained goethite particles were observed in the SEM image (Fig. C.2a). Some larger particles were observed in the sorbed-uranium sample, but were sodium-rich and contained no uranium, suggesting that they resulted from precipitation of the sodium nitrate electrolyte during drying of the sample.

It is interesting to note that the XRD patterns for the aged goethite-schoepite suspensions show only the peaks for goethite and schoepite, but no peaks for the sodium uranyl oxide hydrate clarkeite. During the dissolution of schoepite in goethite-free suspensions, the presence of 0.1 M NaNO_3 ultimately induced the precipitation of a

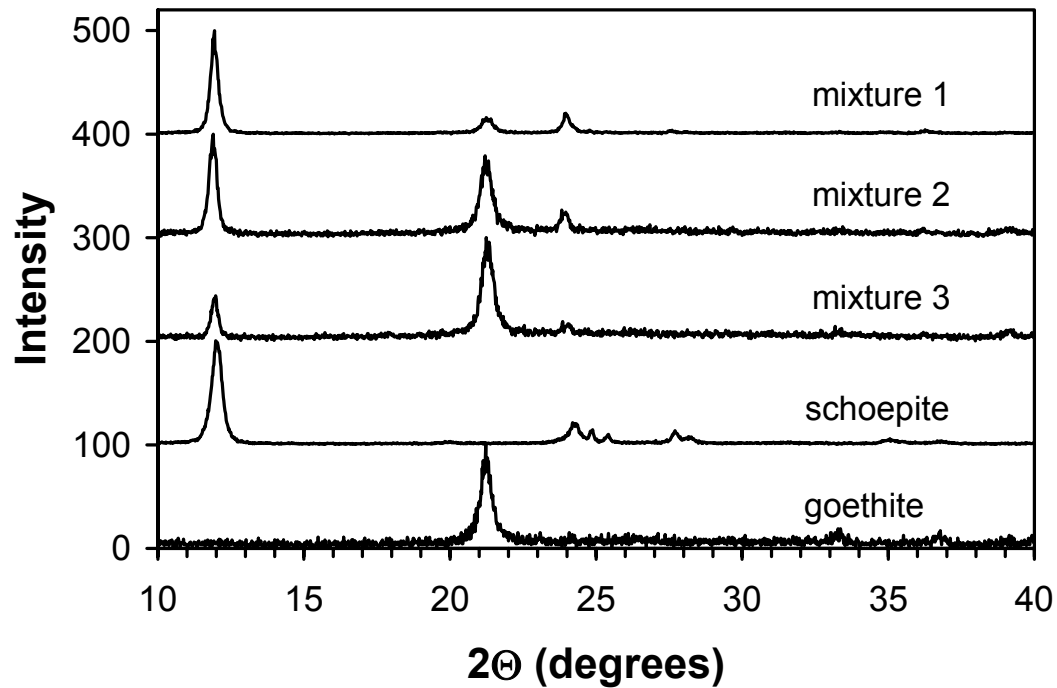


Figure C.1: X-ray diffraction patterns of solids collected from mixed suspensions of schoepite and goethite and the patterns for the stock suspensions from which mixtures were prepared. The uranium contents of mixtures increases from bottom to top: mixture 3 (622 μM), mixture 2 (1060 μM), mixture 1 (5360 μM). All suspensions contained 5.05 g L^{-1} goethite buffered at pH 6 (5 mM MES) in 0.1 M NaNO_3 .

clarkeite-like phase (Chapter 5). It seems that the presence of goethite may inhibit the formation of clarkeite. Schoepite peaks were also the only uranium-containing mineral peaks observed for the uranium-goethite suspensions in surface-precipitation experiments aged for as long as 13 months (Chapter 3). The mechanism by which goethite stabilizes schoepite particles is unknown, but interfacial surface energies may be key parameters. In Chapter 5, it was suggested that the high solubility of schoepite may be due to the high interfacial surface energy associated with the high surface area of very small particles. Through interactions with goethite, the schoepite may have a lower interfacial surface energy and consequently a lower solubility. If the schoepite is more stable (i.e., less

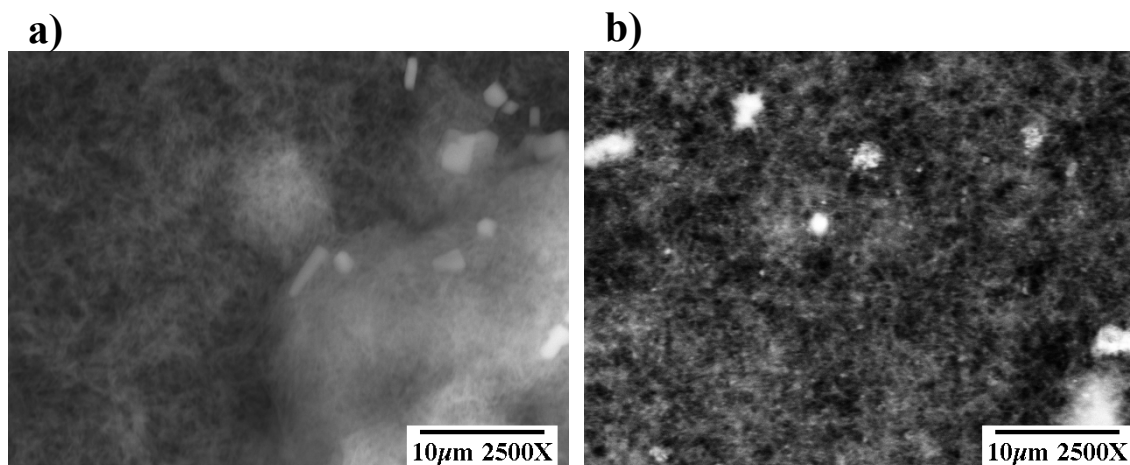


Figure C.2: Scanning electron micrographs of solids collected from suspensions with a) 0.50 g L⁻¹ goethite with adsorbed uranium (21 μmol g⁻¹) and b) 5.05 g L⁻¹ goethite with 0.34 g L⁻¹ schoepite added ([U]_{tot} = 1060 μM). Both suspensions were buffered at pH 6 (5 mM MES) and contained 0.1 M NaNO₃. Energy dispersive X-ray analysis identified the large crystals in (a) as a sodium-rich phase (probably NaNO₃) and the bright particles in (b) as a uranium-rich phase.

soluble) in goethite suspensions, then schoepite may be a thermodynamically more stable phase than clarkeite at 0.1 M NaNO₃.

C.3.2 Release of Uranium Following Dilution

Following the dilution of aliquots of mixed goethite-schoepite stock suspensions into uranium-free solution, the dissolved uranium concentration increased as uranium was released from sorbed and precipitated phases (Fig. C.3). Dissolved uranium concentrations were measured, and the sorbed and precipitated uranium concentrations were calculated using equations 1-3 presented in the previous section.

Uranium release following the 1:1000 dilution of mixture 1 followed two distinct time-scales. Initial uranium-release to solution occurred rapidly with dissolved uranium concentrations increasing from 0.02 μM to 0.35 μM within one minute. The dissolved uranium concentration then increased more slowly from 0.35 μM at ten minutes to 4.0

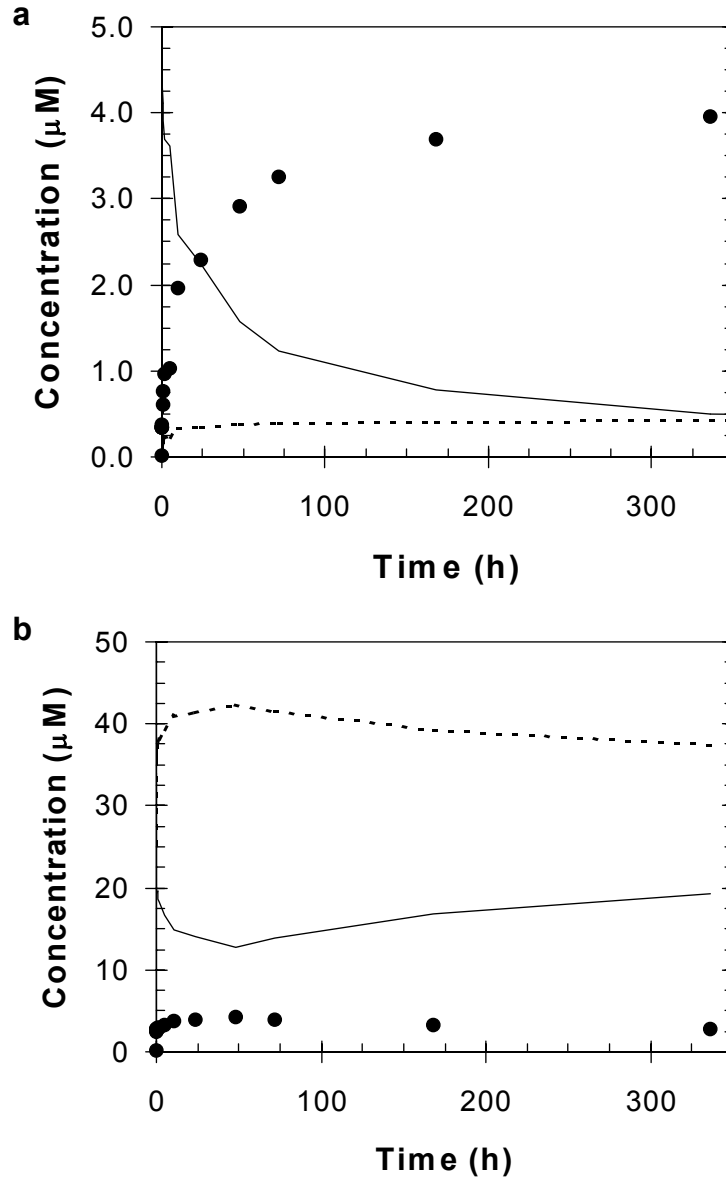


Figure C.3: Evolution of the uranium distribution following the dilution of equilibrated goethite-schoepite suspensions in 0.1 M NaNO₃ solution buffered at pH 6 (5 mM MES): a) 1:1000 dilution of mixture 1 b) 1:10 dilution of mixture 3. Dissolved uranium (●) was measured, sorbed uranium (dashed line) was calculated from the Langmuir isotherm, and precipitated uranium (solid line) was calculated by difference (total - sorbed - dissolved).

µM after two weeks. The short initial time-scale is interpreted as both a rapid initial dissolution period (also observed in Chapter 5-6) as well as desorption from the uranium surface. The slower continuing release of uranium to solution was the result of schoepite

dissolution towards a final concentration of 4.0 μM (observed at three weeks, data not shown). The total uranium concentration in the diluted suspension was only 5.4 μM and, although a trace amount of precipitated uranium is calculated at the end of the experiment, it is likely that the schoepite had dissolved completely.

Uranium release following the 1:10 dilution of mixture 3 had a single fast phase. The dissolved uranium concentration increased from 0.1 μM to 2.5 μM within 30 seconds. The dissolved concentration then increased and decreased slightly over the duration of the experiment (two weeks), but was always within the range 2.5-4.2 μM . The rapid release of uranium to solution for mixture 3 is attributed to rapid schoepite dissolution.

The observations of rapid desorption kinetics and biphasic dissolution kinetics are consistent with the results of the pure desorption and dissolution/precipitation experiments discussed earlier. Sorption plays an important role in taking up uranium released during dissolution, but sorption rates are essentially instantaneous when compared with the rate-limiting dissolution process.

Appendix D

Becquerelite Dissolution and Transformation

* performed as part of Yi-Ping Liu's 1999 SURF research

D.1 Introduction

Becquerelite is a calcium uranyl oxide hydrate mineral with the composition $\text{Ca}(\text{UO}_2)_6\text{O}_4(\text{OH})_6 \cdot 8\text{H}_2\text{O}$. Like most of the uranyl oxide hydrate minerals, becquerelite has a sheet structure. The sheets are composed of edge- and corner-sharing uranyl pentagonal bipyramids and the interlayers between sheets are occupied by calcium ions and water molecules (Burns, 1999). Because of the high calcium concentrations in many groundwaters, becquerelite is widely found in the weathered zones of uranium ore deposits as a secondary mineral formed following the oxidation of uraninite (Finch and Murakami, 1999). Becquerelite was also identified as one of the corrosion products of synthetic uranium (IV) oxide ($\text{UO}_2(\text{s})$) exposed to calcium-rich groundwater in unsaturated experiments (Wronkiewicz and Buck, 1999).

In the paragenetic sequence of uranyl minerals observed at ore deposits and in the corrosion of spent nuclear fuel, becquerelite forms following the initial precipitation of schoepite. In laboratory experiments, schoepite readily transformed into becquerelite in the presence of dissolved calcium (Sandino and Grambow, 1994; Sowder et al., 1996; Sowder et al., 1999; Vochten and Van Haverbeke, 1990). In contact with groundwaters

rich in dissolved silica or phosphate, becquerelite is ultimately replaced by uranyl silicate or phosphate minerals (Finch and Murakami, 1999).

The solubility products of synthetic (Sandino and Grambow, 1994; Vochten and Van Haverbeke, 1990) and natural (Casas et al., 1994; Casas et al., 1997) becquerelite have been determined in laboratory experiments with results differing by more than fourteen orders of magnitude. Becquerelite dissolution in dilute solution was incongruent with the ratio of calcium to uranium released in excess of the stoichiometric 1:6 ratio (Casas et al., 1994).

In the present work, becquerelite was prepared from synthetic schoepite. Batch dissolution experiments were conducted to determine the dissolution rate and the equilibrium solubility of the synthetic becquerelite. Dissolution experiments were conducted in both calcium-free and calcium-rich solutions.

D.2 Materials and Methods

Becquerelite was synthesized from schoepite (Na-synthesis #2 in Chapter 5) by reaction with 1 M calcium nitrate (Alfa Aesar) at a 4:1 uranium to calcium ratio for four days at 90° C. The aged suspension was washed by repeated centrifugation and resuspension in deionized water. Material from the becquerelite stock suspension was measured by X-ray diffraction (XRD) using a Scintag Pad V X-ray powder diffractometer with a Cu k-alpha X-ray source and germanium detector and by Raman spectroscopy with a 782 nm diode laser on a Renishaw MicroRaman Spectrometer with a spectral resolution of 1 cm⁻¹. XRD was performed within weeks of the synthesis, but Raman measurements were performed more than a year after the synthesis. Portions of

the stock suspension were digested in 10% nitric acid and analyzed for uranium and calcium. Concentrations of calcium and uranium in the stock suspension and in samples collected during batch dissolution were determined by inductively coupled plasma mass spectrometry (ICP-MS) on an HP4500 instrument.

Only batch dissolution experiments were conducted. Dissolution experiments were initiated by adding an aliquot of becquerelite stock suspension to 0.1 M NaNO_3 solution buffered at pH 6 with 5 mM MES. Experiments were conducted with 0.01, 0.10, and 0.50 M $\text{Ca}(\text{NO}_3)_2$ added to the solutions, and a pair of experiments were also conducted with no additional calcium. Samples for dissolved uranium and calcium were filtered with 0.2 μm polycarbonate filter membranes (Millipore) and acidified to 1% nitric acid, and samples of suspension for total concentrations were dissolved completely in 10% nitric acid.

D.3 Results

D.3.1 Characterization of Synthetic Becquerelite

The two dominant X-ray diffraction peaks shifted to lower 2θ values (i.e., larger lattice spacings) following the reaction of schoepite with 1 M $\text{Ca}(\text{NO}_3)_2$, indicating that becquerelite was formed (Fig. D.1). The measured and reference patterns for synthetic schoepite and becquerelite are presented in Table D.1, which shows that the measured becquerelite pattern matches well with reference patterns for either synthetic (card #29-0389) or natural (card #13-0405) becquerelite (JCPDS-ICDD, 1999). Digestion and elemental analysis by ICP-MS found that the synthetic becquerelite incorporated calcium;

Table D.1: X-ray diffraction reflections of synthetic uranyl oxide hydrate solids and reference data for related minerals.

Card #	Name/Formula	Dominant Diffraction Maxima (Å)			
		(indexed reflection)			
Synthetic Schoepite (Na-synthesis #2)		7.29	3.65	2.43	1.83
Synthetic Becquerelite		7.46	3.73	3.60	2.48
43-0364	metaschoepite, synthetic $\text{UO}_3 \cdot 2\text{H}_2\text{O}$	$7.33_{(002)}$	$3.67_{(004)}$	$3.58_{(240)}$	$3.22_{(242)}$
29-0389	becquerelite, synthetic $\text{Ca}(\text{UO}_2)_6\text{O}_4(\text{OH})_6 \cdot 8\text{H}_2\text{O}$	$7.49_{(002)}$	$3.74_{(312)}$	$3.55_{(230)}$	$3.21_{(232)}$
13-0405	becquerelite, natural $\text{Ca}(\text{UO}_2)_6\text{O}_4(\text{OH})_6 \cdot 8\text{H}_2\text{O}$	$7.44_{(002)}$	$3.73_{(123)}$	$3.54_{(230)}$	$3.20_{(024)}$

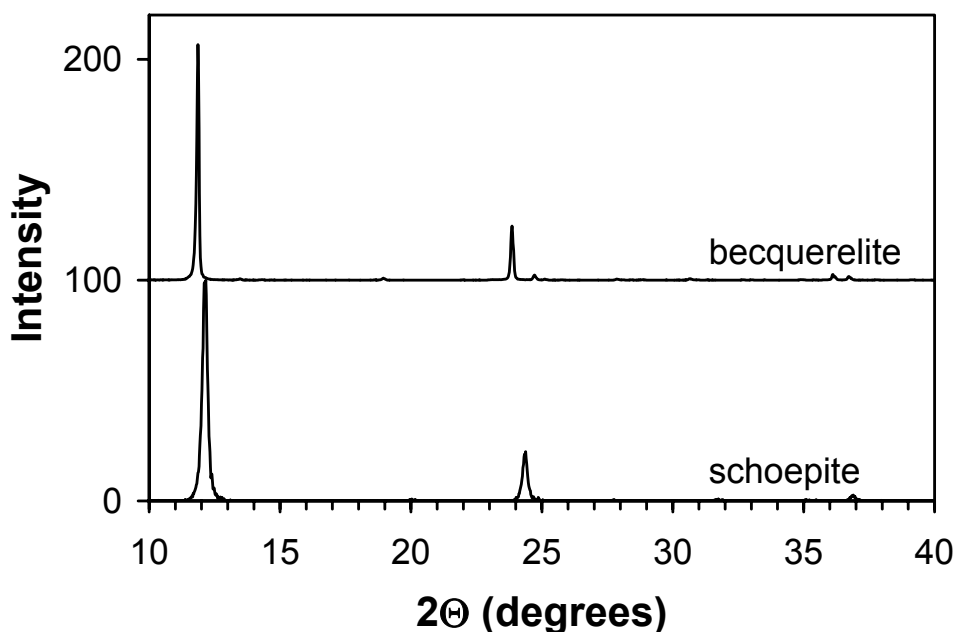


Figure D.1: X-ray diffraction patterns of becquerelite and the schoepite from which it was formed.

the calcium to uranium ratio for becquerelite was expected to be 1:6, but the ratio was measured as 1:7.4. Becquerelite crystals (Fig. D.2) were observed with SEM that are much larger than those observed for the original schoepite (Chapter 5), which is further evidence of becquerelite formation. The Raman spectrum of solids from the becquerelite suspension, albeit collected more than year after the synthesis, was also distinct from the

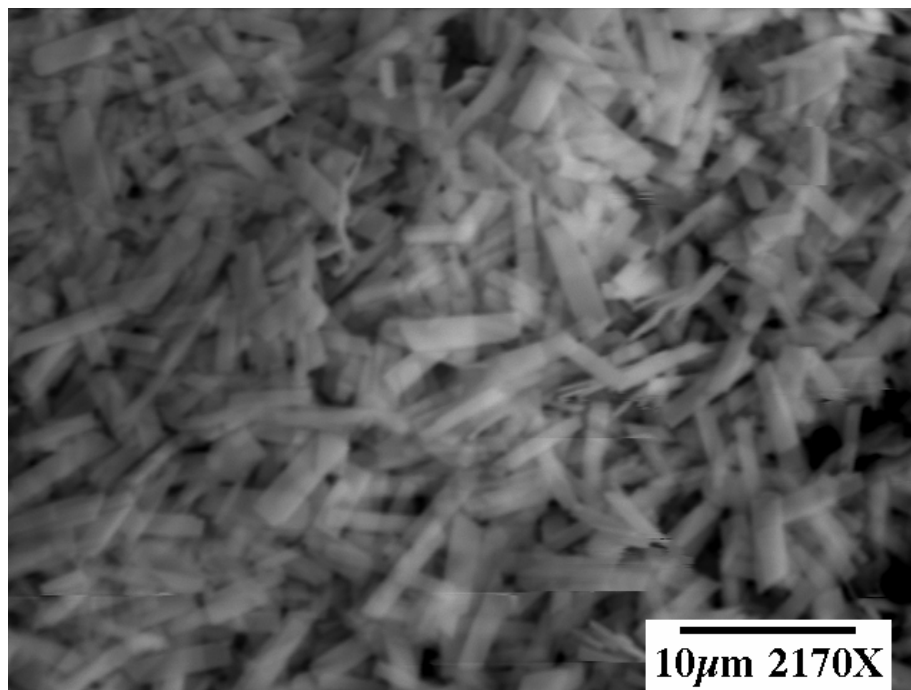


Figure D.2: Scanning electron micrograph of solids from becquerelite synthesis.

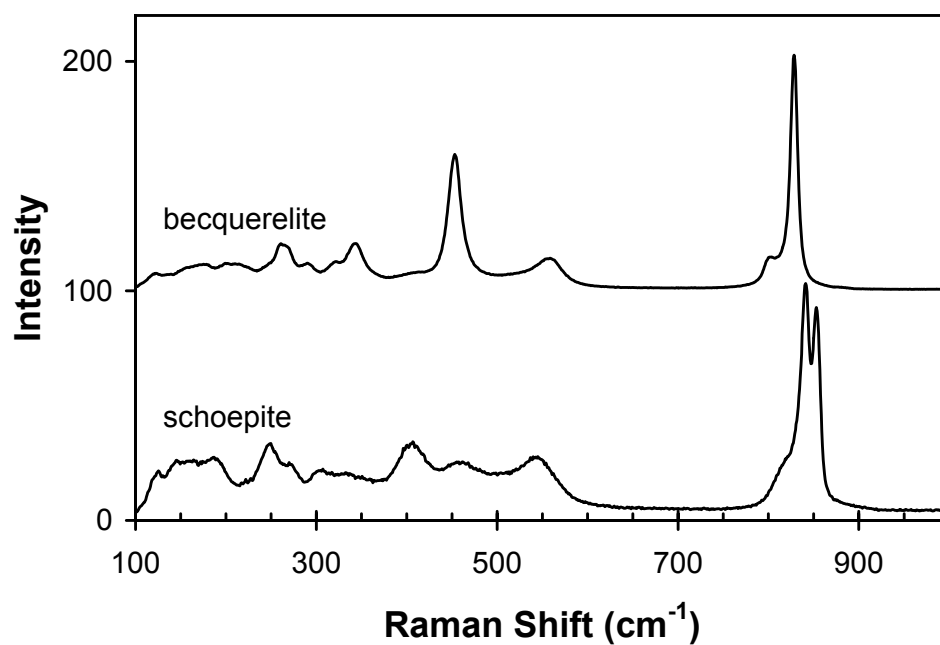


Figure D.3: Raman spectra of schoepite and becquerelite measured with 782 nm diode laser. The dominant peaks in the 750-900 cm⁻¹ region are associated with the symmetric uranyl ion stretch. Lower wavenumber peaks are associated with uranyl bending vibrations and uranium-equatorial oxygen vibrations.

spectrum for schoepite (Fig. D.3). In both spectra, the dominant peaks are those related to the symmetric uranyl ion stretch: for schoepite occurring at 841 and 853 cm^{-1} and for becquerelite occurring at 829 cm^{-1} with a shoulder at a slightly lower wavenumber.

D.3.2 Batch Dissolution Experiments

Batch dissolution in the absence of a calcium nitrate background (Fig. D.4a) was initially rapid, with dissolved uranium concentrations reaching at least 7 μM within 11 hours. The dissolved uranium concentration then increased nearly linearly with time until dropping precipitously between 334 and 672 hours. Once the uranium had reprecipitated from solution, the dissolved concentration was constant at 2.5-3.4 μM for the duration of the experiment. The dissolved calcium concentration increased with an approximately one to one relationship with dissolved uranium, a clear indication of incongruent dissolution. The calcium was ultimately released entirely from the solid phase, and the complete release of calcium roughly coincided with the reprecipitation of uranium.

In the presence of background calcium (Fig. D.4b), dissolution proceeded more slowly and was not subject to a dramatic reprecipitation event as in the absence of background calcium. Following an initial rapid increase in the dissolved uranium concentration, the concentration increased more slowly over the course of the experiment. For 0.01 and 0.10 M background calcium concentrations, some reprecipitation of uranium was observed. Nearing the completion of the dissolution experiments, the dissolved uranium concentrations reached stable values of 1.6, 1.8 and 3.0 μM for 0.01, 0.10, and 0.50 M background calcium concentrations respectively.

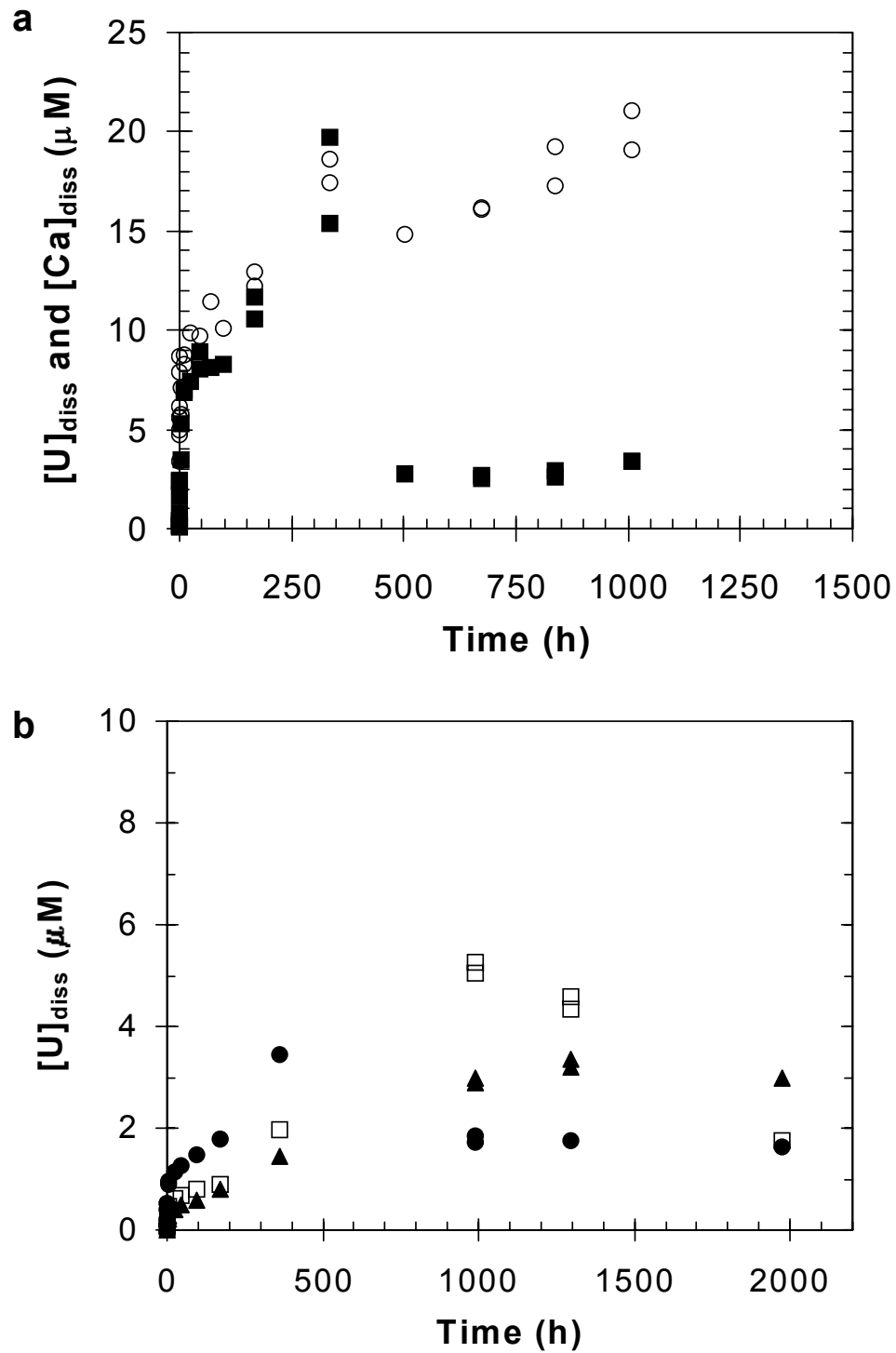


Figure D.4: Batch dissolution of becquerelite buffered at pH 6 (5 mM MES) in 0.1 M NaNO₃ solution with: a) dissolved uranium (■) and calcium (○) with no added calcium; b) dissolved uranium with 0.01 (●), 0.10 (□), and 0.50 (▲) M background Ca(NO₃)₂. Batch dissolution reactors contained total concentrations of approximately 160 μM uranium and 20 μM calcium.

D.4 Discussion

Calcium incorporated during the becquerelite synthesis was not tightly bound. It is quite possible that considerable calcium was extracted from the solid phase during the rinsing of the freshly synthesized material with deionized water. During batch dissolution in 0.1 M NaNO₃ solution, calcium ions in the interlayer were probably replaced by sodium ions by an ion-exchange process. As the ion-exchange process occurred, uranium was released to solution to levels supersaturated with respect to a solubility-limiting phase. The ultimate reprecipitation of uranium in a lower solubility phase was similar to the reprecipitation observed during batch schoepite dissolution experiments. In schoepite dissolution experiments, the reprecipitated phase was identified as a clarkeite-like sodium uranyl oxide hydrate phase by XRD and Raman spectroscopy (Chapter 5). Unfortunately the solid phase reprecipitated in the becquerelite batch reactors was not characterized, but it is reasonable to think that it was also a clarkeite-like phase.

Background dissolved calcium in batch reactors probably inhibited the incorporation of sodium into the interlayers. Calcium ions occupied the interlayer spaces throughout the batch reaction, maintaining a relatively stable phase that did not release significant uranium to solution. Cesium was also quite effective in limiting the release of uranium to solution during the dissolution of schoepite. The general result of incorporating sodium, cesium, or calcium into the interlayers is a decrease in the solubility of the solid phase. It would be informative to conduct schoepite dissolution experiments in calcium nitrate solution analogous to those conducted in sodium and cesium nitrate solutions.

From the final dissolved uranium concentrations in systems with background calcium, a solubility product for becquerelite can be calculated using the following dissolution reaction and solubility product:



$$K_{\text{sp}} = \frac{\{\text{Ca}^{2+}\}\{\text{UO}_2^{2+}\}^6}{\{\text{H}^+\}^{14}} \quad (2)$$

The uranyl ion concentration was calculated from the total dissolved uranium concentration by using the set of dissolved species presented in Table A.1, and ionic strength corrections were made according to the Davies equation. Calculated $\log K_{\text{sp}}$ values are 38.8 in 0.01 M CaNO_3 and 39.8 in 0.1 M CaNO_3 (no calculations were made for the 0.5M CaNO_3 system because of its high ionic strength). The calculated $\log K_{\text{sp}}$ values roughly agree with the values of 41.9 (Sandino and Grambow, 1994) and 43.2 (Vochten and Van Haverbeke, 1990) previously determined for synthetic becquerelite. The data of Vochten and Van Haverbeke were reinterpreted using the NEA database to yield a $\log K_{\text{sp}}$ of 41.4, in even better agreement with the values determined in this work (Casas et al., 1997). A natural becquerelite sample from Zaire was considerably less soluble with a measured $\log K_{\text{sp}}$ of 29 ± 1 (Casas et al., 1997). While natural samples are most representative of minerals found near ore deposits, synthetic phases may be more representative of the secondary phases formed on relatively short time-scales during the corrosion of spent nuclear fuel.